Light Scattering from Complex Rough Surfaces

Colette Turbil

SORBONNE UNIVERSITÉ
CRÉATEURS DE FUTURS DEPUIS 1257

cnrs
dépasser les frontières

SAINT-GOBAIN

THÈSE DE DOCTORAT
SORBONNE UNIVERSITÉ

Spécialité : Physique

École doctorale 397: Physique et Chimie des Matériaux

réalisée au laboratoire

Surface du Verre et Interfaces, UMR 125 CNRS/Saint-Gobain

sous la direction de Ingve Simonsen et Iryna Gozhyk

présentée par

Colette TURBIL

pour obtenir le grade de :

DOCTEUR SORBONNE UNIVERSITÉ

Sujet de la thèse :

Light Scattering from Complex Rough Surfaces

soutenue le 13 décembre 2018

devant le jury composé de :

M.	Mathieu HÉBERT	Maître de Conférence HDR, IOGS/UJM	Rapporteur
Mme	Anne TANGUY	Professeure, INSA Lyon	Rapporteuse
Mme	Agnès MAÎTRE	Professeure, Sorbonne Université	Examinatrice
M.	Gaël OBEIN	Maître de Conférence HDR, CNAM	Examinateur
M.	Kévin VYNCK	Chargé de Recherche, CNRS	Examinateur
Mme	Iryna GOZHYK	Ingénieure de recherche, SGR Paris	Encadrante
M.	Ingve SIMONSEN	Professeur, NTNU	Directeur

Contents

Chapter 1

Introduction

"Whenever there is any doubt, there is no doubt."
Sam, Ronin (1998)

Contents

When light interacts with an object, which can be of the centimeter scale or as small as a nanoparticle, two types of phenomena can occur. Light can be either absorbed or redirected by the medium, and this latter phenomenon is generally referred to as *light scattering*.

Usually, these two types of phenomenon coexist and their respective manifestations depend on the intrinsic properties of the object, in terms of material properties and spatial organization. Thus, a very large variety of complex physical effects can occur from the interaction between light and a surface, as schematically represented in Fig. 1.1. Light can simply be specularly reflected or transmitted, following the Snell relation, or either be diffusely scattered due to the surface roughness or due to inclusions of particles in the material itself. However, other effects, related to the specific structure of a surface can also occur. In this way, multilayer or periodic spatial structure can lead to interference or diffraction effects [1][2], inclusions of small metallic particles can induce plasmonics effects [3], or specific metamaterials organizations can even create physical effects that cannot be found naturally [4][5].

Due to large variety and complexity of these effects, they are usually studied independently from each other, considering model surfaces, which are thereby limited to a specific range of parameters. However in the case of real life samples and surfaces, these complex morphologies and structural organization coexist and give rise to exceptional

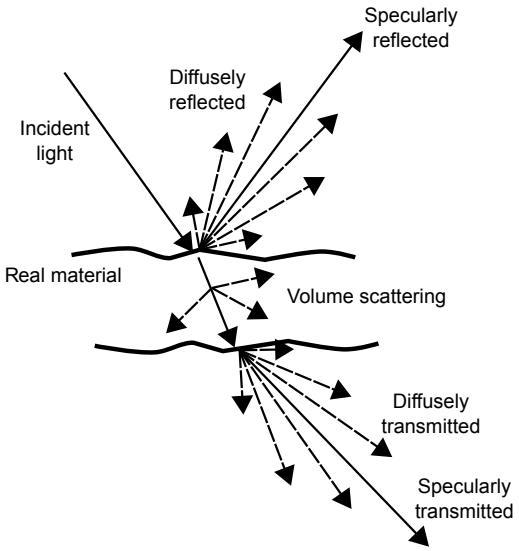

Fig. 1.1 *When light is incident on the real material, numerous light scattering phenomena can occur depending on the material intrinsic properties. Light can be specularly or diffusely reflected. The light can be scattered in the volume of the object. If the material is transparent to the light, this latter can also be specularly or diffusely transmitted.*

properties: as it is the case for the examples presented in Fig. 1.2. The lotus leaf is known for its high hydrophibicity properties which are conferred by its micrometer and nanometer scales surface morphology [6], the color of a butterfly wings originates from a complex photonic structure [7], or finally the complex nano-hair organization on the foot of the Gecko confers it exceptional adhesion properties [8].

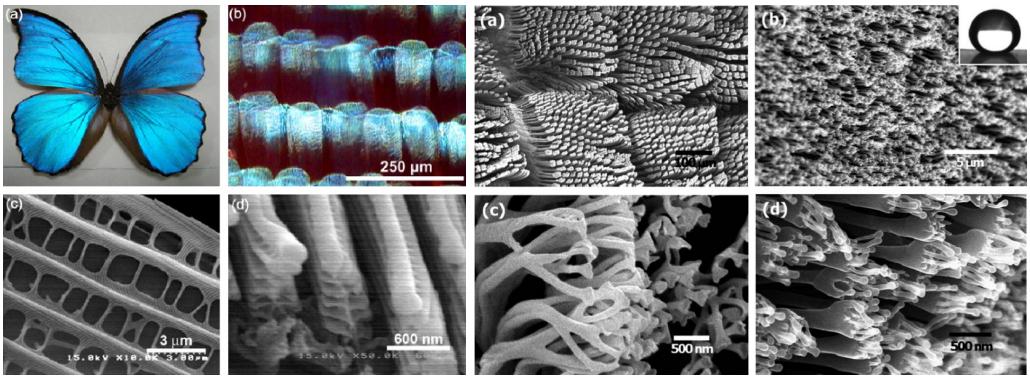

(a) (b)

Fig. 1.2 *Complex and multiscale morphological properties give rise to exceptional properties in the nature: (a) the complex photonic structure of the butterfly wings [7], or (b) the nano-hair organization of the Gecko [8].*

How to build a framework to understand optical properties of an object which is not a model case but rather higher degree of complexity? We address this problem in the case of the impact of surface roughness on optical properties. To this end, we will mainly rely

on the experimental characterization of the properties of both the surface itself and of the light that is scattered from it. Then, these experimental data will be compared to light scattering models. We choose to limit the study to the examination of rough surfaces.

Light scattering from rough surfaces is a physical phenomenon that has been extensively studied over the past decades [9][10][11]. However, the phenomenon is still not fully understood, due to the complex different scales of roughness or to the role of spatial organization of surface elements. Unfortunately, there is no analytic models to predict the optical properties, that is suitable for surface topography of arbitrary multi-scale range. Thereby, scientific community, from academic and industrial sectors, is still concerned about it.
This introductory chapter aims to describe some of the physical notions that are involved in the light scattering phenomenon, and that will therefore be discussed in the dissertation. Then the multiple motivations of the study will be presented, and finally, the organization of the dissertation will be described.

1.1 Light scattering phenomenon

Lets first describe some basic notions to deal with the light scattering phenomenon. When light impinges on an object, several light scattering phenomena can occur in different angular ranges, as presented in Fig. 1.3. Two theoretical limits (never observed in real-life surfaces) are perfect mirror-like reflection (Dirac), generally referred to as *specular reflection* and perfect diffused reflection, generally referred to as *Lambertian reflection*, respectively presented in Fig. 1.3(a) and Fig. 1.3(e). The theoretical specular reflection follows the law of Snell-Descartes [12] and is consequently unidirectional: it could only occur from a perfectly flat surface. On the contrary, in the case of Lambertian reflection [13], the radiance of the light is assumed to be equally distributed all around the sample, without any preferential direction. In reality, the light scattered from a rough surface in a mixed specular/diffuse scattering, as presented in Figs. 1.3(b)-(d), while its angular spread of intensity is related to the surface intrinsic properties and often difficult to forecast.

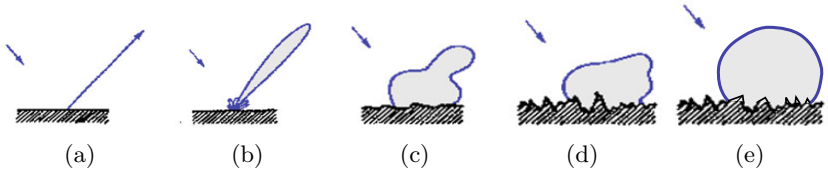

Fig. 1.3 *The two theoretical limits of the light scattering phenomenon are perfect specular reflection (a), and perfect Lambertian diffusion (e). However, in reality, the angular distribution of the scattered light is a mix between specular and diffuse reflection (b), (c) and (d). Adapted from [14].*

Then, depending on the material nature, part of the light can penetrate inside the medium after the refraction through the surface. Finally, part of the light that was re-

fracted in the material can be scattered in its volume and then be scattered at both interfaces, as described in Fig. 1.1. In the same way that the reflected light, the transmitted light can also have an arbitrary angular spread with direct transmission component (specular transmission) and diffused transmission component.
Our principal interest is then to describe the properties of the scattered light in terms of angular distribution, and thereby to evaluate in which directions and with which intensity the light is scattered from a rough surface. Indeed, the angular spread of the light scattered from a surface is directly related to the visual appearance: it is therefore of a particular interest.

The impact of the surface roughness and of the material nature, on the angular distribution of the scattered light can experimentally be illustrated. First, one considers two surfaces, A and B, made of the same material, but with different surface morphologies: the surface A being slightly smoother than the surface B, as presented in Fig. 1.4. The effect on the angular spread of the scattered light is rather significant: the light scattered from the surface A is mainly located along the specular direction, and on the contrary, in the case of the sample B, the light is scattered in a broader angular region. These different optical properties therefore lead to different macroscopic appearances: the sample A is glossier than the sample B.

Then, in order to study the impact of the nature of the material on the light scattering, two surfaces with the same morphology, but made of two different materials are selected: samples B and C. The sample B is made of a polymer mixed with black carbon, and the sample C is a glass sample. The angular distribution of the light scattered from these two surfaces are rather different, as presented in Fig. 1.5. In this case, the width of the angular distribution is quite similar, but their intensities are rather different. Yet, even in such simple case, it is not straightforward to explain the origin of the difference of optical properties between these two samples. It could be related to the difference of refractive index of the material from which they are made, or due to absorption or volume scattering effects caused by the black particles incorporated in the polymer.

The basic notions related to the light scattering phenomenon are then identified, and its main origins have been mentioned. The next section of this introduction chapter will then be dedicated to the study of the existing literature, concerning both the experimental measurement and modeling of the light scattering.

1.2 Literature on light scattering

One of the complexities of the light scattering problematic is that it involves many different scientific communities. Indeed, to cover the whole phenomenon, one must deal with the following fields: surface fabrication, characterization of the surface morphology and surface nature, characterization of the optical properties of the surface, and the modeling of light scattering. Despite the actual skills and knowledge that required these applications, it also requires costly experimental setups and powerful computational resources, in order to manufacture and characterize the examined samples, and to perform

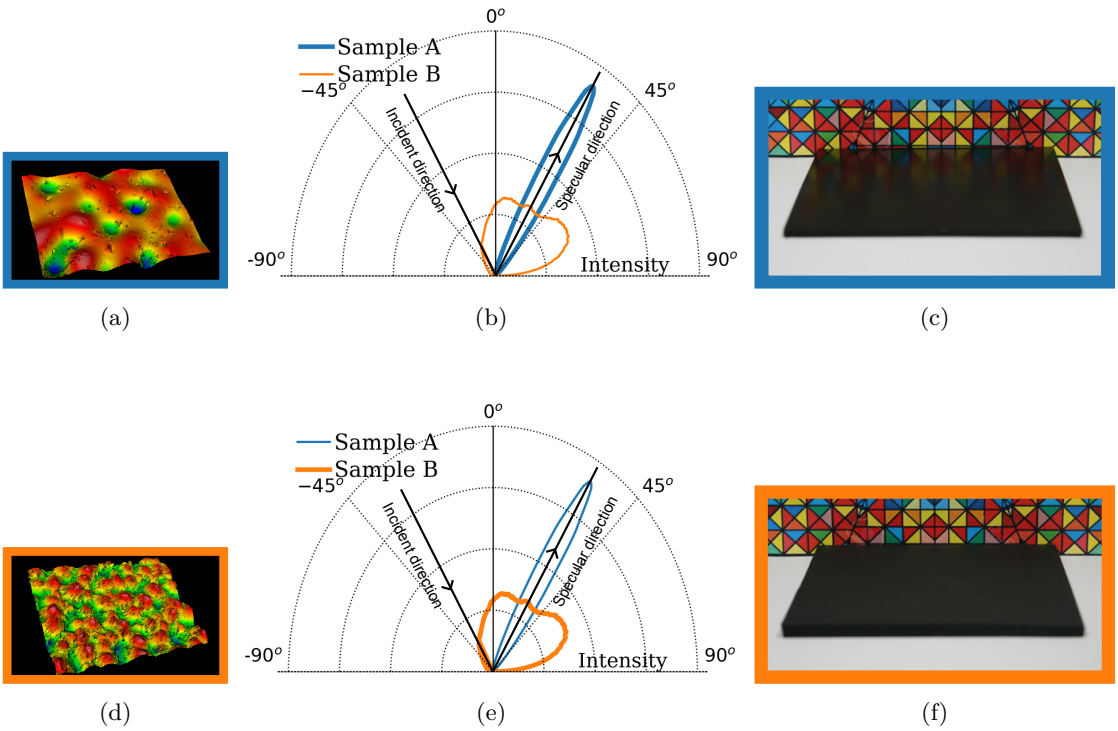

Fig. 1.4 *The light scattering properties and the appearance of a surface are related to its morphology. The two surfaces A and B are made from the same material, a blend of PDMS (which is described later in Sec. 2.1.1.2) and carbon black, but have different morphologies. Here (a) and (d) present the microtopography of the surfaces A and B respectively. The optical properties of A and B are measured in (b) and (e) respectively. Finally, the two surfaces A and B are respectively presented in (c) and (f). The microtopographies were measured by white light interferometry [15], the optical properties were measured with a goniospectrophotometer (see Sec. 4.2) using a white light illumination at 30° of incidence, and the photographs of the samples were taken in a light booth (Spectralight QC X-Rite), under D65 illumination [16].*

the modeling calculations. Due to these limitations, only few studies examining the whole phenomenon have been reported in the literature, and consequently, the subject remains highly challenging for the scientific community. On the other hand, as the light scattering phenomena are highly related to everyday life objects, its comprehension is of particular interest for industrial companies such as Saint-Gobain. In order to answer both academic and industrial questions related to light scattering phenomena, the FRAXOS project was launched in 2016 [17]. The FRAXOS project, in which is included this thesis work, aims to create a unique scientific environment consisting of industry (Saint-Gobain Recherche Paris) and the academic laboratory SVI (Laboratoire Mixte CNRS/Saint-Gobain Surface du Verre et Interfaces), supported by collaborating groups from INSP (Institut des NanoSciences de Paris) and ESPCI (Ecole Supérieure de Physique-Chimie Industrielles, Institut Langevin). In this way, combining the experimental and theoretical competences and resources of all these academic and industrial partners, all the aspects involved in light scattering phenomenon can thereby be covered.

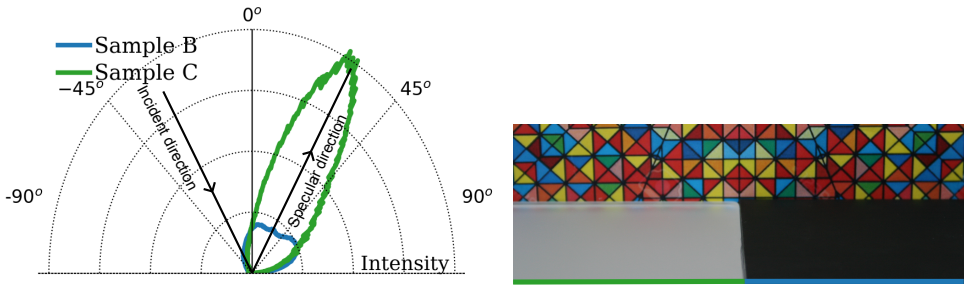

(a) (b)

Fig. 1.5 *Two surfaces with the same morphology but made of two different materials are realized: the sample B is made of a blend of PDMS and carbon black, and the sample C is a glass sample. In (a) the angular distribution of the scattered light and in (b) their macroscopic appearance are presented. The photo of the samples was taken in a light booth (Spectralight QC X-Rite), under D65 illumination, and the optical properties were measured with a goniospectrophotometer using a white light illumination at 30° of incidence. For the sake of readability, the intensity of the light scattered from the surface C is decreased by a factor 2.*

In this section, a non-exhaustive review of the models that exist to describe the light scattering properties of surfaces will be presented. Then, studies related to the experimental characterization of angular distribution of the light scattering will be presented.

1.2.1 Modeling of light scattering

As described in the introduction part of Sec. 1.1, the properties of the scattered light is highly related to the surface properties. As presented in Fig. 1.3, the properties of the scattered light become more complex to evaluate as the degree of roughness of the considered surface increases. Rigorous calculation methods can be employed to estimate the exact properties of the scattered light. However, if one wants to use them, without any approximations (rigorous calculations), they can require months (and even years) of cpu-time to perform, and are therefore really inconvenient. Consequently, approximate models were developed to overcome the time limitation of the rigorous calculations.

These approximate models are based on different assumptions and are usually related to a typical range of degree of roughness, and thereby one talks about models related to either *weakly rough surfaces* or *strongly rough surfaces*. This degree of roughness must also be related to the wavelength of the light that is considered. Thereby, the limits of the model are usually considered according to the ratio between the roughness degree, which is called the rms height (σ), and the wavelength of the incident light (λ). Actually, we will see in Sec. 3, that the description of the surface roughness cannot be restricted to the single value of σ, but we will keep this approximation for the introduction part.

Light scattering from weakly rough surfaces is usually described by the Rayleigh-Rice theory, also known as the small perturbation method (SPM) [9]. In this approach, the roughness of the surface is considered to be a small perturbation of the case of a perfectly flat surface. This assumption remains valid if the roughness is small compared to the wavelength of the incident light. Indeed, one can consider the *Rayleigh criterion* as the

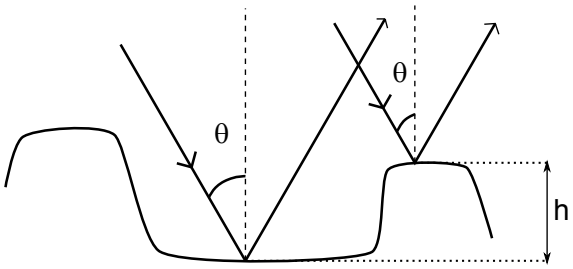

Fig. 1.6 *The Rayleigh criterion is defined considering two rays incident on a surface with typical height variation h, with an angle θ. Scheme adapted from [11]*

limit of the assumption [11]. The Rayleigh criterion is illustrated in Fig. 1.6: considering two planar waves incident on a surface, with irregularities of typical height h, with an angle θ. The path difference between the two rays is then:

$$\Delta r = 2h\cos\theta, \tag{1.1}$$

and hence the phase difference is:

$$\Delta\phi = \frac{2\pi}{\lambda}\Delta r = \frac{4\pi h}{\lambda}\cos\theta. \tag{1.2}$$

If the phase difference is small enough, the rays will almost be in phase, as in the case of perfect specular reflection (when $h = 0$). The Rayleigh criterion states that a surface can be considered as smooth, if $\Delta\phi < \pi/2$, which implies:

$$h < \frac{\lambda}{8\cos\theta}. \tag{1.3}$$

In the case of weakly rough surfaces, the link between the morphological and optical properties of surfaces can quite easily be obtained. Numerous experimental studies have been performed to compare the results of the SPM and experimental optical properties of relatively smooth surfaces [18][19][20]. However, according to Eq. (1.3), if one considers light at normal incidence, with wavelengths in the visible range, $\lambda = 500\ nm$, then h must be lower than 62.5 nm, which is rather restrictive.

The light scattering from rough surfaces, appears to be much more complicated than in the case of weakly rough surfaces [11][21]. Two approximate methods that are often used in the literature will briefly be described here: the microfacet theory and the Kirchhoff theory. A more detailed description of these two approaches is given in Sec. 5.

The microfacet theory is based on a geometrical optics approach, and the light is therefore considered as a collection of rays. The surface is assumed to reflect light as a collection of micrometric and flat reflective facets. The resulting scattered light depends on three components: the statistics on the orientation of such facets, the Fresnel term based on the refractive index of the material, and a masking/shadowing term (these three factors are detailed in Sec. 5.1.1)[22][23]. Models based on the microfacet theory are widely used in the computer graphics community due to their simplicity and relative efficiency [24]. However, as the microfacet theory is based on the law of geometrical optics, it assumes that the light diffraction and interference effects can be safely neglected.

Fig. 1.7 *The tangent plane approximation is a consistent approximation in the case of a small slope (a), but is rather inconsistent in the case of an abrupt slope (b). Schema reproduced from [11].*

Another method to model the optical properties of rough surface is based on the Kirchhoff theory [11]. The Kirchhoff theory is based on waves optics and can therefore correctly predict many diffraction effects. The Kirchhoff approach assumes that the properties of the scattered light at a point of a surface can be approximated by the light scattering properties of a plane that is tangent to the surface at the same point. This assumption remains valid for surfaces described by small slopes but breaks down for abrupt variations of heights, as illustrated in Fig. 1.7(a) and Fig. 1.7(b) respectively. However, this method is known to be rather approximate in the case of grazing angles of incidence and scattering, where multiple scattering starts to play an important role [11][25][26].

More exhaustive reviews of light scattering models based on the geometrical optics and physical optics can respectively be found in [27] and [28].

1.2.2 Experimental characterization of light scattering

The experimental study of the angular distribution of the light scattering from randomly rough surfaces is rather recent. This especially applies to the full angular radiance distribution of the scattered light, and when the polarization states of the incident and scattered light are detected. Indeed, the first experimental setups able to realize such measurements were designed in the 1970s: the angular distribution of the scattered light was then measured along a single plane (usually the plane of incidence), and with a limited angular resolution [29][30][31]. During the 1980s and 1990s, the capabilities of the experimental setups were increased, and the angular resolution of the measurements were significantly improved, up to several tenths of degrees [32][33], but the measurements remained related to model surfaces.

Then in 2003, the MERL (Mitsubishi Electric Research Laboratories) database was published [34]: in this case, the angular distribution of the scattered light from real-life materials were measured, as presented in Fig. 1.8.

In this case, the measurements were realized on the half-sphere around the sample (and not only along a single plane), considering a large number of angular configurations. Unfortunately, this database does not report the intrinsic properties of the materials that were characterized, and readers have therefore no information about the morphological properties or refractive indexes of the materials which were characterized. Consequently,

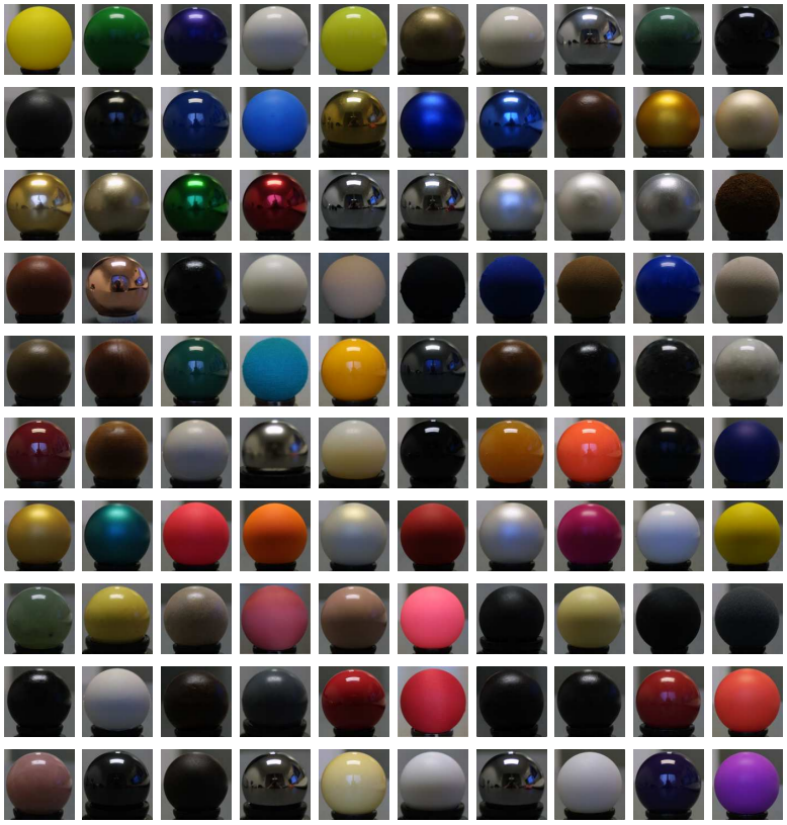

Fig. 1.8 *In 2003, a database including the experimental characterization of light scattering from 100 real life surfaces was published [34].*

such light scattering characterizations cannot be used to build physically-based light scattering models, but they were widely used for the conception of virtual rendering images.

Thanks to the extension of the experimental setups and the computing resources, studies on both experimental and modeling properties of light scattering have been presented since the last decade.

In 2001, McKnight et al. from the National Institute of Standards and Technology (NIST) published a work combining both experimental and modeling results of light scattering [35]. Three samples consisting of clear dielectric isotropic epoxy coatings were examined. Mappings of their morphologies were measured with two different interferometric microscopes, and their rms roughness (σ) were evaluated from 5 nm to 870 nm. Angle-resolved scattering measurements were performed with the STARR [36] at NIST, and as expected, the surfaces give rise to different light scattering distributions. Then the morphology mappings were used as input data for two approximation models based on the Kirchhoff theory. The first optical scattering approximation is related as phase integral approximation: which consists of an electromagnetic plane wave incident on a perfect conductor material. The second approximation is a scalar approach assuming that the local tangent plane assumption, and that the light is specularly reflected by the surface. This second method is more approximate but is less time consuming: according to the authors the computation time can vary from hours to few seconds. In the case of the two

rougher surfaces ($\sigma = 800\ nm$ and $\sigma = 150\ nm$), the two light scattering models give rise to similar results, which are consistent with the experiments. However, in the case of the smoothest surface ($\sigma = 5\ nm$), only the phase integral model forecast consistent results.

In 2011, Schröder et al. realized a similar study on three rough metallic surfaces, with roughness degree of $\sigma = 6\ nm$, $\sigma = 135\ nm$ and $\sigma = 320\ nm$ [37]. The morphology of the rough surfaces were evaluated by white light interferometry and atomic force microscopy. However, contrary to the study of McKnight et al. [35], the morphology mappings were examined and statistical parameters and functions were extracted from it, in order to statistically describe the surfaces. Then the optical properties of the samples were measured at several wavelengths and compared to the results of two different models (with the statistical data of the surface morphology as input) based on the Rayleigh-Rice (RR) theory and on the Generalized Harvey-Shack theory (GHS). The Harvey-Shack theory is similar to the Kirchhoff theory but it overcomes its limitations for high incidence and scattering angles [25]. For the smoothest surface, both RR and GHS predict consistent light scattering results. As expected from the RR approximation, as the degree of roughness of the surface increases, the RR predictions become poor. For the two rougher surfaces, GHS provides reasonable agreement, even if some discrepancies can be observed.

The last study, which is presented here, has been realized by Dong et al. in 2015 [38]. In this work, the authors measured the morphology of five metallic surfaces (one isotropic and four anisotropic surfaces) by white light interferometry (one millimetric mapping is realized for each sample). Then the authors extract normal distribution function (NDF) from this cartography. The NDF represents the distribution of the normal direction on each measured data point. The NDF are used in derived expressions of a microfacet model and of a Kirchhoff theory based model, in order to forecast the optical properties of the samples. In both cases, the results of the models are in good accordance with the experimental characterizations of the samples (both isotropic and anisotropic). However, due to the ray approximation, the authors stress that this approach is only valid to model first-surface reflection, and that consequently it only applies to materials such as metals. Unfortunately, we do not find information about the degree of roughness of the examined samples.

As realized in the three previous studies, the work described in this thesis aims to relate the morphological and optical properties of surfaces. In our work, some approaches used in the different studies will be applied:

- the surface morphology of the samples will be described by statistical parameters, as realized by Schröder et al. [37], in order to describe the light scattering properties of a "kind" of surface, and not a single surface.
- Schröder et al. [37] combine white light interferometry and atomic force microscopy to characterize the surface morphology at different scales. In our work, we will use three different experimental setups for this purpose.
- Following McKnight et al. [35], our study will be restricted to the study of isotropic surfaces (indeed, we will not perform scattering modeling on the anisotropic sample that we have).
- As Dong et al. [38], two models, respectively based on geometrical optics and wave optics will be compared to experimental results. Thereby we will be able to examine

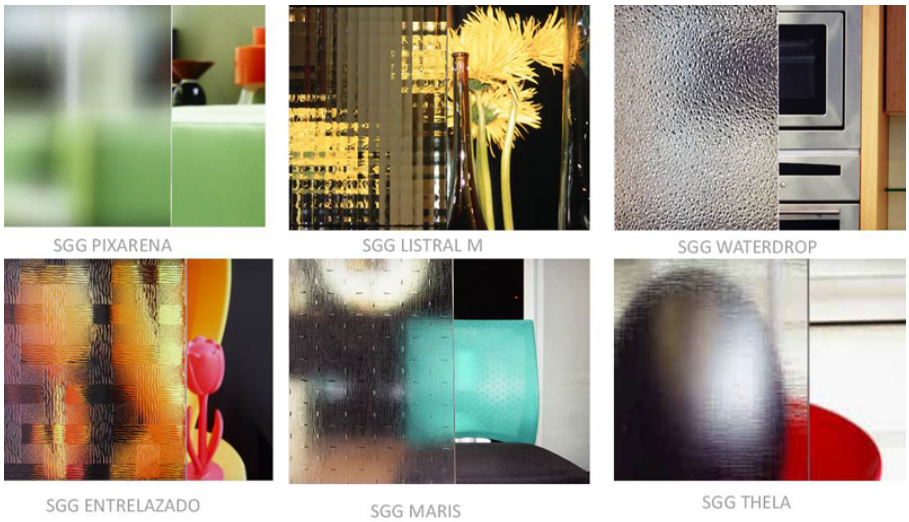

Fig. 1.9 *Saint-Gobain commercialized a wide variety of frosted glasses with very different appearances. The topography of each glass is obtained through different industrial processes. Images obtained from [39].*

the limits of both of these kinds of approaches.

However, in our case, the industrial surfaces that are considered are rougher than in the case of the three presented studies: indeed the roughness degree of our samples ranges from 0.9 μm to 5.2 μm.

1.3 Industrial motivation of the study

Saint-Gobain is a material producer and industrializes a wide range of rough surfaces with very different roughness characteristics: it includes cm-scale patterns on the surface of bricks, cement, refractors or glasses (as the ones presented in Fig. 1.9), to microscale in abrasion, blasting and drilling processes, and finally to nanometer scale in float glass.

Moreover, in the quest of high-performance products, Saint-Gobain exploits additional functionalities that can be obtained through treatments, which modify the physical properties of a surface. The goal of such surface functionalization is to add new properties like wetting, haptics and even some specific optical properties. Surface functionalization treatments involve mechanical or chemical impacts on the surface and deposition of thin films, by for example physical deposition like magnetron sputtering or wet coating techniques. Usually, particular topographies are required to confer new functionalities to the surface, but obviously they can also alter the visual aspect of the surface.

The visual aspect is not an essential criterion for all industrial sectors: indeed the aesthetic is not relevant in the case of mechanical equipment and tools or aeronautic pieces. However, it can be critical when objects and surfaces are intended for general public for everyday use. In such cases, manufacturers must couple functional and aesthetic properties and this can be far from trivial to achieve. The difficulty lays in:

- the complexity of the light scattering properties at some level of roughness,

- The fact that modification of a single parameter of the fabrication or functionalization process may result in modification of several morphological parameters to say nothing of the potential chemical or structural modifications within the material, which can modify its dielectric constant.

The interest for industrial material producer as Saint-Gobain is then double. If one can efficiently model the light scattering properties of rough surfaces, one could:

- deal with the forward problem that consists in forecasting optical properties from surfaces with known morphological properties. In this way, manufacturers would be able to realize digital prototyping, which is time, resources and cost saving. Moreover, such synthesis images could also be used in order to present the new products to customers on digital platforms.
- even if this case is much more difficult to achieve in practice, the understanding of the inverse problem, which consists of deducing the morphological properties from willed optical properties, will also be of significant interest. Indeed, it will open the possibility for the design of new surfaces. Designers and architects could imagine surfaces with interesting optical properties, and surface manufacturers could produce them according to their required morphological properties.

1.4 Objectives of the thesis

The main aims of this thesis are to perform and provide sets of suitable and reliable experimental characterizations of both the morphological and optical properties of rough surfaces, in order to experimentally validate light scattering models of different kinds in order to build a framework for validation of predictive optical models. Hence, based on the large range of abilities provided by the FRAXOS project, the main tasks of this thesis consist of:

- selecting and fabricating rough surfaces of interest for both the academic and industrial partners of the FRAXOS project,
- realizing a careful and exhaustive characterization of the morphological properties of the examined surfaces,
- measure the light scattering properties of the selected rough surfaces with high angular resolution and within several angular configurations,
- performing first comparison with light scattering models, in order to assess the relevance of the experimental data.

1.5 Organization of the thesis

This multidisciplinary thesis is organized in four main chapters that each covers one of the following aspects of the light scattering: the sample fabrication, the characterization of the surface roughness, the characterization of the light scattering and the light scattering models. These four chapters will be followed by a summary and conclusions chapter and by a final chapter that will highlight the perspectives of this work.

Thereby, Chap. 2 is dedicated to the description of the examined samples. Two kinds of samples are considered during this work: model samples and randomly rough surfaces. The model samples were realized by ourselves, and due to their fabrication process (which will be described), their morphology and their refractive index can be highly controlled and are consequently perfectly known.

On the contrary, the randomly rough surfaces were manufactured by different industrial processes, and consequently, their morphology can be quite complex with probably roughness of centimeter, micrometer and nanometer scales. Moreover, this morphology is random over the sample, and we therefore need to multiply the measurements to characterize it properly. All the available details about the fabrication process of the samples will be described in this chapter.

In Chap. 3, the whole characterization process of the morphology of the samples are presented. First, the three experimental setups that were used to measure the surface topography are described. Then, the parameters and functions which were chosen to evaluate the statistical properties of the random rough surfaces are described. The statistical properties of the random rough surfaces allow us to describe them in a global way. Thereby, the results of the light scattering models will be relevant for all the random rough surfaces described by these statistical properties. Finally, the experimental characterization of model surfaces and randomly rough surfaces will be presented.

Chapter 4 is dedicated to the characterization of the optical properties of the rough surfaces. First the parameters and functions chosen to describe the optical properties of the samples will be presented. We choose to use two kinds of descriptive indicators: angle resolved functions, which described the angular spread of the scattered light, and integral parameters, which consider the whole scattered light without taking into account its distribution over the surface. Then, the experimental setup used to characterize the angular distribution of the light, called goniospectrophotometer, will be presented. In the last sections of the chapter, the optical properties of both model and randomly rough surfaces will be presented. The analysis of the results will be realized keeping in mind their actual morphology, in order to see if morphological and optical properties can be simply related.

In Chap. 5, the light scattering models used to relate morphological and optical properties of randomly rough surfaces will be presented. First, one model and one numerical simulation of based on the law of geometrical optics will be described. Then, one model based on the Kirchhoff approximation will be introduced. In both cases, the results of the models will be compared to the actual optical properties of the samples. The potential limitations and discrepancies between modeled and experimental results will be discussed.

A recall of the main results obtained during the thesis will be realized in Chap. 6, highlighting the relation between experimental data and modeling results. Finally, the take-home messages and the perspectives in the context of the FRAXOS project or other potential future collaborations, will be presented in Chap. 7.

Chapter 2

Description of the studied samples

"The greatest teacher, failure is."
Yoda, The Last Jedi (2017)

Contents

As introduced in the previous chapter, there are two main quantities that determine the properties of the light scattered from a surface, namely its morphology and the refractive index of the material it is made from. The visual aspect of the surface is defined by its light scattering properties. One of the goals of this thesis is, in the case of rough surfaces, to link the experimental data of the surface morphology to its light scattering properties. This study therefore requires macroscopic samples with morphological parameters varying over a wide range, ideally with multiscale roughness. Choice of appropriate fabrication techniques is therefore vital for the success of the whole study.

There are two approaches that can be used to study the link between the morphology of a surface and its optical properties:

- Studying model samples, covering a wide range of morphological parameters, as well as made of different materials in order to identify which range of morphological parameters impacts at most the spatial distributions of light scattering;
- Studying samples with different visual properties but obtained with the same or similar technique in order to identify the changes in the morphology that are responsible for the modification of the spatial distributions of light scattering.

In this thesis we explored both of these approaches. Through patterning of glass surfaces we fabricated simple model samples with pre-defined morphology. Since those simple model surfaces only cover a narrow range of the real-world morphologies, we tried to identify industrial samples with notable differences in their visual aspects. In this way, two other sets of samples, both manufactured by industrial processes that generate complex random morphologies, were included in this study: aluminum blasted samples and frosted glasses.

2.1 Simple model surfaces

Probably the simplest non-flat model surface profile is a periodic one. If periodicity is given along one or two of the surface axes, we refer to it as 1D or 2D surfaces respectively. The initial scope of the model 1D and 2D surfaces was to analyze how the aperiodicity, the profile smoothing and the additional sub-micrometer roughness impact the optical properties of periodic microstructures. However, at the end, the study of the impact of the sub-micrometer roughness was discarded due to the lack of time.

Various fabrication techniques allow to produce controlled microscale patterns over macroscopic sample sizes: lithography techniques, laser ablation, two-photon polymerization. Electron-beam lithography (often referred to as e-beam lithography) is a well-documented and widely used technique that consists of scanning a focused beam of electrons over a surface coated with an electron-sensitive layer. The electron beam changes the solubility of the layer, enabling selective removal from the initial layer [40]. This technique allows for the design of custom patterns of sub-10 nm spatial and height resolution [41]. Unfortunately, e-beam lithography is too costly for fabrication of centimeter-size surfaces, due to the scan speed of the focused electron beam.
Other techniques, such as photo-lithography, also consist of locally changing the solubility of a uniform layer (resin) to realize custom patterns [40]. The selection of the exposed and non-exposed areas is determined with a mask that is placed between the coated resin and the illumination source. The mask is designed to be locally permeable to a range of wavelengths. In this way, the light exposure can be quickly realized on large samples. However, the use of such mask drastically decreases the lateral resolution of the pattern due to light diffraction. Depending on the wavelength of the incident source, lateral resolution varies from hundreds of nanometers to micrometers. Moreover, due to the fabrication technique, this is not straightforward to design structure with aspect ratio (height of the structure to width of the structure) bigger than one.

Finally, the nano-imprinting (NI) technique, introduced by Chou [42], consists of replicating an existing surface (referred to as master) on a flat substrate with the help of a mold (the technique is described in detail in Fig. 2.2). We have chosen to apply this technique in the current work, due its significant know-how at SVI laboratory and its successful application to various previous projects [43][44][45]. For example, Rivetti and collaborators used NI to design superhydrophobic silica surfaces and to study the impact of the surface morphology on the wetting properties [46], Brudieu et al. used NI to produce light-trapping structures for photovoltaics [47].

The NI process presents two main assets. First, almost all surfaces can be replicated by this procedure: one only has to check that there is no particular adhesion between the mold and the master surface. In this way, the surface elements picked from existing surfaces (man-made or not) or especially designed surfaces, of different scales (from centimeters down to tens of nanometers) can be replicated with good fidelity. Secondly, the surface of interest can be replicated in a wide range of materials, from transparent to opaque materials, while their refractive index can be varied over a wide range. For instance, Brudieu et al., in their work on Bragg mirrors made with wet-coating techniques, showed the possibility to vary the refractive index from 1.24 to 2.12, by doping the sol-gel matrix with latex nanoparticles (resulting in the air nano-bubbles once the latex is burned) or TiO_2 sol-gel matrix [48].

NI can be applied to pattern a thin layer coating on a substrate, but it can also be used to replicate the surface on the bulk material itself (which allows avoiding any possible interface effects). This can be realized with polydimylsiloxane (PDMS), a transparent viscous material, which can be doped with colored particles to become opaque.

The following section gives a detailed description of the techniques used for the fabrication of the model surfaces and their final geometry.

2.1.1 Fabrication of the model surfaces

Fabrication of the model surfaces is at least a 2-step process: fabrication of the master surface and nano-imprinting (which is itself a 2-step process: fabrication of the mold and surface replication). Then, more elaborated shapes can be produced by additional steps and iterations of this generic 2-step process.
Several techniques exist to design surfaces with high control of the morphology, as mentioned in the introduction of Section 2.1. The master surfaces developped in this work were made by photolithography, since this technique is available at SVI and compatible with our requirements in terms of dimensions of the sample and size of the structure. However, the master samples in themselves, do not correspond to our requirements for the model samples due to some properties the photoresist material: too high refractive index (2, to be compared with the 1.46 of glass in the visible spectrum), toxicity and ageing. Thereby the nano-imprinting stage was necessary. The detailed descriptions of the fabrication of model surfaces by photolithography and by nano-imprinting are given in Fig. 2.1 and Fig. 2.2 respectively.

2.1.1.1 The photolithography process

In this study, a negative photolithography process is used to realize the masters of the model surfaces. It can be divided onto several steps that are summarized in Fig. 2.1.

Realization of the photolithography mask
The photolithography mask is used to design the pattern of the master surface. It is placed between the master surface and the light source, to locally block the light exposure. In this way, only selected parts of the surface are chemically modified (due to light exposure). The mask design must be in accordance with the nature of the photolithography process: in case of positive photolithography, the light exposed resin will be removed

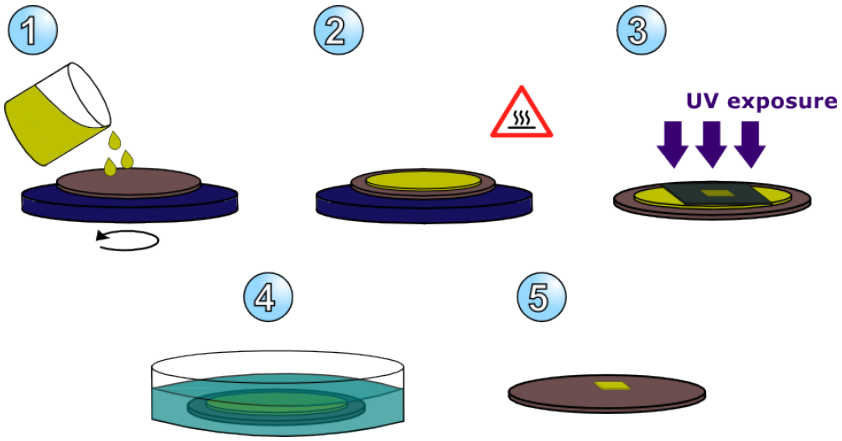

Fig. 2.1 *The photolithography process can be divided onto 5 steps: 1) Deposition of the negative photoresist layer on a clean wafer by spin coating. 2) First soft-baking to evaporate solvent. 3) Thanks to the mask, parts of the negative resin is insolated by UV. Only the insolated resin is cross linked. 4) The wafer substrate is dipped in the developer to remove the uncross-linked resin. 5) The master surface is realized, it can be hard backed to consolidate the structure.*

from the structure. On the contrary, in case of negative photolithography, the exposed resin remains on the sample. The surface of the mask is printed with a UV-opaque ink on a transparent substrate, with high precision inkjet (SELBA S.A, Switzerland).

Deposition of the photoresist (Fig. 2.1 steps 1 and 2)
The SU-8 2015 negative photoresist (MicroChem, USA) is spin-coated on a clean wafer substrate. The spin coating parameters (velocity, ramping up and time) are optimized to achieve the required thickness of the final photoresist layer. Then, the sample is soft baked on a hot plate at 110°C during 180 s (the temperature and duration of the baking were optimized for the different master surfaces).

UV treatment with lithography mask (Fig. 2.1 step 3)
The previously designed mask is placed on the photoresist layer, and the UV exposure is performed (UV-KUB, KLOE setup). Thanks to the lithography mask, only parts of the photoresist are exposed to the UV light and will therefore be cross-linked.

Wafers development (Fig. 2.1 steps 4 and 5)
After postbaking at 110°C during 180 s on the hot plate, the wafer is developed in the SU-8 developer (MicroChem, USA) twice during 60 s and washed in isopropanol to remove the developer overflow. After the development step (step 4), only the cross-linked photoresist remains: the final structure is shaped. Finally, the master is hard baked at 150°C during 15 min.

2.1.1.2 The Nano Imprint process

Nano Imprint (NI) is a highly controllable and efficient process to control the morphology and the physical nature of the produced samples. It can be summarized into several steps

which are presented in Fig. 2.2.

Master surface (Fig. 2.2 step 1)
First, the master surface is selected. The masters of the model surfaces described here have been fabricated by photolithography, as described in Fig. 2.1. NI allows to replicate a surface topography ranges from the nanometer to the centimeter scale. It can therefore be applied on a large panel of surfaces.

Mold fabrication (Fig. 2.2 step 2 and 3)
The mold is obtained by pouring a blend of PDMS (polydimethylsiloxane, (Sylgard 184, Neyco)) with a reticulant agent (also furnished by Neyco) in a 9:1 proportion, on the original master surface. The PDMS material (which is in a liquid state) closely conforms the morphology of the master surface. The PDMS turns to the solid state during a reticulation process, after 4 hours at $80°C$. The PDMS mold can then be demolded. Its morphology is the negative of the master surface.

Preparation of the silica solution (Fig. 2.2 step 4)
The hybrid silica solution is obtained by blending 5 mL of MTEOS (methyltriethoxysilane, Sigma Aldrich, Germany), 1 mL of absolute ethanol and 3 mL of hydrochloric acid (HCl) solution in deionized water with pH=2. The blend is sterred for 45 min at $60°C$ in hot-water-bath, and then cooled at room temperature. The mixture is then spin-coated on a clean glass substrate (of typical size of $5 \times 5\ cm^2$), at 1000 rpm during 60 s, to obtain a micrometric homogeneous layer. The thickness of the silica layer can be tuned from 1 to 5 μm, by modifying the MTEOS composition of the blend and/or adjusting the spin-coating conditions.

Put the mold in contact with the silica layer (Fig. 2.2 step 5)
The mold is gently put in contact with the silica layer. The contact is ensured by adding loads on the mold. The glass sample and the mold are then heated at $45°C$ for 45 min to ensure filling of the mold's cavities. The temperature is then increased to $110°C$ to complete the cross-linking of the silica layer. Finally, the substrate and the mold (still kept in contact by the loads), are cooled to room temperature: the silica layer is then solidified.

Removal of the mold (Fig. 2.2 step 6)
The PDMS mold can gently be removed from the glass substrate. The pattern of the initial master surface is then replicated on the glass substrate. The PDMS mold may be reused many times to replicate the initial surface of the master.

2.1.1.3 Geometry of model samples

All fabricated model surfaces have a similar structure to the one shown in Fig. 2.3. Each sample consists of a glass substrate (2 mm thick) with a patterned hybrid silica layer of micrometric thickness on its top. In this case, the hybrid silica solution is used to fabricate a patterned structure with a refractive index as close as possible to the refractive index of the glass substrate. The refractive index of the hybrid silica layer was evaluated

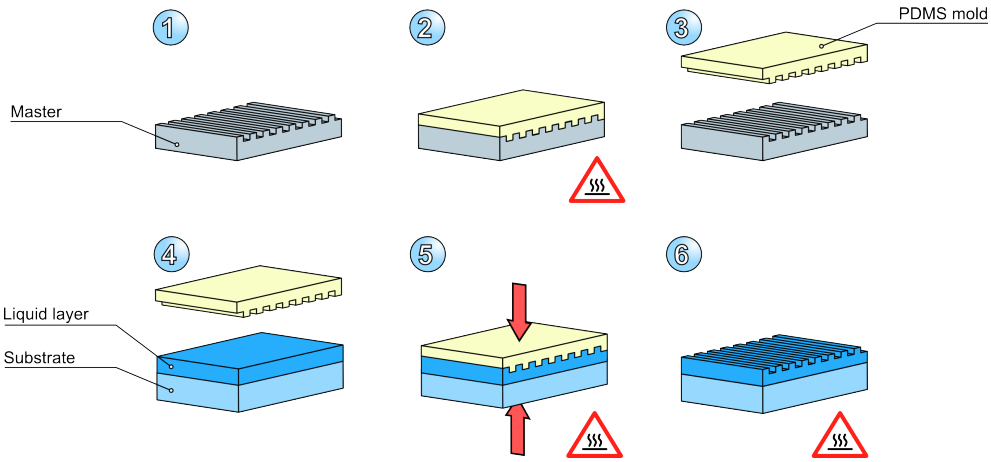

Fig. 2.2 *The Nano-Imprint process is divided into 6 steps: 1) Fabrication or selection of the master surface. 2-3) Fabrication of the PDMS mold: negative surface of the master. 4) Deposition of the liquid layer on the substrate. 5) Contact of the PDMS mold on the liquid layer with pressure and temperature control. 6) Replica of the initial master surface on the substrate.*

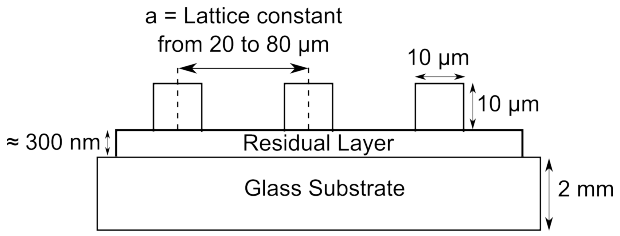

Fig. 2.3 *Schematic representation of the model samples: a 2 mm thick glass substrate with a micrometric pattern on its top.*

(combined ellipsometric and spectrometric measurements) to be 1.46 at 550 nm, which is close to the refractive index of the glass substrate (1.50). In this way, strong optical effects at the interface should be avoided.

For 1D periodic samples, the micrometric pattern consists of line gratings, and for 2D periodic samples, it consists of cylindrical pillar gratings. A residual layer between the glass surface and the micrometric pattern is necessary to provide adhesion. This layer remained homogeneous on the surface and was only 300 nm thick, in order to avoid effect of light guiding.

Together with the lattice constant of the periodic arrangement, a, we use another parameter to differentiate the samples, namely the surface covering ratio ρ, defined as:

$$\rho = \frac{S_{pattern}}{S_{cell}}, \tag{2.1}$$

where $S_{pattern}$ stands for the area of the flat upper part of the pattern, and S_{cell} for the area of one unit cell.

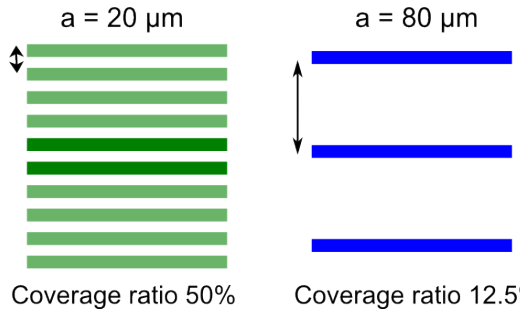

Fig. 2.4 *Spatial organization of the 1D model surfaces: lines gratings of 10 µm width organized with lattice constant comprised between 20 µm to 80 µm.*

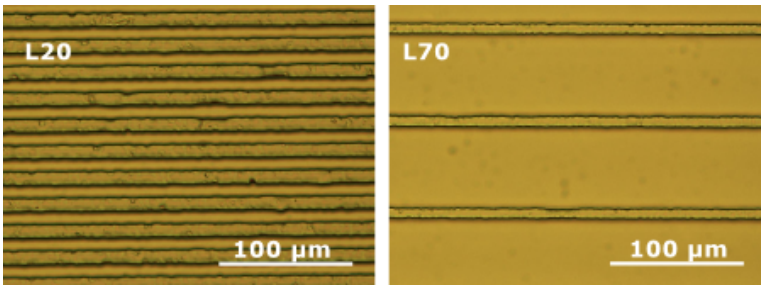

Fig. 2.5 *Optical microscope images of L20 and L70, fabricated by NIL.*

2.1.2 1D model surfaces

1D model surfaces are organized as line gratings. We initially fabricated gratings with a rectangular cross-section. Then the shapes of these gratings were smoothed through thermal relaxation.

2.1.2.1 Line gratings with rectangular cross-section profiles

The cross-section of each rectangular line was 10 μm wide and 10 μm in height. Seven molds were realized with different lattice constants, ranging from 20 μm to 80 μm by steps of 10 μm, which corresponds to a covering ratio from 50% to 12.5%, as presented in Fig. 2.4. The covering ratio is defined as:

$$\rho_{1D} = \frac{l}{a}, \tag{2.2}$$

where l denotes the width of the line and a the lattice constant of the grating (see Fig. 2.3). For the sake of simplicity, the line grating samples will be referred as samples 'L' followed by the corresponding lattice constant: in this way, the line grating sample of period 20 μm will be denoted as 'L20'.

The NIL process was applied to produce all the line gratings. Figure 2.5 presents two optical microscope images of L20 and L70, respectively.

2.1.2.2 Line gratings with smooth cross-section profiles

Due to the photolithography fabrication process, the produced structures are rectangular lines. However, it is possible to slightly and progressively modify the edges of the

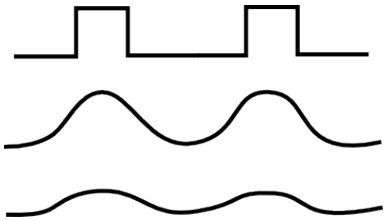

Fig. 2.6 *Schematic representation of the evolution of the structure during the thermal relaxation process*

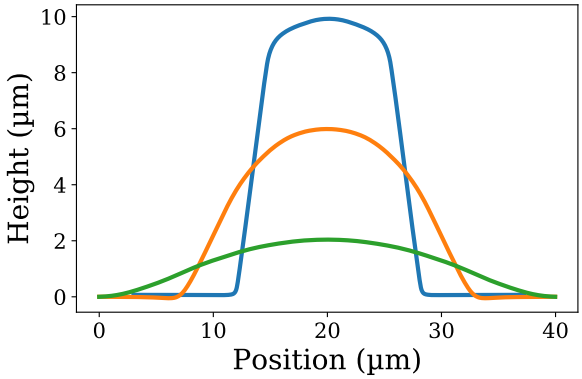

Fig. 2.7 *Profiles of three different relaxed line gratings obtained by thermal relaxation. The three profiles were obtained after 0 min (blue), 120 min (orange) and 810 min (green) of relaxation time.*

structures by another experimental procedure. Instead of using the hybrid silica solution (described in Sec. 2.1.1), the NIL process is performed using a solution of Poly(methyl methacrylate) (PMMA): a thermoplastic polymer. The solution is obtained by mixing a PMMA powder (25 % by weight) and a 4-Methyl-2-pentanone solution. Then, the NIL procedure is followed as described in Sec. 2.1.1, to fabricate a rectangular line grating of PMMA.

Thanks to its thermoplastic properties, the PMMA can be relaxed by heating it to a temperature that is above its glass transition temperature (evaluated at $110°C$). The polymer then goes back to liquid state. Thanks to surface tension forces, the PMMA structure gets gradually smoothed, while its period remains constant, as schematically represented in Fig. 2.6. When the desired structure is obtained, the PMMA is cooled to room temperature and goes back to the solid state. We refer to this experimental procedure as *thermal relaxation*. Such experiments were previously realized at SVI by Teisseire et al.[49].

The thermal relaxation procedure was applied to line gratings of 40 μm period. In this purpose, PMMA line gratings with rectangular cross-sections were produced. In total, 13 identical samples were placed in the oven at $130°C$. They were removed one by one from the oven after different baking times: from 15 min to 810 min. We finally obtain 13 samples with different smoothed cross-sections and thereby different surface slopes: Fig. 2.7 presents three of them. All the relaxed profiles are described in Sec. 3.3.1.

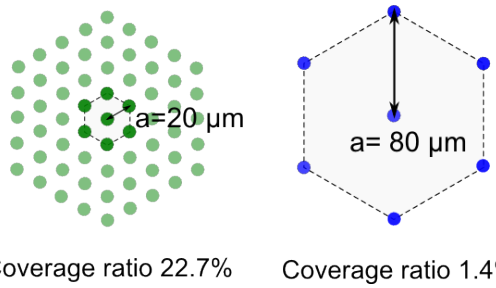

Fig. 2.8 *Spatial organization of the 2D model surfaces: cylindrical pillars of 10 µm diameter organized within an hexagonal lattice. The lattice constant varies from 20 µm to 80 µm.*

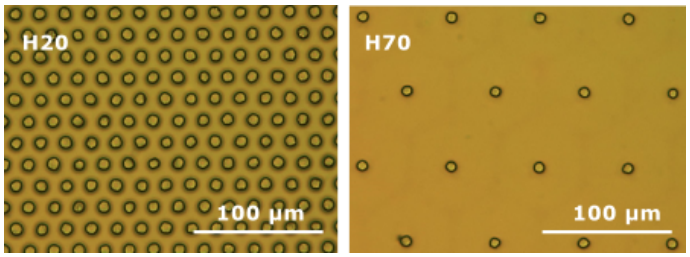

Fig. 2.9 *Optical microscopy images of samples H20 and H70, fabricated by NI.*

2.1.3 2D model surfaces

2D model surfaces are organized as pillar gratings. We initially fabricated gratings with hexagonal organization of cylindrical micropillars (10 μm height and diameter). Then the periodic spatial arrangement is broken by introducing a random dispersion of the positions of the pillars.

2.1.3.1 Periodic arrangement of pillars

The cylindrical pillars of the 2D model surfaces are organized as hexagonal lattice. Each pillar had a 10 μm diameter and 10 μm height. Seven molds were realized with different lattice constants, from 20 μm to 80 μm by steps of 10 μm, which corresponds to a covering ratio from 22.7% to 1.4%, as presented in Fig. 2.8. The covering ratio is defined as:

$$\rho_{2D} = \pi \frac{\sqrt{3}}{6} \frac{d^2}{a^2}, \tag{2.3}$$

where d denotes the diameter of the pillar and a the lattice constant.

For the sake of simplicity, the hexagonal pillar gratings will be referred to as samples 'H' followed by the corresponding lattice constant: in this way, the pillar grating surface with 20 μm period is denoted as 'H20'. Photographs from optical microscopy of the samples H20 and H70 are presented in Fig. 2.9.

2.1.3.2 Random arrangement of pillars

Periodic arrangement of pillars induces several diffraction-related effects that will be discussed in Sec. 4.3. In order to decouple diffraction effects induced by the periodic arrange-

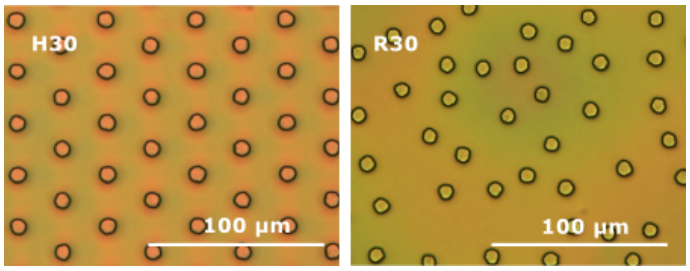

Fig. 2.10 *Optical microscopy images of H30 and R30. In both samples, the geometry of individual pillars (10 µm height and diameter) and the pillar covering ratio (10%) are identical. The spatial arrangement of the pillars is different: hexagonal lattice for H30 and random dispersion for R30.*

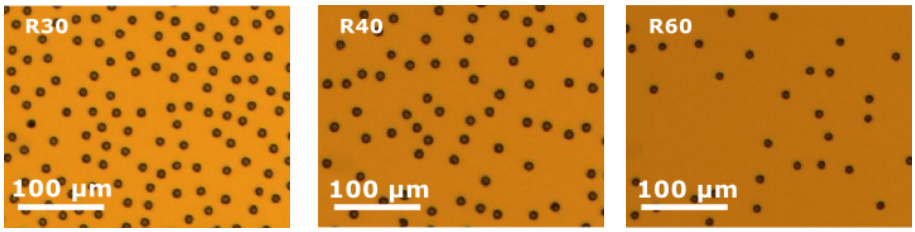

Fig. 2.11 *Optical microscopy images of R30, R40 and R60, surfaces with respectively* 10%, 5.6% *and* 2.5% *of pillars covering ratio, fabricated by NIL.*

ment of several pillars, and the effects induced by the shape of one single pillar, surfaces with randomly dispersed pillars but similar surface covering, were fabricated. For the sake of simplicity, such samples are referred to as 'R' (for 'random'), followed by the value of the lattice constant that a corresponding hexagonal lattice will have of the same surface covering ratio. For the sake of comparison, between hexagonal and random pillars organizations, the dimensions of individual pillars (height and diameter) and the covering ratios of pillars were identical. For example, the sample R30 is manufactured keeping the same pillar covering ratio as H30 (10% of covering). Optical microscopy images of samples H30 and R30 are presented in Fig. 2.10. However, pillars are not fully randomly dispersed on the surface, due fabrication constraints, the following requirements were met:

- in order to avoid pillars intersection and fabrication issues, the minimum distance between the outer edges of two neighboring pillars must be at least 10 μm,
- Pillars are randomly dispersed over a 1×1 cm^2 area, on which the required pillar covering ratio is obtained. Then, this $1cm^2$ area is replicated 25 times to design the 5×5 cm^2 final area,
- Due to the replication of the $1cm^2$ area, the constraint on the intersection and minimal distance between pillar must be enlarged. In this way, a 10 μm width band along the edges of the $1cm^2$ area are free of pillars.

Three types of surface with random pillar dispersion were manufactured : R30, R40 and R60 (Fig. 2.11), with respectively 10%, 5.6% and 2.5% of pillars covering ratio.

2.2 Complex rough surfaces

Surfaces can be produced with several manufacturing processes, such as casting, molding, coating, polishing... Those industrial processes lead to a large variety of surface morphology. In contrast to the model surfaces described in Sec. 2.1, surfaces obtained with such industrial processes are rather complex. Indeed, these manufacturing processes give rise to "real" surfaces: even if their morphology can be approximately controlled at a large scale, we cannot control the position, height and width of specific elements of the surface. Moreover, the fabrication processes are usually composed of tens of parameters, and each of them can strongly impact the final morphology of the surface. In this way, the produced complex surfaces can have roughness components at different scale levels: one can easily imagine a centimeter waviness implied by a first manufacturing process (such as pressing or rolling) with an additional micrometer or nanometer scale roughness component on top, arising from a second fabrication procedure. For these reasons, a statistical approach to describe the surface morphology is required to account for the randomness and the complexity of these surface morphologies.

Two kinds of rough complex surfaces, produced by two different manufacturing processes are presented here. First, several sets of blasted metallic surfaces are examined. Varying the parameters of the blasting process (which is described in Sec. 2.2.1), one can significantly alter the visual aspect and then the optical properties of such surfaces. Then, five frosted glass samples which have been manufactured by different fabrication techniques are examined. These latter surfaces present different visual aspects, from slightly blurring transmission properties to highly diffuse ones. In both cases, our objective is to establish links between the morphology induced by a manufacturing process and the optical properties of the surfaces.

2.2.1 Blasted metallic surfaces

Abrasive blasting, also known as sandblasting, is a mechanical technique of surface treatment. It consists of propelling a high pressure stream of abrasive material on a surface in order to modify its superficial structure. This technique can have several purposes: prestress operations, in order to improve the mechanical properties of the treated surfaces ; or surface cleaning and finishing to modify the visual aspect of the surface. The final properties of the treated surfaces are related to several parameters of the process, such as:

- The sample material.
- The material, shape and size of the abrasive particles.
- The manufacturing parameters such as the flow rate and the direction of the particle stream.

Industrial sectors, such as automotive and aerospace, use the blasting process to improve the physical properties of structural items. Those physical properties are usually related to the topographic properties of the surface. Thereby, Slatineanu et al. [50] studied the relation between fabrication parameters (average dimensions of particles, distance between the blasting nozzle and the surface, angle between the surface and the particles

stream) and simple roughness parameters such as rms roughness, and find empirical laws to describe tendencies. The rms roughness has appeared in several recent studies which aimed to correlate it to various physical properties, such as the surface wettability [51] or the covering ratio of post-blasting coatings [52]. However, to the best of our knowledge, there is no study that relates the fabrication parameters of blasting to an extended characterization of the resulting surface morphology, including a larger range of topographic parameters.
Blasting process is also employed to produce a wide range of visual aspects for luxury objects (such as watches, smartphones,...). By varying the size and/or the shape of the particles, a wide range of visual aspects can be achieved. However the optical properties of such surfaces, that are highly related to their aesthetic, have not been studied yet.

The blasted surfaces which are studied here, have been manufactured by ZirPro, a business of the Saint-Gobain company, located at the research center Saint-Gobain Research Provence, in Cavaillon, France. ZirPro commercializes a wide range of high-performance particles to blast surfaces made of different materials. Working in collaboration with J. Cabrero, research engineer from ZirPro, this study aims to improve the knowledge of Saint-Gobain regarding the morphological and optical properties of blasted metallic surfaces. In this purpose, several sets of aluminum blasted samples were manufactured with different fabrication parameters. Nevertheless, some fabrication parameters are fixed for all blasted samples that we study: abrasive particles are propelled by compressed air, at normal incidence onto the surface. The samples produced in this manner as well as the untreated (raw) aluminum samples are presented in the following subsections.

2.2.1.1 Untreated aluminum sample

All studied samples are manufactured from $5 \times 5\ cm^2$ area of a 1 mm thick plate of a 6061 aluminum alloy [53]. The plate is shown in Fig. 2.12. The sample looks very glossy at grazing angles. Figure 2.12 also reveals some strong anisotropy: 1D grooves aligned with one of the sample edges. These superficial defects can easily be explained by the manufacturing process of such metallic plates, which are produced by the rolling process: the metal is passed through two rolls to obtain a metal sheet of uniform thickness. It is widely agreed that defects on the surface of the rolls can imply such anisotropic grooves on the rolled metal [54]. Those aligned grooves are easier to observe at the microscopic scale with the use of an optical microscope, as presented in the right panel of Fig. 2.12. The typical distance between two consecutive grooves is around 10 μm.

2.2.1.2 Variation of the beads diameter

The first set of samples is composed of three blasted surfaces. Aluminum plates are blasted by spherical ceramic beads with varying diameters: 45-90 μm, 125-250 μm and 400-600 μm. For the sake of simplicity, these three different diameters will respectively be referred to as: *small*, *medium* and *large*. As shown in Fig. 2.13, the three samples have different visual aspects: the microstructure of the surface gets more visible when the bead size increases. Moreover, the initial anisotropy of the raw aluminum plate seems to be suppressed by the blasting process.
Through the observation with the microscope (Fig. 2.14), the increase of the size of the

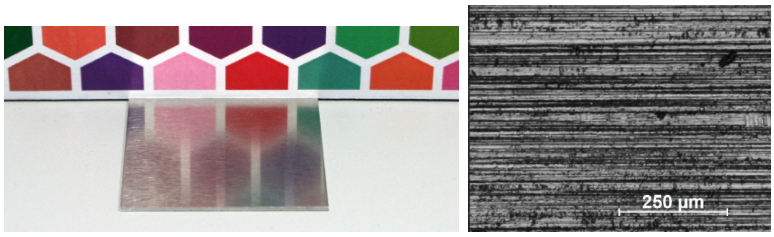

Fig. 2.12 *Left: Photograph of the raw aluminum sample in a light booth (Spectralight QC X-Rite), under D65 illumination. Right: Microstructure of the raw aluminum sample observed with an optical microscope.*

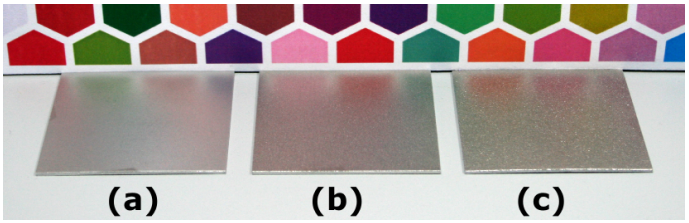

Fig. 2.13 *Photograph of the three samples treated with different bead diameters: (a) small beads: 45-90 µm, (b) medium beads: 125-250 µm and (c) large beads: 400-600 µm, in a light booth (Spectralight QC X-Rite), under D65 illumination.*

microstructure elements appears obvious. The size of the craters, formed by the impacts of the beads, becomes larger when the diameter of the beads increases. From a quick evaluation of the microscopy images, the typical diameter of the craters ranges from 3-6 μm, 50-60 μm to 100-120 μm for the three increasing granulometries respectively.

2.2.1.3 Variation of the covering ratio

The second set of samples is composed of four blasted surfaces and is presented in Fig. 2.15. The aluminum plates are all blasted with spherical beads of 125-250 μm diameter (medium beads). The duration of the blasting treatments is varied between the four samples. The covering ratio of impact of the surface is then varied. The covering ratio of blasted surface is empirically evaluated with surfaces of reference. Four different covering ratios are then achieved, 30%, 50%, 75% and 93%. This set of samples allows to observe the anisotropy erasure during the blasting process.

For the untrained eye, it appears difficult to visually discern those samples (Fig. 2.15). However, looking at the microscale of the samples in Fig. 2.16, the variation of covering ratio is much more obvious. Indeed, the large bright areas of the pictures can easily be

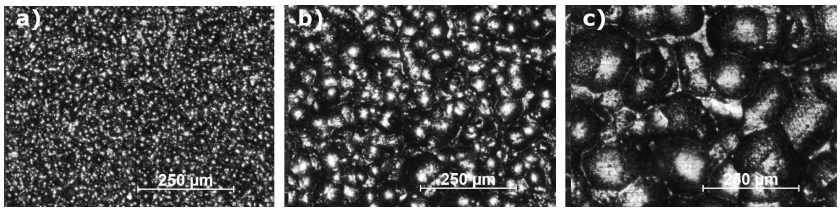

Fig. 2.14 *Microstructure of the three samples treated with different bead diameter: (a) 45-90 µm, (b) 125-250 µm and (c) 400-600 µm, observed with an optical microscope.*

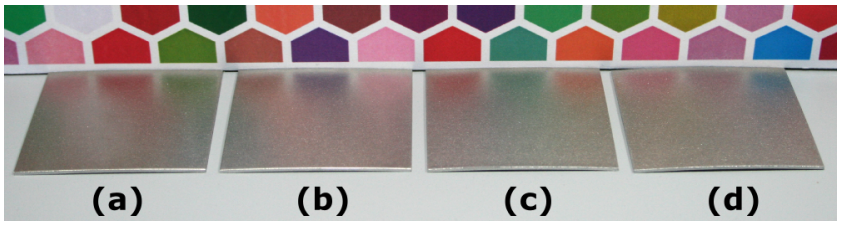

Fig. 2.15 *Photograph of the four samples treated with beads of 125-250 µm diameter with different covering ratio of blasting: (a) 30%, (b) 50%, (c) 75% and (d) 93%, in a light booth (Spectralight QC X-Rite), under D65 illumination.*

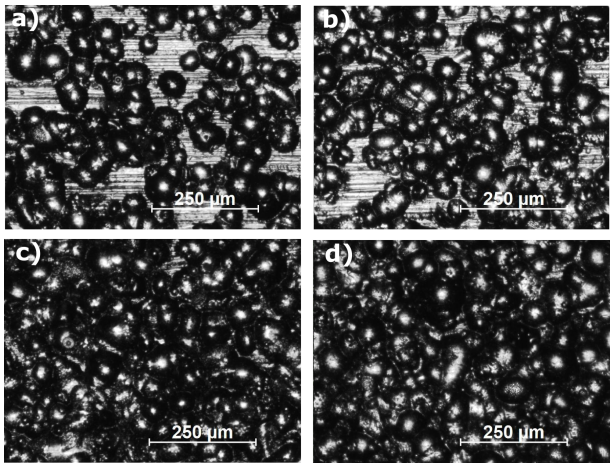

Fig. 2.16 *Microstructure of the four samples treated with beads of 125-250 µm diameter with different covering ratio: (a) 30%, (b) 50%, (c) 75% and (d) 93%, observed with an optical microscope.*

identified as the initial anisotropic defects of the raw plate. Naturally, the unblasted area is decreasing with the duration of the blasting process.

2.2.1.4 Variation of the shape of the particle

The third and last set of blasted metallic samples is composed of four blasted surfaces, which are presented in Fig. 2.17. Those four samples are all treated with particles of the same typical diameter (30-60 μm), but of different shapes.

Three kinds of particles are used: beads, rough beads and grains, as it can be seen from the Scanning Electron Microscope (SEM) images presented in Fig. 2.18. The bead (Fig. 2.18(a)) is a spherical particle with a smooth surface. The global shape of the rough bead is also spherical, but its surface is covered with an additional nanometers roughness (Fig. 2.18(b)). The grain has sharp edges and its surface is highly irregular (Fig. 2.18(c)).

It appears that these different particles give rise to surfaces with very different visual aspects as illustrated by the images in Fig. 2.17. Surfaces treated with beads (Fig. 2.17(a)) and with a mix of beads and grains (Fig. 2.17(c)) have a similar visual aspect. However the surfaces treated with rough beads (Fig. 2.17(b)) and with grains (Fig. 2.17(d)), present a much more diffuse aspect. Nevertheless, if surfaces treated with rough beads and with grains both have diffusive optical properties, their visual aspects are quite different.

The microscopic observations of the samples are presented in Fig. 2.19. Surfaces

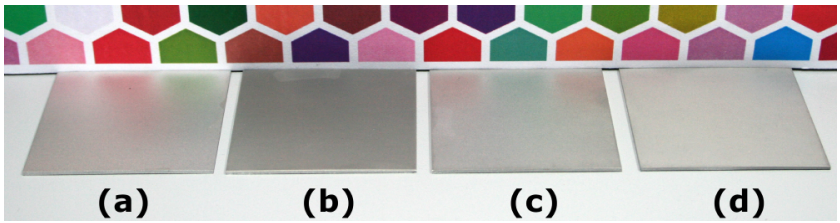

Fig. 2.17 *Photograph of the four samples treated with media of 30-60 µm diameter but of different nature : (a) beads, (b) rough beads, (c) mix of beads and grains, and (d) grains, in a light booth (Spectralight QC X-Rite), under D65 illumination.*

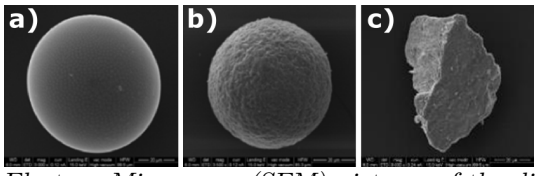

Fig. 2.18 *Scanning Electron Microscope (SEM) pictures of the different particles used for blasting process: (a) beads, (b) rough beads and (c) grains. SEM images provided by Julien Cabrero.*

treated with beads and with a mix of beads and grains seem to have similar topography, dominated by the presence of craters, even if the density of craters seems smaller in the sample blasted with a mix of beads and grains.

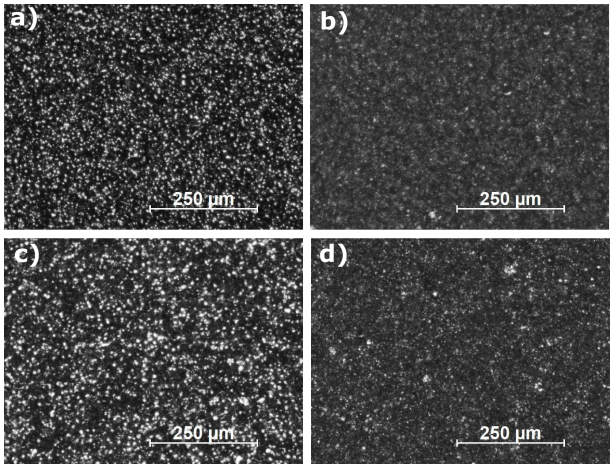

Fig. 2.19 *Microstructure of the four samples treated with particles of 30-60 µm diameter but of different shapes: (a) beads, (b) rough beads, (c) mix of beads and grains, and (d) grains, observed with an optical microscope.*

2.2.2 Frosted glass surfaces

Frosted glass is a glass whose surface morphology has been modified by an industrial process, in order to change its optical properties and/or visual aspect. Indeed, by roughening the initial surface of flat glass, one can progressively disturb its highly specular property to end up with very hazy properties.

The modification of the glass surface is mainly achieved by two techniques: acid-etching and blasting. The blasting process was described in Sec. 2.2.1 for metallic surfaces, but it is applied in the same way on glass substrates. However, blasting of metallic or glass substrates will lead to different morphologies due to the different mechanical properties of these two materials. The acid-etching of glass is usually realized by dipping the glass in a hydrofluoric acid (HF) bath. Frayret and collaborators demonstrated that varying the composition and concentration of the acid bath can influence the shape and the depth of the obtained morphologies [55]. In this way, one can tune the slope distribution of the surface, and as a result, changes the optical properties of the treated surface [55]. Pápa et al. showed that the duration of the acid-etching also impacted the lateral size and depth of the glass texturation [56]. Then the authors examine the relation between the thickness of the pattern and the haze property of the glass surface: thicker the pattern is, hazier the surface is.

By coupling the diffuse optical properties with the other intrinsic properties of glass (high transmittivity in the visible range, excellent chemical inertness,...), frosted glasses can be used for several applications. Such diffuse glasses are widely used to fabricate greenhouse roofs [57]. Indeed, it optimizes the quality of the light that enters in the greenhouse. By controlling the diffuse properties of the glass (designed to imitate as much as possible the natural light), one can significantly improve the growth of crops. Frosted glasses are also designed for privacy related applications. Indeed, frosted glass walls can combine a high level of transparency and a privacy component thanks to their hazy properties: in this way, they are widely used to build meeting rooms or bathrooms.

Five frosted glass samples will be examined here. They have been manufactured by several methods, and present different visual aspects. Only one side of each sample is frosted, and to the naked eye, all of them seem to present isotropic morphology and visual aspects. In order to examine the impact of the frosting on the visual aspects, all the frosted glass samples are compared to a Planilux glass (a standard flat glass used in glazing). In all photos, there is 5 cm between the glasses and the background pattern, and 30 cm between the glasses and the camera. The samples are presented by the order of increasing haze properties, and are referred to as G1, G2, G3, G4 and G5.

2.2.2.1 G1 glass

A photograph of G1, compared to the Planilux sample, is shown in Fig. 2.20(a). The two vertical black lines indicate the edges of the two glasses (consequently, the central area, between the two black lines, is free of glass samples). The sample G1 is the less diffusive sample among this set of surfaces. The hexagonal pattern, behind the sample is slightly distorted: only the edges of the hexagons are slightly blurred. This sample was manufactured by acid-etching. Its microscopic texture, presented in Fig. 2.20(b), is composed of micrometric objects of low surface density, which could be the source of this soft diffuse property.

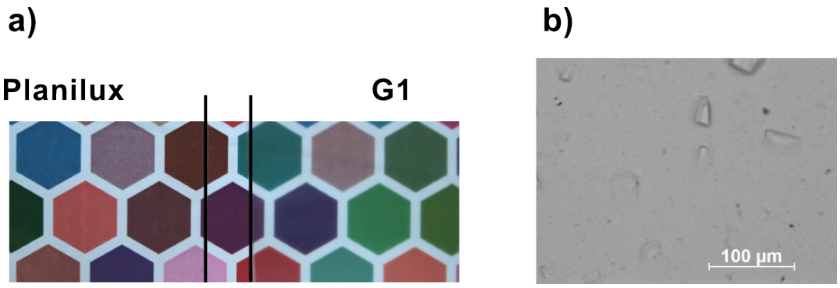

Fig. 2.20 *G1 frosted glass: a) Macroscopic photo at normal incidence of a Planilux glass and G1 glass, in a light booth (Spectralight QC X-Rite), under D65 illumination. b) Microscopic structure of G1 glass, observed with an optical microscope.*

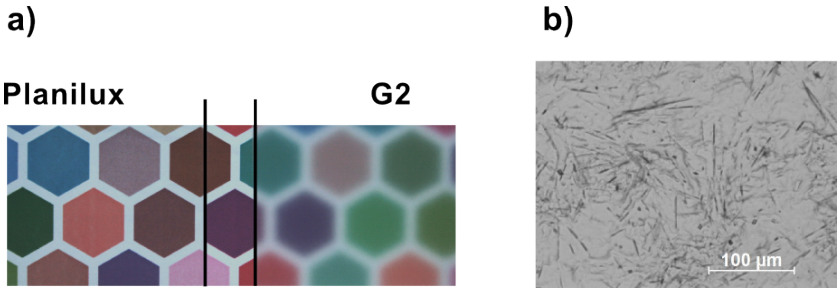

Fig. 2.21 *G2 frosted glass: (a) Macroscopic photo at normal incidence of a Planilux glass and G2 glass, in a light booth (Spectralight QC X-Rite), under D65 illumination. (b) Microscopic structure of the G2 glass, observed with an optical microscope.*

2.2.2.2 G2 glass

Sample G2 is shown to the right in Fig. 2.21(a). It exhibits stronger light diffusion than the sample G1. Indeed the hexagons of the background picture are still easily recognizable, but their borders (white and colored areas) are slightly hazy. This sample is also manufactured by acid etching. Its microstructure is presented in Fig. 2.21(b): it consists of a dense arrangement of needle-shaped scratches.

2.2.2.3 G3 glass

A photograph of G3, compared to the reference flat glass, is shown in Fig. 2.22(a). Behind this sample, it is difficult to identify the hexagonal pattern of the background picture, even if the position of the white edges are still distinguishable. The diffusive properties of G3 are obtained through an abrasion manufacturing process, which is consistent with its scratched microstructure presented in Fig. 2.22(b).

2.2.2.4 G4 glass

Sample G4 is presented in Fig. 2.23(a). The hexagonal pattern is no longer recognizable: only contrasting colors can be distinguished. These strong diffusive properties are obtained through a process that combines acid-etching and blasting. Its microstructure, presented in Fig. 2.23(b), is composed of circular patterns, which recalled the microstructure of metallic samples blasted with spherical beads (Fig. 2.14).

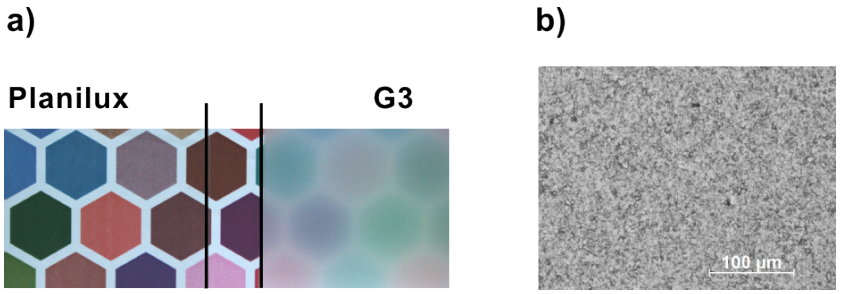

Fig. 2.22 *G3 frosted glass: a) Macroscopic photo at normal incidence of a Planilux glass and G3 glass, in a light booth (Spectralight QC X-Rite), under D65 illumination. b) Microscopic structure of the G3 glass, observed with an optical microscope.*

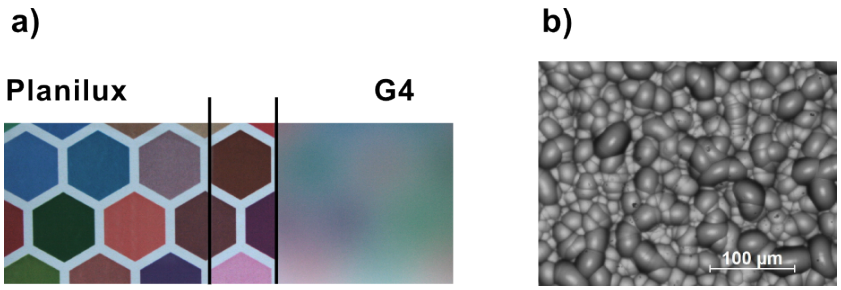

Fig. 2.23 *G4 frosted glass: a) Macroscopic photo at normal incidence of a Planilux glass and G4 glass, in a light booth (Spectralight QC X-Rite), under D65 illumination. b) Microscopic structure of the G4 glass, observed with an optical microscope.*

2.2.2.5 G5 glass

Sample G5 is presented in Fig. 2.24(a), next to the flat glass surface. Just like sample G4, the G5 glass has strong diffusive properties: only a few color patches are visible through the sample. This glass surface is manufactured by acid-etching, which leads to a micrometric structure presented in Fig. 2.24(b). The surface is textured with micrometric inverted pyramids.

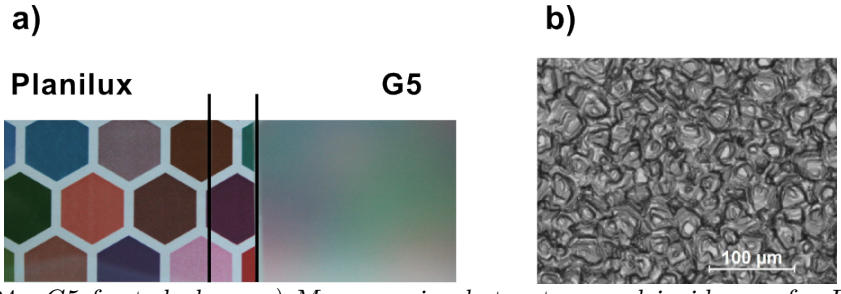

Fig. 2.24 *G5 frosted glass: a) Macroscopic photo at normal incidence of a Planilux glass and G5 glass, in a light booth (Spectralight QC X-Rite), under D65 illumination. b) Microscopic structure of the G5 glass, observed with an optical microscope.*

2.3 Conclusion

Samples with a wide variety of surface morphologies were presented in this chapter.

First, simple model surfaces fabricated by the photolithography and nanoimprint processes were presented. With these fabrication techniques, the morphology and the refractive index of the produced samples can be accurately controlled. 1D (rectangular line gratings) and 2D (cylindrical pillar gratings) surfaces were then fabricated. Slight and controlled structural modifications were applied on these micrometric structures, in order to evaluate their impact on the optical properties of the surfaces.

Secondly, we examined two kinds of complex rough surfaces: blasted metallic surfaces and frosted glass samples. These rough surfaces are manufactured by industrial processes which are defined by tens of fabrication parameters: their morphology is therefore highly complex and varied. Several sets of samples were designed by varying only one fabrication parameter: in this way, we will be able to evaluate the impact of each fabrication parameter on the actual morphological and optical properties of the resulting surface.

An extended study of the morphological and optical properties of those samples is presented in the following chapters.

Chapter 3

Morphological characterization

"You have been weighed, you have been measured, and you have been found wanting."
Adhemar, A Knight's Tale (2001)

Contents

Everyone can easily notice that surfaces have different roughness degrees and morphological properties. It is also generally assumed that when even the smoothest surface is observed with enough details, it will exhibit roughness and morphological patterns, and that finally no surface is perfectly smooth. However, it is not straightforward to describe a surface morphology with quantitative and representative terms. Indeed, one can easily say that a window glass is smoother than the surface of a brick, but it is harder to be more specific. To do so, one would need to observe and measure these surface morphologies, and then to be able to express them with quantitative values in order to compare them

with each other. Of course, these values must be statistically representative and not be impacted by numerical or measurement artifacts.
This chapter aims to describe how the surface morphology should be characterized experimentally and what information relevant for optical properties of the surface should be deduced from the topography. First, experimental setups, which allow to measure the surface morphology from the millimetric shape to the nanometric roughness, will be presented. Secondly, we will review the common terms used to describe a surface morphology with statistical parameters and functions, indeed, in the case of randomly rough surfaces, a statistic description is required. The way to extract these statistical parameters and functions from experimental measurements will also be described. Finally, the morphological characterizations of the samples studied in this work will be presented and analyzed.

3.1 Description of the experimental setups

Numerous techniques exist to measure the morphology of a surface, such as: mechanical stylus methods, optical methods, scanning probe microscopy, electron microscopy. All these techniques use different physical approaches and have therefore different fields of application and technical limitations. As an example, Scanning Electronic Microscopy (SEM)[58] is a method widely used to perform highly resolved images of objects, from the macroscopic to the nanometer scale. However, it has several drawbacks: SEM cannot be used on all kinds of samples (specimens must be conductive or coated with a conductive material), specimens have to be placed in a vacuum, and finally it can be difficult to derive quantitative morphological data from the images. On the contrary Atomic Force Microscopy (AFM) [59], a technique used to scan a surface morphology at the nanometer scale can be used on every kind of sample. Unfortunately, this method is only dedicated to nanometric or micrometric observations, and can be highly time consuming. Mechanical stylus and optical methods are dedicated to the observation of sample morphology with micrometric or millimetric structures, but their height and lateral resolution are obviously worse than the ones of AFM.

As it is usually difficult to combine high experimental resolution and large areas of measurements on a single setup, it appears more efficient to combine several experimental methods. J.M. Bennett is one of the pioneers of this scientific community: indeed a large part of her work was dedicated to the experimental study of the surface morphology, combining AFM, profilometry and optical experimental setups [10][60][61]. Moreover, Poon and collaborators studied the morphology of optical surfaces (which are highly smooth surfaces), with AFM, stylus profilometry and optical method. They showed that the comparison of such different measurements are not straightforward and they studied the impact of the measurements characteristics (resolution, size of a scan, size of tips...) on simple roughness parameters [62]. In a similar way, Duparre et al. [63] also studied the morphology of optical surfaces with AFM, mechanical profilers, white-light interferometry and confocal microscopy. They showed that such different experimental measurements can be compared using a bandwidth frequency region that is common to all experimental

setups, otherwise, the comparison is much more difficult.

Three different setups, which are available at Saint-Gobain Recherche Paris, were used to measure the surface morphology of our samples:

- Chromatic Confocal Profilometry
- Stylus Profilometry
- Atomic Force Microscopy

These three different techniques allow to measure the surface morphology with different resolutions. In this way, we will be able to measure a wide range of roughness degrees, which can impact the light scattering properties of the surfaces. In the following sections, we will review these three methods, which are central methods for measuring the surface morphology.

3.1.1 Chromatic Confocal Profilometry

Chromatic confocal profilometry is a point scanning optical method used to image a surface morphology without contact with the surface [64]. The operating principle of chromatic confocal profilometry is presented in Fig. 3.1. The white light, coming from a LED source, passes through a set of lenses, called an optical pen. Every optical pen has a high and controlled degree of chromatic aberration [65]. The chromatic aberration of the lenses will vary the focal distance of each wavelength of the incoming white light. Consequently, each wavelength will focus on a different distance from the optical pen, creating a measurement range (which is proper to each optical pen), as shown in Fig. 3.1. When a surface height is scanned, a single wavelength will be in focus (the green wavelength in Fig. 3.1) while all others are out of focus. The light is then reflected through the optical pen, and crosses a pinhole that only allows the focused wavelength to pass through to the spectrometer. The spectrometer indicates the wavelength in focus, which corresponds to a specific distance between the surface and the lens. This experimental technique has been used numerous times to measure surfaces morphologies [66][67]. The chromatic confocal microscope used for this study has been manufactured by the company STIL. The optical pen used during the measurements can measure height variation from 300 nm up to 1 mm.

This experimental technic allows to perform non-destructive measurements of topography with a rather good height resolution. Millimeters areas can be measured with this setup, but as all points scanning techniques, it can be rather time consuming. However, the lateral resolution of the measurement (distance between two consecutive measured heights) is limited to 1 μm due to the size of the focused beam. Finally, the examined samples must be reflective enough to be measured.

The morphology of all random complex surfaces presented in Sec.2.2, was characterized by chromatic confocal profilometry. Table 3.1 summarizes the measurement parameters performed on each set of samples.

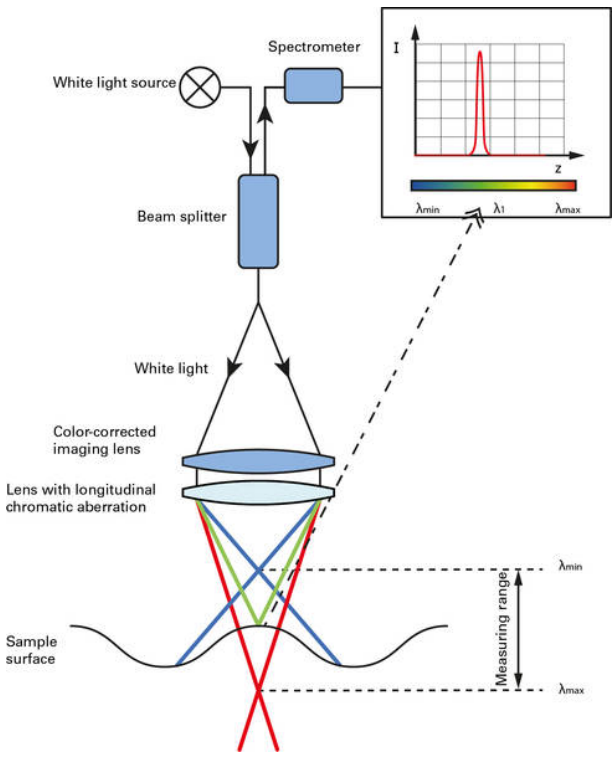

Fig. 3.1 *Scheme of the operating principle of chromatic confocal profilometry, reproduced from [68].*

Series	Sample	Area (mm^2)	Lateral resolution (μm)	Number of scans
Aluminum	Untreated	5×5	2	8
Beads diameter (μm)	45-90	1×1	2	9
	125-250	2×2	2	9
	400-600	3×3	2	7
Covering ratio (%)	30	2×2	2	6
	50	2×2	2	6
	75	2×2	2	6
	93	2×2	2	6
Particle shape	Beads	2×2	1	4
	Rough beads	2×2	1	4
	Beads and grains	2×2	1	4
	Grains	2×2	1	4
Frosted Glass	G1	2×2	1	4
	G2	2×2	1	4
	G3	2×2	1	4
	G4	2×2	2	6
	G5	2×2	2	6

Table 3.1: Summary of the measurements parameters used to characterize the complex rough surfaces with chromatic confocal profilometry.

3.1.2 Stylus Profilometry

Stylus profilometry (also referred to as Contact Profilometry), is a technique used to characterize a surface morphology. Stylus profilometers use a tip to detect the scanned surface. The displacement of the tip is coupled with a feedback loop, which maintains a constant force on the tip, allowing to acquire the surface height information. In this way, both lateral and vertical positions of the tip are recorded during the scan. Due to the force applied on the tip, this experimental technique is not suitable for soft, fragile or viscous materials, which could be damaged by the stylus. Moreover, the study of viscous or fibrous surfaces can also lead to the tip contamination. Such tip contamination could then lead to strong measurement artifacts. A typical stylus profilometer can measure height variations from 10 nm to 500-600 μm. The lateral resolution of the setup is affected by the radius of the tip (which usually range from hundreds of nanometers to tens of micrometers), and the speed of the scan.

The stylus profilometer used during this work is Dektak XT, commercialized by Bruker. A 2 μm diameter tip is installed on the setup, which therefore limits the detection of cavities of smaller dimensions. The profilometer is able to detect a height variation of 10 nm. The measurements of areas are obtained by acquisition of a succession of 1D profiles. Unfortunately, it leads to measurement artifacts along the short scanning direction (direction along which the succession of scans is realized). As we plan to study the spatial distribution of the surface heights (see Sec. 3.2.2), we would like to avoid such artifacts. Consequently, only 1D profiles will be measured with the contact profilometer. However, measurements are performed in two orthogonal directions in order to evaluate if the scanned surfaces are isotropic or anisotropic.

The profilometer was used to characterize the morphology of the model surfaces obtained by thermal relaxation process (described in Sec 2.1.2.2). Five scans were realized on each of the relaxed 1D model surfaces, in order to check for surface homogeneity. Moreover, the morphology of all random complex surfaces presented in Sec. 2.2, were characterized by stylus profilometry. Table 3.2 summarizes the measurements performed on each set of randomly rough surfaces. In all cases, measurements are realized in two orthogonal directions (which is denoted by the $\times 2$ in the 'Number of scans' column of the summary table).

3.1.3 Atomic Force Microscopy

Atomic Force Microscopy (AFM) [59] is a scanning probe technique which allows to measure a surface roughness at the nanometers scale. The height detection of an AFM range from the atomic scale up to a ten of micrometers. The nanometer tip of the AFM contacts the surface directly, and the interaction mechanism is provided by Van der Waals forces. In this way, the AFM technique allows to measure the morphology of surfaces of any kind, including ceramics, polymers, biological samples [69], and is therefore not restricted to conducting surfaces as other techniques such as Scanning Tunneling Microscopy.

The AFM used for this study is a Bruker Dimension Icon, and we use a tip with a radius smaller than 10 nm to perform the measurements. The AFM produces images of

Series	Sample	Scan length (mm)	Lateral resolution (nm)	Number of scans
Aluminum	Untreated	30	500	10×2
Beads diameter (μm)	45-90	6	100	20×2
	125-250	15	200	20×2
	400-600	30	300	10×2
Covering ratio (%)	30	15	400	15×2
	50	15	400	15×2
	75	15	400	15×2
	93	15	400	15×2
Particle shape	Beads	8	400	10×2
	Rough beads	8	400	10×2
	Beads and grains	8	400	10×2
	Grains	8	400	10×2
Frosted Glass	G1	10	400	10×2
	G2	10	400	10×2
	G3	10	400	10×2
	G4	10	400	10×2
	G5	10	400	10×2

Table 3.2: Summary of the measurements parameters used to characterize the complex rough surfaces with stylus profilometry.

512×512 pixels, which implies that the lateral resolution of the measurement is related to the actual dimensions of the scanned area. In order to have a good balance between measurement time and scan resolution, we realized measurements of 20×20 μm^2 dimensions. In this way, scans have 49 nm of lateral resolution and are realized in 20-25 min.

Since such AFM characterizations are rather time consuming, only parts of the samples were examined with the AFM. The following rough complex surfaces were measured, at four different locations:

- Set of aluminum samples blasted with different sizes of beads (presented in Sec. 2.2.1.2)
- Set of aluminum samples blasted with different shapes of particles (presented in Sec. 2.2.1.4)

3.1.4 Conclusion

The three techniques used to measure the morphology of the studied surfaces were described. These techniques are complementary in terms of: lateral and height resolutions, size of the measured areas and/or profiles. They allow to access information on the surface topography at different scales. The main characteristics of the three techniques are summarized in Table 3.3.

	Height detection range	Lateral resolution	Type of scan realized	Maximal scan size realized
Chromatic Confocal Profilometry	300 nm - 1 mm	1 μm	2D	5 mm $\times$ 5 mm
Stylus Profilometry	50 nm - 500 μm	$\sim$100 nm	1D	30 mm
Atomic Force Microscopy	1 nm - 10 μm	49 nm	2D	20 $\mu m\times$ 20 μm

Table 3.3: Summary of the characteristics of the setups used to characterize the surface morphology of the sample

3.2 Description of the surface morphology

"When you can measure what you are speaking about, and express it in numbers, you know something about it, when you cannot express it in numbers, your knowledge is of a meager and unsatisfactory kind [...]"

William Thomson, 1^{st} Baron Kelvin

This quote of William Thomson perfectly introduces Section 3.2.1, which aims to describe the numerical parameters and functions that express the surface morphology. Indeed, these numerical parameters and functions are highly convenient to quantitatively compare the morphological properties of several surfaces, and therefore to classify them. They are also required for the light scattering models that link the morphological and the optical properties of a surface. The two communities interested in modeling the light scattering (physical optics and geometrical optics communities, as mentioned in Sec. 1.2.1), use different parameters to describe the surface morphology. In order to be as exhaustive as possible, we choose to explore both of these approaches and then to express the morphology by the parameters of these two communities.
The physical optics community takes a particular interest to the description of the surface morphology. Several functions and parameters, which are used in other scientific communities (tribology, geophysics,...), are used to accurately describe the surface morphology. They are widely described in the different literature domains [21][60][70]. One can classify those parameters and functions into two sets. First, the height probability density function of the morphology is analyzed, and the parameters used to describe the shape of this distribution. Then, functions allowing to describe the spatial correlation of the heights are evaluated. In the geometrical optics community, the description of the morphology is way simpler. Usually, the surface morphology is only described by its slope distribution[23].

This section aims to describe the parameters and functions used in physical optics and geometrical optics for the description of surface morphology. First, we focus on parameters related to the height distribution. Then, functions describing the spatial correlation of heights will be introduced. Then, several methods used to evaluate the slope distribution of a surface will be presented. Finally, we will briefly describe a numerical study that we realized, in order to identify suitable experimental parameters to perform adapted and representative measurements of the surface topography.

Figure 3.2(a) and Fig. 3.2(b) present the coordinate systems used to study the morphology of 1D profiles and 2D areas respectively. The function $h(x)$, which describes the height (along z axis) of the profile morphology is defined along the x axis. The function $h(x, y)$, which describes the height (along z axis) of the surface morphology is defined along the x and y axes. We will assume that $h(x)$ and $h(x, y)$ are ergodic processes, which implies that the statistical properties of these random processes can be deduced from a single and sufficiently long realization of the process.
However, in the experimental world, $h(x)$ and $h(x, y)$ do not have equation forms, and are actually sampled at discrete locations with a finite number of points. This is why the

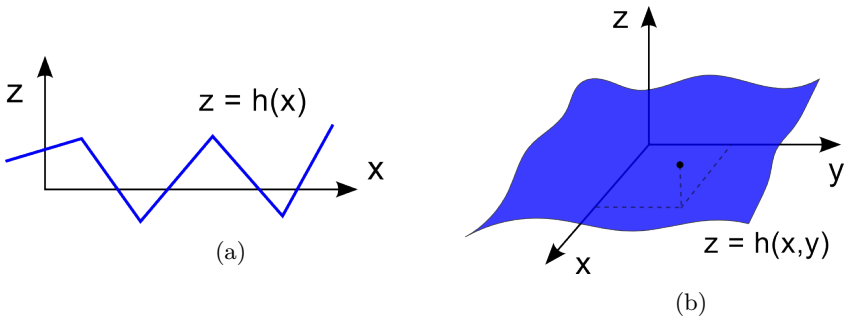

Fig. 3.2 *Representation of the coordinate systems used during this study. (a) Profiles are defined as $z = h(x)$ along the two axes x and z. (b) Areas are defined as $z = h(x, y)$ along the three axes x, y and z.*

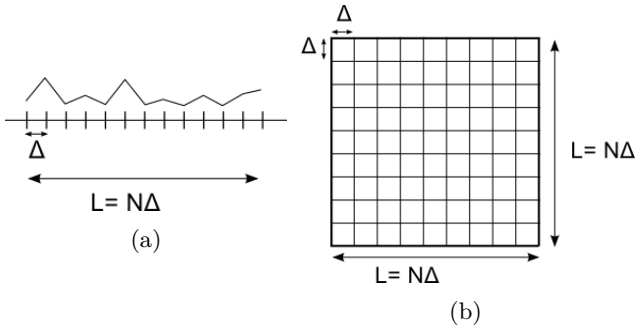

Fig. 3.3 *Representation of sampled data of (a) 1D profile of length L, sampled of even N points with a Δ sampling distance. (b) 2D square area of edge length L is sampled by even N^2 points with Δ sampling distance along the x and y axes.*

present section also aims to describe the way to evaluate morphological parameters from sampled data, which is not a straightforward task that must be carefully realized [71][72]. The notation used to describe sampled data of profiles ($h(x)$) and areas ($h(x, y)$) are presented in Fig. 3.3. The 1D profile, presented in Fig. 3.3(a), is L long and is composed of N different points, all equally sampled by a distance Δ, with N even. The square 2D area, presented in Fig. 3.3(b), has edge of length L, composed of N points, sampled by the distances Δ. The 2D square area is then composed of N^2 even points.

3.2.1 The height probability density function

3.2.1.1 Analytical expression

One of the main morphological characteristics of a surface is its height probability density function (pdf), which is referred to as $p(h)$. The quantity $p(h)dh$ is the probability to find an individual height between h and $h + dh$. The distribution $p(h)$ is a non-negative function of h and is normalized so that:

$$\int_{-\infty}^{+\infty} p(h)dh = 1. \tag{3.1}$$

As an example, a surface topography and its height pdf are presented in Fig. 3.4. To

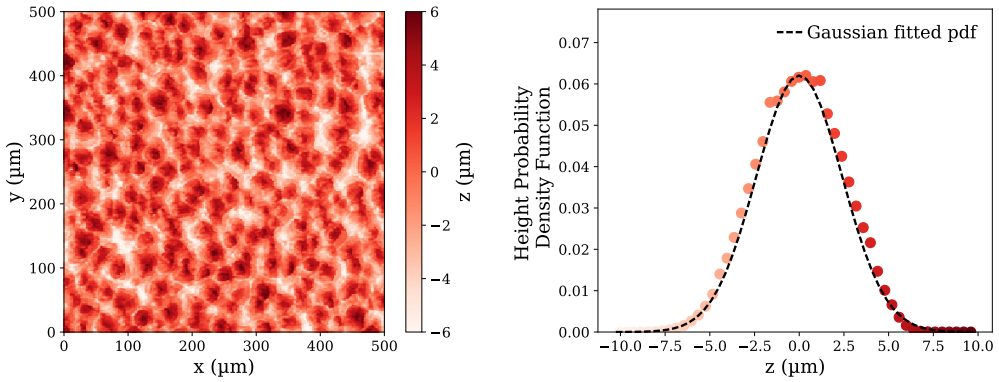

(a) (b)

Fig. 3.4 *(a) Experimental surface topography of a rough surface evaluated by confocal chromatic profilometry, and (b) its experimental height probability density function (dots) compared with a Gaussian probability density function (dashed line), fitted with the mean level and the standard deviation of the experimental height pdf.*

describe some of the properties of the variable h, one can use statistical parameters evaluated from the height probability density function. The n^{th}-order moment of $p(h)$, is a powerful numerical tool to describe the surface height pdf. It is defined as:

$$m_n = \int_{-\infty}^{+\infty} h^n p(h) dh, \tag{3.2}$$

More generally, one can define the n^{th}-order central moment,

$$v_n = \int_{-\infty}^{+\infty} (h - \bar{h})^n p(h) dh, \tag{3.3}$$

where $\bar{h}$ denotes the mean level of the surface (which is also the 1^{st} order moment, m_1). The 2^{nd}-order central moment of the variable h appears to be one of the most important physical parameters. It is referred to as the *variance*, and is defined as:

$$\sigma^2 = v_2 = \int_{-\infty}^{+\infty} (h - \bar{h})^2 p(h) dh, \tag{3.4}$$

where σ is referred to as the *root mean square* (rms) of the surface, and has the unit of a length. If the other roughness parameters (described in Sec. 3.2.2) are held fixed, higher the value of σ is, rougher the surface is. The rms is the most widely used parameter to describe the surface roughness. Indeed, in the case of surface function described by Gaussian statistics (i.e, that the height distribution can be described by a Gaussian function), one only needs to evaluate the first two order moments to fully describe it.

In case of non-Gaussian processes, the joint probability functions of any orders are required [73]. For surface morphologies measured at a discrete set of points in the xy-plane, a full characterization of non-Gaussian processes can never be achieved. On the other hand, measured data can be used to determine if the random process is non-Gaussian. To

this end, two higher moments of the height distribution are usually used: the *skewness* and *kurtosis*.

The third order moment, referred to as *skewness*, is defined as:

$$\gamma_3 = \frac{v_3}{\sigma^3} = \frac{1}{\sigma^3}\int_{-\infty}^{+\infty}(h-\bar{h})^3 p(h)dh \tag{3.5}$$

As presented in Fig. 3.5(a), the skewness expresses the symmetry of the height pdf with respect to the surface mean-level. It is usually convenient to compare the skewness of a height pdf with the skewness of a surface characterized by a Gaussian height pdf, defined as:

$$p(h) = \frac{1}{\sigma\sqrt{2\pi}}\exp\left(-\frac{(h-\bar{h})^2}{2\sigma^2}\right). \tag{3.6}$$

Indeed, for such Gaussian process, the skewness equals zero, $\gamma_3 = 0$, meaning that its height pdf is perfectly symmetrical around the mean level of the surface. However, a surface composed by a collection of bumps would be characterized by a positive skewness. On the contrary, a surface with a collection of indents would be characterized by a negative skewness (see Fig. 3.5(a)).

The fourth order moment, referred to as *kurtosis*, is defined as:

$$\gamma_4 = \frac{v_4}{\sigma^4} = \frac{1}{\sigma^4}\int_{-\infty}^{+\infty}(h-\bar{h})^4 p(h)dh \tag{3.7}$$

As presented in Fig. 3.5(b), the kurtosis is another descriptor of the shape of the height pdf. The kurtosis expresses the fatness of the tails of the height pdf. For a surface with Gaussian height pdf, the kurtosis is equal to 3, $\gamma_4 = 3$. Height distributions with kurtosis lower than 3, are referred to as *platykurtic*: their tails are less fat than the ones of surface with Gaussian height pdf (see the red drawing in Fig. 3.5(b)). On the contrary, height pdf with kurtosis higher than 3, are said to be *leptokurtic*: they are central peaked distributions, as presented in the blue drawing in Fig. 3.5(b).

The evaluation of the variance, the skewness and the kurtosis parameters (see respectively Eqs. (3.4), (3.5) and (3.7)) does not take into account the actual position of the heights. Consequently, one can analyze profiles ($h(x)$) and areas ($h(x,y)$) in the same manner, and additional expressions of the parameters in the 2D case are not required.

3.2.1.2 Sampled data

Here we provide expressions of the first four orders in the case of discrete data sets. Their evaluation is illustrated on the example of the G1 and G5 frosted glass surfaces (see Sec. 2.2.2). The rms, skewness and kurtosis parameters are extracted from chromatic confocal profilometry measurements of samples G1 and G5, presented in Fig. 3.6 and Fig. 3.7 respectively. We recall here the sampling notations defined in Fig. 3.3: the surface has N^2 even points, with a constant sampling interval Δ along the x and y axes. The mean level of each surface, $\bar{h}$, is then defined as:

$$\bar{h} = \frac{1}{N^2}\sum_{j=0}^{N-1}\sum_{k=0}^{N-1} h(x_j, y_k), \tag{3.8}$$

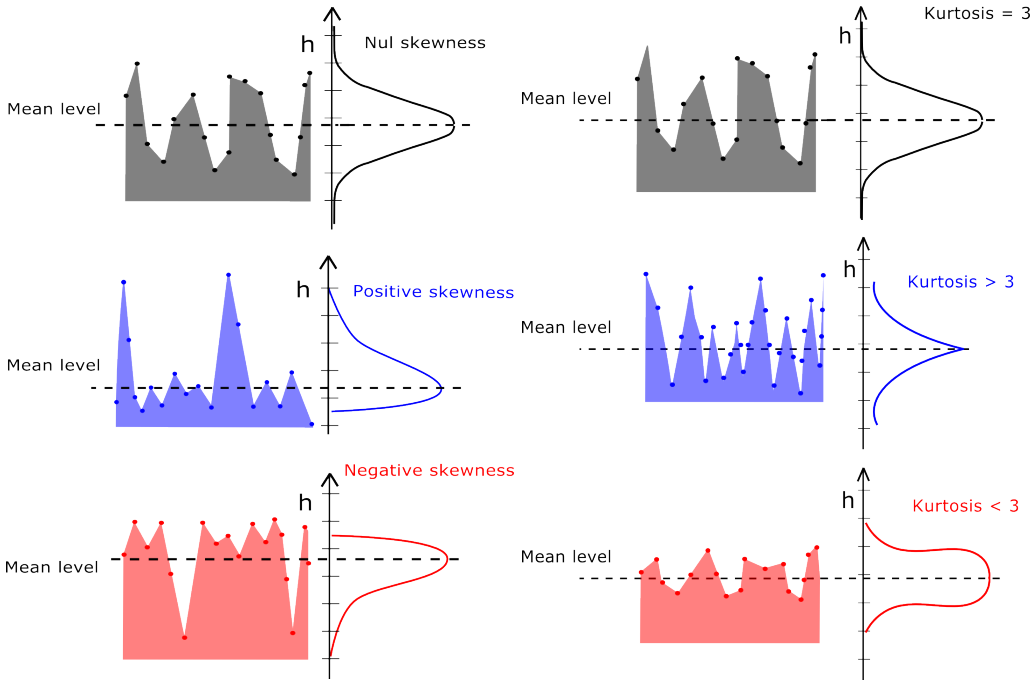

Fig. 3.5 *Schematic representation of surfaces exhibiting different values of higher orders of pdf: (a) the third order or skewness parameter indicates the symmetry of the height pdf. (b) The fourth order or kurtosis parameter indicates the tailedness of the height pdf.*

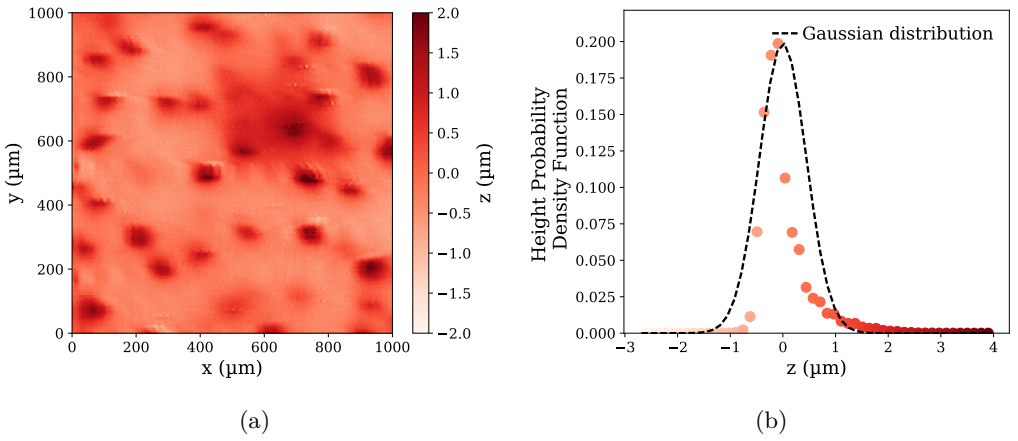

Fig. 3.6 *Confocal chromatic profilometry measurement of frosted glass G1 (a) 2D area of measured height, and (b) height probability density function of G1 ($\sigma = 0.4\mu m$, $\gamma_3 = 1.9$ and $\gamma_4 = 8.1$) compared with a Gaussian distribution, fitted with the mean level and the standard deviation of the experimental height pdf. Experimental parameters of the measurements were presented in Table 3.1.*

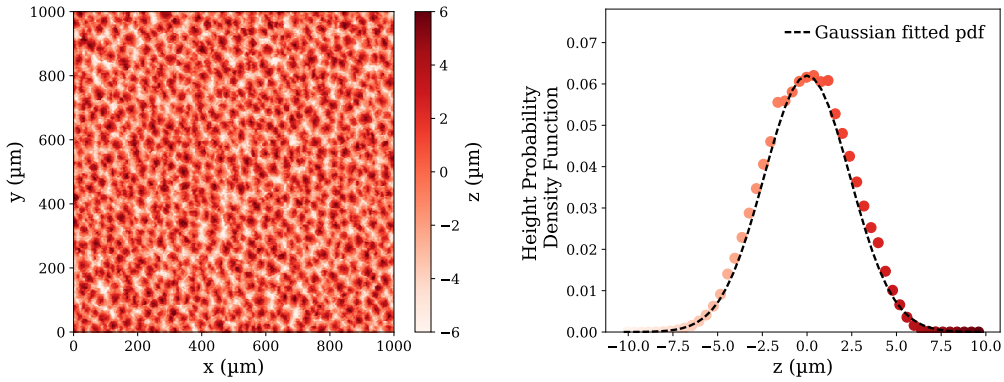

(a) (b)

Fig. 3.7 *Confocal chromatic profilometry measurement of frosted glass G5 (a) 2D area of measured height, and (b) height probability density function of G5 ($\sigma = 2.4\mu m$, $\gamma_3 = -0.1$ and $\gamma_4 = 2.6$) , compared with a Gaussian distribution, fitted with the mean level and the standard deviation of the experimental height pdf. Experimental parameters of the measurements were presented in Table 3.1.*

where $x_j = j\Delta$ and $y_k = k\Delta$ are the sampled points with $j = 0, 1, 2, ..., N-1$ and $k = 0, 1, 2, ..., N-1$ along the x and y axes respectively. The rms (σ), the skewness (γ_3) and the kurtosis (γ_4) of each experimental data set are evaluated as:

$$\sigma = \sqrt{\frac{1}{N^2}\sum_{j=0}^{N-1}\sum_{k=0}^{N-1}(h(x_j, y_k) - \bar{h})^2} \tag{3.9}$$

$$\gamma_3 = \frac{1}{\sigma^3}\frac{1}{N^2}\sum_{j=0}^{N-1}\sum_{k=0}^{N-1}(h(x_j, y_k) - \bar{h})^3 \tag{3.10}$$

$$\gamma_4 = \frac{1}{\sigma^4}\frac{1}{N^2}\sum_{j=0}^{N-1}\sum_{k=0}^{N-1}(h(x_j, y_k) - \bar{h})^4 \tag{3.11}$$

Experimental results for the two surfaces G1 and G5 are presented in Table 3.4.

The rms of the samples G1 and G5 are respectively 0.4 μm and 2.4 μm. This is consistent with the width of the height pdf of those two samples. Indeed, as presented in Fig. 3.6(b) and Fig. 3.7(b), the height pdf of the sample G1 is narrower than that of sample G5.

The skewness of the samples G1 and G5 are respectively 1.9 and -0.1. The height pdf of sample G5 is well approximated by a Gaussian pdf (see Fig. 3.6(b) in dashed line), this is consistent to find a skewness close to zero. As presented in Fig. 3.6(a), sample G1 consists of a flat surface with a collection of bumps. Consequently, the distribution is extended for positive height, and as schematically presented in Fig. 3.5(a), the skewness is positive.

Finally, the kurtosis of the samples G1 and G5 are respectively 8.1 and 2.6. As the sample G1 consists of a collection of bumps on an otherwise flat surface (Fig. 3.6(a)), there are fewer points in the vicinity of the surface mean-level, and more points in the positive tail of the distribution (which corresponds to the heights measured on the top of

	RMS (μm)	skewness	kurtosis
G1	0.4	1.9	8.1
G5	2.4	-0.1	2.6

Table 3.4: The rms, skewness and kurtosis parameters extracted from height probability density function of samples G1 (Fig. 3.6) and G5 (Fig. 3.7).

the bumps). It is then consistent to end up with a kurtosis higher than 3. Once again, the height pdf of sample G5 is well approximated by a Gaussian pdf, so this is consistent that kurtosis parameter is close to 3.

3.2.2 Spatial correlation of the heights

The rms, the skewness and the kurtosis are parameters used to describe the shape of the height probability density function of a surface. However these parameters only describe the statistical properties of a variable at individual positions. Consequently they do not express the correlation between these individual positions. For this reason, it is often referred to as one-point statistics since surface height at only one point at the time is needed. As a result, two different rough surfaces can have the same height pdf. As an example, the two profiles in Fig. 3.8 have exactly the same height pdf, but their profiles are different due to the spatial correlations of each of their individual heights. Thereby the study of the correlation of the heights is critical.

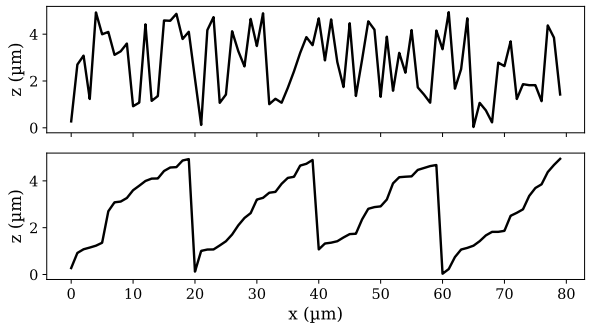

Fig. 3.8 *Two different profiles with the same height pdf: they look highly different because their heights are differently correlated along the profile.*

Two kinds of functions exist to describe the statistical spatial correlation of the heights that composed profiles or areas: the *power spectrum density function* and the *autocorrelation function*. The expressions of the power spectrum density and of the autocorrelation functions will be examined in the cases of 1D profiles and 2D mappings.

3.2.2.1 Case of 1D profiles

Height profiles are defined by the function $h(x)$, which describes the evolution of the height along the z axis as a function of its spatial position along the x axis (see Fig. 3.2(a)).

Analytical expressions

Autocovariance function is used to compare a data set with a translated version of itself. Such autocovariance functions can then be used to study the spatial correlation of heights that composed a profile $h(x)$. As $h(x)$ is considered as an ergodic process, its statistical properties can be approximated with the mean of the statistical properties of a sufficiently long length, which is denoted as L. Moreover, since $h(x)$ is a real function, one can then express the autocovariance function $G(\tau)$ as:

$$G(\tau) = \frac{1}{L}\int_0^L h(x)h(x+\tau)\,\mathrm{d}x, \tag{3.12}$$

where τ denotes the amount of translation (between the initial signal and its translated version), which is usually referred to as *delay* or *lag* [74]. From Eq. (3.12), one can deduce that:

$$G(0) = \frac{1}{L}\int_0^L h^2(x)\,\mathrm{d}x, \tag{3.13}$$

$$= \sigma^2. \tag{3.14}$$

The unit of $G(\tau)$ is then a length to the second power. One also usually considers *autocorrelation function*, referred here to as $C(\tau)$. Autocorrelation function is a normalized version of the autocovariance function, and it is defined as:

$$C(\tau) = \frac{G(\tau)}{G(0)} = \frac{G(\tau)}{\sigma^2}. \tag{3.15}$$

Both autocovariance and autocorrelation functions have then the same shape, but they differ by an amplitude factor σ^2, and consequently, $C(\tau)$ has no unit. As $G(\tau)$ and $C(\tau)$ share statistical properties, we chose to study only one of them: $C(\tau)$.

For random surfaces, $C(\tau)$ usually decays to 0 with increasing τ. The rate of the decay depends on the distance over which two points become uncorrelated, which is related to the profile morphology. In order to quantify the rate of decay, the *correlation length* was defined as the value of lag length at which the autocorrelation function drops to 1/e. The shape of the decay depends on the type of random surface, and can therefore be fitted by different functions such as Gaussian, exponential, power law functions, as presented in [70]. The function $C(\tau)$ has the following properties:

- $C(\tau)$ is a function without units,
- $C(\tau) \leq C(0) = 1$,
- $C(\tau)$ is an even function, meaning that: $C(-\tau) = C(\tau)$,
- $-1 \leq C(\tau) \leq 1$,

The *power spectrum density* (PSD) function describes the spatial frequencies (and their relative contribution) which compose the profile $h(x)$. It is here referred to as, $S(f_x)$, where f_x denotes the spatial frequencies along the x axis (in cycles per length unit). The power spectrum density can be expressed as the squared amplitude of the Fourier transform of $h(x)$ per unit of length [71][75]:

$$S(f_x) = \frac{1}{L}\left|\int_0^L h(x)\exp(-2i\pi f_x x)\,\mathrm{d}x\right|^2. \tag{3.16}$$

Moreover, as stated by the Wiener-Khinchin theorem, $S(f_x)$ can be expressed as the Fourier transform of the autocovariance function, as stated in [74]:

$$S(f_x) = \int_{-\infty}^{+\infty} G(\tau) \exp(-2i\pi f_x \tau)\, \mathrm{d}\tau. \tag{3.17}$$

From Eqs. (3.17) and (3.16), one can deduce that $S(f_x)$ has the unit of a length to the third power. In the same manner, one can define $G(\tau)$ as the inverse Fourier transform of $S(f_x)$:

$$G(\tau) = \int_{-\infty}^{+\infty} S(f_x) \exp(2i\pi f_x \tau)\, \mathrm{d}f_x, \tag{3.18}$$

and consequently, from Eq. (3.15):

$$C(\tau) = \frac{1}{\sigma^2} \int_{-\infty}^{+\infty} S(f_x) \exp(2i\pi f_x \tau)\, \mathrm{d}f_x. \tag{3.19}$$

Sampled data

As this study is based on the use of experimental data, one must define the expressions of the power spectrum density function and of the autocorrelation function, for sampled data which are L long, sampled by N even points with a sampling interval Δ (see Fig.3.3 for the sampling notations). The PSD function, $S(f_x)$, is evaluated from the sampled height profile, and consequently, Eq. (3.16) turns into:

$$S(f_{x,n}) = \frac{\Delta^2}{L} \left| \sum_{j=0}^{N-1} h(x_j) \exp\left(\frac{-2i\pi nj}{N}\right) \right|^2, \tag{3.20}$$

$$= \frac{\Delta}{N} \left| \sum_{j=0}^{N-1} h(x_j) \exp\left(\frac{-2i\pi nj}{N}\right) \right|^2, \tag{3.21}$$

where $x_j = j\Delta$ is the sampled length along x, where $j = 0, 1, 2, .., N-1$ denotes the index of the sampled length, $f_{x,n} = n/(N\Delta)$ is the sampled frequency along the x axis where $n = -N/2, ..., N/2$ denotes the index of sampled frequency. Consequently, there are $N+1$, and not N, values of n: it will turn out that the two extreme values of n are equal, but all the others are independent: which finally reduces the count to N. These two extreme frequencies are denoted as the Nyquist frequency [74].

Figure 3.9 presents a hypothetical PSD function, and much information can be extracted from it. The Nyquist frequency, f_N, and the sampling frequency, f_S, are limit frequencies which are related to the sampling parameters of the data profile:

$$f_N = \frac{N}{2L} = \frac{1}{2\Delta}, \tag{3.22}$$

$$f_S = \frac{1}{L}. \tag{3.23}$$

The Nyquist frequency, f_N, is the highest frequency that can be examined: it is related to the actual value of Δ. The sampling frequency, f_S, is the first positive and non-zero

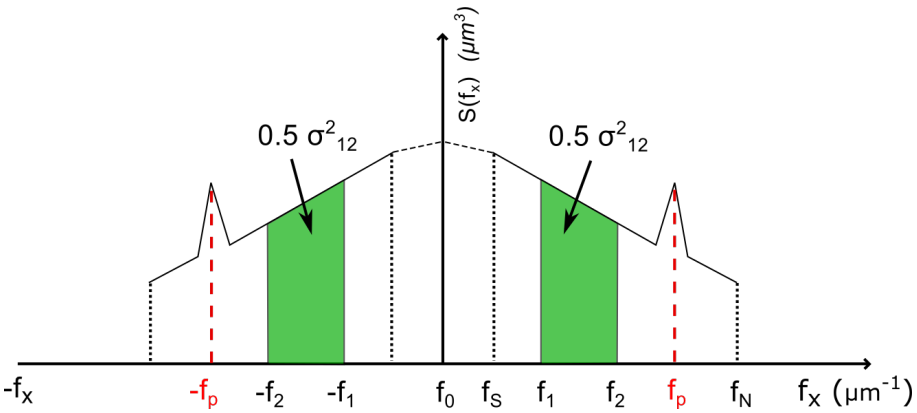

Fig. 3.9 *A hypothetical experimental power spectrum density function of a 1D profile, showing the different properties of a PSD. Adapted from [75].*

frequency: it is defined from the total length of the measured profile. For Eqs. (3.20) and (3.21) the Nyquist frequency, f_N, is obtained with $n = \pm N/2$ and the sampling frequency, f_S, is obtained with $n = 1$. The peak at f_p is due to a periodic structure in the profile of typical period $1/f_p$. The integral from f_1 to f_2 allows to calculate a bandwidth-limited value of the variance σ_{12}^2.

$$\sigma_{12}^2 = \int_{f_x=f_1}^{f_x=f_2} S(f_x)\,\mathrm{d}f_x + \int_{f_x=-f_2}^{f_x=-f_1} S(f_x)\,\mathrm{d}f_x, \tag{3.24}$$

$$= 2\int_{f_x=f_1}^{f_x=f_2} S(f_x)\,\mathrm{d}f_x. \tag{3.25}$$

The autocorrelation function of the profile can be deduced from the PSD function of the profile, from Eq. (3.19) as:

$$C(\tau_{x,k}) = \frac{1}{\sigma^2 N\Delta}\sum_{n=-N/2}^{N/2-1} S(f_{x,n})\exp\left(\frac{2i\pi nk}{N}\right), \tag{3.26}$$

where $\tau_{x,k} = k\Delta$ is the sampled length along x, where $k = -N/2, ..., N/2-1$ denotes the index of the sampled length. In this way, $C(\tau_{x,k})$ is defined from $-L/2$ to $L/2-\Delta$.

Experimental example

The periodic profile presented in Fig. 3.10 is a 1D model surface obtained by thermal relaxation as described in Sec. 2.1.2.2. The profile was measured by stylus profilometry along the cross-section direction of the grating. This is a profile of period 40 μm. The PSD and the autocorrelation functions were evaluated with Eqs. (3.21) and (3.26).

The complete PSD function of the profile is presented in Fig. 3.11(a), but as $S(f_x)$ is even, usually only its positive side is presented (Fig. 3.11(b)). Due to the periodic properties of the profile, the PSD exhibits several peaks which reflect this periodicity. In Fig. 3.11(b), one can easily see peaks at 0.024 μm^{-1}, 0.048 μm^{-1}, 0.072 μm^{-1}, 0.096 μm^{-1} and 0.12 μm^{-1}, with decreasing intensities. The main frequency, at 0.024 μm^{-1}, corresponds to a length of 41.6 μm, which is very close to the period of 40 μm of the profile. This small discrepancy may originate from a small misalignment between the cross-section

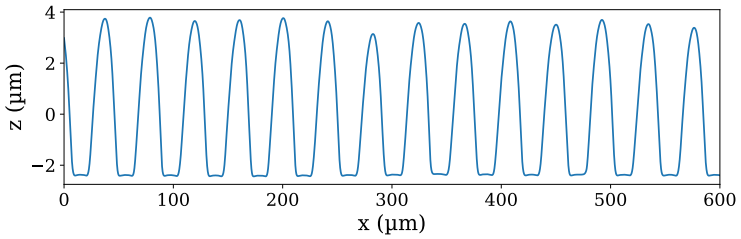

Fig. 3.10 *Measurement of the cross section of a line grating of period 40 μm (see Sec. 2.1.2.2), measured with stylus profilometer.*

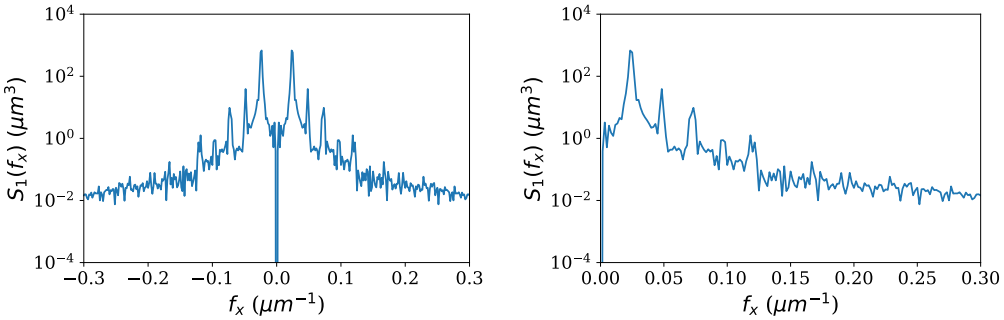

(a) (b)

Fig. 3.11 *1D PSD obtained from the periodic profile of Fig. 3.10 with Eq. (3.21).(a) The complete PSD is an even function (b) usually only its positive side is represented.*

of the profile and the direction of measurement. The other peaks represent the frequencies of the functions that composed the periodic but non-sinusoidal profile: indeed, if the profile would have been a perfect sinusoidal, the PSD function would have consisted of a single peak.

The autocorrelation function of the periodic profile (Fig. 3.10) is presented in Fig. 3.12(a), and its positive part in Fig. 3.12(b). Without lag (meaning that the profile is compared with itself, $C(\tau_x = 0)$), $C(\tau_x)$ is maximum and equal to one. $C(\tau_x)$ is then decreasing up to its minimal value, -0.9 for a lag of 20.8 μm, which corresponds to the half period of the periodic profile: the profile and its translated version are then in opposite phase. Afterwards, $C(\tau_x)$ is oscillating between maximal and minimal values (the lag between two consecutive peaks is equal to 41 μm), with decreasing amplitudes, describing the succession of in phase and opposite phase of the profile and its translated version. If the grating and the measurement alignment would have been perfect, $C(\tau_x)$ would have constantly oscillated between 1 and -1 with a 40 μm period.

3.2.2.2 Case of 2D surfaces

The surface $h(x, y)$ is defined over an area of dimensions L, composed of N^2 even points, equally sampled by a distance Δ along both x and y axes (see Fig. 3.2(b)).

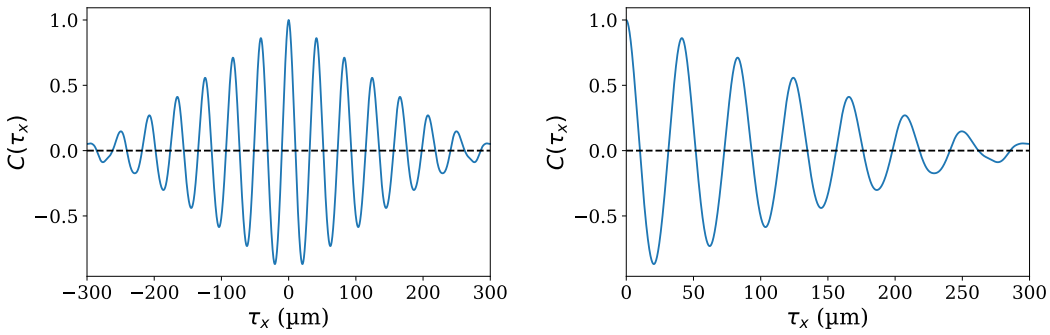

(a) (b)

Fig. 3.12 *Autocorrelation function (ACF) obtained from the periodic profile of Fig. 3.10 with Eq. (3.26).(a) The complete ACF is even.(b) Usually only its positive side is represented.*

Analytical description

One can easily extend the expressions of the 2D power spectrum density and 2D autocorrelation functions from their 1D expressions (see Eqs. (3.16) and (3.19) respectively). The 2D power spectrum density function, which is referred to as $S(f_x, f_y)$, is defined as:

$$S(f_x, f_y) = \frac{1}{L^2} \left| \int_0^L \int_0^L h(x, y) \exp\left(-2i\pi(f_x x + f_y y)\right) \mathrm{d}x \, \mathrm{d}y \right|^2, \tag{3.27}$$

where f_x and f_y denote the frequencies along the x and y axes respectively. The unit of $S(f_x, f_y)$ is a length to the fourth power (while $S(f_x)$ has the dimension of length to the third power). A 1D PSD function, $S(f_x)$, can be extracted from a 2D PSD function, $S(f_x, f_y)$, by integrating $S(f_x, f_y)$ over one frequency axis, as suggested by Church [76]:

$$S(f_x) = \int_{-\infty}^{+\infty} S(f_x, f_y) \, \mathrm{d}f_y. \tag{3.28}$$

If we only consider the positive side of the PSD, Eq. (3.28) is rewritten as:

$$S(f_x) = 2 \int_0^{+\infty} S(f_x, f_y) \, \mathrm{d}f_y. \tag{3.29}$$

The 2D autocorrelation function can be evaluated from the inverse Fourier transform of the 2D PSD function:

$$C(\tau_x, \tau_y) = \frac{1}{\sigma^2} \int_{-\infty}^{+\infty} \int_{-\infty}^{+\infty} S(f_x, f_y) \exp\left(2i\pi(f_x \tau_x + f_y \tau_y)\right) \mathrm{d}f_x \, \mathrm{d}f_y. \tag{3.30}$$

where τ_x and τ_y denote the lags along x and y axes respectively.

Sampled data and experimental example

Figure 3.13 presents the surface that will illustrate the evaluation of the power spectrum density and autocorrelation functions in the case of a 2D random surface. Figure 3.13 is

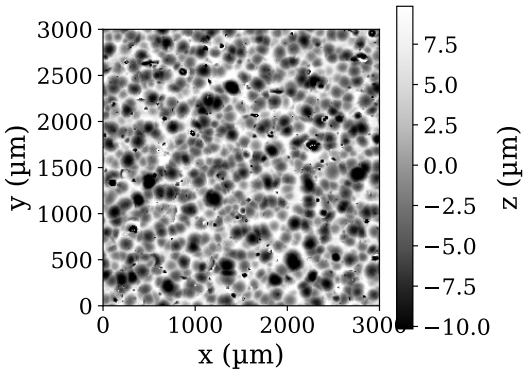

Fig. 3.13 *Experimental surface topography of an aluminum surface blasted with large beads (400 − 600 μm diameter) evaluated by confocal chromatic profilometry. Here, $L = 3000$ μm, $\Delta = 2$ μm*

.

an example of confocal chromatic profilometry data of an aluminum surface blasted with large beads (400-600 μm diameter). The 2D PSD function, $S(f_x, f_y)$, can be evaluated from experimental sampled data and it is evaluated as:

$$S(f_{x,n}, f_{y,m}) = \frac{\Delta^4}{L^2}\left|\sum_{j=0}^{N-1}\sum_{k=0}^{N-1} h(x_j, y_k)\exp\left(-2i\pi\left(\frac{nj}{N}+\frac{mk}{N}\right)\right)\right|^2 \tag{3.31}$$

$$= \frac{\Delta^2}{N^2}\left|\sum_{j=0}^{N-1}\sum_{k=0}^{N-1} h(x_j, y_k)\exp\left(-2i\pi\left(\frac{nj}{N}+\frac{mk}{N}\right)\right)\right|^2, \tag{3.32}$$

here $x_j = j\Delta$ and $y_k = k\Delta$ denote the sampled lengths along the x and y axes respectively, where $j = k = 0, 1, 2, .., N-1$ denote the indices of the sampled lengths, $f_{x,n} = n/(N\Delta)$ and $f_{y,m} = m/(N\Delta)$ denote the sampled frequencies along the x and y axes respectively where $n = m = -N/2, ..., N/2-1$ denote the indices of sampled frequencies.

Figure 3.14(a) presents the 2D PSD function obtained from experimental data of Fig. 3.13 with Eq. (3.31). The signal of the PSD function is mainly distributed in the center of the image, for frequencies close to zero, and it quickly decreases away from the center. However, for a fixed absolute value of frequency, the power appears to be constant whatever the direction (with the center of the image as a starting point), which is a characteristic of isotropic surface.

For isotropic PSD function, it is more convenient to study only one radius of the PSD function or its radial average $S_r(f_x)$, which consists of averaging the power values of all points at equal distance from the center of the image [72]. Figure 3.14(b) presents $S_r(f_x)$, the radial average of the 2D PSD function of Fig. 3.14(a), where it is easier to identify the main frequencies of the surface. Indeed frequencies ranged from 0.0018 μm^{-1} and 0.0036 μm^{-1} are stronger. These main frequencies correspond to typical lengths range from 558 μm to 277 μm, which can be directly related to the diameter of the beads used

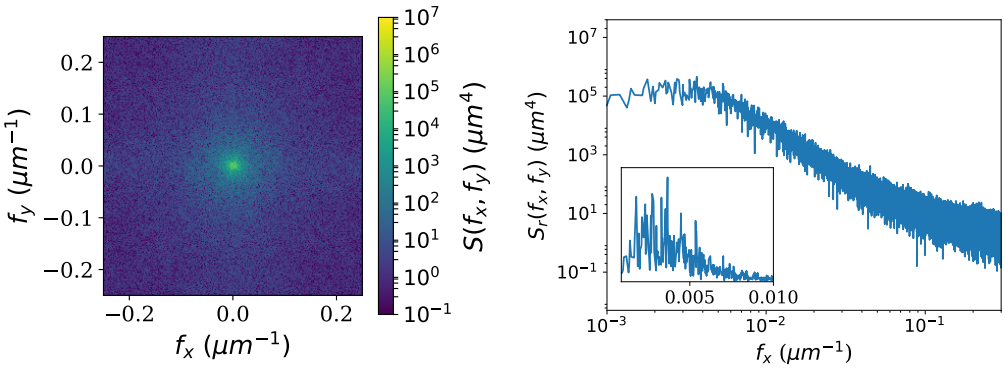

(a) (b)

Fig. 3.14 *2D PSD function obtained from 2D random surface of Fig. 3.13 with Eq. (3.31).(a) The PSD function is a 2D function, which is in this case isotropic.(b) $S_r(f_x)$ is the radial average of the 2D PSD function in log-log scale and in linear-linear scale in the inset.*

for the blasting treatment (400-600 μm diameter).

As the PSD function is a representation of the spatial frequencies which compose a surface topography, one can then construct a PSD master curve, which covers a large range of frequencies, using the three experimental setups. Such PSD master curves were already reported in the literature by Duparre et al.[63] or by Gujrati et al.[77]. In our case, the PSD master curve is obtained from experimental measurements of confocal chromatic profilometry, stylus profilometry and atomic force microscopy, and it finally covers four decades of frequencies, as presented in Fig. 3.15. As the measurements from stylus profilometry are 1D profiles, the 2D PSD functions evaluated from confocal chromatic profilometry and atomic force microscopy measurements are converted into 1D PSD functions, as described in Eq. (3.28).

The 2D autocorrelation function of the surface can be deduced from the 2D PSD function, by performing its inverse Fourier transform (Eq. (3.30)):

$$C(\tau_{x,j}, \tau_{y,k}) = \frac{1}{\sigma^2 N^2 \Delta^2} \sum_{n=0}^{N-1} \sum_{m=0}^{N-1} S(f_{x,n}, f_{y,m}) \exp\left(2i\pi\left(\frac{nj}{N} + \frac{mk}{N}\right)\right). \tag{3.33}$$

where $\tau_{x,j} = j\Delta$ and $\tau_{y,k} = k\Delta$ are the sampled lags along the x and y axes respectively, where $j = k = -N/2, ..., N/2 - 1$ denote the indices of the sampled lags.

The 2D autocorrelation function obtained with Eq.(3.33) is presented in Fig.3.16(a). As expected, $C(\tau_x, \tau_y)$ is maximal and equal to one in the center of the image (where there is no lag). Then $C(\tau_x, \tau_y)$ is decreasing when the absolute value of the lag increases.

For such isotropic autocorrelation function, this is more convenient to represent the radial average of the function, $C_r(\tau_x)$, as presented in Fig.3.16(b). $C_r(\tau_x)$ is maximum without lag, then it decreases to zero for a lag value of 100 μm. The correlation length of $C_r(\tau_x)$, which corresponds to the lag value at which $C_r(\tau_x)$ drop to 1/e, is 47.5 μm. Then

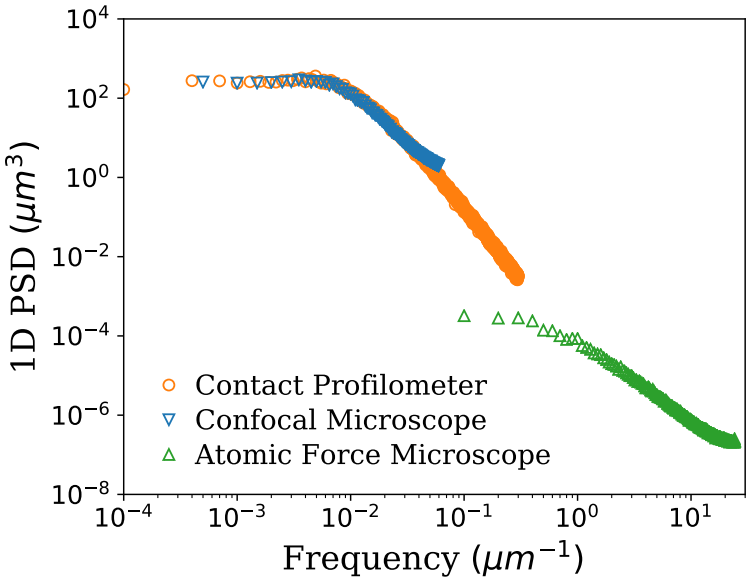

Fig. 3.15 *1D PSD master curve calculated from morphology measurements of three different experimental setups. The five decades frequency range is obtained with setups with confocal chromatic profilometry, stylus profilometry and atomic force microscopy.*

$C_r(\tau_x)$ goes to negative values to reach its minimal value, -0.05, for a lag value of 140 μm, which means that the surface is slightly uncorrelated. In practical terms, this means that starting from a random point in the surface with a height h, all points 140 μm away from it have bigger chance to have a height of the opposite sign of h. Finally, $C_r(\tau_x)$ goes back to zero and oscillates around it.

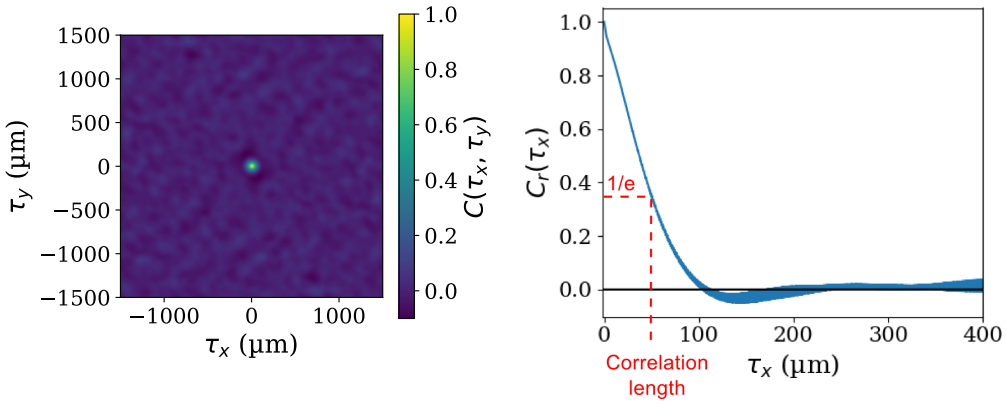

(a) (b)

Fig. 3.16 *2D autocorrelogram obtained from 2D random surface of Fig. 3.13 with Eq. (3.33).(a) The autocorrelation function is a 2D function, which is, in this case, isotropic.(b) Radial average of the 2D autocorrelation function allows to easily evaluate the correlation length of the surface.*

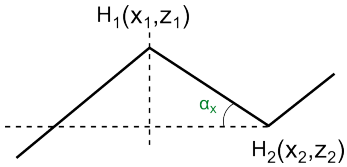

Fig. 3.17 *The 1D slope, α_x, can be evaluated with the coordinates of the two points H_1 and H_2, in the x-z plane.*

3.2.3 The slope distribution

The slope distribution is the main factor used to describe a surface morphology in the geometrical optics community. A rough surface can be seen as a collection of sloped facets, where the slope can be positive or negative and the facets can be oriented along different directions with respect to the macroscopic mean level. Each facet can be characterized by its slope, while the statistics of the slope distribution are key elements of the microfacet theory [23].
This section aims to describe three ways to evaluate the slope distribution of a rough surface. First we will describe an approach to evaluate the local slope of each measured height, along the x and y axes. Secondly, a formulation, described by Nayar [23], which links the width of the slope distribution to the rms of the height distribution and to the correlation length of the surface, will be presented. The last approach consists in approximating the vicinity of each height by a plane, in order to consider the slope of micrometric facets. Finally, the results of these three approaches will be compared.

3.2.3.1 1^{st} method: Local approach

The evaluation of the local slope is rather simple to perform. Indeed, knowing the altitude and the spatial position of the points, one can evaluate the local slope. In the x-z plane, the two points H_1 and H_2, respectively defined by the coordinates (x_1, z_1) and (x_2, z_2), are parts of a profile, and are presented in Fig.3.17. The local slope, α_x, is defined as:

$$\alpha_x = \arctan\left(\frac{z_1 - z_2}{x_1 - x_2}\right). \tag{3.34}$$

If this approach is rather simple to numerically implement, it is highly sensitive to noisy data.

The local slope of a surface can be evaluated knowing the coordinates of the experimental points. Here $g_x(j,k)$ and $g_y(j,k)$ denotes the gradients, or surface derivatives, along the directions x and y respectively, and are evaluated as:

$$g_x(j,k) = \frac{h(x_{j+1}, y_k) - h(x_{j-1}, y_k)}{2\Delta} \tag{3.35}$$

$$g_y(j,k) = \frac{h(x_j, y_{k+1}) - h(x_j, y_{k-1})}{2\Delta} \tag{3.36}$$

Then the slopes $\alpha_x(j,k)$ and $\alpha_y(j,k)$ are evaluated as:

$$\alpha_x(j,k) = \arctan\left(g_x(j,k)\right) \tag{3.37}$$

$$\alpha_y(j,k) = \arctan\left(g_y(j,k)\right). \tag{3.38}$$

Consequently, the sign of $\alpha_x(j,k)$ is related to the sign of $h(x_{j+1},y_k) - h(x_{j-1},y_k)$, and the sign of $\alpha_y(j,k)$ to the sign of $h(x_j,y_{k+1}) - h(x_j,y_{k-1})$.

In order to improve the signal to noise ratio, we apply a Sobel filter [78], to the points in the vicinity of $h(x_j,y_k)$. It consists of using two 3×3 kernels to estimate weighted gradients in the x and y directions. Its application is adapted to the detection of the edges of rough surfaces [79]. The two Sobel gradients along the x and y directions, SG_x and SG_y, are expressed as:

$$SG_x(j,k) = \frac{g_x(j,k-1) + 2g_x(j,k) + g_x(j,k+1)}{4} \tag{3.39}$$

$$SG_y(j,k) = \frac{g_y(j-1,k) + 2g_y(j,k) + g_y(j+1,k)}{4}. \tag{3.40}$$

Then, one can evaluate the two slopes (along x and y axes) for each point $h(x_j,y_k)$, from $SG_x(x_j,y_k)$ and $SG_y(x_j,y_k)$, following Eqs. (3.37) and (3.38):

$$\alpha_x(j,k) = \arctan\left(SG_x(j,k)\right) \tag{3.41}$$

$$\alpha_y(j,k) = \arctan\left(SG_y(j,k)\right). \tag{3.42}$$

As an example, the slope distributions of the frosted glass samples G1 and G5 were evaluated. Figure 3.18(a) and Fig. 3.18(b) respectively present the height cartographies of the samples G1 and G5.
The local slopes are evaluated along x and y axes, as described in Eqs. (3.41) and (3.42). The calculations give rise to two slope cartographies (one along each axis), that are presented in Fig. 3.19(a) and Fig. (b) for the sample G1, and in Fig. 3.19(c) and Fig. (d) for the sample G5. As expected, these two slope cartographies are quite noisy.

From these slope cartographies, one can evaluate the joint probability density function of the slopes α_x and α_y. These latter are evaluated for the samples G1 and G5, and are presented in Fig. 3.20(a) and (b) respectively. The two slope joint probability density functions are drastically different but are isotropic. One can then examine the marginal probability of the slope α_x, fixing $\alpha_y = 0$, as presented in Fig. 3.20(c). In this way, the comparison is easier, and one can estimate the difference between the two distributions.

The sample G1 is mainly composed of slopes of small angles, ranging from -5° to 5°: the surface is then mainly flat. The full width height maximum (FWHM) of the marginal slope distribution of the sample G1 is 3.8°. On the other hand, the sample G5 is composed of a wider range of slopes, from -40° to 40°. The FWHM of the marginal slope distribution of the sample G5 is 45.6°.

3.2.3.2 2^{nd} method: Nayar approach

As the geometrical optics and physical optics communities are rather different, few works try to compare and examine both these approaches. In 1991, Nayar et al.[23] present a comparative study of a model based on physical optics approach (Beckmann-Spizzichino) with a model based on geometrical optics approach (Torrance-Sparrow). In this study,

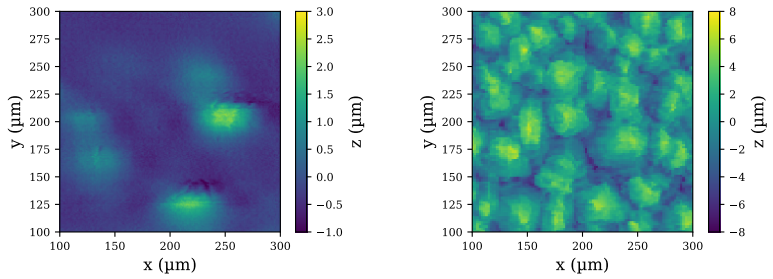

Fig. 3.18 *The experimental height cartographies of the samples (a) G1 and (b) G5, are used to evaluate the local slope distribution.*

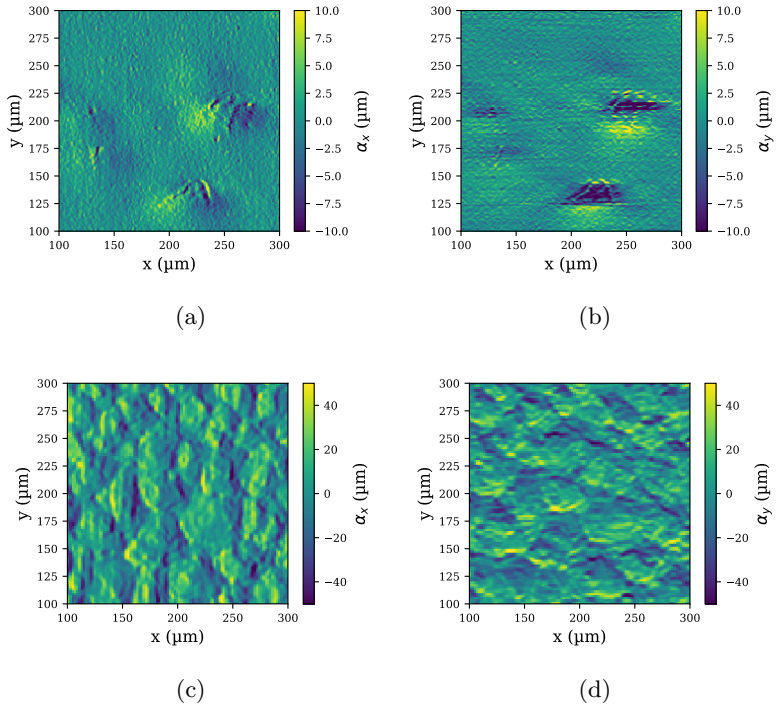

Fig. 3.19 *Evaluation of the 1D slope distributions of the frosted glass sample G1 (a) along the x axis, (b) along the y axis ; and of the frosted glass sample G5 (c) along the x axis, (d) along the y axis.*

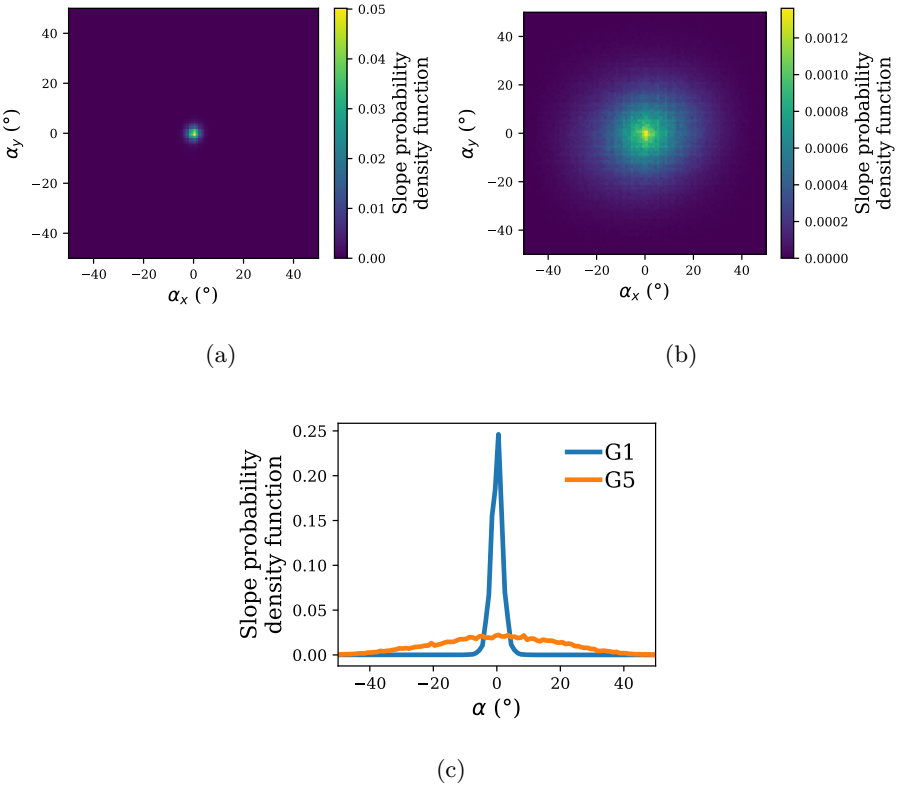

Fig. 3.20 *The joint probability density functions of the slopes α_x and α_y of the sample (a) G1, and the sample (b) G5, are isotropic but rather different. This difference is stressed in (c), which presents the marginal probability of the slope α_x fixing α_y to zero*

the authors present the following relation that relates the two kinds of morphological parameters:

$$\sigma_\alpha = \frac{1}{\sqrt{2}} \arctan\left(\frac{2\sigma}{l_c}\right), \tag{3.43}$$

where σ_α denotes the standard deviation of the slope distribution, σ is the standard deviation of the height distribution and l_c is the correlation length of the surface. It has to be mentioned that Nayar et al., assume that the slope and the height distributions are Gaussian like processes. However, we saw in the previous section (Fig. 3.6 and Fig. 3.20), this is not always the case.
In the case of the frosted glass samples G1 and G5, σ_α, are respectively 1.2° and 18.6°, which leads to the two Gaussian slope distributions presented in Fig. 3.21. The FWHM of the two slope distributions are 2.8° and 43.3° for the samples G1 and G5 respectively.

3.2.3.3 3^{rd} method: Plane approach

In this third approach, the slopes are evaluated by fitting the best linear plane in the vicinity of the considered height. In this way, the impact of the noise of the experimental data should be decreased. However, this approach is limited to the study of rough surfaces, with rather long correlation length.

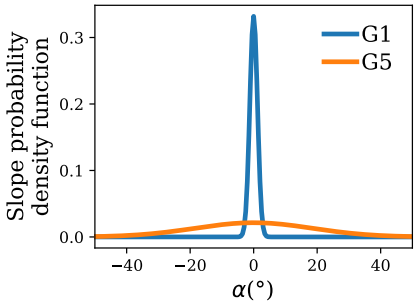

Fig. 3.21 *Assuming a Gaussian height distribution of the samples G1 and G5, one can evaluate a Gaussian slope distribution from Eq. (3.43). The rms of the sample G1 and G5 are respectively 0.42 μm and 2.4 μm, and their correlation length are respectively 28.3 μm and 9.7 μm.*

In order to be consistent with the microfacet theory, the dimensions of the fitted plane are fixed to $5 \times 5\ \mu m^2$. Due to the lateral resolution of the measurements realized by chromatic confocal profilometry, the plane is at least fitted with 10 experimental points. Each area of $5 \times 5\ \mu m^2$, is fitted by a linear plane, such as:

$$z = c_1 x + c_2 y + c_3. \tag{3.44}$$

Then, two angles, α and ϕ_s are evaluated, as presented in Fig. 3.22. The angle α between the normal of the fitted plane, $\mathbf{n_s} = (c_1, c_2, 1)$, and the the normal of the surface $\mathbf{z} = (0, 0, 1)$, is evaluated by dot products:

$$\cos(\alpha) = \frac{\mathbf{n_s} \cdot \mathbf{z}}{\|\mathbf{n_s}\| \|\mathbf{z}\|}. \tag{3.45}$$

Then the angle ϕ_s between the azimuth reference $\mathbf{x} = (1, 0, 0)$ and the orthogonal projection of $\mathbf{n_s}$ on the xy plane, is evaluated as:

$$\phi_s = \text{atan}_2(c_2, c_1). \tag{3.46}$$

Each fitted plane (e.g slope) is then defined by the couple of angles α and ϕ_s.

As an example, the angles α and ϕ_s are evaluated for the frosted glass samples G1 and G5. The joint distributions of α and ϕ_s are evaluated for each sample, and are presented in Figs. 3.23(a) and (b) for the samples G1 and G5 respectively.

The two slope distributions have different shapes, but they both seem to be isotropic. Consequently, one can examine marginal distributions of the angle α, fixing the angle ϕ_s to 0° and 180°. In this way, marginal slope distributions are presented in Fig. 3.23(c). The shape of the slope distribution of the sample G1 is rather similar to the previous ones (see Fig. 3.20(c) and Fig. 3.21), and its FWHM is 1.8°. On the other hand, the shape of the slope distribution of the sample G5 is different: indeed, its maximum is not for $\alpha = 0°$, but for $\alpha = \pm 11°$. Its FWHM (considered from the maximum obtained for $\alpha = 11°$) is 44.8°.

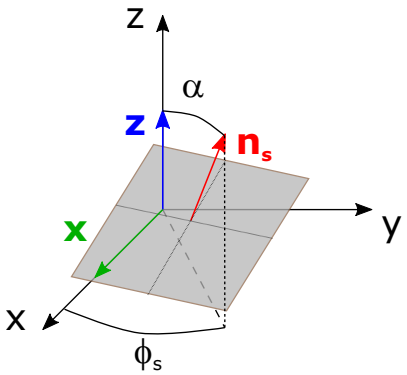

Fig. 3.22 *Two angles are defined to characterize the slope: the angle, α, between the normal of the surface* **z** *and the normal of the plane* $\mathbf{n_s}$*; and the angle ϕ_s between the azimuth reference* **x** *and the orthogonal projection of* $\mathbf{n_s}$ *on the xy plane.*

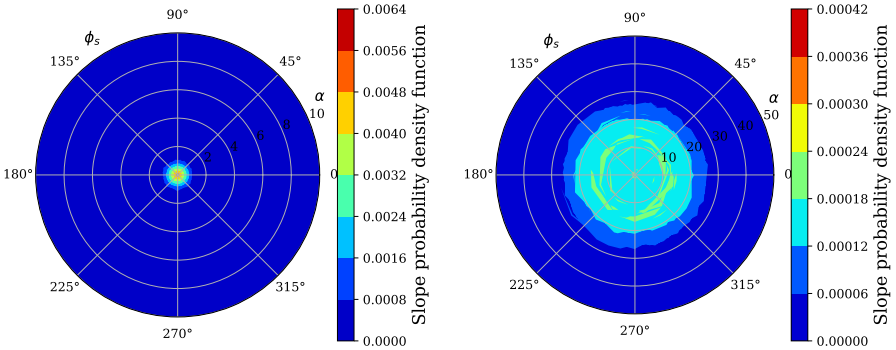

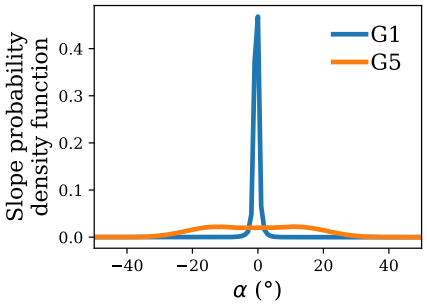

Fig. 3.23 *The joint distributions of α and ϕ_s are evaluated for the sample G1 (a), and for the sample G5 (b). The angle α is read along the radius of the circle and ϕ_s along the circumference of the circle. A marginal slope distribution is extracted from the two slope joint distributions, fixing ϕ_s to 0° and 180°, are presented in (c).*

3.2.3.4 Conclusion: Comparison of the three approaches

The Sec. 3.2.3 presents three different approaches to evaluate the slope distribution of a surface. For each method, the slope distributions of two glass surfaces were evaluated.

Figure 3.24(a) presents the slope distributions obtained by the three approaches for the sample G1. In the three cases, the distribution is narrow around $\alpha = 0°$, which indicates a globally flat surface. However, one can observe discrepancies between the three curves, as reflected by their FWHM values which are recalled in Table 3.5. The distribution evaluated by the "Local" approach is the largest and the less isotropic one. These two effects could be related to the high level of sensitivity of noisy data of this approach.

The slope distributions obtained for the sample G5 are presented in Fig. 3.24(b), and their FWHM values are recalled in Table 3.5. The slope distributions evaluated from the "Local" and "Nayar" approaches are in very good accordance. Except the noise of the "Local" slope distribution, the two curves are rather similar. However, the slope distribution evaluated by the "Plane" approach is different. Even if its FWHM is similar to the two others, the curve has two local maximum for $\alpha = \pm 11°$, and consequently, the tails of the distribution are lower.

Nevertheless, this unusual slope distribution is not inconsistent with the actual topography of the sample G5. Indeed, as presented in Fig. 3.18(b), the surface is made of pyramids. Consequently, it is not inconsistent to find a slope distribution with two symmetric local maxima. Such kind of distribution cannot be obtained by the "Nayar" method, as the slope distribution is Gaussian by assumptions. However, this slope distribution could have been reached by the "Local" approach, but it has probably been smoothed due to the noise sensitivity of the method.

In the rest of the thesis, we will use the "Plane" method to evaluate the slope distribution of the surface. However, in the case of anisotropic surfaces, the "Local" method will be preferred, in order to stress the anisotropy of the surface, along the two measurement directions. In the case of large discrepancies between the two methods (as for the sample G5), the results will be discussed.

	Local	Nayar	Plane
Benefits	Fast Experimental	Very fast	Experimental Microfacet
Drawbacks	Noise sensitive	Gaussian assumption	Limited to rough surfaces
FWHM G1 (°)	3.8	2.8	1.8
FWHM G5 (°)	45.6	43.3	44.8

Table 3.5: The three methods presented to evaluate the slope distribution are referred to as "Local", "Nayar" and "Plane", and were described in Secs. 3.2.3.1,3.2.3.2 and 3.2.3.3 respectively. These three approachs have their benefits and drawbacks, which are recalled here. The FWHM of the slope distributions of samples G1 and G5 are also recalled.

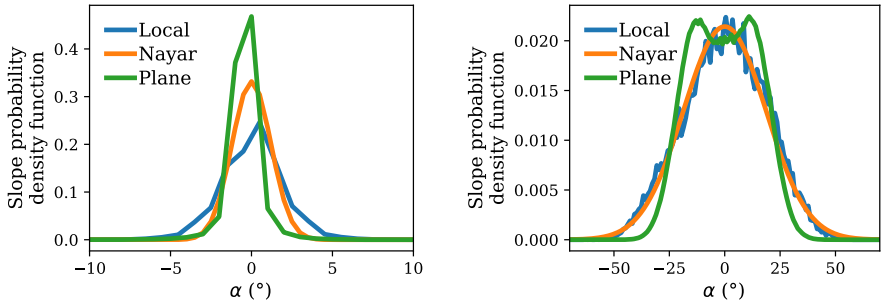

Fig. 3.24 *The slope distributions were evaluated by three methods, which are referred to as: "Local", as described in Sec. 3.2.3.1, "Nayar", as described in Sec. 3.2.3.2 and "Plane", as presented in Sec. 3.2.3.3. The slope distributions of the sample G1 is presented in (a), and the ones of the sample G5 in (b).*

3.2.4 Determination of consistent experimental settings

The experimental setups used to measure a surface topography were presented in Sec. 3.1. We saw that these different techniques allow to measure the morphology at different scales, by using different lateral resolutions and measuring over areas of different dimensions.

In Sec. 3.2.1, the parameters used to describe the surface morphology were described. Their expressions are related to the lateral resolution (which was denoted Δ) and to the dimensions of the measured area (which were denoted L). Consequently, these two measurement settings, must be carefully chosen.

To this end, we realized a numerical study in order to examine the impact of these two measurement settings on the evaluated rms height and correlation length. This study is performed using profiles and surfaces numerically produced, with Gaussian height distribution and with known values of rms height and autocorrelation functions. Such numerical profiles and areas were designed using the so-called Fourier Filtering Method [80][81].

3.2.4.1 Case of 1D profiles

The numerical 1D profile, L, is 1000 μm long and its lateral resolution, Δ, is 0.027 μm. Its rms height, σ is 0.5 μm and its autocorrelation function has an exponential form with a correlation length, l_c, of 1.6 μm. The impact of the profile dimensions and of the lateral resolution, on the accuracy of the statistical parameters will be evaluated independently.

First, we examine the impact of the length of the profile. To this end, sub-profiles of different lengths L_{50}, L_{200} and L_{500}, which are parts of L, are defined such as:

- $L_{50} = 50l_c$,
- $L_{200} = 200l_c$,
- $L_{500} = 500l_c$.

For each of the three lengths L_{50}, L_{200} and L_{500}, we picked 100 different sub-profiles from

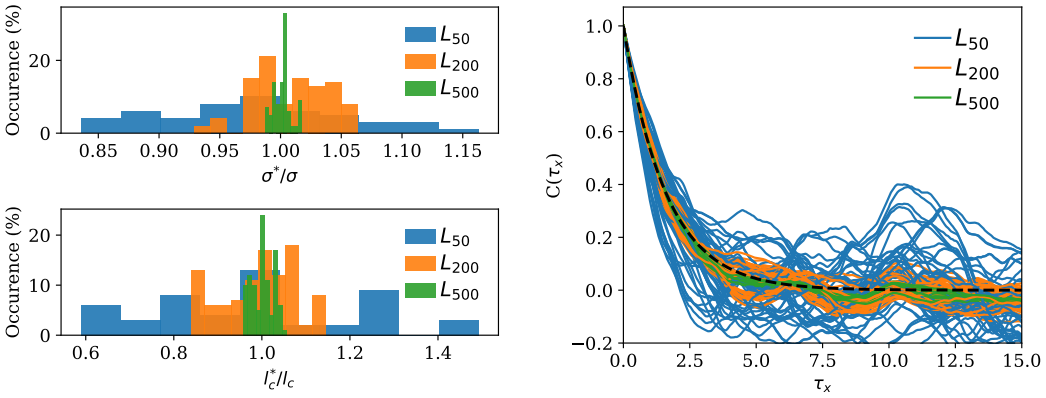

(a) (b)

Fig. 3.25 *Evaluation of the rms and ACF of sub-profiles of different lengths, L_{50}, L_{200} and L_{500} in order to examine the impact of the length of the sub-profile on these two parameters. (a) The dispersion of the rms and correlation length values as a function of the sub-profile length. (b) The ACF function is evaluated for each sub-profile and is compared to the actual ACF of the initial profile (dashed black line).*

the initial profile L (first point of each sub-profile is randomly picked in L). Then, the rms height and correlation length of each series of sub-profiles, which are denoted as σ^* and l_c^*, are evaluated, and compared to the actual rms height(σ) and correlation length (l_c) of the initial profile L.

The rms height and the correlation length values, σ^* and l_c^*, which were evaluated from the sub-profiles are presented in Fig. 3.25(a), and the autocorrelation function evaluated from these same sub-profiles are presented in Fig. 3.25(b).

In both figures, one can observe that the length of the profile has a strong impact on the evaluation of the parameters. Indeed, the dispersion of the evaluated values is decreasing as the length of the sub-profile is increased. For L_{50} sub-profiles, the standard deviations of the σ^*/σ and l_c^*/l_c values are respectively 20% and 60%. Such uncertainties are not reasonable. On the other hand, when the sub-profile is L_{500} long, the uncertainties are more appropriate: the standard deviations of the σ^*/σ and l_c^*/l_c values are respectively 2% and 5%. The dimension of the examined profile is then a critical parameter.

Moreover, from Fig. 3.25(b), we can observe that even considering a length L_{500}, the evaluated ACF are not stable for high values of τ_x. Consequently, one needs to realize several measurements to average these oscillations.

In the second stage of this study, we focus on the impact of the lateral resolution, by considering a different number of points for each sub-profile of length L_{500}:

- $\Delta = 0.027\ \mu m$ (all points are considered),
- $\Delta_5 = 5 \times 0.027\ \mu m$, (one fifth of the points are considered),
- $\Delta_{10} = 10 \times 0.027\ \mu m$, (one tenth of the points are considered),

Once again, for each sub-resolution, Δ, Δ_5 and Δ_{10}, 100 different sub-profiles are ran-

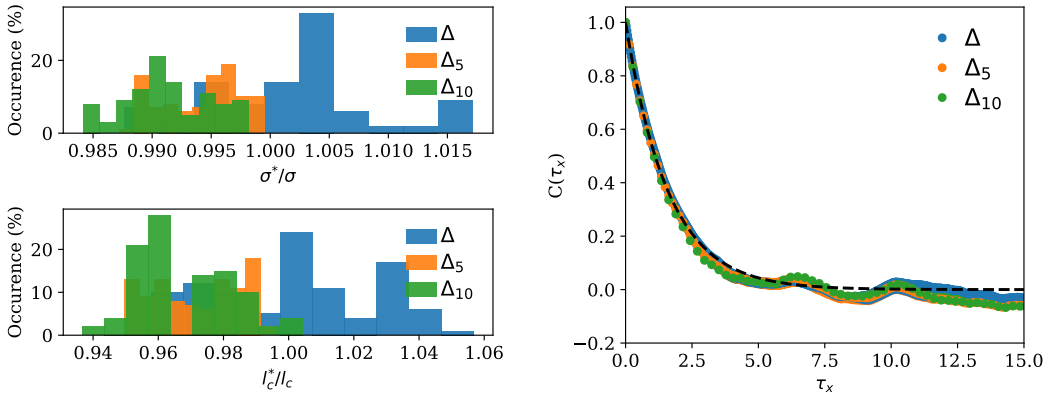

(a) (b)

Fig. 3.26 *Evaluation of the rms and ACF of sub-profiles of length L_{500}, with different lateral resolutions in order to examine its impact on these two parameters. (a) The dispersion of the rms and correlation length values as a function of the lateral resolution of the profile. (b) The ACF function is evaluated for the profiles with different lateral resolution and is compared to the actual ACF of the initial profile (dashed black line).*

domly picked from the initial data. The results are presented in Fig. 3.26, in the same manner as in Fig. 3.25. It appears that the lateral resolution is a less critical parameter. Indeed, the standard deviations of the σ^*/σ and l_c^*/l_c values are up to few percent for the three different lateral resolutions. However one can notice that for Δ_5 and Δ_{10}, the rms and the correlation lengths are under-evaluated.

3.2.4.2 Case of 2D areas

A similar study is realized in the case of 2D surfaces numerically generated. As in the 1D case, it appears that the dimensions of the area are critical to evaluate correct rms and correlation length values, and that the spatial resolution is less essential. Major results are presented in the following section.

3.2.4.3 Analysis of the results

This study suggests that one should privilege the dimensions of the area (or profile), rather than the lateral resolution. We will then focus on the impact of the dimensions of the scan to build our experimental protocol. The Fig. 3.27 presents the results of the dispersion of the correlation length values (which appears to be the most sensitive parameter) according to the size of the considered sub-areas or sub-profiles. As the actual correlation length of the initial profile and initial area are different, these sizes are expressed as a number of considered correlation lengths.
In Fig. 3.27(a), one profile and one area are considered, and one can see that:

- The measurement of a very small area (about 10×10 correlation length measured) leads to very high uncertainties. It implies that in the case of quick measurement, one should favor a 1D characterization.

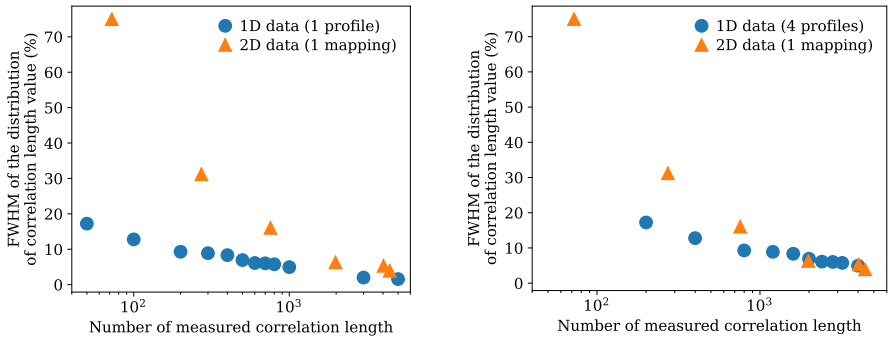

(a) (b)

Fig. 3.27 *The FWHM of the dispersion of the correlation length values obtained from the analysis of different sub-profiles and sub-areas dimensions (as the one presented in Fig. 3.25(a)) are plotted as a function of the number of correlation lengths that composed the corresponding sub-profiles or sub-areas. (a) One measured profile and one measured area are considered. (b) One area and four profiles are considered in order to take into account the potential anisotropy of the surface.*

- The evaluation of the parameters seems to be more efficient in the 1D case than in the 2D case. Indeed, for a similar profile length measured (expressed here in terms of the number of measured correlation length), the uncertainties are smaller in the case of 1D data.
- For a high number of measured correlation lengths (about 3000), the uncertainties reach a plateau and are approximately equal for 1D and 2D cases.

However, the results presented in Fig. 3.27(a), only consider the evaluation of a single 1D profile. Consequently, such measurements cannot characterize the isotropy or anisotropy of the surface. Then, we consider that at least four 1D measurements have to be taken into account in order to access this information. The results, considering four 1D profiles, are presented in Fig. 3.27(b). In this case, the same conclusions remain, except that the level of uncertainty is closer for the two types of data.

3.2.4.4 Deduction of experimental protocol

Several points were highlighted from this numerical study:

- The dimensions of the considered profile/area are parameters that must carefully be considered. To obtain an evaluation of the correlation length which is correct (less than 10% of dispersion around the actual value), one must measure at least 2000 times the correlation length. This corresponds to an area of dimensions about 45 times the correlation length, or to four profiles of 500 times the correlation length.
- The lateral resolution of the measurement is less critical. We consider here that the lateral resolution should be at least 10 times smaller than the correlation length.
- One must multiply the number of measurements (at different locations on the sample) in order to average the oscillations of the autocorrelation function.

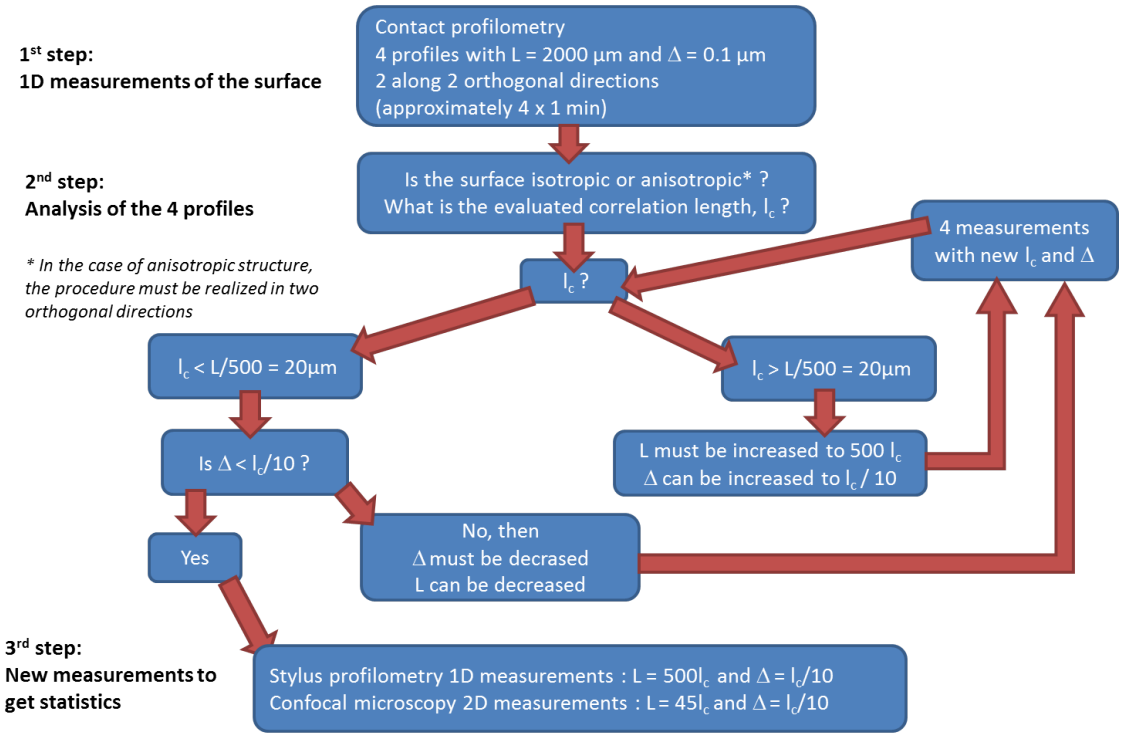

Fig. 3.28 *Diagram which presents the 3 steps and conditions on the dimensions of the measured profile (L) and measured area (L^2) and on the lateral resolution Δ, in order to perform suitable evaluation of the actual correlation length, l_c, of the examined surface.*

- For a quick measurement, it is safer to measure 1D long profile than a small 2D area of the surface.

Finally, we came up with a measurement protocol, composed of several steps, which is presented in the diagram in Fig. 3.28. The procedure consists in realizing a first standard measurement of 1D profiles of the surface, in order to get a first estimation of the correlation length of the surface. Then the length of the profile and its lateral resolution are adjusted in order to be adapted to the actual correlation length of the surface. When suitable parameters have been determined, measurements can be realized in 2D and be repeated in order to improve statistics.

3.2.5 Conclusion

The aim of this section was to report the conventions used in the thesis to analyze the experimental data of surface morphology. It allows us to define the surface properties and to evaluate if the examined surfaces present Gaussian statistics or not. Three kinds of parameters and functions, related to the description of the surface morphology, were described:

- Parameters related to the description of the shape of the height probability density function (Sec. 3.2.1), which are the root mean square, the skewness and the kurtosis (defined in Eqs. (3.4), (3.5) and (3.7)). These three parameters describe the statistical properties of a variable at individual positions.

- Functions related to the spatial correlations of the height (Sec. 3.2.2), which are the power spectrum density function or equivalently the autocorrelation function. These two functions were evaluated in the cases of profiles and surfaces.
- Distributions describing the slopes that composed a rough surface (Sec. 3.2.3), which allow to classify the surface morphologies by the width of their slope distributions. We present three different approaches to characterize a slope distribution.

These three kinds of parameters and functions have to be considered carefully. Indeed, even if their numerical evaluation can be automatized, the results must be examined individually.
Finally, we present the results of a numerical study, which allow us to implement a robust experimental procedure (Sec. 3.2.4). Indeed, we saw that the rms height and the correlation length depend on the topography itself, but also on the measurements settings (lateral resolution and dimensions of scans).
The next section will provide quantitative and qualitative properties of the surface topography, which will be evaluated with these parameters and functions.

3.3 Morphological properties of simple model surfaces

The model surfaces were designed to have specific and controlled morphology, as presented in Sec. 2.1.1. However, some of those model samples went through structural modifications such as smoothing of the line gratings edges and spatial organization of the pillar gratings. Their morphologies differ from initial design and were examined. First, the morphological properties of the modified line gratings will be examined. Then, we will compare the morphological properties of the pillar surfaces with periodic hexagonal arrangement and randomly dispersed arrangement.

3.3.1 1D line gratings

Line grating samples are 1D surfaces, meaning that we assume that their surface morphology is invariant along one direction. Consequently, their morphology can be evaluated with a single 1D profile, along the cross-section of the lines. In this way, the study of the modified line gratings, obtained by thermal relaxation process (see Sec. 2.1.2.2), was performed using experimental height profiles measured by stylus profilometry.

However, the measurements of structures with high slopes (as it is the case for rectangular cross-section lines) can lead to measurement artifacts [82], as the one presented in the top in Fig. 3.29. Indeed, due to the high slope and to the tip size, the measurement of the real surface is hardly accessible, and appears highly asymmetrical. However surfaces produced by the same fabrication process have extensively studied at SVI [45][83], and such asymmetry has never been observed by Scanning Electron Microscopy (technique which is less sensitive to such kind of artifact). In order to present as accurately as possible the morphology of the surfaces, we choose to consider that they are symmetric and consequently the side of the measured cross section which is highly impacted by the measurement artifact due to the setup geometry (left part on the top of Fig. 3.29) is replaced by the symmetry of the less impacted side of the measurement, as presented in the bottom of Fig. 3.29.

All the 12 relaxation levels of the initial line grating of 40 μm period were measured by stylus profilometry. For each measurement, we performed the symmetry modification described in Fig. 3.29. Figure 3.30 presents a single line cross-section of each of all 12 levels of relaxation.

As expected, the cross section of the line is progressively smoothed: the slope of the structure is progressively decreasing, due to the diminution of the height of the line and to its enlargement. The decrease of height is confirmed by the evolution of the rms height (defined in Eq. (3.4)), which is decreasing as the relaxation time increases, as presented in Fig. 3.31.

The local slope α_x of the surface was evaluated as described in Eq.(3.34). The local slopes of 4 different states of relaxation, 0 min, 120 min, 330 min and 810 min are presented in Fig.3.32. In the case of the rectangular line cross-section, Fig.3.32(a), α_x, is first equal to 0° (due to the flat intraline space) and quickly reaches its maximal slope at 75° (for a perfectly rectangular cross-section this maximal slope should be 90°, but due

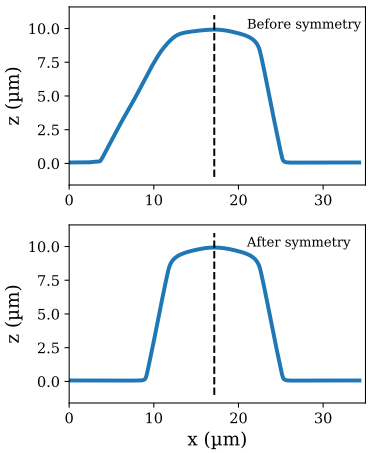

Fig. 3.29 *Measurements of high slopes with contact profilometry can lead to artifacts related to the shape of the tip (see left part of the figure on the top). To represent as exactly as possible the real morphology of the surface, a modified profile is realized by symmetry (see figure on the bottom).*

to measurement artefacts and to manufacturing constraints, the basis of the structure is always larger than the top of the structure). Then the α_x is progressively decreasing to 0°, on the top of the line (which is also locally flat).

As the relaxation time increases, the evolution of the slope changes:

- The length of profile with a slope equal to 0° decays, meaning that the flat surface

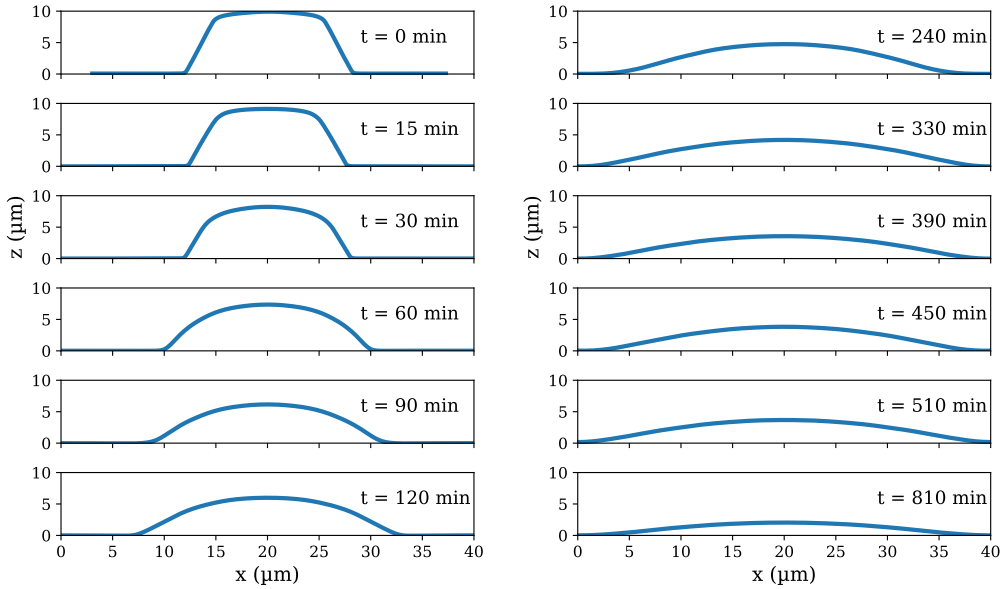

Fig. 3.30 *Evolution of the cross section of the line grating after different times of thermal relaxation. Measurements were realized by stylus profilometry ($L = 1$ mm and $\Delta = 400nm$). For the sake of readability, the cross section of a single line is presented.*

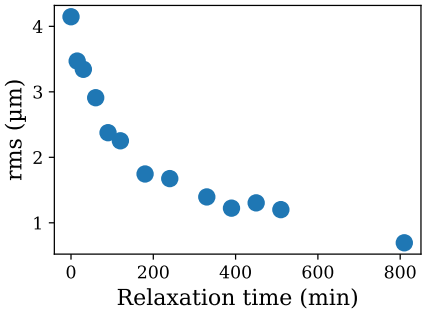

Fig. 3.31 *Evolution of the rms height parameter as a function of the time of relaxation of the line gratings.*

area is decreasing in size, which is due to the enlargement of the structure.

- The maximum slope is decreasing when the relaxation time increases: 43°, 24° and 12°.

Finally, the PSD functions of the profiles were examined: five of them are presented in Fig. 3.33. All PSD functions present a peak at 0.25 μm^{-1}, which corresponds to the 40 μm period of the initial grating. The PSD function of the rectangular line cross-section (corresponding to 0 *min* of relaxation time) is composed of numerous peaks, which indicate the frequencies of the sinusoids needed to describe such sharp profile. While the relaxation time increases, the peaks are progressively disappearing from the PSD functions, as the structure approach a sinusoid shape.

3.3.2 2D pillar gratings

The initial 2D model surfaces are cylindrical pillars, organized as hexagonal gratings, with varying periods (from 20 μm to 70 μm), as described in Sec. 2.1.3. Surfaces with the same pillar covering ratio but with randomly dispersed pillars were also manufactured (see Sec. 2.1.3.2).

We examine here the morphological properties of two samples with the same pillar covering ratios, but with two different spatial organizations: H30, where pillars are periodically organized, and R30, where pillars are randomly dispersed. Measurements realized with chromatic confocal profilometry of samples H30 and R30 are presented in Fig. 3.34.

The rms height of the samples H30 and R30 are 2.2 μm and 1.9 μm respectively. These two close values of rms are consistent, considering that the pillar covering ratio of 10%, is holding fix for the two surfaces. The rms height parameter was evaluated from similar experimental measurements of the samples H40, R40, H60 and R60. The results are consistent with the different pillar covering ratios of the samples, and are summarized in Table 3.6.

However, the change of spatial arrangement is easily observable in Fig. 3.34. The ACF of the two experimental measurements were evaluated and are presented in Fig. 3.35. In Fig. 3.35(a), the hexagonal spatial organization of the surface H30 is confirmed by its ACF, which is periodic along 3 different directions with a period of 30 μm. However, in

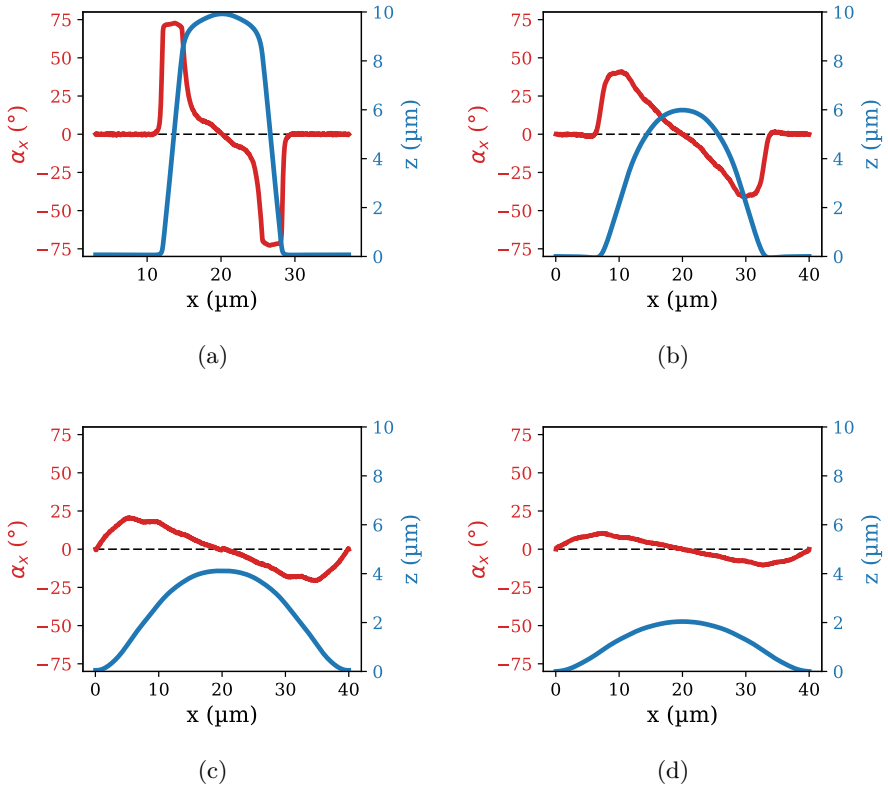

Fig. 3.32 *Evaluation of the slope α_x of line gratings thermally relaxed during* 0 *min (a),* 120 *min (b),* 330 *min (c) and* 810 *min (d).*

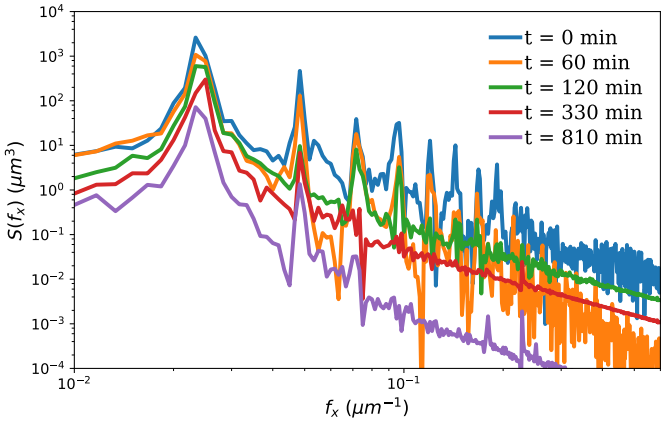

Fig. 3.33 *Power spectrum density functions of five levels of relaxation:* 0 *min,* 60 *min,* 120 *min,* 330 *min and* 810 *min. Experimental measurements were realized by stylus profilometry along the lines cross-sections.*

Sample	Pillar covering ratio (%)	rms (μm)
H30	10	2.21
R30	10	1.97
H40	5.2	0.90
R40	5.2	0.82
H60	2.5	0.41
R60	2.5	0.45

Table 3.6: Summary of the rms values calculated from chromatic confocal profilometry measurements of samples H30, H40, H60, R30, R40 and R60.

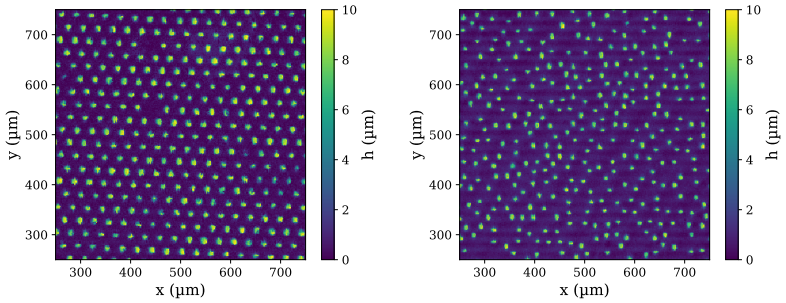

(a) (b)

Fig. 3.34 *Measurements realized by chromatic confocal profilometry of sample H30 (a) and sample R30 (b). In both cases, the measured area is* 1×1 mm^2 *with* $\Delta = 2$ μm*, but for the sake of visibility only a* 500×500 μm^2 *portion of it is presented.*

Fig. 3.35(b), the ACF of sample R30 does not present periodicity, which confirms that the pillars are randomly dispersed.

Cuts of ACF of the samples R30, R40 and R60 are examined in Fig. 3.36. For the three samples, the ACFs go to negative values at a lag of approximately 14 μm, length that can be related to the bottom diameter of a pillar. This anticorrelation is consistent with the sample structure (a pillar dispersion on a flat substrate).

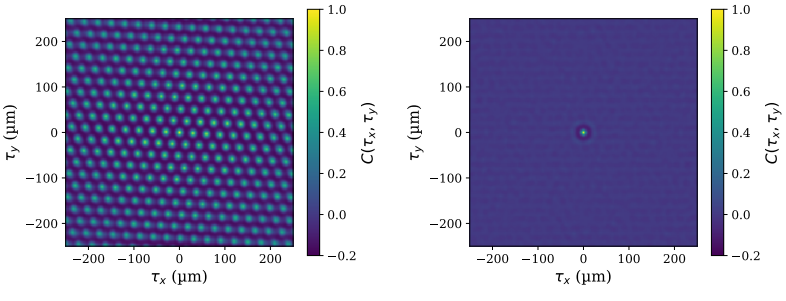

(a) (b)

Fig. 3.35 *(a) The 2D autocorrelation function (ACF) of sample H30 is evaluated from the measurements presented in Fig. 3.34(a).(b) The 2D ACF of sample R30 is evaluated from the measurements presented in Fig. 3.34(b).*

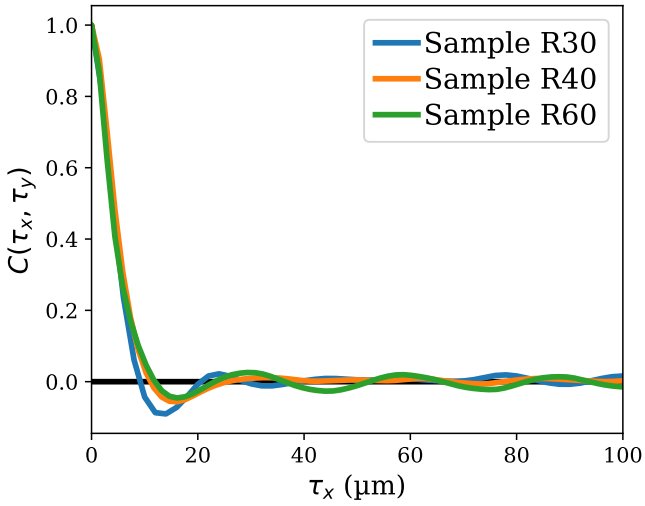

Fig. 3.36 *Cuts of the 2D ACF of samples R30, R40 and R60, calculated from chromatic confocal profilometry.*

3.3.3 Conclusion

The morphological characterization of 1D and 2D model surfaces were realized with stylus profilometry and confocal chromatic profilometry. The line gratings which were thermally relaxed were characterized. The studied surfaces presented slopes from 75° for the quasi-rectangular cross-section, to 12° for the most relaxed surface. The 2D model surfaces (with constant pillars covering ratios) organized with periodic hexagonal gratings and random pillar dispersion were examined. The study of the samples H30 and R30 reveals that we were able to keep a close rms height of two surfaces, while drastically changing the spatial arrangement of the heights.

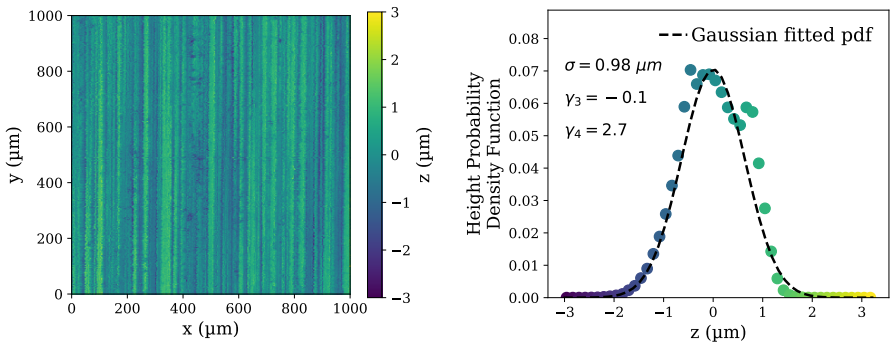

(a) (b)

Fig. 3.37 *(a) Measurement realized by chromatic confocal profilometry of the untreated surface (the total area measured is $5 \times 5mm^2$ with $\Delta = 2$ μm). (b) The experimental height pdf of the surface (averaged over 8 realizations) is well approximated by a Gaussian fit (dashed line).*

3.4 Morphological properties of complex surfaces

The complex rough surfaces are manufactured from different industrial processes, and unlike the model surfaces, their morphologies can be rather complex and is fully unknown. As we aim to perform suitable and representative characterizations of the morphology, the experimental data presented are obtained from several experimental setups and from several realizations (see Sec. 3.1).

3.4.1 Blasted metallic surfaces

The blasted metallic surfaces have been described in Sec. 2.2.1. The aluminum untreated surface and three sets of blasted surfaces, with varied fabrication parameters, are examined in this section. As we have available parts of the fabrication parameters of the blasted surfaces, these latter will be, as much as possible, related to the morphological characterization.

3.4.1.1 Untreated surface

The untreated aluminum sample (see Sec. 2.2.1.1) is the surface that has not been blasted yet and that is highly anisotropic.

Study of the height probability density function

This surface was examined by chromatic confocal profilometry, and one of the experimental measurements is presented in Fig. 3.37(a), where the presence of rolling grooves is undoubtful. The experimental height pdf of the surface is presented in Fig. 3.37(b), and can be well approximated by a Gaussian height pdf. The rms, skewness and kurtosis of the surface are presented in Fig. 3.37(b), and respectively are 0.98 μm, -0.1 and 2.7.

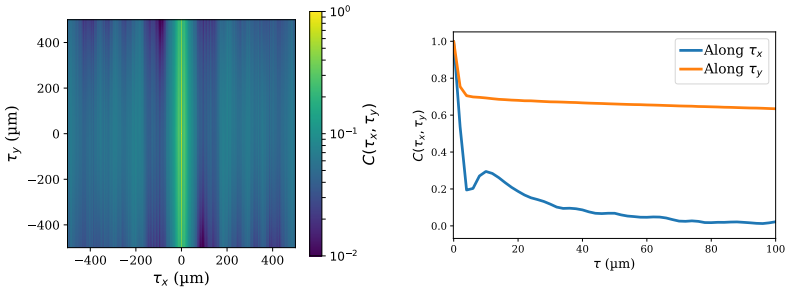

(a) (b)

Fig. 3.38 *(a) The 2D ACF (averaged over several realizations) of the untreated surface. (b) As the ACF is highly anisotropic, two cuts of the 2D functions are plotted (along τ_x and τ_y).*

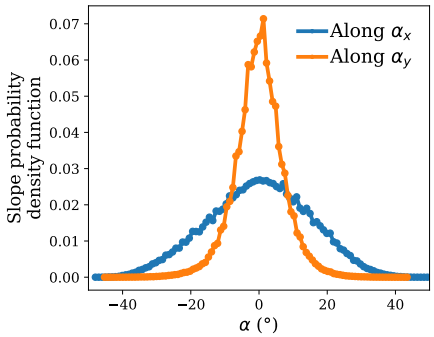

Fig. 3.39 *The slope distributions are evaluated along the x and y axes with the "Local" approach, described in Sec. 3.2.3.1.*

Study of the spatial correlation of height

The ACF of the untreated sample is evaluated from the experimental measurements and is presented in Fig. 3.38: it is as expected highly anisoptropic. Thereby, two cuts along τ_x and τ_y extracted from Fig. 3.38(a) are presented in Fig. 3.38(b). Along τ_x, the ACF presents a peak at 11 μm, which denotes the spatial correlation of the surface due to the presence of the grooves. Then the ACF along τ_x goes to zero. On the other hand, along τ_y, the ACF level stays at a high level (above 0.6) up to 100 μm of lag. It corresponds to the morphology along the line, and denotes that the surface is highly correlated in this direction.

Study of the slope distribution

As the surface is highly anisotropic, we chose to evaluate the slope distribution by the "Local" method (described in Sec. 3.2.3.1). As expected, the slope distributions, along α_x and α_y are rather different, as presented in Fig. 3.39. The slope distribution is logically broader along α_x, which is the direction of the line cross-section than along α_y.

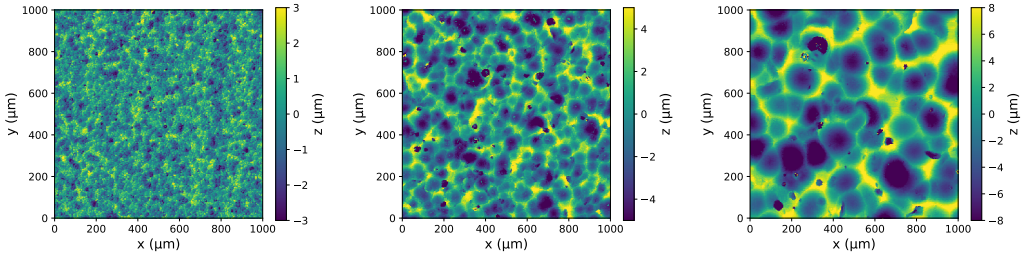

(a) (b) (c)

Fig. 3.40 *Experimental measurements* ($1 \times 1mm^2$) *realized by chromatic confocal profilometry of the aluminum blasted samples:(a) with small beads* ($1 \times 1mm^2$ *with* $\Delta = 2\ \mu m$*), (b) with medium beads* ($2 \times 2mm^2$ *with* $\Delta = 2\ \mu m$*), (c) with large beads* ($3 \times 3mm^2$ *with* $\Delta = 2\ \mu m$*).*

Beads size	rms (μm)	skewness	kurtosis
Small	1.18 ± 0.06	-0.13 ± 0.03	3.56 ± 0.2
Medium	2.55 ± 0.02	-0.16 ± 0.04	4.22 ± 0.4
Large	5.26 ± 0.1	-0.1 ± 0.1	5.06 ± 1

Table 3.7: Summary of the rms, skewness and kurtosis values of aluminum samples blasted with small, medium and large beads. The uncertainty values are obtained from the standard deviation of the parameters calculated from all experimental measurements realized on one surface.

3.4.1.2 Variation of the beads size

This first set of aluminum blasted samples is composed of three surfaces, blasted with small (45-90 μm), medium (125-250 μm) and large (400-600 μm) beads. Their morphologies were examined with the three different experimental setups.

Study of the height probability density function

Figures 3.40(a),(b) and (c) present confocal chromatic profilometry measurements of the surfaces treated with small, medium and large beads respectively. The morphology of the blasted samples seems to be isotropic, and present circular patterns. The diameter and the depth of these circular patterns increase with the diameter of the beads. The experimental height pdf of the three samples, evaluated from measurements of chromatic confocal profilometry and stylus profilometry are presented in a semi-log plot in Fig.3.41, and their respective rms, skewness and kurtosis parameters are presented in Table 3.7.

In a semi-log representation, the negative heights of the experimental height pdf of the samples blasted with medium and large beads deviate from a Gaussian height pdf. This can be explained by the presence of the craters. Indeed, as the diameter and the depth of the crater increase (while the bead size increases), the number of points with negative heights increases (points inside the craters), which leads to a deviation from a Gaussian height pdf.

Study of the spatial correlation of height

The 1D PSD master curves of each sample are evaluated from experimental measurements

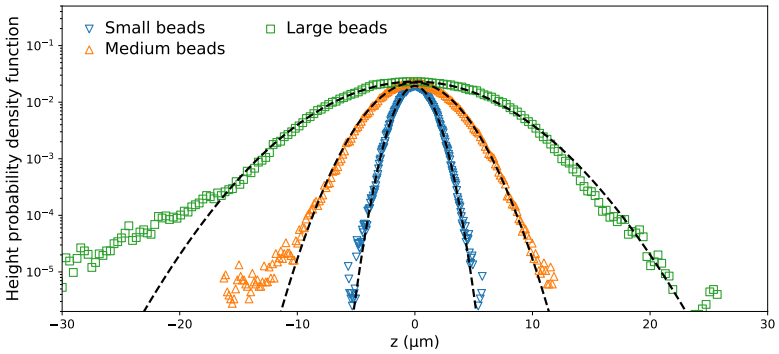

Fig. 3.41 *Experimental height probability density functions of aluminum samples blasted with small, medium and large beads, evaluated from stylus profilometry. The heights pdf are averaged over several measurements.*

.

of the three different setups, and they are presented in Fig. 3.42(a). The experimental points of the PSD functions over the whole frequency range are in good accordance with each other, and we do not need normalization factors to build the PSD master curves. For each PSD master curve, one can identify a dominant spatial frequency, before the drop of the PSD curve. These dominant spatial frequencies are 0.02 μm^{-1}, 0.008 μm^{-1} and 0.003 μm^{-1} for the small, medium and large beads respectively. They respectively correspond to characteristic lengths of 50 μm, 125 μm and 350 μm, which are close to the diameters of the beads used during the blasting. One can then relate the PSD function to one essential fabrication parameter of the surface. The high frequencies of the PSD (extracted from AFM measurements) appear to be negligible, as the PSD value is approximately five decades lower than the PSD level at low frequencies.

The ACF of the three samples are presented in Fig. 3.42(b). The ACF of the three samples present similarities: for surfaces blasted with medium and large beads, the ACF goes to a minimal negative value, which are obtained lag values of 74 μm and 147 μm respectively. These two latter values can be correlated to the average size of the crater diameter, which are respectively 81 μm and 138 μm. However the sample blasted with small beads does not present this negative value. The experimental ACF were fitted with the empirical functions presented in Table 3.8. In this way, the morphology of the surfaces can be described by similar functions, which mainly differ by the amplitude factor a.

	Small beads	Medium beads	Large beads
Function	$\left(1+\frac{x^2}{a^2}\right)^{-\frac{5}{4}}$	$\cos\left(\frac{x}{a}\right)\left(1+\frac{x^2}{a^2}\right)^{-\frac{5}{4}}$	
a (μm)	9.7	30.6	60.9

Table 3.8: Empirical functions used to fit the experimental ACF of the three blasted samples, presented in Fig. 3.42(b).

Study of the local surface curvature

In order to emphasize the local curvature of the surface, topography maps of surfaces

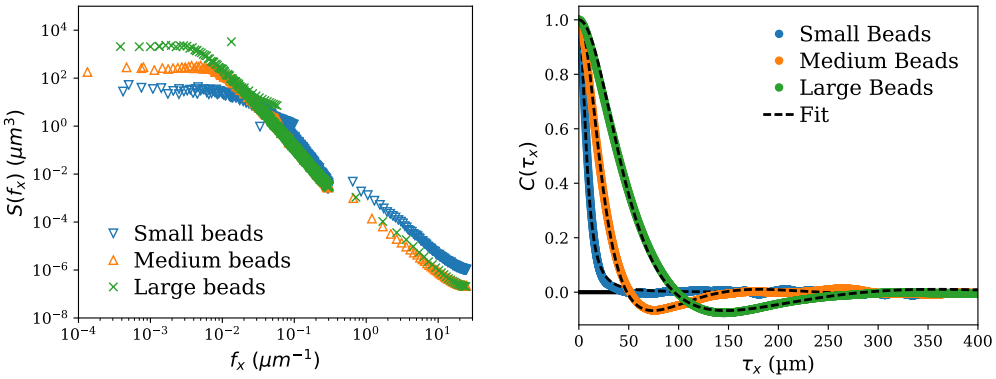

(a) (b)

Fig. 3.42 *(a) Experimental 1D PSDs master curves of aluminum samples blasted with small, medium and large beads. The PSD master curve is obtained from confocal chromatic profilometry, stylus profilometry and atomic force microscopy.(b)Experimental ACF of aluminum samples blasted with small, medium and large beads. ACF are calculated from measurements realized with chromatic confocal profilometry and stylus profilometry. The dashed lines correspond to empirical fits described in Table 3.8.*

blasted with medium and large beads are presented in Fig. 3.43, using a shape index representation. As described by Koenderink and Doorn [84], the shape index progressively describes the local curvature from a spherical cup to a dome (respectively from -1 to 1). The shape indexes were evaluated with the scikit-image package of Python [85]. The craters are surrounded by crests described by small positive local curvatures. Finally, the intersection between several crests results in local maxima (dome like shape).

The shape index probability density functions of the three samples are presented in Fig. 3.44. As the bead size increases, the numbers of spherical cups (craters) and domes are increasing. Nevertheless, the spherical cups, which correspond to crater topography, are more probable than dome structures.

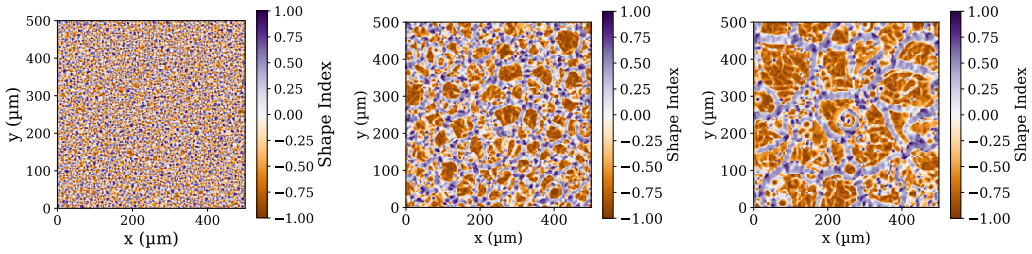

(a) (b) (c)

Fig. 3.43 *Representation of the shape index of the surface blasted with (a) small beads, (b) medium beads and (c) large beads. The shape index representation denotes the local curvature of the surface, from a spherical cup to a dome (respectively from -1 to 1).*

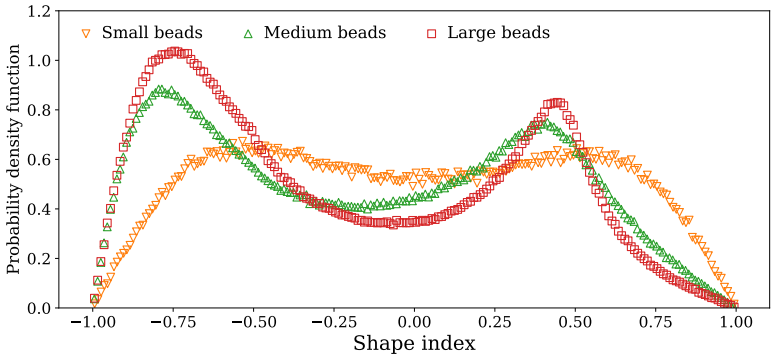

Fig. 3.44 *Shape index probability density function of the surface blasted with (a) small beads, (b) medium beads and (c) large beads. The shape index representation denotes the local curvature of the surface, from a spherical cup to a dome (respectively from -1 to 1).*

The shape of the craters and the hills were examined by image processing on experimental measurements similar to the one presented in Fig. 3.40. As the craters of the sample blasted with small beads are rather small, they are only defined by few experimental points and the examination of their shapes is hard to perform. Consequently, this analysis was only performed on samples blasted with medium and large beads.

First, the local minima (corresponding to the bottom of the craters) are located. Then the areas in the vicinity of the local minima are fitted with paraboloid expressions:

$$z = \left(\frac{x}{c_x^c}\right)^2 + \left(\frac{y}{c_y^c}\right)^2, \tag{3.47}$$

where c_x^c and c_y^c are constant that denote the level of curvature in the xz and yz planes respectively. Smaller c_x^c and c_y^c are, higher the local curvature of the surface is. The dimensions of the fitted areas are chosen with respect to the mean size of the craters.

Parameters c_x^c and c_y^c were evaluated through fitting of approximately 200 craters for each surface. The numerical values of c_x^c and c_y^c are reported in Table 3.9 for the two samples. For samples blasted with medium and large beads, the average values of c_x^c and c_y^c are very close. This denotes the fitting of a revolution paraboloid, which is consistent with the use of spherical beads during the blasting process.

A similar procedure was applied to examine the local shape of the hills. In this case, one identifies the local maxima and examine the points in the close vicinity of it ($20\mu m$ area around each local maxima). These areas are also fitted by a paraboloid function:

$$z = -\left(\left(\frac{x}{c_x^h}\right)^2 + \left(\frac{y}{c_y^h}\right)^2\right), \tag{3.48}$$

The numerical values of c_x^h and c_y^h are reported in Table 3.9 for the two samples.

Bead radius (μm)	c_x^c (μm)	$c_y^c(\mu m)$	c_x^h (μm)	c_y^h (μm)
60-125	94.1	91.2	31.7	37.8
200-300	126.5	131.9	40.2	37.3

Table 3.9: Numerical values of the fitted levels of curvature of the sample blasted with medium and large beads, which were described in Eqs. (3.47) and (3.48).

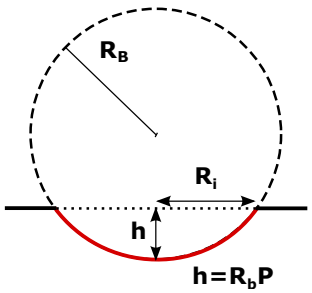

Fig. 3.45 *Schematic representation of the erosion model*

Consequently, it appears that the shape and the dimensions of the craters are directly related to the diameter of the spherical beads used during blasting. On the contrary, the shape of the hills is not described by revolution paraboloids and their dimensions are not impacted by the beads diameter.

Simulation of the blasted topography

In order to have a better understanding of the topographical properties of the blasted surfaces, we develop a simple erosion model to simulate the blasting process. It assumes an initial flat surface which is blasted with a perfect sphere, at random location. Each impact of spheres locally modifies the surface: the surface is not flat anymore, but it has the shape of a truncated sphere, as schematically presented in Fig. 3.45. This model is rather simple and does not take into account the real surface modification of a sphere indentation that has been described in the literature [86][87]. Indeed, as presented in Fig. 3.45, our model does not take into account the material removal as described in different erosion studies [88][89]. This is one of the major axis of amelioration of the model. The radius of the circular impact, R_i, is defined as:

$$R_i = \sqrt{R_b^2 - (R_b - h)^2} \tag{3.49}$$

$$= \sqrt{2R_b h - h^2}, \tag{3.50}$$

where R_b denotes the radius of the beads, and h the depth of penetration of the bead into the surface. In our model we approximate the penetration depth, $h = R_b P$, where P denotes the penetration coefficient of the sphere in the surface, which can vary from 0 to 1. The sphere of radius R_b, centered in the origin of the coordinate system (x_0, y_0, z_0), is defined as:

$$R_b^2 = (x - x_0)^2 + (y - y_0)^2 + (z - z_0)^2, \tag{3.51}$$

$$= x^2 + y^2 + z^2, \tag{3.52}$$

$$= r^2 + z^2, \tag{3.53}$$

	R_b	l	P	P_a	N
Small Beads	30	200	0.04	0.3	10000
Medium Beads	125	500	0.04	0.3	1500
Large Beads	250	500	0.04	0.3	280

Table 3.10: Numerical values of the parameters used in the calculation in order to model the blasting process for the three different surfaces.

where $r^2 = x^2 + y^2$ is introduced to simplify the notation. However, the cap sphere is centered in $(x_0, y_0, z_0 + R_b - h)$, which leads to:

$$R_b^2 = r^2 + (z - (R_b - h))^2. \tag{3.54}$$

The height variation along the cap sphere is then defined as:

$$z^2 - 2z(R_b - h) + r^2 + h^2 - 2Rh = 0, \tag{3.55}$$

which has two solutions z_1 and z_2:

$$z_1 = -(h - R_b + \sqrt{R_b^2 - r^2}), \tag{3.56}$$

$$z_2 = -(h - R_b - \sqrt{R_b^2 - r^2}). \tag{3.57}$$

However, as z_2 describes the spherical cup of the top of the bead, and therefore only z_1 is valid in our case.

The initial flat surface is then shaped by the sphere impact, producing cap sphere morphology. The parameters of the model are:

- the beads radius R_b,
- the size of the initial surface l,
- the coefficient of penetration between 0 and 1, P,
- an attenuation factor of the penetration between 0 and 1, P_a,
- the number of impacts N.

The attenuation factor of the penetration was defined after first attempts of modelisation. Indeed, the model gives rise to topography with impacts deeper than the real ones. To correct this, P_a was implemented: in this way, if the surface location of an impact (randomly picked) as already been deformed, the penetration of the bead in such area will be modulated by P_a.
The calculations were launched to model the three different surfaces, with the parameters summarized in Table 3.10. For each set of parameters, ten surface realizations were numerically simulated.

The corresponding numerical height topographies are presented in Fig. 3.46, their height probability density functions are presented in Fig. 3.47 and their rms, skewness and kurtosis parameters in Table 3.11. For the sake of visibility, the mean value of each height topographies presented in Fig. 3.46, was fixed to zero: this is why there are positive heights in the mappings.

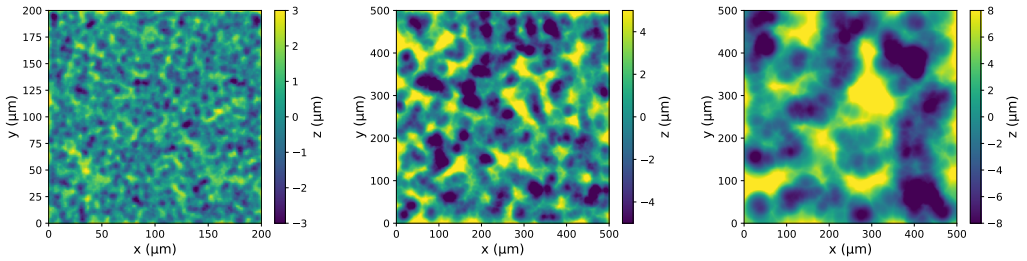

(a) (b) (c)

Fig. 3.46 *Numerical surface topographies realized with erosion model with the parameters described in Table 3.10. The three surface topographies model the samples blasted with (a) small beads, (b) medium beads and (c) large beads. The corresponding experimental measurements can be found in Fig. 3.40.*

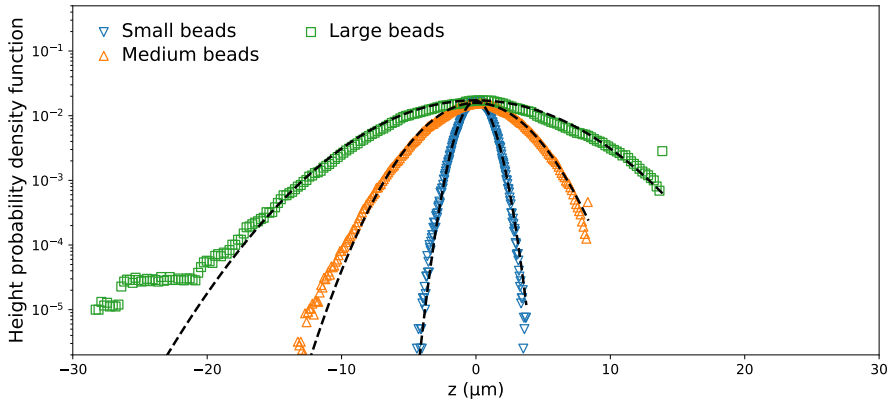

Fig. 3.47 *Heights probability density functions of numerical topographies of samples blasted with small, medium and large beads. The heights pdf are averaged over 10 numerical realizations. The corresponding experimental height pdf can be found in Fig. 3.41.*

Beads size	rms (μm)	skewness	kurtosis
Small	0.98	-0.12	3.03
Medium	2.88	-0.16	3.06
Large	5.36	-0.1	3.2

Table 3.11: Summary of the mean rms, skewness and kurtosis values of the numerical surfaces that model the samples blasted with small, medium and large beads, presented in Fig. 3.46. The corresponding experimental values can be found in Table 3.7.

Even if the model is rather simple, it shows rather good agreement with the experimental data. Indeed, the numerical values of rms and skewness are similar in both cases. In the case of the numerical model, the kurtosis parameter is undervalued: this could be related to the assumption that there is no material removal. This assumption also explains the lack of positive heights for medium and large beads numerical realizations in Fig. 3.47.

In summary, this simple model allows to reproduce the height pdf of the experimental measurements, knowing the beads size diameters and assuming a penetration coefficient of the bead in the metal (which remains constant for all realizations). There are two main axes of improvement for this model: the consideration of the material removal and the consideration of the non flat initial surface (see Sec. 3.4.1.1).

Study of the slope distribution

The slope distributions, evaluated by the "Plane" method (described in Sec. 3.2.3.3), of the three surfaces are presented in Fig. 3.48. The three distributions are rather similar. However, it appears that the slope distribution gets slightly narrower as the bead size increases: the FWHM of the distributions are summarized in Table 3.12. This result is consistent with the diameter of the beads.

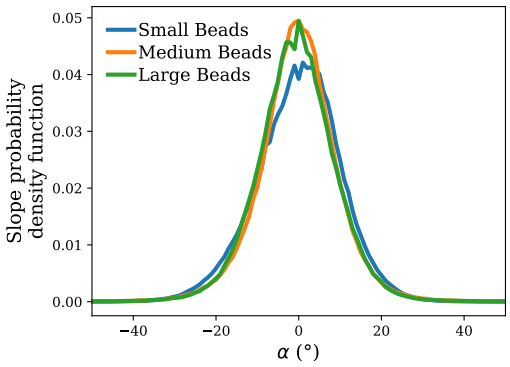

Fig. 3.48 *Slope distributions of the surfaces blasted with small, medium and large beads, evaluated from chromatic confocal profilometry measurements.*

Beads size	FWHM (°)
Small	21.4
Medium	17.8
Large	17.5

Table 3.12: Summary of the FWHM of slope distribution, for the samples treated with small, medium and large beads.

3.4.1.3 Variation of the covering ratio

This second series of samples is composed of four surfaces, which were treated with spherical beads of $125-250\ \mu m$ of diameter. The four samples were blasted during four different times, which leads to four different surfaces covering ratios, as described in Sec. 2.2.1.3.

Covering ratio (%)	rms (μm)	skewness	kurtosis
30	2.61 ± 0.01	-0.83 ± 0.02	5.59 ± 0.24
50	2.63 ± 0.09	-0.63 ± 0.09	5.47 ± 0.76
75	2.97 ± 0.06	-0.29 ± 0.07	4.64 ± 0.37
93	3.1 ± 0.06	-0.33 ± 0.05	4.45 ± 0.31

Table 3.13: Summary of the rms, skewness and kurtosis values of aluminum samples with surface covering ratio of 30%, 50%, 75% and 93%.

Study of the height probability density function

The four surfaces were examined by chromatic confocal profilometry and stylus profilometry. The experimental measurements realized by chromatic confocal profilometry are presented in Fig. 3.49, where it can be observed that the surface covering ratio is progressively increasing. The height probability density functions of the four surfaces are presented in Fig. 3.50, and their rms, skewness and kurtosis parameters are presented in Table 3.13.

In Fig. 3.50(a), one can observe that the height pdf of the 30% sample is not Gaussian like. This is also confirmed by the skewness and kurtosis parameters given in Table 3.13. The peak in the height pdf seems to be related to the morphology of the untreated surface, as stressed in Fig. 3.50(a), by the superposition of the height pdf of the untreated sample. The morphology of the sample 30% consists in the untreated sample morphology in which holes (negative heights) are added. In Fig. 3.50(b), the height pdf of the sample 50% is presented: the amplitude of the initial peak is progressively decreasing and the amount of negative heights is increased. Finally, in Figs. 3.50(c) and (d), the height pdf of the samples 75% and 93% tend to reach Gaussian distribution. Their skewness and kurtosis values (given in Table 3.13), progressively decrease to 0 and 3 respectively.

Study of the spatial correlation of height

The power spectrum density function and autocorrelation function are calculated from chromatic confocal profilometry measurements (as the one presented in Fig. 3.49). Figures 3.51(a) and (b) present the 2D ACF (in the close vicinity of the maximum of the function) of the samples with 30% and 93% of surface covering ratios respectively. For this delay range, the two ACF seem rather similar, and only a slight anisotropy can be detected.

On the other hand, when the ACF function is examined in its full range, as presented in Figs. 3.51(c) and (d), it is easier to differentiate the two samples. Indeed, the ACF of the sample with 30% of surface covering ratio (Fig. 3.51(c)) is anisotropic: one can distinguish a directional pattern along τ_y, which is the direction of the grooves present on the surface before the blasting. However, the ACF of the sample with 93% of surface covering ratio (Fig. 3.51(d)) does not have any preferential direction, and seems isotropic on short and long delay range, which can be explained by a higher surface covering ratio.

Consequently, the ACF must be carefully examined: one can not only consider the close vicinity of the maximum of the function, but the function in its whole delay range

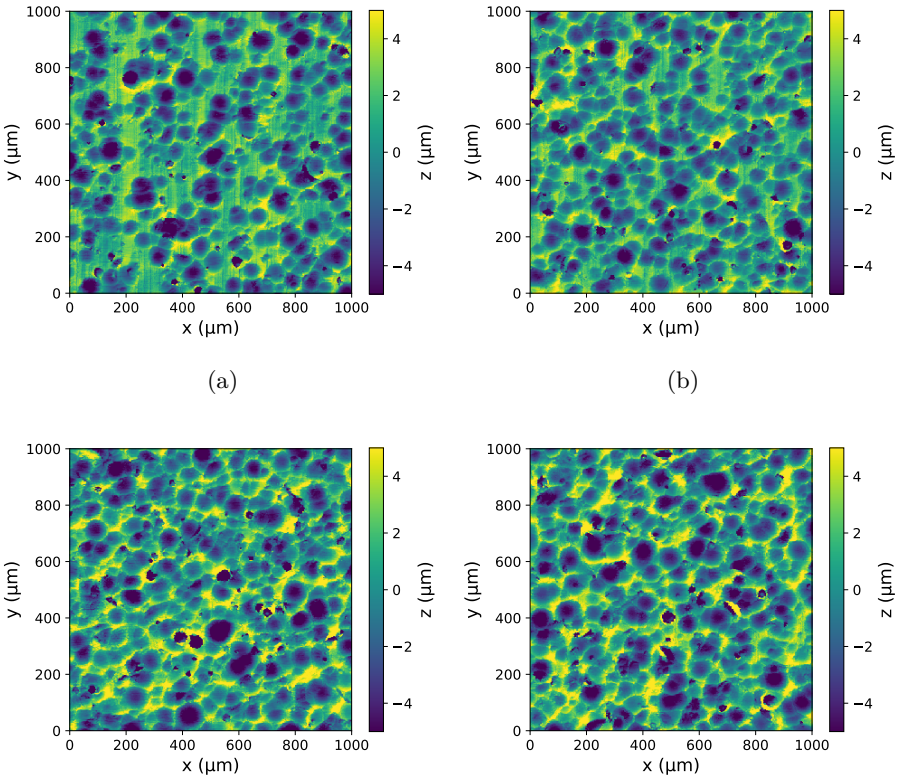

Fig. 3.49 *Experimental measurements ($1 \times 1mm^2$) realized by chromatic confocal profilometry of the aluminum blasted samples, with surface covering ratio of:(a) 30% , (b)50%, (c)75% and (d)93%. Each measurement is $2 \times 2mm^2$ with $\Delta = 2\mu m$.*

must be studied. The correlation lengths of the four surfaces are $28\mu m$, $29\mu m$, $31\mu m$ and $31\mu m$ respectively for the samples with surface covering ratios of 30%, 50%, 75% and 93%.

Cuts along f_x of the 2D PSD functions of the four samples are presented in Fig. 3.52. The maximum PSD level is obtained for frequencies close to $f_x = 0.0067\mu m^{-1}$, which correspond to lengths of 150 μm, and can be correlated to the diameter of the beads used for blasting. As presented in Fig. 3.52, the PSD level is increasing while the surface covering ratio increases. It indicates that the number of impacts increases in the surface. In this way, the PSD function allows to follow the blasting fabrication process.

Study of the slope distribution

The slope distributions of the four surfaces are presented in Fig. 3.53. The four distributions are rather similar, their maximal slope and FWHM are summarized in Table 3.14. The slope distributions of the samples 75% and 97% are slightly larger than the two other ones. This is consistent with the increase of the surface covering ratio, the slope distribution of blasted surface being larger than the slope distribution of the untreated surface. However, with any of the two methods of slope calculation, we were not able to see the

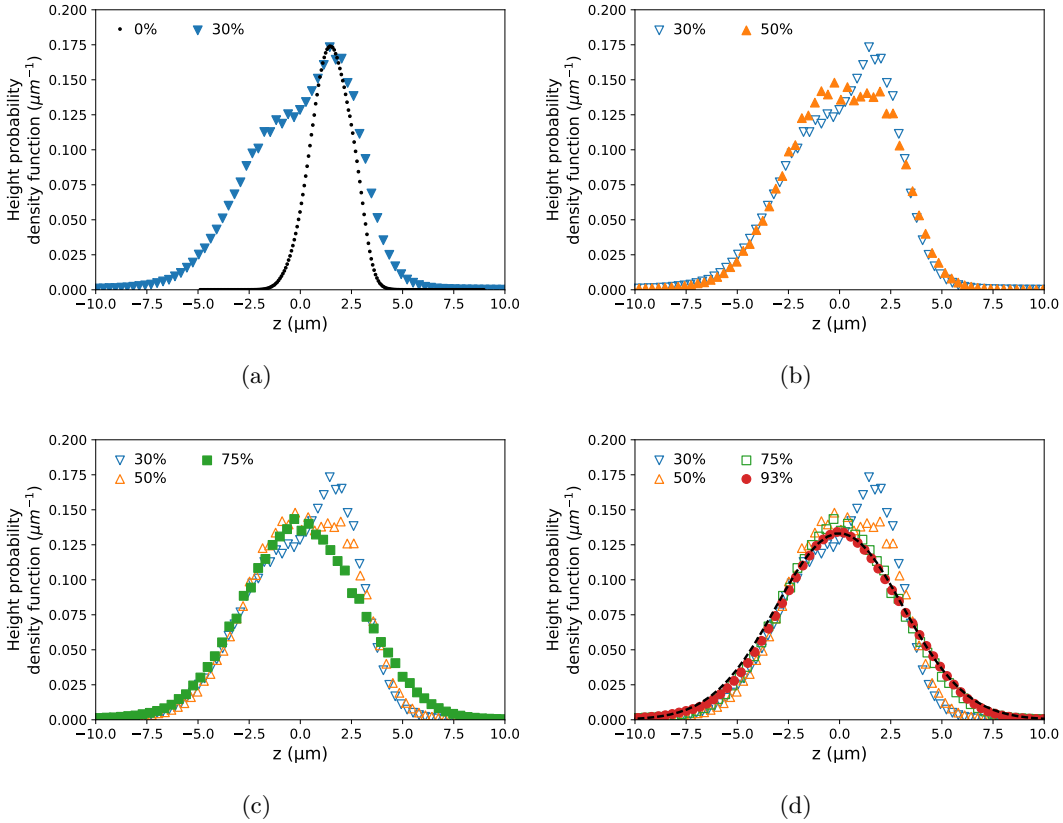

Fig. 3.50 *Experimental height pdf of samples with different surface covering ratio. (a) The untreated sample (0% of surface covering ratio) is compared to the sample with 30% of covering ratio. The mean and the amplitude of the height pdf of the 0% sample has been adapted in order to be compared to the 30% sample. For the sake of visibility, the height pdf of the samples with 50%, 75% and 93% have been added one by one in (b), (c) and (d). In (d) the black dashed line is a Gaussian height pdf fitted from the mean and standard deviation of the height pdf of the sample 93%.*

anisotropy of the slope distribution.

3.4.1.4 Variation of the particle shape

The third series of blasted aluminum samples is composed of four surfaces, which were treated with particles of similar diameter ($30 - 60\ \mu m$), but of different shapes (see

Covering ratio (%)	FWHM (°)
30	17.2
50	18.6
75	19.5
93	19.6

Table 3.14: Summary of the FWHM of the slope distribution, for the samples with surface covering ratios of 30%, 50%, 75% and 93%.

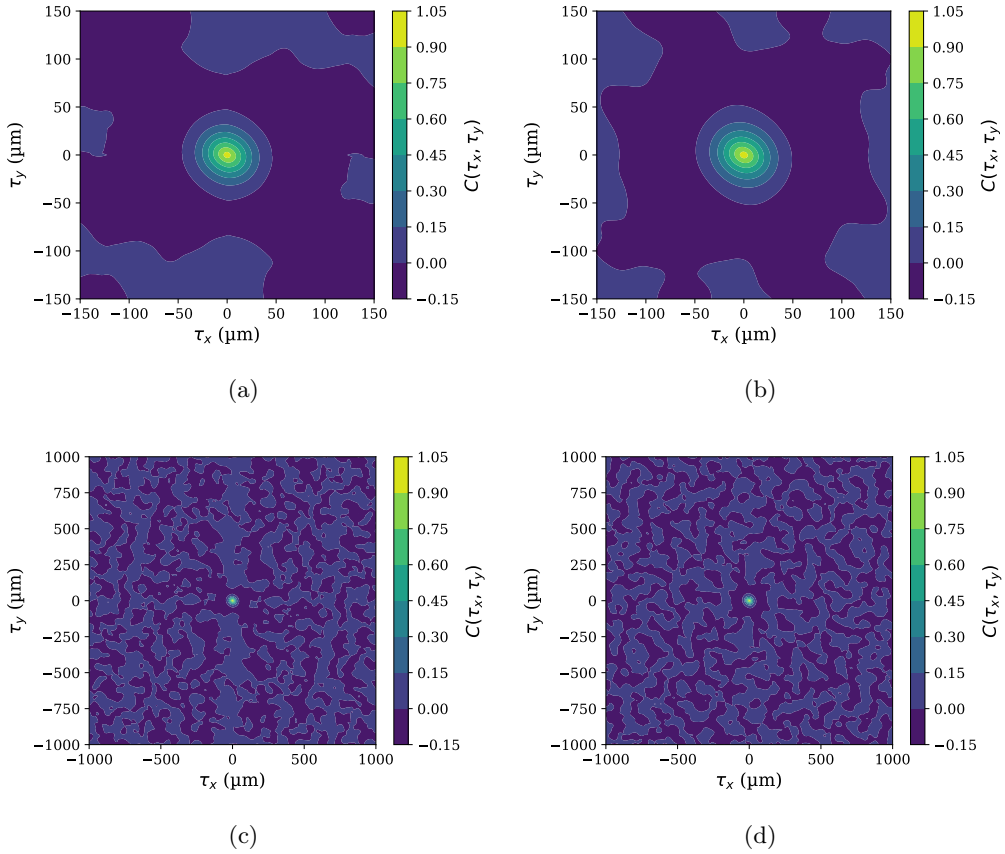

Fig. 3.51 *2D ACF plotted from $-150\mu m$ to $150\mu m$ along τ_x and τ_y, calculated from experimental data of: (a) the sample 30%, and (b) the sample of 93%. 2D ACF plotted from $-1000\mu m$ to $1000\mu m$ along τ_x and τ_y, calculated from experimental data of: (c) the sample 30%, and (d) the sample of 93%.*

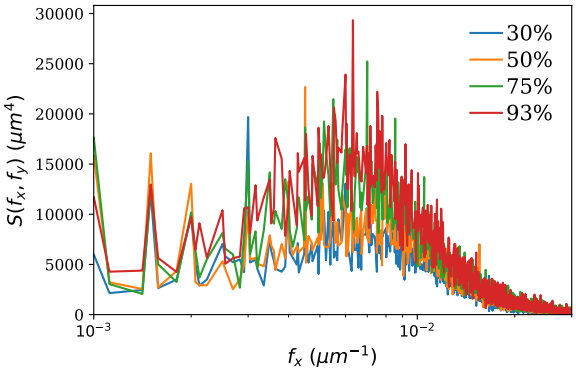

Fig. 3.52 *Cuts along f_x of the 2D PSD functions of the four samples, centered on the maximal PSD value, obtained for $f_x = 0.0067\mu m^{-1}$.*

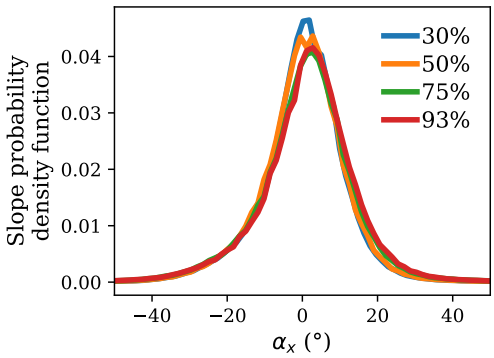

Fig. 3.53 *Slope distributions of the samples with different surface covering ratios, evaluated from chromatic confocal profilometry measurements.*

Particle shape	rms (μm)	skewness	kurtosis
Beads	1.40 ± 0.01	-0.1 ± 0.01	3.01 ± 0.05
Rough Beads	1.09 ± 0.06	0.09 ± 0.01	3.00 ± 0.03
Beads & Grains	1.04 ± 0.08	-0.14 ± 0.01	3.72 ± 0.05
Grains	1.20 ± 0.03	-0.34 ± 0.02	4.07 ± 0.12

Table 3.15: Summary of the rms, skewness and kurtosis values of aluminum samples blasted with beads, rough beads, a mix of beads and grains, and grains.

Sec. 2.2.1.4). We examined the morphology of samples treated with beads, rough beads, a mix of beads and grains and grains. Due to the small dimensions of the particle and their different shape, one must carefully examine the morphology of these samples at different scales. Consequently, the samples were examined with all three experimental setups.

Study of the height probability density

Confocal chromatic profilometry measurements of the four samples are presented in Fig. 3.54, their height pdf are presented in Fig. 3.55 and their rms, skewness and kurtosis values are summarized in Table 3.15.

The topography of these four surfaces are rather thin compared to the one presented in the last two sections (see Secs. 3.4.1.2 and 3.4.1.3). Indeed, treatment with particles of small diameters results in less deep impacts on the surface, and consequently the rms values of the surfaces are lower. Moreover, the height pdf of the surfaces are closer to Gaussian height pdf, as expressed by the skewness and kurtosis parameters summarized in Table 3.15. However, from the experimental measurements presented in Fig. 3.54, one can observe that the samples have anisotropic morphologies: linear patterns can be observed along the y axis. We assume that this anisotropic feature is related to the grooves present on the surface before blasting (see Sec. 3.4.1.1). The blasting process did not suffice to completely erase the anisotropy of the untreated surface.

Study of the spatial correlation of height

The experimental 2D PSD functions of the four samples were evaluated from confocal

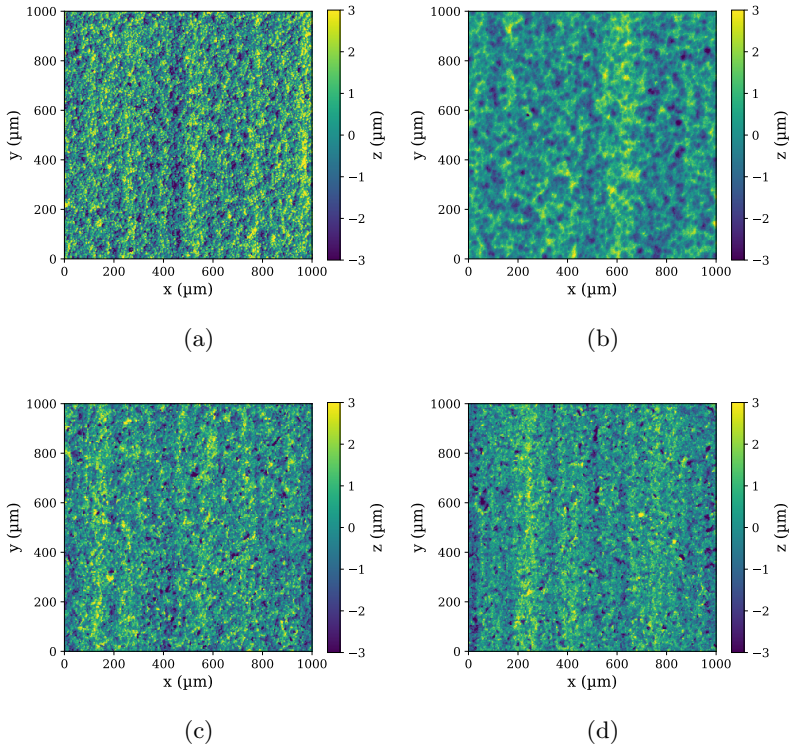

Fig. 3.54 *Experimental measurements* (1×1 mm^2) *realized by chromatic confocal profilometry of the aluminum samples blasted with:(a) beads , (b) rough beads, (c) a mix of beads and grains and (d) grains. Each measurement is* 2×2 mm^2 *with* $\Delta = 1.5$ μm.

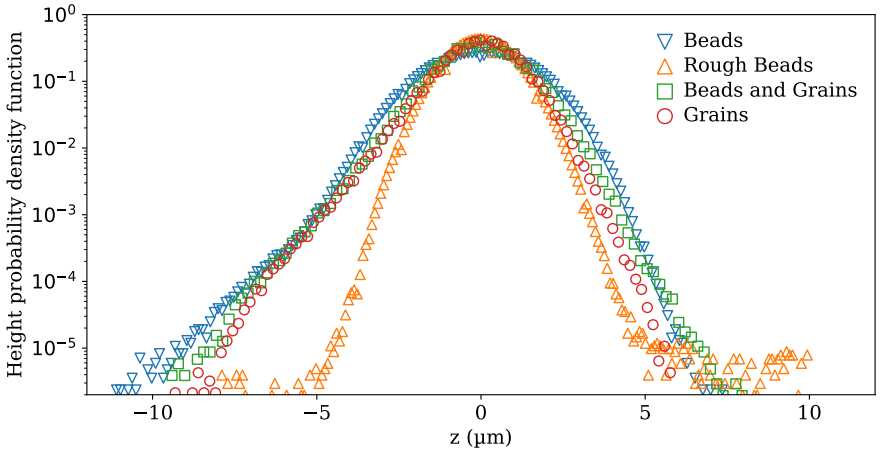

Fig. 3.55 *Experimental heights probability density functions of aluminum samples blasted with beads, rough beads, a mix of beads and grains, and grains.*

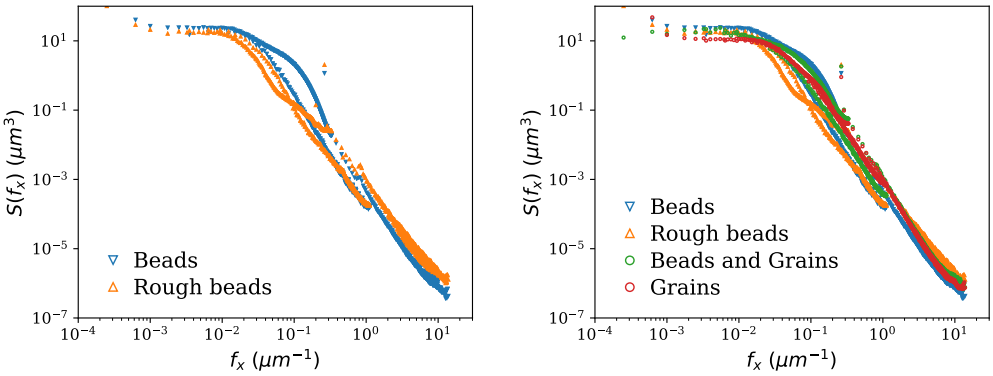

(a) (b)

Fig. 3.56 *1D PSD master curves extracted from experimental measurements realized with the three different setups. For the sake of visibility,(a) presents samples blasted with beads and rough beads and (b) presents samples blasted with mix of beads and grains, and grains.*

chromatic profilometry measurements, and they are as expected anisotropic. However, the optical properties of the samples are not strongly anisotropic (see Sec. 4.4.1.4) and the light scattering models used, do not take into account anisotropic surfaces: consequently, the morphological properties of these surfaces will be treated as if they were isotropic.

The 1D master PSD curves are evaluated from experimental measurements of the 3 different setups. They are presented in Figs. 3.56(a) and (b). The 1D PSD master curves of the samples treated with beads and rough beads are presented in Fig. 3.56(a). Due to the actual anisotropy of the surfaces, the combination of the experimental data, obtained from the different setups, is less consistent. Consequently, one can observe discrepancies in the PSD master curves. Apart from this, the two 1D PSD master curves are consistent with each other. In the low frequency range, the PSD of the sample blasted with beads is higher. But in the high frequency range, this is the PSD of the sample blasted with rough beads which is higher. These to different PSD levels are consistent with the actual morphologies of the particles. Indeed, as the rough beads are covered by an additional roughness, the blasted surface should be described by higher frequency components.

The 1D PSD master curves of the samples treated with a mix of beads and grains and with grains are presented in Fig. 3.56(b). In this case, in the low frequency range, the PSD of the sample blasted with a mix of beads and grains is higher ; and in the high frequency range, both PSD levels are similar. This can also be explained by the actual shape of the particles: for the two surfaces, the grains are shaping the high frequency range of the surface topography.

For the four samples (Fig. 3.56(a) and Fig. 3.56(b)), the PSD level falls for $f_x = 0.025\ \mu m^{-1}$. This is consistent with the typical diameter of the four particles of $30-60\ \mu m$.

Finally, Fig. 3.57 presents the 1D PSD function obtained from AFM measurements of the sample treated with rough beads, and the sample blasted with large beads of

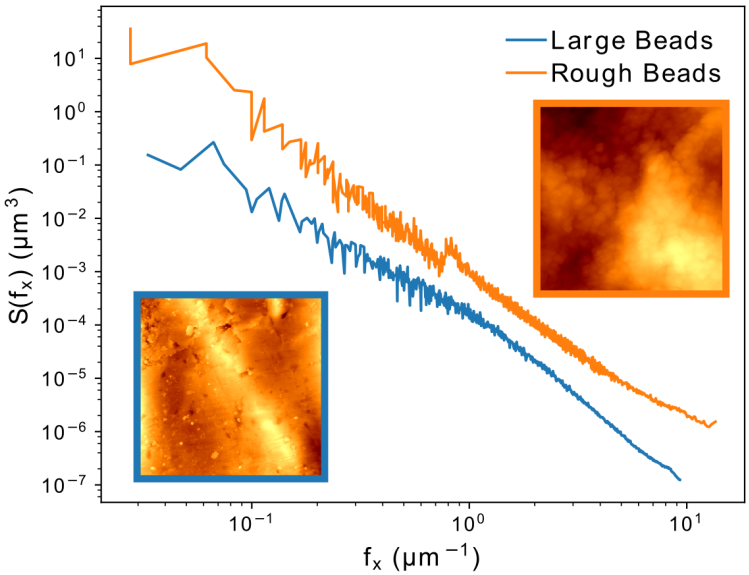

Fig. 3.57 *1D PSD of samples blasted with large spherical beads (400−600 μm diameter) and rough beads (30−60 μm diameter), extracted from AFM measurements. Each inset is a AFM measurement of 30×30 μm^2 size.*

Sample	FWHM (°)
Beads	41.4
Rough Beads	13.2
Beads & Grains	25.8
Grains	21.3

Table 3.16: Summary of the FWHM of slope the distribution, for the samples blasted with beads, rough beads, a mix of beads and grains, and grains.

$400 - 600$ μm of diameter (see Sec. 3.4.1.2). In this frequency domain (from 0.1 μm^{-1} to 10 μm^{-1}), the PSD level of the sample blasted with rough beads in nearly 10 times higher than the other one. This PSD level difference denotes the existence of an additional roughness degree for the sample treated with rough beads.

Study of the slope distribution

The four slope distributions of the samples are presented in Fig. 3.58. As presented in Table 3.16, the four samples are characterized by different slopes. Again, the samples blasted with a mix of beads and grains, and grains present similarities.

3.4.2 Frosted glass surfaces

The series of frosted glass samples is composed of five surfaces, which were manufactured by different industrial processes (see Sec. 2.2.2). The topography of each sample was examined by confocal chromatic profilometry and contact profilometry.

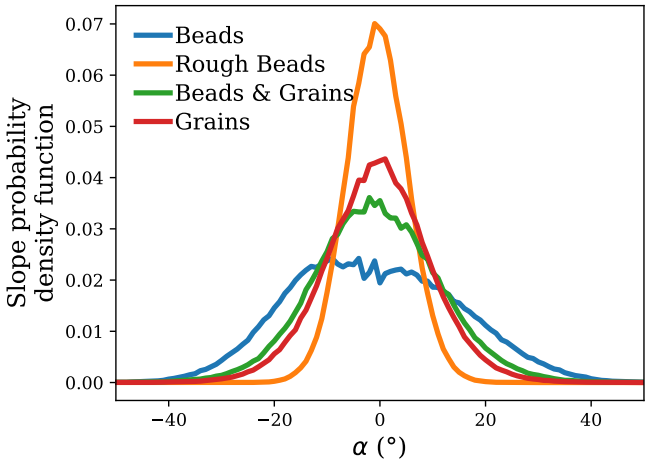

Fig. 3.58 *Slope distributions of the surfaces blasted with beads, rough beads, a mix of beads and grains, and grains, evaluated from chromatic confocal profilometry measurements.*

Sample	rms (μm)	skewness	kurtosis
G1	0.42 ± 0.01	1.82 ± 0.11	7.92 ± 0.52
G2	0.90 ± 0.03	-0.03 ± 0.03	3.10 ± 0.08
G3	0.65 ± 0.02	-0.26 ± 0.12	4.22 ± 0.41
G4	2.91 ± 0.11	-0.40 ± 0.08	3.28 ± 0.13
G5	2.4 ± 0.01	-0.08 ± 0.01	2.62 ± 0.05

Table 3.17: Summary of the rms, skewness and kurtosis values of the five frosted glass samples.

Study of the height probability density

Measurements realized by chromatic confocal profilometry of the five frosted glass samples are presented in Fig. 3.59. Their height probability density function and their related rms, skewness and kurtosis parameters are presented in Fig. 3.60 and Table 3.17 respectively. According to the parameters presented in Table 3.17, the height pdf of the samples G2 and G5 could be well approximated by a Gaussian height pdf. However, the samples G3 and G4 have respectively kurtosis and skewness values rather different from a Gaussian surface. The kurtosis value of the sample G5 is very far from a Gaussian surface.

As presented in Sec. 2.2.2, the five samples are ordered by their level of haze (with increasing values from G1 to G5). However, one cannot simply relate the haze properties to the rms roughness degrees presented in Table 3.17.

Study of the spatial correlation of height

The radial average of the experimental autocorrelation functions evaluated from confocal chromatic profilometry measurements are presented in Fig. 3.61. The Fig. 3.61 stresses that the morphological properties of rough surfaces are described by a high variety of ACF, and not only by exponential or Gaussian forms. Indeed, the five ACF do not only differ by their correlation lengths, but also by the shape of the function. To fully describe

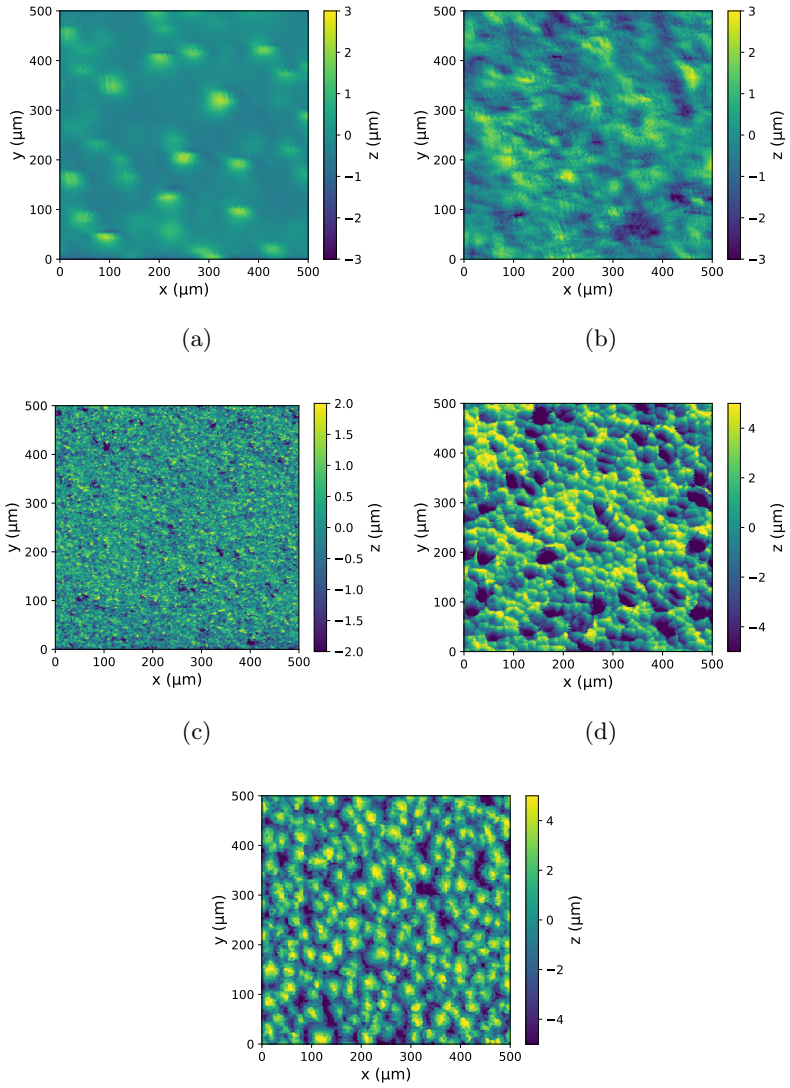

Fig. 3.59 *Experimental measurements* (1×1 mm^2) *realized by chromatic confocal profilometry of the frosted glass samples:(a) G1, (b) G2, (c) G3, (d) G4 and (e) G5. The measurements parameters are recalled in Table 3.1.*

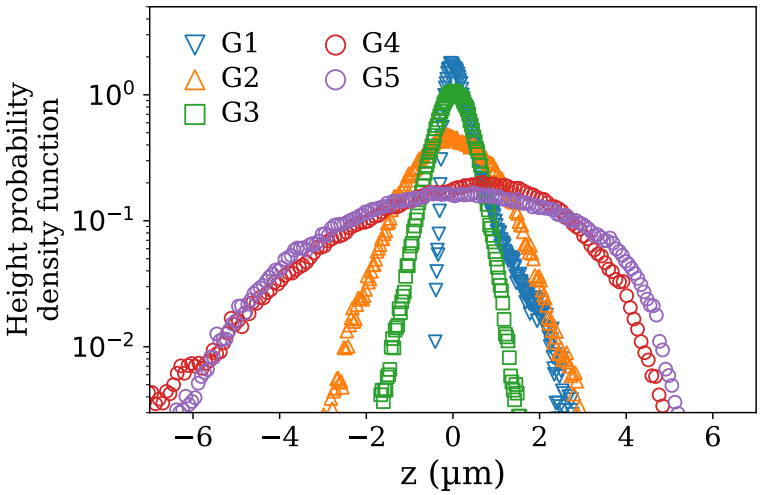

Fig. 3.60 *Experimental heights probability density functions of frosted glass samples.*

the spatial correlation of the height of these surfaces, one must fit these ACF by empirical functions. However, for the sake of time, and as in our case, these expressions are useless to model the light scattering properties of transparent surfaces, these empirical fits were not realized.

Study of the slope distribution

The slope distributions of the five frosted glass surfaces are presented in Fig. 3.62. The five distributions are quite different, their FWHM are summarized in Table 3.18.

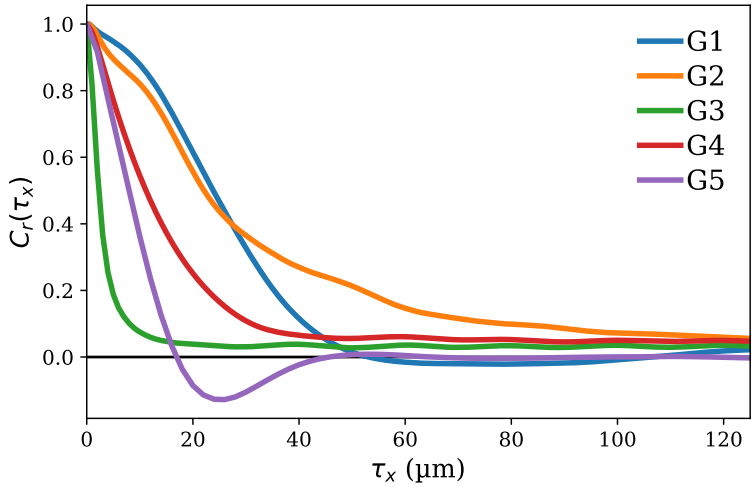

Fig. 3.61 *2D radial ACF of the five frosted glass samples. The ACF are averaged over several measurements.*

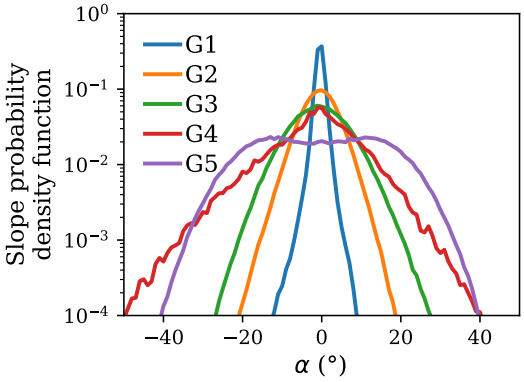

Fig. 3.62 *2D Slope distributions of the five frosted glass samples, evaluated from chromatic confocal profilometry measurements.*

Sample	FWHM (°)
G1	2.4
G2	9.2
G3	15.6
G4	13.1
G5	44.6

Table 3.18: Summary of the FWHM of the slope distribution, of the five frosted glass samples.

3.4.3 Conclusion

The topographies of samples manufactured from different fabrication processes were measured and analyzed in the Sec. 3.4. For each series of samples, the topography of the surfaces were examined with different setups. In each case, numerical parameters describing the surface topography were evaluated (some of these numerical parameters are recalled in the Table 3.19). The difference between the two parameters l_c and a is worth being stressed. The parameter l_c is the correlation length of the surface: the value of lag length at which the autocorrelation function equal 1/e. On the other hand, the parameter a, is related to the analytic form of the autocorrelation functions deduced from the experimental results. The different analytic functions obtained to fit the experimental ACF are recalled in Table 3.20. These numerical results and functions allow us to quantify the topography of the samples and to compare them with each other. It appears that these surfaces present highly different morphological properties.

The topography of the blasted metallic samples was carefully examined. The study of the power spectrum density function can be related to the size of the particles used during the blasting process. In the same way, some parts of the autocorrelation function (anticorrelation component) are related to the mean size of the craters that shape the surface. These two functions allow to directly link the fabrication process to the morphology it induced.

Sample	rms (μm)	Gaussian-like	l_c (μm)	ACF form	a (μm)	FWHM (°)
Untreated aluminum	0.63	Yes	3.1/-	-	-	20.1/38.2
Small beads	1.18	Yes	10.4	P5	9.7	21.4
Medium beads	2.55	No	25.2	CP	30.6	17.8
Large beads	5.26	No	50.0	CP	60.9	17.5
30%	2.61	No	22.6	CP	28.2	17.2
50%	2.63	No	22.9	CP	29.4	18.6
75%	2.97	No	23.6	CP	31.0	19.5
93%	3.10	No	23.8	CP	31.4	19.6
Beads	1.40	Yes	6.2	P7	11	41.4
Rough beads	1.09	Yes	11.6	S	8.8	13.2
Beads & Grains	1.04	No	10.1	S	8.1	25.8
Grains	1.2	No	7.8	S	5.9	21.3
G1	0.42	No	28.3	-	-	2.4
G2	0.90	Yes	31.4	-	-	9.2
G3	0.65	No	3.1	-	-	15.6
G4	2.91	No	15.3	-	-	13.1
G5	2.40	Yes	9.7	-	-	44.6

Table 3.19: Summary of the numerical parameters extracted from experimental measurements: the rms, the correlation length l_c, the type of autocorrelation function and its length parameter a (when evaluated), and the FWHM of the slope distribution. The Gaussian like column expresses if we consider that the height pdf could be approximated by a Gaussian height pdf: the criteria depend of the skewness value (which should be included between -0.3 and 0.3) and the kurtosis value (which should be included between 2.5 and 3.5). These numerical criteria are arbitrary chosen.

	Analytic ACF
P5	$\left(1+\frac{x^2}{a^2}\right)^{-\frac{5}{4}}$
P7	$\left(1+\frac{x^2}{a^2}\right)^{-\frac{7}{4}}$
CP	$\cos\left(\frac{x}{a}\right)\left(1+\frac{x^2}{a^2}\right)^{-\frac{5}{4}}$
S	$\exp\left(-\frac{\lvert x\rvert}{a}\left(1-\exp\left(\frac{-\lvert x\rvert}{a}\right)\right)\right)$

Table 3.20: Analytic functions used to fit the experimental autocorrelations functions. The parameter a corresponds to a characteristic length of the sample, which is different from the correlation length l_c.

3.5 Conclusion

This chapter described the different steps involved in the characterization of the morphology of rough surfaces. First, the experimental setups used during this work were described. The confocal chromatic profilometry, the stylus profilometry, and the atomic force microscopy are techniques which allow us to characterize the surface topography at different scales (Sec. 3.1). With these three setups, we are able to catch all the morphology that could be involved in the light scattering properties of the surfaces.

Then the parameters and functions used to quantify a surface morphology were described in Sec. 3.2. These latter were chosen from the two communities which deal with the light scattering properties of surfaces. The first two, used by the physical optics community, but also in other domains of the physics, are related to the height probability density function (rms, skewness and kurtosis parameters) and to the spatial correlation of the heights (power spectrum density function and autocorrelation function). The third one, mainly used by the geometrical optics community is related to the evaluation of the slope distribution. We showed that the evaluation of these parameters and functions are not straightforward, and that they rely on carefully chosen acquisition features and measurements statistics A numerical study, based on numerically generated surfaces, was realized in order to build an efficient experimental protocol.

Finally, the morphological properties of the studied surfaces were presented in Secs. 3.3 and 3.4, for the model surfaces and complex surfaces respectively.
In the case of the 1D model surfaces, we showed that we have been able to manufacture line gratings described by different cross sections, thanks to thermal relaxation process.
For the 2D model surfaces, we presented surfaces with similar height probability density functions, but with completely different spatial organizations: one periodic and the other one being random.
We examined the morphology of two kinds of 2D complex surfaces: metallic aluminum blasted surfaces and frosted glass samples. The study of the blasted metallic surfaces allows us to make links between the fabrication process parameters and the morphology of the samples. Thereby, the evaluation of the statistical parameters allows us to identify the typical size of the particles used during the blasting process, but also to differentiate their shape. A statistical study of the topography of the samples blasted with beads of different sizes also allow us to follow the creation of craters and hills on the surface topography.
The morphology of the frosted glass samples was analyzed by the same methods and proved to be an excellent illustration on how different fabrication process can lead to a very large range of morphological properties.
In view of these different morphological properties and appearances, we expect that these surfaces give rise to a large range of optical properties. Thereby, the following chapter will be dedicated to the evaluation of the optical properties of the surfaces.

Chapter 4

Optical characterization

"- So what do we do?
- Nothing. Strangely enough, it all turns out well.
- How?
-I don't know. It's a mystery."
Hugh Fennyman and Philip Henslowe, Shakespeare in Love (1998)

Contents

In everyday life, we face surfaces with different visual aspects, which can be opaque, translucent, colored, transparent, glossy or matte. Glossy and matte correspond to two extreme cases of the angular spread of scattered light. Glossy, or specular reflection consists of a very narrow angular spread of the reflected light around the specular direction (which should be a Dirac delta function in the case of perfectly specular reflection). On the other hand, the perfect matte diffuser, called a Lambertian, spreads the scattered light with equal radiance in all the directions of space. In reality, these two extreme cases are rather rare, and the majority of the light scattering properties of the surfaces

consists in intermediate angular spreads. Actually, the spread of scattered light is usually described by lobe components: the specular and the diffuse lobes [23]. According to the surface properties, the two lobes differ in width and magnitude.
The analysis of these specular and diffuse lobes is critical in order to understand the optical properties of surfaces. This is why angle resolved experimental studies have to be carried out.

Due to the complexity of the experimental equipment required, these studies are rather recent: the first being from the 1970s. The first purpose of these early study was to characterize the light scattering properties of model surfaces along the plane of incidence, as realized by Colby et al. in [31] or by Chandely et al. in 1976 [30].

In the 1980s, the angular resolution capabilities of the experimental setups was improved up to tenths of degrees, and more precise characterization were performed, as realized by O'Donnell and Mendez in 1987 [32], or by Kim et al. in 1990 [33]. However, these experimental measurements were still related to model surfaces, with limited range of properties.

In the 1990s, further studies were performed [90][91] to meet the needs of virtual representations of items of everyday life. In this purpose, Dana et al. published a first database of experimental measurements of everyday life surfaces [92]. Then in 2003, the MERL (Mitsubishi Electric Research Laboratories) database, composed of experimental measurements of 100 everyday life surface, was published [34], and is still widely used nowadays for virtual rendering. However, the MERL database does not present the actual morphological properties of the characterized surfaces, hence, those optical measurements cannot be used for predicting light scattering models, but only to fit analytic model of light scattering (as it is currently in the virtual rendering industry).

However, recent studies presented by Ged et al.[93][94], show that the relation between the appearance of an object and its measured optical properties may be hard to assess. Indeed, if we want to understand the appearance of an object, one must at least measure the optical properties with an angular resolution which is comparable than that of the human eye, which is actually 0.03° [95]. Unfortunately, experimental setups with such angular resolution are of course not widely spread. Moreover, to be fully understood, the appearance notion must also be related to the observer's sensations and perceptions [94].

This work does not aim to describe the complex notion of appearance, which is related to the psychophysics domain. The purpose of this study is to describe the physical light scattering properties of surfaces, and to bring pieces of knowledge about their physical origins. The links between optical properties and the appearance of surfaces that are mentioned in this work are only related to common sense and quick visual observations.

This chapter aims to present the optical characterizations realized during this study. First, the parameters and the functions used to describe and quantify the optical properties of a surface, in reflection and in transmission, will be described. Secondly, the experimental setup, a goniospectrophotometer, which was used to realize the major part of the optical characterizations, will be presented. Finally, the experimental optical properties of the studied surfaces will be presented: starting with the model surfaces, and then

the complex rough surfaces. The analysis of the experimental optical data will be done keeping in mind the morphological properties of the samples: so we can see if simple and logical links can be made between these two kinds of properties.

4.1 Description of the parameters and functions

The light scattering can be described by different physical entities that can be either *integral values* or *angle resolved functions*. The integral values are rather quick and simple to evaluate, and do not require expensive tools. They are then widely used in the industry as they allow to realize quick and qualitative comparisons between samples and can be exploited to control specimens on a production line. On the other hand, the angle resolved functions require expensive and less compact equipment to be evaluated. However, the angle resolved functions are required if one must precisely describe the light scattering properties of surfaces.

4.1.1 Integral parameters

Two kinds of integral values will be described in the next section. The *reflectance* and the *transmittance* are respectively two values to assess the total amount of light (all around the sample) that is reflected or transmitted through the sample. The two other parameters, which are referred to as *gloss* and *haze*, assess the amount of light that has been reflected or transmitted in a particular angular region around the sample. The gloss parameter describes the light that is reflected along the specular direction, and the haze refers to the light that is scattered away from the specular direction.

4.1.1.1 Evaluation of the optical properties in reflection

Two integral parameters related to the reflection properties of a surface are described here: *the gloss* and *the reflectance*. The reflectance describes the portion of the incident light that is reflected by a surface, when the gloss describes the portion that is reflected in the vicinity of the specular direction.

The measurement of the gloss of a surface is defined by the 2813:2014 ISO standard [96], where it is defined as the property of a surface to reflect light in the specular direction. The glossmeter is the device used to evaluate the gloss of a sample. The gloss index is defined as 100 times the ratio of the flux reflected by a specimen in the specular direction on the flux reflected by the reference sample (a piece of black glass [96]) in the specular direction. This ratio is expressed in an arbitrary unit called Gloss Units (G.U.). The reference sample is set to be 100 G.U.. Big G.U. values indicate glossy surfaces while matte samples have low G.U. values. One must mention that 100 G.U. is not the upper limit of the gloss index: mirror-like surfaces have gloss index up to 1000 G.U..

Depending on the optical properties of the sample, the measurements can be realized at different angles of incidence (20°, 60° and 85°), as presented in Fig. 4.1. Indeed, as described by the Fresnel equation [97], for a flat surface, the amount of reflected light increases with the angle of incidence. Consequently, the gloss of matte surfaces should be

	In plane of measurement (°)	Perpendicular to plane of measurement (°)
20° receptor	1.8	3.6
60° receptor	4.4	11.7

Table 4.1: The angular apertures of the glossmeter receptors at 20° and 60° are described in [96].

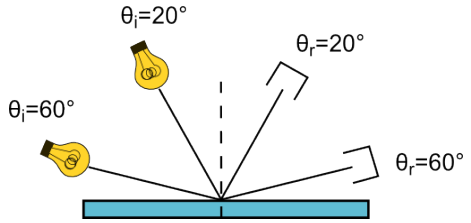

Fig. 4.1 *Schema of operating principle of the glossmeter.*

evaluated at high incidence angles (in order to maximize the reflected intensity) and on the contrary, glossy samples should be examined at a low incidence.

The angular apertures of the different sensors of the glossmeter are at least of some degrees around the specular direction and are different for all incident angles. For 20° and 60° (the two angles available with our glossmeter), the angular apertures are mentioned in Table 4.1.

The measurements are quick and simple, and can easily be adapted on industrial lines. However, it has been shown by Leloup et al. that glossmeters suffer from reproducibility and repeatability issues [98]. Moreover, the authors show that, as the reflected light in integrated over several degrees around the specular direction, it can be rather complex to distinguish several surfaces from each other. In this study, the glossmeter used is a "Pico Glossemaster Model 500" commercialized by Enrichsen.

The second integral parameter that will be studied here is the reflectance function. The reflectance, R, is defined as:

$$R = \frac{\Phi_R}{\Phi_I}, \tag{4.1}$$

where Φ_R denotes the flux reflected by a surface and Φ_I is the flux incident on the surface. The reflectance is therefore ranging from 0 to 1 (or from 0 to 100 if expressed in percent). The reflectance is usually evaluated as a function of the wavelength of the incident light. Its evaluation can be made with spectrophotometer devices, where the whole reflected light is collected with an integrating sphere.

4.1.1.2 Evaluation of the optical properties in transmission

Two integral parameters related to the transmission properties of a surface are examined here: *the transmittance* and *the haze*. The transmittance describes the portion of the incident light that is transmitted through a surface, and the haze represents the portion of light that is transmitted out of the specular direction.

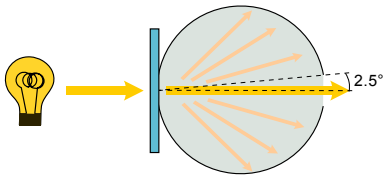

Fig. 4.2 *Schematic representation of the evaluation of the diffused transmittance, which corresponds to the light that has been deviated from the specular direction more than 2.5°. Experimentally, a 2.5° window is removed from the integrating sphere in order to avoid the collection of the undeviated transmitted light.*

Similarly to the reflectance, the transmittance, T_t, is defined as:

$$T_t = \frac{\Phi_T}{\Phi_I}, \tag{4.2}$$

where Φ_T denotes the flux transmitted through a surface. The transmittance is also evaluated as a function of wavelength and is evaluated with spectrophotometer devices.

The haze of a surface is defined by the D1003-13 ASTM standard [99], and it expresses *"the scattering of light by a specimen responsible for the reduction in contrast of objects viewed through it."* It is defined as *"the percent of transmitted light that is scattered so that its direction deviates by more than a specified angle from the direction of the incident beam."*[99], the specified angle being 0.044 rad (2.5°). The haze is then defined as:

$$\text{haze} = 100 \times \frac{T_d}{T_t}, \tag{4.3}$$

where T_d denotes the diffuse transmittance, which is the amount of light that is transmitted and deviated from the specular direction more than 2.5°, as presented in Fig. 4.2. Consequently, bigger the haze of a sample is, bigger will be the reduction in contrast of the objects viewed through it.

The device used to evaluate the haze is called a hazemeter and is quick and easy to use. The measurements are realized using a broadband light source, at normal incidence. During this study, the haze of the surfaces were evaluated with the hazemeter "Haze-gard plus" commercialized by BYK Gardner.

4.1.2 Angular resolved functions

The integral parameters described in the Sec. 4.1.1 are useful in order to realize qualitative comparisons between several samples. However, as they are not resolved in angle, they are not sufficient to understand the visual aspect of surfaces. The Bidirectional Reflectance Distribution Function (BRDF) and the Bidirectional Transmittance Distribution Function (BTDF) are angular resolved functions which are related to the visual appearance of surfaces. The BRDF was first defined by Nicodemus in 1965, and it can be expressed as the ratio of the differential radiance reflected by a surface, and the differential irradiance received by this surface [100]. The BRDF, here referred to as f_R, is defined by several parameters:

- Two angles which define the incident irradiance direction: the polar angle θ_I and the azimuth angle ϕ_I,

- Two angles which define the reflected radiance direction: the polar angle θ_R and the azimuth angle ϕ_R,
- The wavelength of the incident and reflected light, λ_I and λ_R,
- The polarization states of the incident light and reflected light, $\epsilon_{\mathbf{I}}$ and $\epsilon_{\mathbf{R}}$.

When the incident direction is (θ_I, ϕ_I), then the specular direction is ($\theta_R = \theta_I$, $\phi_R = \phi_I - \pi$). The schematic of the angular convention used in this work in presented in Fig. 4.3. The BRDF can be expressed as:

$$f_R(\theta_I, \phi_I, \theta_R, \phi_R, \lambda_R, \epsilon) = \frac{dL_R(\theta_I, \phi_I, \theta_R, \phi_R, \lambda_I, \epsilon_{\mathbf{I}})}{dE_I(\theta_I, \phi_I, \lambda, \epsilon_{\mathbf{R}})}, \tag{4.4}$$

where L_R and E_I respectively denote the reflected radiance and the incoming irradiance. The surface irradiance is the light flux incident on the surface per unit of illuminated area. The reflected radiance is the light flux reflected in a direction through a solid angle Ω_R, per unit of solid angle per unit of projected area normal to the considered direction. The BRDF is then equivalent to:

$$f_R = \frac{\Phi_R/(\Omega_R A \cos(\theta_R))}{\Phi_I/A} \equiv \left[\frac{W m^{-2} sr^{-1}}{W m^{-2}}\right] \equiv \left[sr^{-1}\right], \tag{4.5}$$

where Φ_I and Φ_R respectively denote the incident and reflected flux, A is the illuminated surface area, and Ω_R is the solid angle of detection. Notice that the units of the BRDF is then the inverse of a steradian, sr^{-1}, and that depending on the relative value Ω_R, the BRDF can either take large or small values. Indeed, considering a good mirror-like surface, Phi_R/Phi_I is approximately 1, the BRDF value then approaches $1/\Omega_R$, and can therefore approach $10^5 - 10^6$ sr^{-1} for small solid angles. This Ω_R dependency accounts for the complex notion of experimental BRDF, which is consequently, related to the actual Ω_R value of the experimental setup.

The BRDF has two important properties, which are *reciprocity* and *conservation of energy*. The Helmholtz reciprocity [101] states that if the sense of the traveling of the light is reversed, then the value of the BRDF remains unchanged, which can be written as:

$$f_R(\theta_I, \phi_I, \theta_R, \phi_R) = f_R(\theta_R, \phi_R, \theta_I, \phi_I), \tag{4.6}$$

where the spectral and polarization dependencies of f_R are dropped from its expression. The energy conservation principle states that the total quantity of light that is scattered cannot exceed the incident quantity of light. It means that the sum over all outgoing directions of the BRDF times the projected solid angle cannot exceed 1 (and also must equal the reflectance of the surface):

$$\int_\Omega f_R(\theta_I, \phi_I, \theta_R, \phi_R) \cos\theta_R d\Omega_R \leq 1, \tag{4.7}$$

which indicates that a surface cannot reflect more light than it has received. This is why, one can also find the *cosine-corrected BRDF* term in the literature, here referred to as

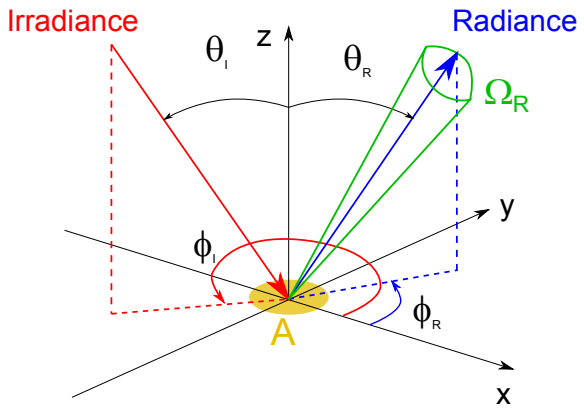

Fig. 4.3 *Angular representation of the Bidirectional Reflectance Distribution Function (BRDF), defined by the four angles θ_I, ϕ_I, θ_R and ϕ_R. The illuminated area A and the solid angle of the radiance, Ω_R, are also represented.*

ccBRDF, which is defined as $f_R \cos(\theta_R)$. In this study, we will usually use the cosine-corrected BRDF, in order to be consistent when comparing experimental measurements and results of light scattering models. However, one must notice that in the case of experimental data, the reflectance values measured from the integrative sphere setup can slightly differ from these evaluated from the integral of the ccBRDF signal (up to 10% discrepancies).

The BTDF, f_T, is defined in a similar way, as:

$$f_T(\theta_I, \phi_I, \theta_T, \phi_T, \lambda, \epsilon_\mathbf{T}) = \frac{dL_T(\theta_I, \phi_I, \theta_T, \phi_T, \lambda, \epsilon_\mathbf{T})}{dE_I(\theta_I, \phi_I, \lambda, \epsilon_\mathbf{I})}, \tag{4.8}$$

with L_T the transmitted radiance. As in the case of the cosine-corrected BRDF, the integral of the cosine-corrected BTDF over the whole half space is the transmittance. Usually, for the sake of simplicity, one defines the Bidirectional Scatter Distribution Function (BSDF), which includes both BRDF and BTDF.

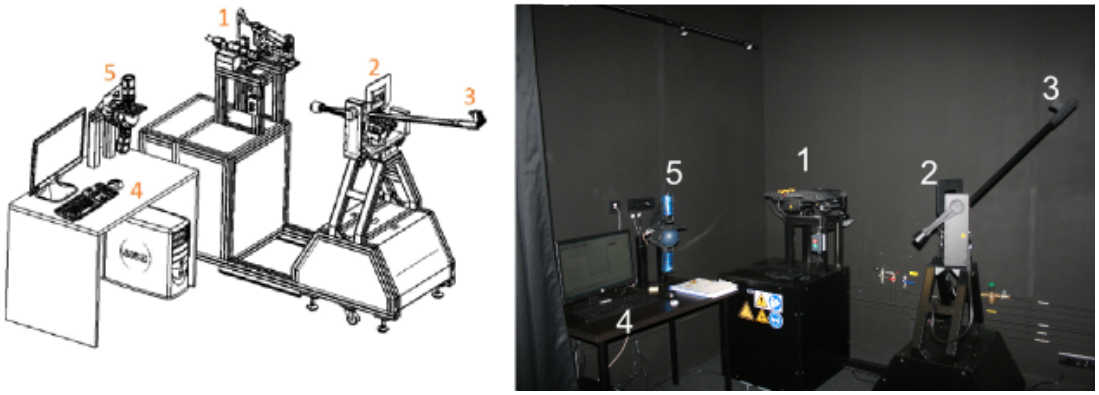

Fig. 4.4 *Schematic representation of the OMS4 [105](left panel) and picture of the setup in the dark room (right panel). The OMS4 is composed of 5 different parts: 1) Illumination system, 2) Sample holder, 3) Detection system, 4) Workstation and 5) Spectral measurement.*

4.2 Description of the goniospectrophotometer

Goniospectrophotometers are devices that measure the angular spread of the radiance of light from a surface: the so-called BRDF and BTDF functions. To measure those, classical goniospectrophotometers need three different parts: the illumination system, the sample holder and the detection system. In order to measure the scattered light intensity all around the sample, some of these systems must be mobile.

There is no rule about the design of the fixed and mobile parts of the setup. Sometimes, the illumination and the detection systems are mobile and the sample holder is fixed [102]. In other cases, the illumination and the sample holders are mobile while the detection remains fixed [94]. Usually, these goniospectrophotometers are rather cumbersome, as the length between the sample and the detector is directly related to the angular resolution of the setup. On the other hand, goniospectrophotometers, based on imaging systems also exist: as the ones commercialized by ELDIM [103] or Radiant Imaging [104] companies. They are built in a different way and are usually more compacted. The scattered light is usually collected through a set of lenses. The measurements can be quickly executed, but due to the imaging system, parts of the information, such as the polarization state of light can be lost.
During the first year of the PhD (which was also the first year of the FRAXOS project), several devices were tested to choose the one to be purchased as part of the study.

In this study, the OMS4 is the goniospectrophotometer was used to characterize the BRDF and BTDF of the samples. The OMS4 is an industrial setup, commercialized by the company ANSYS-OPTIS [105], and it is presented in Fig. 4.4. In this case, the sample holder and the detection systems (respectively marked 2 and 3 in Fig. 4.4) are mobile, and the illumination system is fixed (noted 1 in Fig. 4.4). The OMS4 is also composed of two other parts: the computer workstation, and the spectral measurement setup, which are respectively noted 4 and 5 in Fig. 4.4. As it can be seen from the right part in Fig. 4.4, the OMS4 is placed in a dark room, in order to prevent stray light. This section aims to present the OMS4 goniospectrophotometer and its relevant characteristics. Then

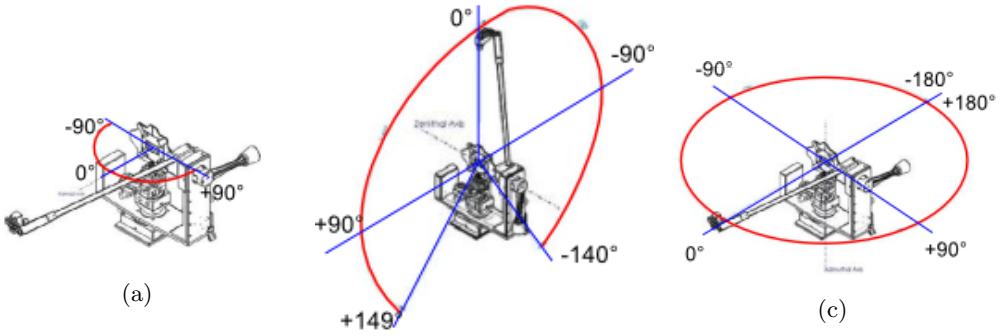

Fig. 4.5 *The sample holder and the detection systems allow to examine the whole space around the sample. This displacement is realized by three motorized axes: (a) incident axis, (b) vertical axis and (c) horizontal axis.*

some surfaces with different ccBRDF properties will be examined in order to present the technical abilities of the OMS4.

4.2.1 Illumination system

The illumination system is a fixed part of the OMS4. Four different sources are available to illuminate the sample:

- Three diode lasers of wavelength: 447 nm, 513 nm and 637 nm. The divergence of the three lasers is less than 0.1°.
- A broadband Xenon source, equipped with a filter wheel consisting of 15 color filters, which allows to select a narrow band of the broadband source. The divergence of the Xenon lamp is evaluated to be 1.5°.

The three laser diodes are circularly polarized, and the Xenon illumination is unpolarized. However, a set of polarizers for each source is available, and can be installed in front of the sources to create linear s or p polarizations.

4.2.2 Detection and sample holder systems

The detection arm and sample holder are the two mobile parts of the OMS4. The sample holder can perform a horizontal rotation around its center, from $-90°$ to $90°$, as presented in Fig. 4.5(a). This rotation controls the angle of incidence of the light source on the sample. Thereby this motor axis is referred to as incident angle axis. The detection arm is moving along two axes with two different motors, which are denoted as vertical and horizontal motors. The vertical and horizontal angles vary from $-140°$ to $149°$ and from $-180°$ to $180°$ respectively, as presented in Fig. 4.5(b) and (c). Using the incident, vertical and horizontal motorized axes, two half spheres around the sample (in transmission and reflection) can be examined by the detection system.

The detection of light is done by a photomultiplier tube placed at the end of the arm, with a 10^7 dynamic range. A set of diaphragms that can be placed in front of the detector (one diaphragm at time). For the Xenon lamp, one diaphragm aperture is available,

which corresponds to an angular resolution of 0.5°. With the lasers, three diaphragms (equipped with a diffuser to prevent saturation effects) with different aperture sizes are available. The choice of the diaphragm impacts the solid angle of the detection, which leads to a change of the angular resolution. The three available diaphragms correspond to angular resolution of 0.2°, 0.4° and 0.8°.

4.2.3 Measurements acquisition and presentation

The evaluation of the angular distribution of the scattered light can be realized in two ways. First, one can evaluate the full ccBRDF or ccBTDF of a sample for different incident angles, which means that the detection device will examine both half spheres around the sample for each incident angle: these measurements will be referred to as *full ccBSDF*. On the other hand, the angular spread of the scattered light can be measured along a single plane: these measurements will be referred to as *simple scan*.

Depending of the angular resolution, the full ccBSDF measurements can be rather long: between 40 and 60 min for each half sphere and a single angle of incidence. For each incident angle, the measured data are organized according to a polar representation, as presented in Fig. 4.6(a). The measured signal is organized according to two angles, the polar angle θ_R and the azimuth angle ϕ_R. The polar angle varies from 0° to 90°, from the center of the circle (corresponding to the normal incidence) to its border (corresponding to grazing angles). The azimuth angle is read on the circle circumference and it varies from 0° to 360°. One recalls that according to the angular configuration used in this work, if the direction of incidence is (θ_I,ϕ_I), then the specular direction is ($\theta_R = \theta_I$, $\phi_R = \phi_I - \pi$). On this full BSDF representation, ϕ_I always equals 180°. Consequently, the backward directions have azimuth angles ranged from $180° \pm 90°$ (left part of Fig. 4.6(a)) and the forward directions have azimuth angles ranged from $0° \pm 90°$ (right part of Fig. 4.6(a)). The Fig. 4.6(a) presents the organization of a full ccBRDF measurement, but the organization of full ccBTDF measurements is similar.

One can also perform a quick measurement (1 or 2 min), along a single plane (not obligatory the incidence plane), referred to as *simple scans*. In this case, one of the vertical or horizontal motorized axes is held fixed. For example, if we referred to the Figs. 4.5(b) and (c), to measure the plane of incidence of a surface in reflection, the vertical motor must be fixed at 90° and the detector will move along the horizontal axis, from −90° to 90°. The Fig. 4.6(b) presents an example of simple scan measurement in the plane of incidence. The ccBRDF value is plotted as a function of the detected polar angle θ_R. In order to represent the forward and the backward directions in the same plot, we choose to assign negative values to polar angles in the backward direction ($\phi_R = 180°$).

Due to the design of the setup, there are locations that the detection system cannot access. In the case of measurement in reflection, presented in Fig. 4.7(a), and in transmission, presented in Fig. 4.7(b), there are three inaccessible angular regions. In both cases, the locations #1 correspond to shadowed areas: a part of the detection system passes in front of the source, and consequently the sample is not illuminated anymore

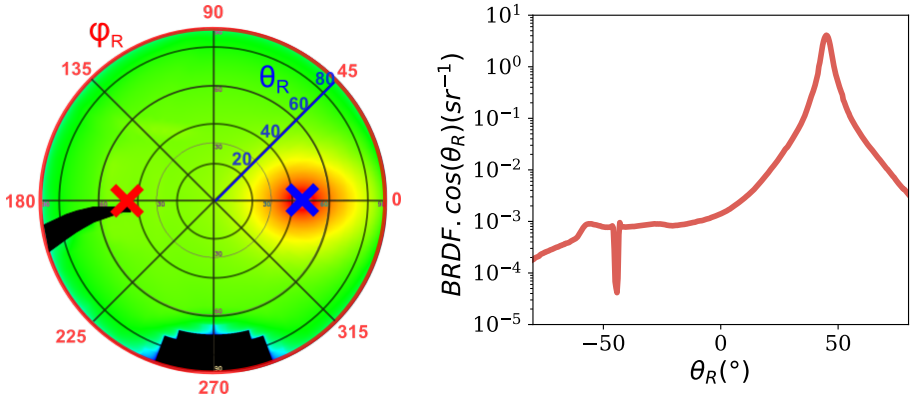

(a) (b)

Fig. 4.6 *Representation of the experimental ccBRDF measured at ($\theta_I = 45°$, $\phi_I = 180°$): (a) for a full BRDF, the ccBRDF signal is organized according to the polar angle θ_R and the azimuth angle ϕ_R. In this case, the incident direction is represented in the plot by the red cross. Consequently, the specular direction is (45°, 0°), and is represented by the blue cross. In all full ccBSDF representations, $\phi_I = 180°$. The black areas of the plot correspond to areas that have not been measured. (b) For a simple scan measurement in the plane of incidence (for $\phi_R = 0°$ and $\phi_R = 180°$), the ccBRDF signal is plotted as a function of the polar angle, where positive polar angles denote the forward directions ($\phi_R = 0°$), and the negative polar angles denote the back forward directions ($\phi_R = 180°$). The signal cannot be measured at $\theta_R = -\theta_I$, which leads to a drop of the measured ccBRDF.*

and consequently there is no detected light. The locations #2 correspond to the hood of the OMS4, and can then not be accessed. Finally, the locations #3 correspond to very grazing angles, which are difficult to measure and consequently hard to interpret. For the sake of clarity, these non-measured angular regions are marked in black in full ccBSDF representation. In the case of a *simple scan*, the non-measured area consists in a sharp decrease of the signal.

4.2.4 Examples of measurements

In order to assess the technical abilities of the OMS4, and to approach the link between appearance and experimental ccBRDF, the first set of measurements were realized on a custom gloss series (3C Conseil) made of black-coated papers. The set of samples is composed of 10 surfaces with very different levels of gloss, providing a nice overview of light scattering from opaque surfaces. Three of these samples, with different Gloss Unit values, and different visual appearances are presented in Fig. 4.8.

The full ccBRDF of these three samples were evaluated at ($\theta_I = 45°$,$\phi_I = 180°$) of incidence, using the broad band Xenon lamp. The three experimental measurements are presented in Fig. 4.9. As expected, the three samples present different optical properties. In the case of the surface of 90 G.U. (Fig. 4.9(left)), the major part of ccBRDF signal is located in the vicinity of the specular direction ($\theta_R = 45°$ and $\phi_R = 0°$). This means

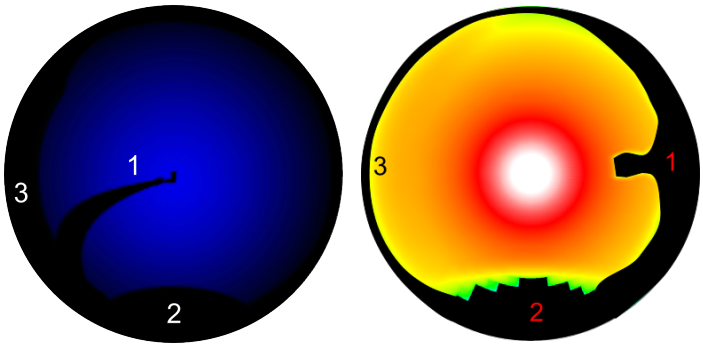

(a) (b)

Fig. 4.7 *Due to the design of the setup some locations of the space are not accessible, they are numbered for the measurement in (a) reflection and (b) transmission. Locations 1 correspond to shadowed areas. Locations 2 correspond to the hood of the OMS4. Locations 3 correspond to scattering at grazing angles of detection.*

Fig. 4.8 *Photograph of three samples of the 3C Conseil scale, with Gloss Unit of 90, 50 and 2, observed in a light booth (Spectralight QC X-Rite), under D65 illumination.*

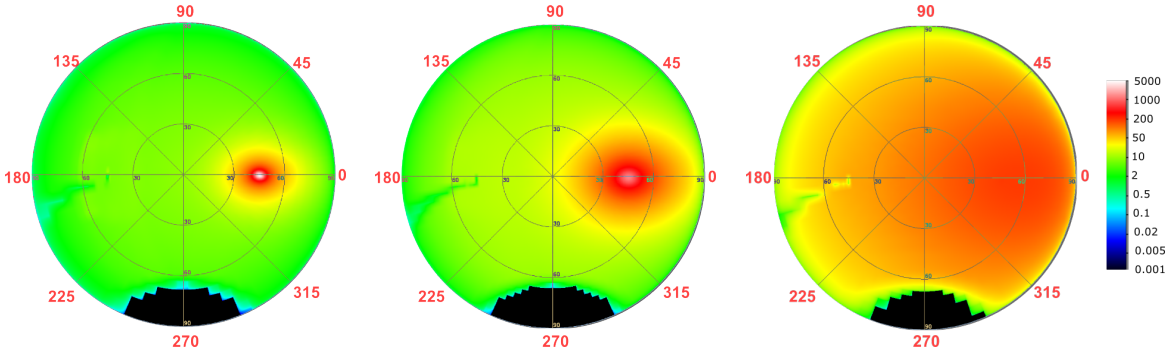

(a) (b) (c)

Fig. 4.9 *Full ccBRDF measurements of the 3C samples presented in Fig. 4.8, realized at ($\theta_I = 45°$, $\phi_I = 180°$) of incidence, using the broad band Xenon lamp: (a) sample of 90 G.U., (b) sample of 50 G.U. and (c) sample of 2 G.U.. The logarithmic color scale is the same for each plot.*

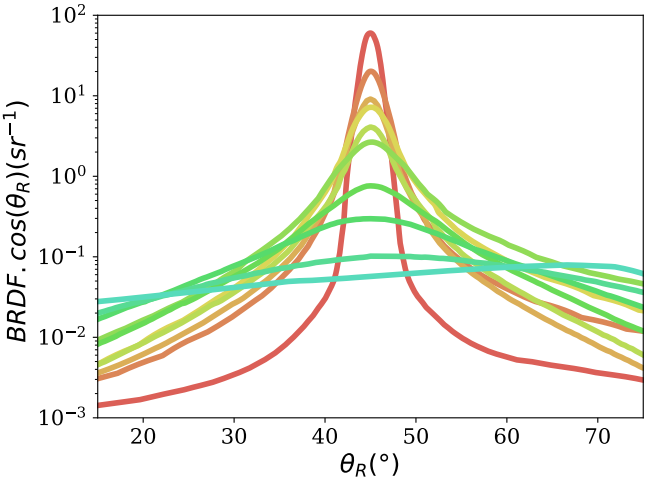

Fig. 4.10 *Simple scans along the plane of incidence of the ten samples of the 3C scale, measured at 45° of incidence, using the broadband Xenon lamp. The G.U. of the samples is progressively decreasing with the color scale from red to blue curves.*

that almost all the light is reflected in the specular direction, which is consistent with the glossy appearance of the sample. When the gloss level decreases to 50 G.U. (Fig. 4.9(middle)), the lobe around the specular direction becomes wider and less intense (the maximal value of ccBRDF is lower). This is why the back front hexagonal pattern of the Fig. 4.8 is difficult to observe. Finally, for the last sample, with 2 G.U., the ccBRDF is more equally distributed in all directions. This is consistent with its diffuse appearance of this sample in Fig. 4.9(right). However, even if these three samples present distinct ccBRDF, their reflectance levels are rather similar: 5.6%, 5.5% and 5.2%, for the 95 G.U., 50 G.U. and 2 G.U. samples respectively.

Simple scans along the plane of incidence, were realized for the whole series of the 3C scale samples, at ($\theta_I = 45°$, $\phi_I = 180°$). The measurements, centered in $\theta_R = 45°$, are presented in Fig. 4.10. The detection system of the OMS4 is sensitive enough to distinguish the angular distribution of the ten samples. This augurs well for the optical characterization of the samples studied during this work.

Finally, the ccBRDF of the reference sample of the glossmeter (a black piece of glass) was also measured. Thereby, we will be able to compare the gloss values measured from the glossmeter to those evaluated from ccBRDF measurements. Indeed, if we evaluate the integral of the ccBRDF measurements, in the close vicinity of the specular direction, we should be able to get back to an approximation of gloss level. The glass reference sample reflects 4.5% of the incident light in the vicinity of the specular direction (the angular aperture is described in Sec. 4.1.1) at ($\theta_I = 20°$, $\phi_I = 180°$) and 12% of the incident light at ($\theta_I = 60°$,$\phi_I = 180°$). These numerical values will be used in order to evaluate the

gloss from BRDF measurements, as:

$$\mathrm{Gloss}^{20}_{\mathrm{BRDF}} = 100\frac{\mathrm{R}^{20}_{\mathrm{BRDF}}}{\mathrm{Ref}^{20}_{\mathrm{BRDF}}} = 100\frac{\mathrm{R}^{20}_{\mathrm{BRDF}}}{0.045}, \tag{4.9}$$

$$\mathrm{Gloss}^{60}_{\mathrm{BRDF}} = 100\frac{\mathrm{R}^{60}_{\mathrm{BRDF}}}{\mathrm{Ref}^{60}_{\mathrm{BRDF}}} = 100\frac{\mathrm{R}^{60}_{\mathrm{BRDF}}}{0.12} \tag{4.10}$$

where $\mathrm{R}^{20}_{\mathrm{BRDF}}$ and $\mathrm{R}^{60}_{\mathrm{BRDF}}$ respectively denote the integral of the ccBRDF of the studied surface, and $\mathrm{Ref}^{20}_{\mathrm{BRDF}}$ and $\mathrm{Ref}^{60}_{\mathrm{BRDF}}$ respectively denote the integral of the ccBRDF of the reference sample. These four latter integrals are evaluated in the close vicinity of the specular direction (see Table 4.1). As described in the standard [96], the gloss values, $\mathrm{Gloss}^{20}_{\mathrm{BRDF}}$ and $\mathrm{Gloss}^{60}_{\mathrm{BRDF}}$, will be truncated to the closest integer.

4.3 Optical properties of the simple model surfaces

Studied in this manuscript, are 1D and 2D periodic and randomly dispersed structures with characteristic dimensions of pattern of 10 to 80 μm. Their detailed fabrication process and morphology were given in Sec. 2.1.1 and Sec. 3.3 respectively.

Periodic systems have been well studied in the literature due to their unusual optical properties, which are related to the diffraction effect [106][107][108]. As a matter of fact, when light interacts with a periodic structure, it can be diffracted into several beams which travel in different directions [109]. These preferential directions, which are also referred to as diffraction orders, are described by the grating equation. The grating equation describes the relationship between the diffraction orders, the period of the grating and the illumination conditions (wavelength and incident angle of the incoming light)[109]. The angular position of the diffracted order can then be evaluated for any kinds of grating, of any period. However, the evaluation of the relative efficiency of each is not that straightforward. Indeed, except in the case of 1D periodic structures with perfect sinusoidal cross-section, where the efficiency of each diffracted order can be analytically evaluated [110], this is more difficult for other structures.

Usually, most of the gratings considered in the literature have submicronic periods, and only few studies are related to the optical properties of gratings with micrometric periods. However, as described by Kumar and Whitesides, the study of the optical properties of micrometric gratings can be an efficient and non-destructive method to control the quality and the period of the structures [111]. Moreover, we also notice that such kind of gratings, with micrometric patterns, were good samples to assess the actual angular resolution of goniospectrophotometer. Indeed, as the angular position of the diffracted order, is perfectly known and distinct over several tenth of degrees (depending of the period), one can observe if the actual angular resolution of the experimental setup is consistent to the announced. Actually, these samples were used in order to select our goniospectrophotometer device, the OMS4.

This section aims to present the optical properties of the simple model surfaces. First, the experimental optical properties of the 1D model surfaces will be presented. The initial line gratings (with rectangular cross sections) and the relaxed structures will be presented independently. Then, the optical properties of the 2D model surfaces will be examined and we will compare the experimental results of surfaces with periodic and random dispersion of pillars.

4.3.1 1D model surfaces

In theory, the light scattering from 1D surface is mathematically simpler to describe than from 2D surface [14]. Indeed, if a plane wave illuminates a 1D surface, and that the plane of incidence is perpendicular to the grooves of the surfaces, the light should only be scattered along a simple plane. However, in the case of an experiment, the situation is complicated by the following factors:

- the imperfect alignment of the 1D structure compared to the incident plane,

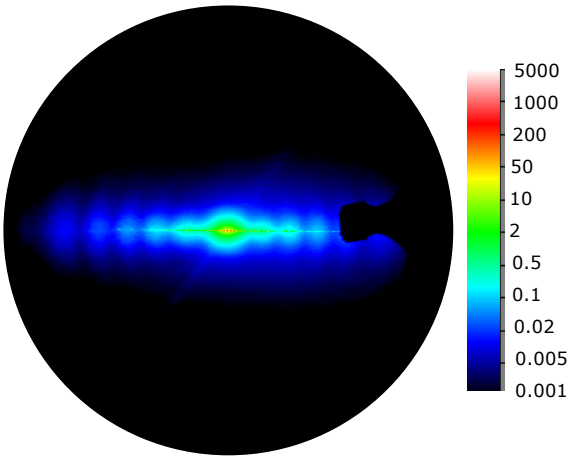

Fig. 4.11 *Experimental ccBTDF of the sample L20. The measurements were realized at ($\theta_I = 0°$,$\phi_I = 180°$) and the lines of the samples were oriented perpendicularly to the plane of incidence. The measurements are realized with the blue laser diode (447 nm).*

- the spatial dimension of the incident light beam, which are all except 1D,
- the local defects of the surface, which are always present, and then turn the surface into an effective 2D surface.

The full ccBTDF measurement of the sample L20 (which refers to a line grating of 20 μm period, see Sec. 2.1.1.3) is presented in Fig. 4.11. The majority of the transmitted signal is actually located in the plane of incidence. For the sake of time, the ccBTDF measurements of such 1D surfaces will be limited to the plane of incidence.

4.3.1.1 Line gratings with rectangular cross-section

The transmitting light scattering properties of the seven line gratings were evaluated with the OMS4. The experimental measurements, realized at normal incidence with the green laser, are presented in Fig. 4.12. As expected by the diffraction theory, light is scattered into discrete directions, which leads to the peaks patterns in Fig. 4.12. According to the grating equation, when light incidents on the grating, the transmitted light has maxima at angles θ_m for:

$$\sin\theta_m = \sin(\theta_I) - m\frac{\lambda}{a} \tag{4.11}$$

where a is the grating period, m is an integer representing the propagating order and λ is the wavelength of the incident light. As expected, as a increases, the absolute value of the angle θ_m decreases. Experimental and theoretical values of θ_1 (1^{st} diffraction order, when $m = 1$) are in good accordance, as presented in Table 4.2. The small mismatches between experimental and theoretical values could be related to a small misalignment of the sample on the goniospectrophotometer, and to the reach of the actual angular resolution of the setup. The ccBTDF at $\theta_T = \theta_1$ is also presented in Table 4.2: it increases while the period of the grating increases, which is consistent with the actual aspect of the samples.

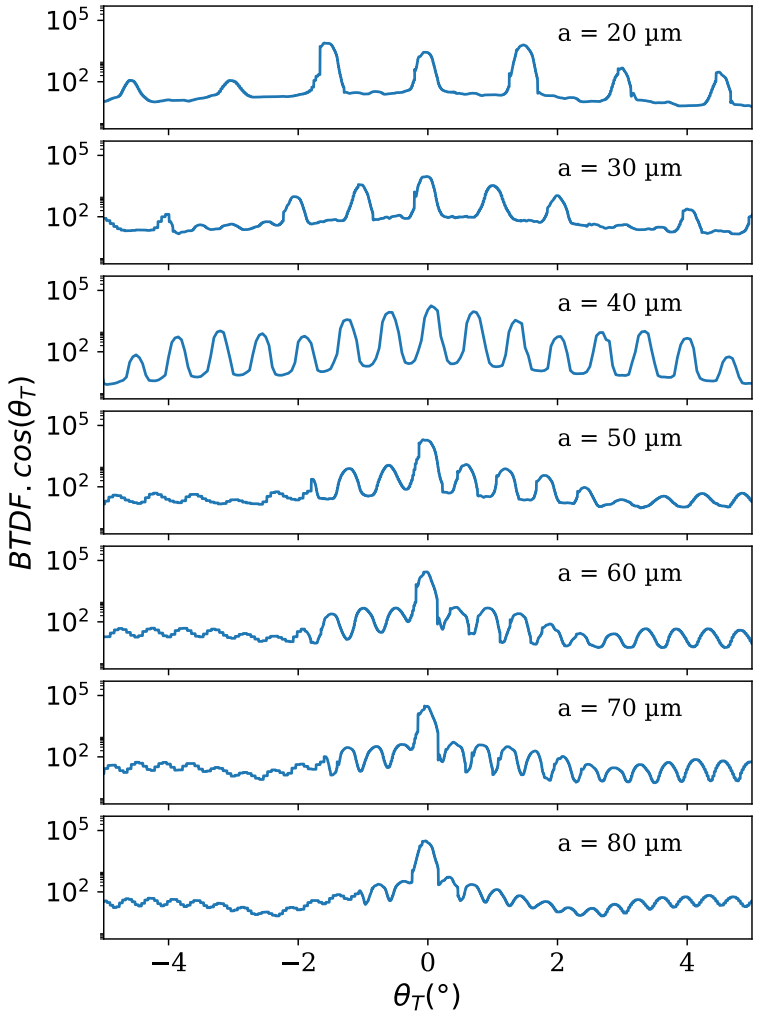

Fig. 4.12 *Experimental BTDF of the line gratings of different periods a. The measurements were realized at normal incidence, with the green laser diode (513 nm).*

a (μm)	20	30	40	50	60	70	80
Experimental θ_1 (°)	1.49	1.02	0.76	0.58	0.46	0.40	0.36
Theoretical θ_1 (°)	1.46	0.97	0.73	0.58	0.48	0.42	0.36
ccBTDF (sr^{-1}) at θ_1	2773	9342	16541	18653	27649	30347	31392

Table 4.2: Comparison of the experimental and theoretical values of θ_1, for several periods of grating, a. Theoretical θ_1 values are evaluated from Eq. (4.11) with $\lambda = 513\ nm$. The experimental ccBTDF at $\theta_T = \theta_1$ is also presented.

4.3.1.2 Line gratings with relaxed cross-section

The transmitted light scattering properties of six of the relaxed line gratings are presented in Fig. 4.13. The measurements were realized at normal incidence, with the line oriented perpendicularly to the plane of incidence, with the blue laser diode. As presented in Fig. 4.13, the change of the cross-section shape of the line grating (due to thermal relaxation) strongly impacts the light scattering properties of the gratings. Indeed, if the diffracted directions remain the same (which is consistent as the period of the grating is not modified), the efficiency of the different diffractive orders are impacted by the shape of the line cross-section.

With the increase of the relaxation time (which is correlated to the decrease of the slope of the cross section, see Sec. 3.3.1), the intensity of some higher diffraction orders (appearing at large scattering angles) decays substantially. The angular region containing relatively efficient diffractive orders decreases significantly with the relaxation time. The width of this efficient angular window is evaluated by the angular directions that correspond to the ccBTDF threshold. The width of the angular efficient window is plotted as a function of the maximal slope of the sample: the results are presented in Fig. 4.14. The fit gives overestimated width in the case of $\alpha_x = 0$. In fact, in this case, the surface is flat and no diffraction order should occur, which is indicated by the orange triangle in Fig. 4.14. Finally, there is a rather good linear correlation ($R^2 = 0.97$) between the maximal slope of the surface, α_x, and the width of the angular window. However this result is just a first observation and does not explain the optical properties of the surfaces.

4.3.2 2D model surfaces

As presented in Sec 2.1.1.3, the 2D model surfaces are composed of micrometric cylindrical pillars, which are periodically (denoted by the letter H) or randomly dispersed (denoted by the letter R) on a glass substrate.

4.3.2.1 Diffractive properties of 2D periodic surfaces

The study of the periodic 2D model samples was described in [112]. Thanks to our collaboration with the 'Laboratoire commun de Métrologie LNE-Cnam', with G. Obein and G. Ged, we were able to examine the diffraction properties in reflection of the periodic surfaces in the very close vicinity of the specular direction. In this study, the BRDF of the samples were measured with the world-class goniospectrophotometer ConDOR [94].

4.3.2.2 Comparison between periodic and random dispersion of pillars

The results that are presented in this section will be submitted in a scientific journal before the PhD defense, and have already been published in [113].

The haze and gloss properties of the samples with periodic and random dispersion of pillars were evaluated, and results are presented in Fig. 4.15. These two parameters seem to be linearly related to the pillar covering ratio. Indeed, the spatial organization of the

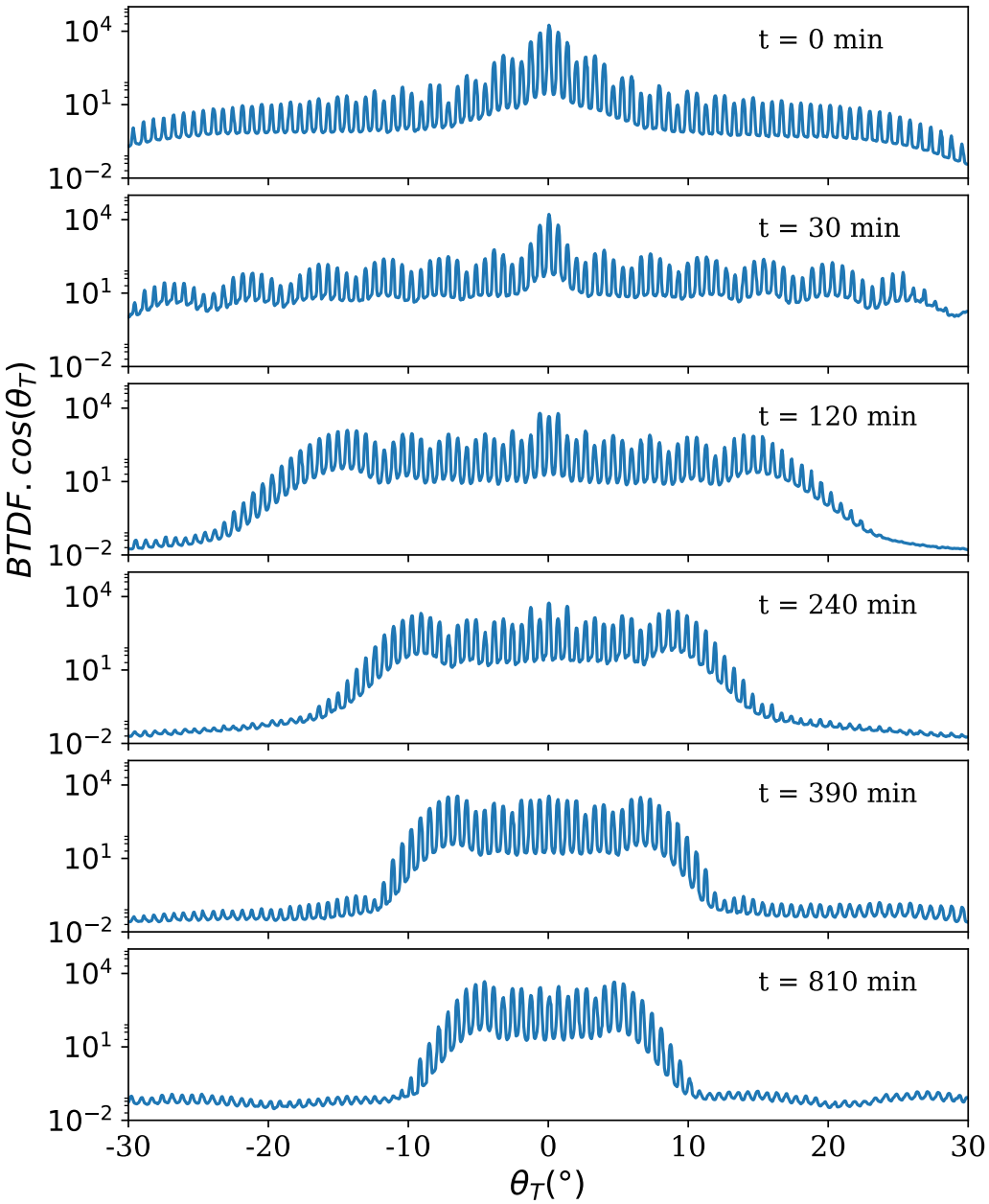

Fig. 4.13 *Experimental ccBTDF of the relaxed line gratings of 40 μm period. The measurements were realized at ($\theta_I = 0°$,$\phi_I = 180°$) and the lines of the samples were oriented perpendicularly to the plane of incidence, with the blue laser diode (447 nm).*

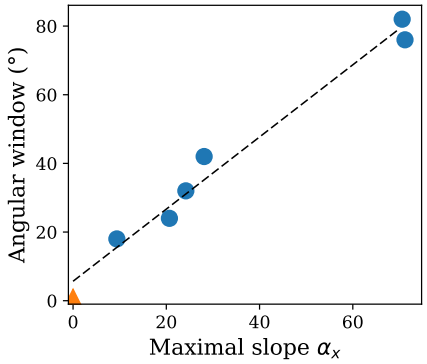

Fig. 4.14 *The widths of the angular windows of efficient diffractive orders are plotted as a function of the maximal slopes of the line cross-sections. The orange triangle denotes that for a flat surface ($\alpha_x = 0$) ,the width of the angular windows should be 0.6° (the width of the 0^{th} order). The black dashed line is a linear regression between α_x and the width of the angular window.*

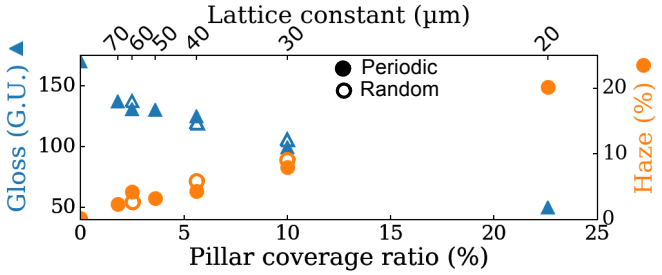

Fig. 4.15 *Measurements of gloss ($\theta_I = 20°$) and haze ($\theta_I = 0°$) realized for the 2D model surfaces with periodic (full symbols) and random (open symbols) dispersion of pillars. Experimental values of 0% of pillars covering ratios denote the untextured glass substrate.*

pillars does not impact these parameters: for example samples H40 and R40 (5.6% of pillars covering ratio) have similar haze and gloss values.

The full ccBTDF of samples H30 and R30 were evaluated with the OMS4, at different incident angles, with the broadband light source with the 535 nm color filter. The results are presented in Fig. 4.16. We identify four different elements in the results:

- In the vicinity of the specular direction, for the periodic dispersion of pillars (lower part of the plots in Fig. 4.16), one can easily observe the diffractive pattern induced by the periodic arrangement of pillars. As expected, this effect is not present in the case of the surface with random dispersion of pillars (upper part of the plots in Fig. 4.16).
- A circular pattern is observable, at $\theta_T = \theta_I$, in Fig. 4.16(b) and (c), and highlighted by a black dashed line. Based on ray-tracing simulations and Finite Difference Time Domain (FDTD) simulations [114] realized at LPICM (CNRS-Polytechnique), it could be related to the cylindrical shape of the pillars. However, the ccBTDF level of the pattern appears to be slightly lower in the case of the sample R30. This could

be related to a locally smaller density of pillars. Indeed, as the samples H30 and R30 have equal density of pillars over a $1 \times 1cm^2$ area, the local illuminated area of the sample R30 could be less dense in pillars.

- Concentric patterns in the vicinity of the specular direction and centered on it, can be observed in the insets of the Figs. 4.16. Based on the angular position of these oscillations and on the micrometric size of the cylindrical pillars, we assume that this pattern is related to the well-known Airy disk [115].
- Concentric patterns centered in $\theta_T = 0°$, can also be observed on the three measurements of Fig. 4.16. This effect could be related to the light scattering phenomena inside the sample. Indeed, we realized a similar full ccBTDF measurement with a black opaque fabrics which covers the sample. Two small holes are made in the cover in order to let the incident gets through the sample. The measurements are presented in Fig. 4.17. In this way, the measured ccBTDF only originates from the local illuminated area. The concentric pattern, centered in $\theta_T = 0°$, is not observable anymore.

Integral measurements of gloss and haze are meant to help classify samples as gloss or matte. But such integral measurements miss a lot of information related to the actual optical properties of the samples, as we have shown in case of glass patterned with periodic and random arrangements of micro-pillars. Despite their micrometric dimensions, the optical properties of the studied samples are strongly affected by light diffraction effects. Thanks to angle resolved setups, we were able to experimentally highlight three different features induced by such kind of samples: diffraction around the specular direction, presence of a diffuse ring and two types of concentric undulations.

Moreover, the existing measurement configurations for haze and gloss exaggerate the angular region around specular direction, which can lead to misinterpretations. Indeed, a quick comparison between the measured value of haze (measured on the hazemeter) and two values of haze evaluated from ccBTDF measurements, was realized for the samples H30 and A30. The results are presented in Table. 4.3. The two integrals of the ccBTDF are evaluated as:

- the integral over a 2.5° window around $\theta_T = 0°$ of a full ccBTDF measurement, realized at normal incidence with the 525 nm illumination, is evaluated, and is referred to as $S_{2.5}$. Then the haze is evaluated with the transmittance T of the sample as $H_{2.5} = 100(T - S_{2.5})/T$.
- the integral over a 1° window around $\theta_T = 0°$ of a ccBTDF measurement, realized at normal incidence with the 525 nm illumination, is also evaluated. The haze is then calculated as $H_1 = 100(T - S_1)/T$.

Lets first consider the sample H30. As expected, the haze measured from the hazemeter and $H_{2.5}$ are rather similar. In this case, the first diffractive orders ($m = \pm 1$ in Eq.(4.11)) are included in the integral, and then contribute to decreasing the haze value. However, when we consider the value H_1, the first diffractive orders are not included anymore in the integral, which logically leads to a drop of the S_1 value and consequently to an increase of H_1.

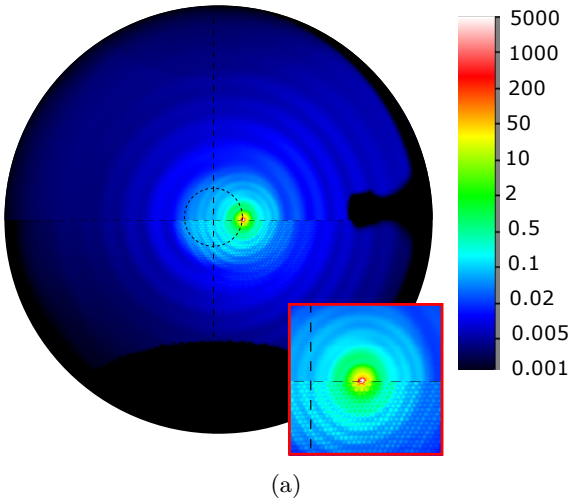

(a)

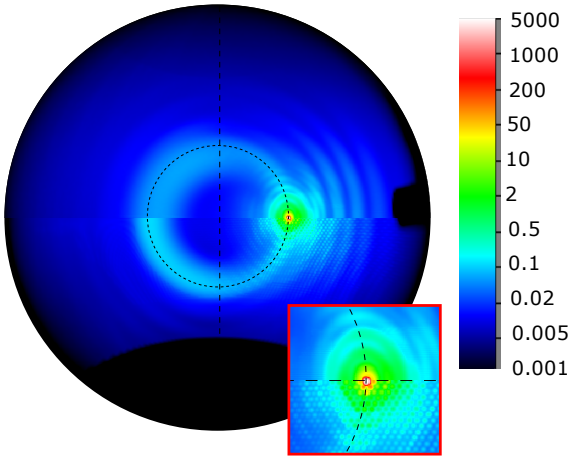

(b)

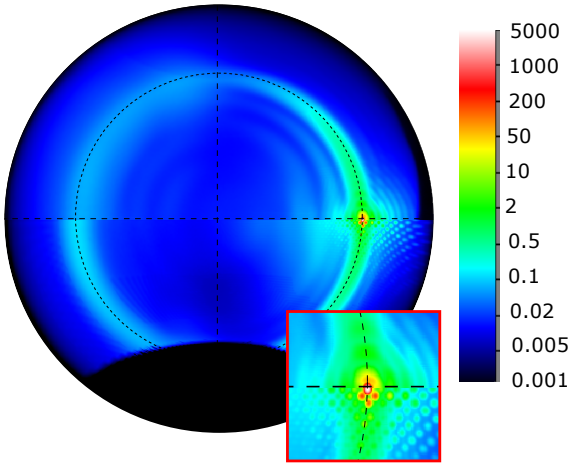

(c)

Fig. 4.16 *Full BTDF measurements of the R30 (upper part of the plot) and H30 (lower part of the plot) samples. The measurements were realized using the Xenon lamp with a color filter centered at 535 nm and 10 nm of FWHM, at three incident angles: (a) ($\theta_I = 10°$,$\phi_I = 180°$), (b) ($\theta_I = 30°$,$\phi_I = 180°$), and (c) ($\theta_I = 60°$,$\phi_I = 180°$). The data are presented in $BTDF.cos(\theta_T)$. The inset in the lower part of the figures are zooms in the vicinity of the specular direction.*

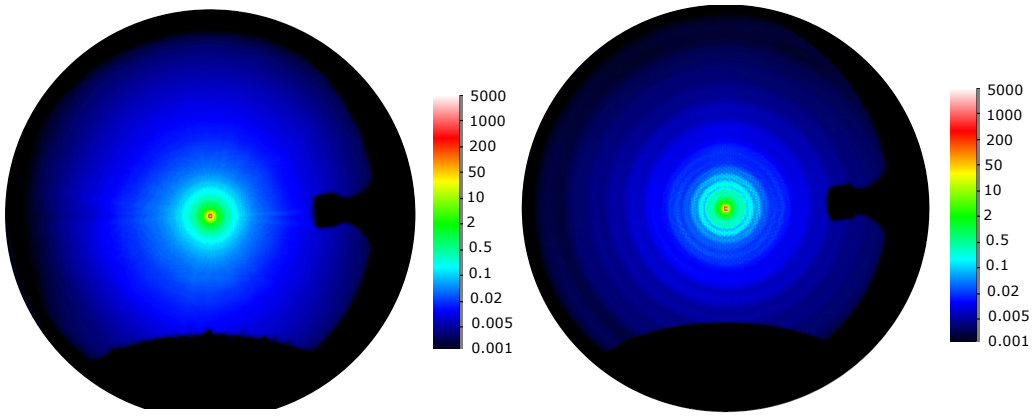

(a) (b)

Fig. 4.17 *BTDF measurements of the sample H30, realized using the Xenon lamp with a color filter centered at 535 nm and 10 nm of FWHM, at normal incidence. The data are presented in $BTDF.cos(\theta_T)$. (a) The sample is covered with a black and opaque fabrics. The film has two small holes (in both sides of the sample) to let the incident light get through the sample. (b) The sample is not covered.*

Sample	Haze (%)	$H_{2.5}$(%)	H_1(%)
H30	8.1	8.7	14
R30	9.2	11.3	13.3

Table 4.3: A comparison between the haze value measured with the hazemeter at normal incidence, and two haze values estimated from ccBTDF measurements,$H_{2.5}$ and H_1. $H_{2.5}$ evaluated from the integral of the ccBTDF over a 2.5° window around $\theta_T = 0°$ and H_1 is evaluated from the integral of the ccBTDF over a 1° window around $\theta_T = 0°$. The comparison is realized for the samples H30 and R30.

However, in the case of the sample R30, as there is no diffractive orders, the two values H_1 and $H_{2.5}$ are rather similar and in good accordance with the haze measured from the hazemeter. However, as the ccBTDF level is not so low in the vicinity of the specular direction, the value of H_1 is higher than we expected.

4.3.3 Conclusion

The optical properties of the model surfaces were characterized by different techniques.

The ccBTDF of the 1D model surfaces were evaluated along the plane of incidence. The high angular resolution of the OMS4 allows to observe the diffraction patterns induced by the different periods of the line gratings, and to resolve diffraction orders 0.36° distinct. We were able to relate the angles of these patterns to the grating equation. Those samples could then become reference samples to assess the actual angular resolution of goniospectrophotometers.

The relaxed line gratings were also examined. We find a linear correlation between the slope of their cross-sections and the optical properties. However, this relation is just a

first experimental observation, and it does not allow us to explain the optical properties of the surface. Thereby, we are currently working on it with collaborators of the FRAXOS project.

The optical properties of the 2D model surfaces were measured. The light scattering properties of the 2D model surfaces appear to be highly complex due to the combination of several physical effects: light diffraction from the pillar grating, scattering from a single pillar, Airy effect and scattering inside the glass substrate. All these effects were identified through the use of angle resolved measurements. Indeed, if the study was limited to the use of integral experimental setups (hazemeter and glossmeter), those effects would have been missed. Finally, when examining periodic structure, the integral measurements must be really carefully considered, since they exaggerate the angular spread of the specular direction, they do not allow to distinguish samples with light diffraction due to periodic arrangement, from those without any periodic pattern.

Sample	Gloss (G.U.) 20°	Gloss (G.U.) 60°	Reflectance (%) 550 nm / 6°
Untreated aluminum	120±5	150±5	63.5±2.9
Small beads	3±1	16±2	62.9±2.3
Medium beads	3±2	17±1	52.8±1.9
Large beads	3±1	16±0	48.6±2.9
30%	10±1	37±1	42.5±2.4
50%	7±2	33±2	44.0±2.5
75%	3±1	16±1	41.9±1.9
93%	3±1	16±2	41.9±2.0
Beads	3±1	15±1	62.1±2.0
Rough beads	0	5±1	21.3±1.9
Beads & Grains	2±1	11±1	43.3±2.1
Grains	1±1	4±1	37.0±1.8

Table 4.4: Summary of the gloss values (expressed in G.U.) at 20° and 60°: the consistency of the measurements, according to the properties of the surface and to the incident angle of the measurements (see Sec. 4.1.1.1) are denoted by the green (consistent) and red (inconsistent) colors of the gloss values. The reflectance levels at 550 nm with $\theta_I = 6°$ of incidence are measured with the integrative sphere device. For the three kinds of data, the measurements were realized on five different locations on the sample.

4.4 Optical properties of complex rough surfaces

The complex rough surfaces studied here have rather different appearances as presented in Sec. 2.2. In the previous chapter, we showed that their topographies, described by several parameters, were also quite different, as highlighted in Table 3.19. This section aims to present the experimental optical properties of the complex rough surfaces. The analysis of the experimental data will be realized keeping in mind the topography of the surface, with hope to establish some relation between surface morphology and optical properties.

4.4.1 Blasted metallic surfaces

The blasted metallic surfaces were presented in Sec. 2.2.1, and their morphological properties were evaluated in Sec. 3.4.1. Since these samples are opaque in the visible range, only their optical properties in reflection will be measured.

The full ccBRDF of each sample was evaluated at several angles of incidence. In the case of anisotropic samples, the full angular distributions of light are presented. However, for the sake of readability, in the case of isotropic samples, only the ccBRDF in the plane of incidence are presented.

The integral optical properties of the surfaces (gloss and reflectance), were also measured and are summarized in Table 4.4. The values will be examined for each series of samples, but their diversity already shows the different optical properties of the samples.

4.4.1.1 Untreated surface

The anisotropy of the untreated surface is observable from the sample itself (see Fig. 2.12) and also from the analysis of its topography (see Sec. 3.4.1.1). We therefore expect anisotropic optical properties.

The gloss at 20° of the sample is 120 ± 5 G.U. (see Table 4.4). This high value of gloss is in good agreement with the glossy aspect of the sample. The measurements were realized along the groves and along its orthogonal direction, but it does not drastically change the measured gloss value. On the other hand, the evaluated gloss values were not really reproducible, and therefore lead to a large variation of gloss value. The reflectance level of the surface is 63.5%. This value is lower than the reflectance level of pure and smooth aluminum, which is usually evaluated close to 90% (depending on the alloys). This could be related to the topography of the sample, which is far from a perfectly flat surface, and to a possible oxidation of the sample. This value is rather consistent with the reflectance measurements realized on rolled aluminum plates realized by Lindseth et al.[116].

The ccBRDF evaluated at ($\theta_I = 10°$, $\phi_I = 180°$) of incidence are presented in Fig. 4.18. In Fig. 4.18(a), the grooves are aligned with the plane of incidence, and in Fig. 4.18(b), the grooves are perpendicular to the plane of incidence. As expected, the ccBRDF is highly anisotropic: the major part of the measured signal is located in a single plane. The maximal value of the ccBRDF and its FWHM evaluated at ($\theta_I = 10°$,$\phi_I = 180°$) of incidence, along the plane of incidence, are 56.7 sr^{-1} and 4.6° when the grooves are perpendicular to the plane of incidence, and 53.6 sr^{-1} and 1.2° when the grooves are aligned with the plane of incidence.

According to Eq. (4.9), gloss values can be extracted from the two ccBRDF measurements: corresponding to the two alignments of the grooves with respect to the plane of incidence. When the grooves are aligned with the plane of incidence:

$$Gloss^{20}_{BRDF} = 71, \tag{4.12}$$

and when the grooves are perpendicular to the plane of incidence:

$$Gloss^{20}_{BRDF} = 56. \tag{4.13}$$

These two values are not in good accordance with the measurements realized with the glossmeter. Indeed the two levels of gloss deduced from the ccBRDF measurements, $Gloss^{20}_{BRDF}$ are below 100 G.U., which means that the sample reflects a smaller amount of light in the specular direction than the reference sample, which seems consistent. Moreover, the gloss value $Gloss^{20}_{BRDF}$ is dependent on the alignment of the grooves.

4.4.1.2 Variation of the beads size

The first set of aluminum blasted surfaces have been blasted with spherical beads of different diameters: small, medium and large beads (see Sec. 2.2.1.2). Their morphological

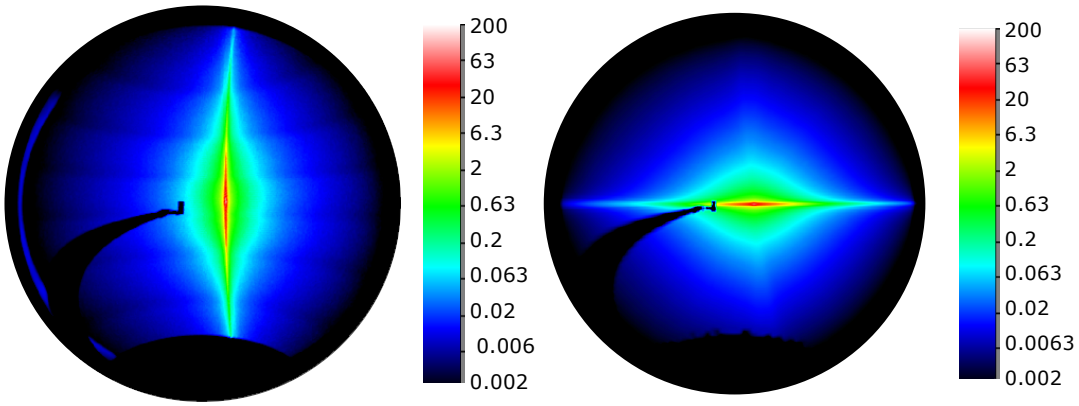

(a) (b)

Fig. 4.18 *ccBRDF measurements of the untreated aluminum sample, realized at (θ_I = 10°,ϕ_I = 180°) of incidence with the Xenon lamp. In (a) the grooves of the sample are in the same plane as the incident plane, while in (b) there are orthogonal to it.*

properties were described in Sec. 3.4.1.2.

According to Table 4.4, the three samples have similar gloss values, and the reflectance level of the surfaces decreases when the diameter of the beads increases. This should indicate that the ccBRDF in the vicinity of the specular direction is the same for the three samples, and that it only differs at large scattered angles.

The ccBRDF measured in the plane of incidence, for measured at (θ_I = 0°,ϕ_I = 180°) and (θ_I = 45°,ϕ_I = 180°) are respectively presented in Fig. 4.19(a) and (b). The maximum ccBRDF values and the FWHM of the ccBRDF, measured at normal incidence, are presented in Table 4.5, as well as the $Gloss^{60}_{BRDF}$ values.

One can first notice discrepancies with the observation made from gloss measurements. Indeed, the $Gloss^{60}_{BRDF}$ values allow to distinguish the three samples, as observed in Fig. 4.19(b), the ccBRDF in the close vicinity of the specular direction are different. The difference between the three samples at (θ_I = 60°,ϕ_I = 0°) is even bigger than at (θ_I = 45°, ϕ_I = 0°).

The FWHM of the ccBRDF is decreasing when the diameter of the beads increases. However, the maximum level of the ccBRDF cannot be linearly related to the diameter of the beads. Nevertheless, all the morphological parameters evaluated from these three surfaces, monotonically evolved with the diameter of the beads (see Table 3.19). Consequently, one cannot establish a simple relation between these indicators of the morphological and optical properties of the samples. However, one should mention that both the slope distribution and the ccBRDF are rather similar for the three samples, and could therefore be related to each other.

4.4.1.3 Covering ratio

This second series of samples is composed of four surfaces, which were blasted with spherical beads of medium diameter. The duration of blasting was varied in this series, leading

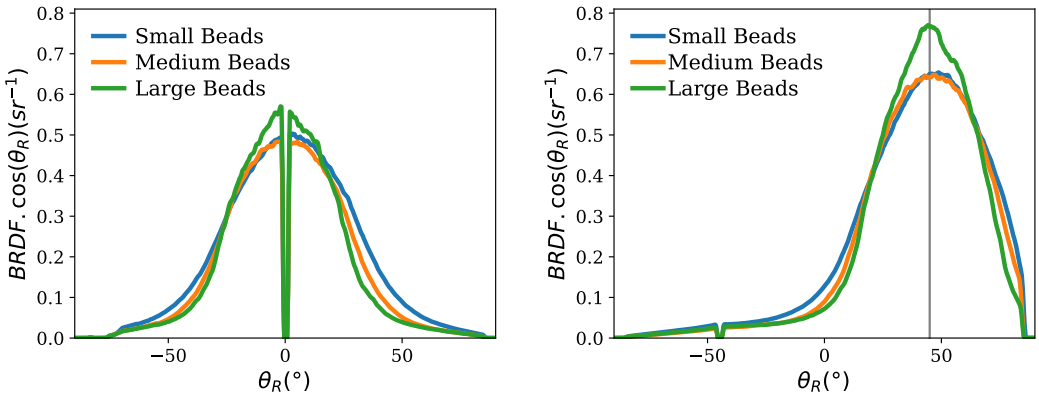

(a) (b)

Fig. 4.19 *In plane ccBRDF measurements of the samples blasted with beads of different sizes. The grey line indicates the specular direction ($\theta_R = \theta_I$). The measurements were realized with the Xenon lamp, at (a) $\theta_I = 0°$, $\phi_I = 180°$) and (b) ($\theta_i = 45°$, $\phi_I = 180°$) of incidence.*

Sample	Maximum ccBRDF (sr^{-1})	FWHM (°)	$Gloss^{60}_{BRDF}$
Small Beads	0.50	63.7	10
Medium beads	0.48	56.8	8
Large beads	0.57	51.5	13

Table 4.5: Maximum level of ccBRDF and FWHM of the ccBRDF in the plane of incidence, of the three samples blasted with different diameters of beads, measured at normal incidence, with the Xenon lamp. The gloss values are evaluated from ccBRDF measurements at ($\theta_I = 60°$, $\phi_I = 180°$)

to four different covering ratios of impact (see Sec. 2.2.1.3). The first three samples of the series have anisotropic morphologies. However, on the last sample (covered at 93%), this anisotropy seems completely erased (see Sec. 3.4.1.3).

The gloss values and the reflectance of the four samples are presented in Table 4.4. The reflectance of the surface is nearly constant for the four samples, however, their gloss values decrease when the covering ratio of impact increases. This is consistent with the gloss value of the untreated sample, which is the highest one: thereby as the impact covering is increasing (and consequently the initial pattern in erased), the gloss value is decreasing. Consequently, it means that four samples reflect the same amount of light, that is scattered at larger angles when the covering ratio of impact increases.

The full ccBRDF of the four surfaces, measured at ($\theta_I = 10°$, $\phi_I = 10°$), with the residual grooves oriented along the plane of incidence, with the Xenon lamp are presented in Fig. 4.20. The anisotropic properties of the samples with 30% and 50% of covering ratios are easily observable, in Figs. 4.20(a) and (b) respectively. As the covering ratio of the surface increases, the anisotropy of the intensity pattern is decreasing. This result is stressed in Fig. 4.21, where the ccBRDF along the plane of incidence of the untreated sample and the four samples of the series are presented. The FHWM of the ccBRDF and

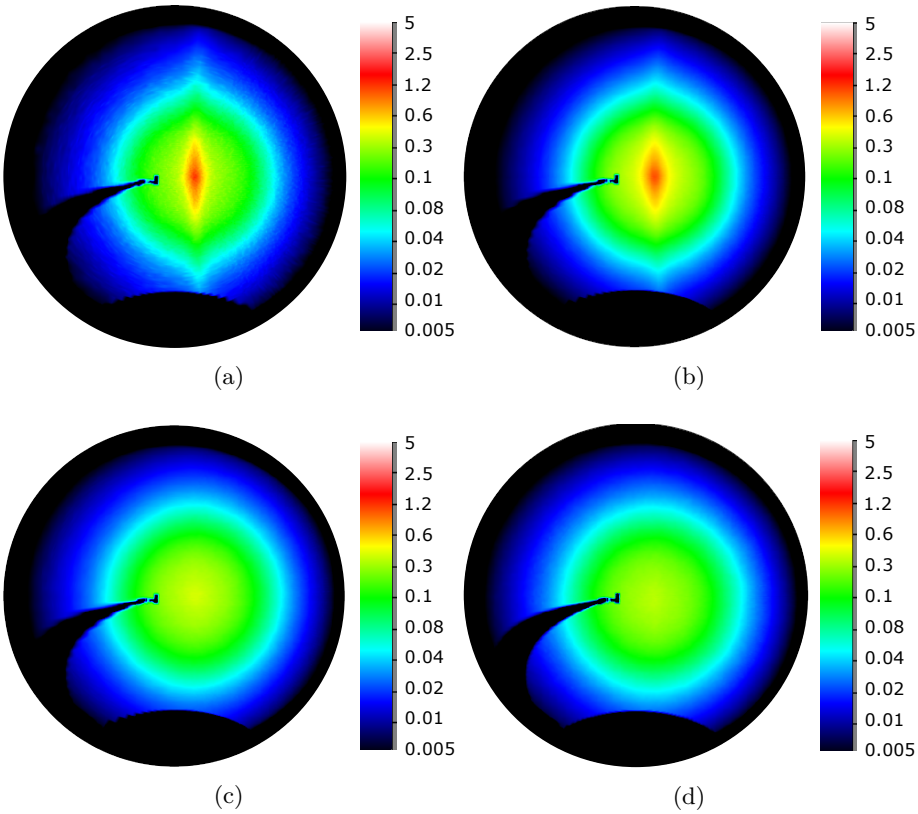

Fig. 4.20 *ccBRDF measurements of the samples with different covering ratio: (a) 30%, (b) 50%, (c) 75% and (d) 93%. The measurements were realized at 10° of incidence, with the Xenon lamp. The residual grooves were oriented along the plane of incidence.*

its maximum value is reported in Table 4.6 for each sample.

The morphological properties of these samples were presented in Table 3.19 and are actually rather similar. Consequently, there is no simple parameter that could explain the difference of the ccBRDF measurements between samples with 50% and 75% of covering ratios.

Finally, the optical properties of the sample with 93% of covering could reasonably be compared with that of the sample blasted with medium beads, as they were fabricated in similar conditions. Their optical parameters are rather similar even if the ccBRDF of the sample "Medium beads" is higher in the vicinity of the specular direction: its maximum level of ccBRDF, its $Gloss^{60}_{BRDF}$ and reflectance values being slightly higher than those of the sample "93%". These small discrepancies could occur from their morphological properties that are slightly different (see Table. 3.19). Moreover, the surface of the sample "93%" is not as flat as that the sample "Medium beads", which could also be a source of discrepancies.

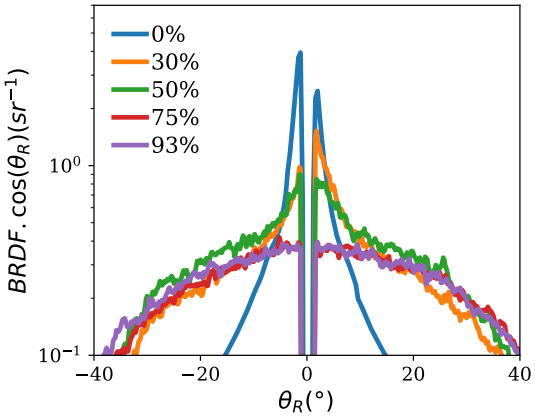

Fig. 4.21 *ccBRDF measurements in the plane of incidence of the untreated sample and of the samples with different covering ratios. The measurements were realized at normal of incidence. The untreated sample (0%) is measured with the Xenon lamp, and the four other samples with the blue laser.*

Sample	Maximum ccBRDF (sr^{-1})	FWHM (°)	$Gloss^{60}_{BRDF}$
30%	1.78	7.8	18
50%	0.91	16.1	17
75%	0.39	56.8	8
93%	0.37	56.2	7

Table 4.6: Maximum level of ccBRDF and FWHM of the ccBRDF in the plane of incidence, of the four samples with different covering ratio, measured at normal incidence, with the blue laser. The $Gloss^{60}_{BRDF}$ values are also presented.

4.4.1.4 Variation of the particle shape

The third series of sample is composed of four surfaces, which were treated with particles of similar diameter, but of different shapes (see Sec. 2.2.1.4). The morphological study of these samples, summarized in Table 3.19, shows that the surfaces are described by very different morphological parameters, and that the use of particles such as rough beads or grains implies a multi-scale roughness.

The glossmeter and the reflectance measurements of the samples are presented in Table 4.4. According to both of these values, the samples have rather different optical properties: the gloss values varying from 4 G.U. to 15 G.U. and the reflectance levels from 20% to 60% for the samples respectively blasted with rough beads, and with beads. From these measurements, those four samples could be classified onto two categories:

- the samples blasted with rough beads and grains, which are highly diffusive with a low level of reflectance.
- the samples blasted with beads, and a mix of beads and grains, which reflect a higher amount of light in a narrower angular area.

Moreover, the sample blasted with a mix of beads and grains has intermediate optical properties (see Table 4.4). This could suggest that the optical properties of this latter

sample could originate from the highly diffuse properties induced by the grains, and from the glossier properties induced by the spherical beads.

The ccBRDF of the four surfaces, measured in the plane of incidence, for $\theta_I = 0°$ and $\theta_I = 45°$, are presented in Fig. 4.22(a) and (b) respectively. As expected, the ccBRDF of the samples are quite different: the FWHM of the ccBRDF and their maximum values are presented in Table 4.7.

The angle resolved measurements confirm the classification of samples that we present previously: the samples blasted with rough beads, and with grains are highly diffusive, the glossiest one is the sample blasted with beads, and the sample blasted with a mix of beads and grains appears as an intermediate sample.

However, the ccBRDF measurements bring additional information: lets first consider the samples blasted with beads and with a mix of beads and grains. The add of grains to beads for blasting leads to a drop of 20% of the reflectance value (Table 4.7) originates both from the drop of the maximum ccBRDF level (from 0.46 $sr{-}1$ to 0.39 $sr{-}1$) and from the drop of the FWHM of the ccBRDF (from 65° to 50°). However, usually the FWHM value of the ccBRDF is related to the diffuse property of the surface: the bigger the FWHM is, the more diffusive the surface is ; and this is actually not the case here (see Fig. 2.17). However, the ccBRDF of the sample blasted with a mix of beads and grains is higher for large scattering angles, as presented in both Figs. 4.22(a) and (b). This effect, which is, of course, not accessible from integral measurements (gloss and reflectance values), could be at the origin of the diffuse appearance of the sample blasted with a mix of beads and grains. As this effect increases with the θ_I, it could probably originates from multiple scattering effect.
As expected from their appearances (see Fig. 2.17), the ccBRDF measurements of the samples blasted with rough beads and grains are highly diffusive. Indeed, as stressed by the values of the FWHM of their ccBRDF, these two samples scatter light in a very large angular region. This effect is once again intensified when θ_I increases (see Fig. 4.22(b)), and could therefore also originate from multiple scattering effect. Moreover, one can also observe in Figs. 4.22(b), that for $\theta_I = 45°$, the highest level of ccBRDF is slightly shifted from the specular direction.

These observations tend to suggest that the specular lobe of the ccBRDF could be related to the low frequency range of the morphology (induced by the spherical beads), and that the diffuse lobe could be related to high-frequency components of the topography (induced by rough beads and grains).

Attempting to relate these optical properties to the actual slope distributions of the samples is quite difficult. Indeed, according to the microfacet theory (which is deeply presented in Sec. 5.1.1), the larger the slope distribution is (and then steeper the slopes are), the larger the angular spread of the reflected light is. Considering this assumption and the slope distributions of the samples, which were presented in Fig. 3.58, the FWHM of the ccBRDF of the sample blasted with rough beads should have been the narrowest, and that of the sample blasted with the beads the largest. This lack of consistence has two possible explanations: for such submicronic component of surface topography, the slope description is not suitable anymore ; or the roughness is too small to be fully characterized by confocal profilometry, and therefore the slope distribution is not well evaluated.

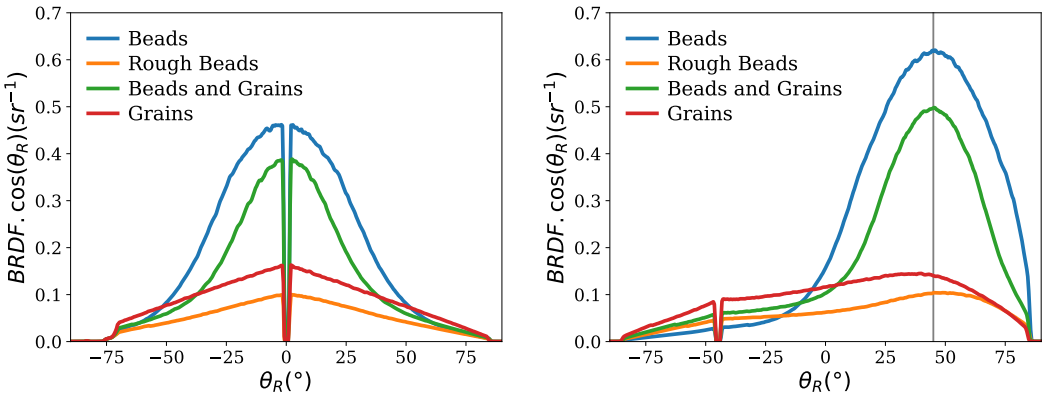

(a) (b)

Fig. 4.22 *In plane ccBRDF measurements of the samples blasted with particles of different shapes. The grey line indicates the specular direction. The measurements were realized with the Xenon lamp, at (a) ($\theta_I = 0°$,$\phi_I = 180°$) and (b) ($\theta_I = 45°$,$\phi_I = 180°$) of incidence.*

Sample	Maximum ccBRDF (sr^{-1})	FWHM (°)	$Gloss^{60}_{BRDF}$
Beads	0.46	64.9	8
Rough beads	0.10	83.2	2
Beads and Grains	0.39	50.1	6
Grains	0.16	90.9	2

Table 4.7: Maximum level of ccBRDF and FWHM of the ccBRDF in the plane of incidence, of the four samples blasted with particles of different shapes, measured at normal incidence, with the Xenon lamp. The $Gloss^{60}_{BRDF}$ of the samples are also presented.

4.4.2 Frosted glass surfaces

The series of frosted glass samples is composed of five surfaces, which were manufactured by different industrial processes. The analysis presented in the last chapter shows that these five samples have highly different morphologies (see Table 3.19). For the sake of clarity, the optical properties in reflection and in transmission of the samples will be presented independently.

4.4.2.1 Reflection properties

The gloss values and the reflectance of the five frosted glass samples are presented in Table 4.8. The reflectance of all samples are rather similar, even if that of sample G3 is slightly higher. However, their gloss values are rather different, which imply that their ccBRDF should also be rather different. From these gloss measurements, one can sort the samples into three groups: G1 with a high level of gloss, G2 with a medium level of

gloss, and G3, G4 and G5 with a low level of gloss.

The ccBRDF of the five surfaces, measured in the plane of incidence, for $\theta_I = 10°$ and $\theta_I = 60°$, are presented in Figs. 4.23(a) and (b) respectively. The ccBRDF evaluated at $\theta_I = 10°$ is presented instead that of $\theta_I = 0°$, in order to prevent for the miss of information due to the shadowing by the detection arm (see Fig. 4.7), which can be problematic in the case of a narrow specular lobe. The FWHM of each BRDF and their maximum values are presented in Table 4.9.

The quick classification of the samples, established from the gloss values of the samples, is rather consistent with the ccBRDF curves:

- For the two incident angles, the sample G1 is highly specular, with a high level of ccBRDF and a narrow angular spread in the vicinity of the specular direction. At high incidence angles (Fig. 4.23(b)), a weak back-scattering signal can be measured ($\theta_R = -60°$).
- The ccBRDF of the sample G2 is similar to that of sample G1, except that the angular spread is slightly larger. To compensate this enlargement and maintain a similar reflectance level, the amplitude of the ccBRDF is logically lower than that of sample G1.
- The ccBRDF of the sample G3 are different for the two incidence angles. At low incidence, the ccBDRF is composed of three components: a narrow specular peak, a large specular lobe, and a diffuse lobe (which is the highest of the five samples). However, for high incidence angle, the specular peak is missing and the diffuse lobe is still the most prominent one.
- The ccBRDF of the sample G4 are similar at both angles of incidence: it is composed of a large specular lobe and an intermediate diffuse component.
- For the sample G5, the specular lobe is the lowest, however, for both incidences, its diffuse component is rather high.

The $Gloss^{20}_{BRDF}$ and $Gloss^{60}_{BRDF}$ are consistent with the gloss values and the ccBRDF. We could have taken the relatively low level of gloss of the sample G3 for a measurement artifact, however, due to the vanishing of the narrow peak at higher incidence, this is consistent.

4.4.2.2 Transmission properties

The haze and transmittance values of the five frosted glass samples are presented in Table 4.10. From the haze measurements, one can sort the samples into the same three groups as defined in reflection. As in the case of reflectance, the transmittance of the sample G3 is slightly different from the ones of the other samples: the transmittance of the sample G3 is slightly lower than for the other samples.

The ccBTDF of the five surfaces, measured in the plane of incidence, for $\theta_I = 0°$ and $\theta_I = 45°$, are presented in Fig. 4.24(a) and (b) respectively. The maximum level of ccBTDF and their FWHM are presented in Table 4.11.

Sample	Gloss (GU) 20°	Gloss (GU) 60°	Reflectance (%) 550 nm / 6°
G1	93±2	111±1	8.4±1.9
G2	17±1	35±1	8.5±1.1
G3	3±1	10±2	10.8±1.8
G4	3±1	15±1	8.1±1.9
G5	3±1	12±1	7.8±1.3

Table 4.8: Summary of the gloss values (expressed in G.U.) at 20° and 60°: the consistency of the measurements, according to the properties of the surface and to the incident angle of the measurements (see Sec. 4.1.1.1) are denoted by the green (consistent) and red (inconsistent) colors of the gloss values. The reflectance levels at 550 nm with $\theta_I = 6°$ of incidence are measured with the integrative sphere device. For the three kinds of data, the measurements were realized on five different locations on the sample.

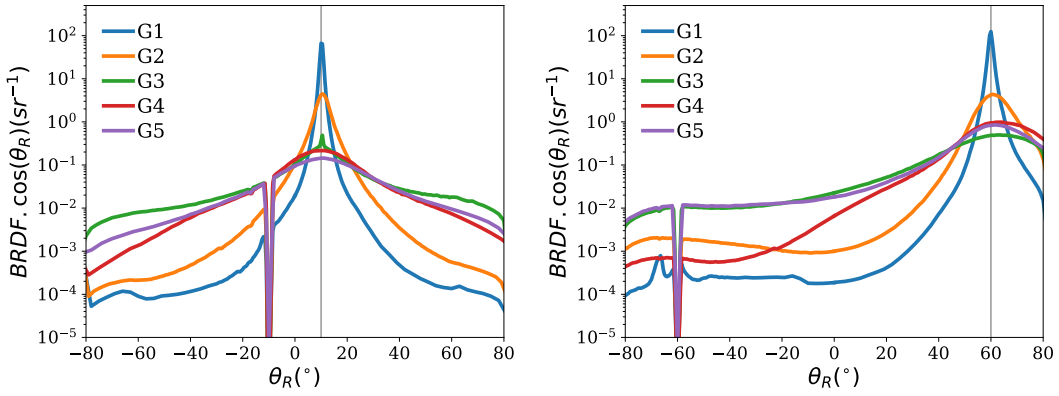

Fig. 4.23 *In plane ccBRDF measurements of the frosted glass samples. The grey line indicates the specular direction. The measurements were realized with the Xenon lamp, at a) 10° of incidence, and b) 60° of incidence.*

Sample	Maximum ccBRDF (sr^{-1})	FWHM (°)	$Gloss^{20}_{BRDF}$	$Gloss^{60}_{BRDF}$
G1	65.2	1.2	111	-
G2	4.41	4.7	-	23
G3	0.52/0.28	3/14.6	-	4
G4	0.22	25.6	-	7
G5	0.15	29.1	-	7

Table 4.9: Maximum level of ccBRDF and FWHM of the ccBRDF in the plane of incidence, of the five frosted glass samples, measured at $\theta_I = 10°$, with the Xenon lamp. The $Gloss^{20}_{BRDF}$ value of the sample G1 and the $Gloss^{60}_{BRDF}$ values of the samples G2, G3, G4 and G5 are presented. In the case of sample G3, two values of maximum ccBDF and FWHM are considered, the first one corresponds to the actual ccBRDF, while the second one corresponds to the ccBRDF without its narrow specular peak.

Sample	Haze (%)	Transmittance (%) 550 nm / 8°
G1	2.58±1.5	90.9±1.9
G2	21.9±1.7	92.1±2.2
G3	79.5±1.2	85.2±2.1
G4	89.0±1.7	90.4±1.8
G5	96.7±1.1	89.3±2.0

Table 4.10: Summary of the haze value, and the transmittance level at 550 nm with 8° of incidence measured with the integrative sphere device, of the five frosted glass samples.

The ccBTDF of the samples are similar to the ccBRDF. For the samples G1, G2 and G4, similar observations can be made as in reflection: G1 is highly translucent, G2 is translucent but with a slightly larger angular spread, and G4 has a very large regular lobe and its diffuse component is intermediate (considering that of G3 and G5). In the case of the sample G3, the ccBTDF is also composed of the narrow regular peak and a high diffuse component (the highest of the five samples). However, the regular peak gets more intense as the incidence angle increases (while it was vanishing in the ccBRDF). As in reflection, the sample G5 is highly diffusive in transmission, however, for both incidences, in the vicinity of the specular direction, the ccBTDF has three local maximums. At normal incidence, the highest is located $\theta_T = 0°$, and the two others at $\theta_T = -6°$ and $\theta_T = 6°$. The ccBTDF of the sample, in the vicinity of the plane of incidence, is presented in Fig. 4.25. One can observe that the two local maximums, highlighted in Fig. 4.24, are parts of a circular pattern, which appears for $\theta_T = 6°$ and for all azimuth angles. This effect is visible for all the incident angles which were measured.
This effect could maybe be related to the shape of the slope distribution of the surface: indeed, as presented in Fig. 3.62, the slope distribution of the sample G5 presents two local maximums for $\alpha = \pm 11°$.

Similarly to the study made for the gloss, a haze indicator is extracted from the ccBTDF measurements realized at normal incidence. The haze is evaluated as described in Eq.(4.3). To evaluate the diffuse transmittance, one calculates the integral of the ccBTDF in a 2.5° cone around the specular direction, and subtracts it from the transmittance of the surface. The evaluated hazes, denoted as Haze_{BTDF}, are reported in Table 4.11. The values are in good accordance with the ones measured with the hazemeter, even if they are slightly overestimated. This overestimation could be related to the evaluation of the transmittance, which is calculated as the integral of the whole ccBTDF. Indeed, as presented in Fig. 4.7(b), some parts of the half space cannot be measured by the OMS4. This could lead to an undervaluation of the transmittance, and therefore to an overestimation of the haze.

4.4.3 Conclusion

The optical properties of the complex rough surfaces were characterized in reflection and in transmission in the case of transparent samples.

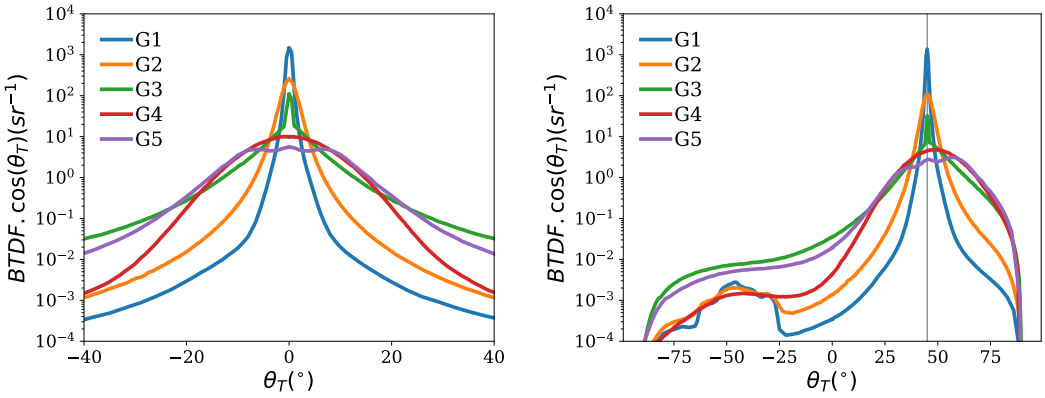

(a) (b)

Fig. 4.24 *In plane ccBTDF measurements of the frosted glass samples. The grey line indicates the specular direction. The measurements were realized with the Xenon lamp, at a) 0° of incidence, and b) 45° of incidence.*

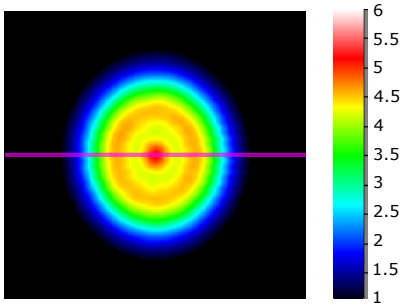

Fig. 4.25 *Part of the BTDF of the sample G5, in the vicinity of the plane of incidence, measured at normal incidence with the Xenon lamp. The purple line denotes the plane of incidence, which was measured in Fig. 4.24(a).*

Sample	Maximum ccBTDF (sr^{-1})	FWHM (°)	Haze_{BTDF}(%)
G1	1522.4	1.1	4.4
G2	250.5	2.5	33.7
G3	114.0/19.5	1.0/6.2	87.0
G4	10.6	16.4	93.7
G5	5.7	21.9	96.7

Table 4.11: Maximum level of ccBTDF and FWHM of the ccBTDF in the plane of incidence, of the five frosted glass samples, measured at normal incidence, with the Xenon lamp. In the case of sample G3, two values of maximum ccBRDF and FWHM are considered, the first one corresponds to the actual ccBRDF, while the second one corresponds to the ccBRDF without its narrow specular peak. The haze values, evaluated from full ccBTDF measurements at $\theta_I = 0°$ are also presented.

Integral parameters (such as reflectance, gloss, transmittance and haze) and angle resolved distribution functions of the scattered light in reflection and in transmission (BRDF and BTDF) were thereby used to describe these optical properties. The major indicators of the light scattering properties of the samples are recalled in Table 4.12 and 4.13, for the reflection and transmission properties respectively. As expected from their visual aspects and from their morphological properties, the studied samples present a large range of optical properties, going from specular to highly diffuse properties. It appears that the blasted metallic surfaces are highly diffusive surfaces, indeed the angular spread of almost all their ccBRDF is 1 to 1.5 times larger than the one of the most diffusive glass surfaces.

The limit of the integral properties was stressed: gloss and haze meant to help to classify samples as gloss or matte, but they are not sufficient to characterize optical properties. Indeed, in the case of the metallic samples blasted with beads of different sizes, despite their different ccBRDF, the gloss values of the samples were the same. Moreover, the unusual optical properties of the samples G3 (narrow specular peak and highly diffusive component) and G5 (circular pattern of the intensity in the vicinity of the specular direction) in transmission would have been missed if the study of the optical properties was limited to the haze measurement.

For each sample, the analysis of the optical properties were realized keeping in mind their actual morphology. The correlation between optical and morphological properties cannot be easily done. However, studying the ccBRDF of the metallic samples blasted with particles of different shapes, it can be mentioned that an important specular lobe could be related to a surface topography composed of relatively low spatial frequencies (spherical beads), and that the diffuse optical component could be related to surface topography composed of high frequencies (grains and rough beads).

Sample	Maximum ccBRDF (sr^{-1})	FWHM (°)	Reflectance (%)
Untreated aluminum Groove aligned in PI	56.7	4.6	63.5
Untreated aluminum Groove perpendicular to PI	53.6	1.2	63.5
Small beads	0.42	63.7	62.9
Medium beads	0.39	56.8	52.8
Large beads	0.51	51.5	48.6
30%	1.78	7.8	42.5
50%	0.91	16.1	44.0
75%	0.39	56.8	41.9
93%	0.37	56.2	41.9
Beads	0.39	64.9	62.1
Rough beads	0.09	83.2	21.3
Beads & Grains	0.31	50.1	43.3
Grains	0.14	90.9	37.0
G1	65.2	1.2	8.4
G2	4.41	4.7	8.5
G3	0.52/0.28	3.0/14.6	10.8
G4	0.22	25.6	8.1
G5	0.15	29.1	7.8

Table 4.12: Summary of the numerical parameters extracted from experimental measurements in reflection: the maximum level of the ccBRDF, the FWHM of the ccBRDF, evaluated along the plane of incidence, and the reflectance level of the surface (measured with the integrative sphere device). The evaluation is realized at $\theta_I = 10°$ of incidence for the five glass samples and for the untreated metallic sample. For the other samples, the evaluation is realized at $\theta_I = 0°$ of incidence. In the case of sample G3, two values of maximum ccBRDF and FWHM are considered, the first one corresponds to the actual ccBRDF, while the second one corresponds to the ccBRDF without its narrow specular peak.

Sample	Maximum ccBTDF (sr^{-1})	FWHM (°)	Transmittance (%)
G1	1522.4	1.1	90.9
G2	250.5	2.5	92.1
G3	114.0/19.5	1.0/6.2	85.2
G4	10.6	16.4	90.4
G5	5.7	21.9	89.3

Table 4.13: Summary of the numerical parameters extracted from experimental measurements in transmission at $\theta_I = 0°$: the maximum level of the ccBTDF, the FWHM of the ccBTDF and the transmittance level of the surface. In the case of sample G3, two values of maximum ccBTDF and FWHM are considered, the first one corresponds to the actual ccBTDF, while the second one corresponds to the ccBTDF without its narrow specular peak.

4.5 Conclusion

This chapter describes the study of the experimental optical characterization of rough surfaces.

In the first section of the chapter, the parameters and functions chosen to express the optical properties were described. Integral parameters, such as gloss and haze, are usually used in the industrial domains due to their quick and easy evaluation. However, we show that these indicators are not sufficient to fully characterize and understand the light scattering properties of a surface. To do so, one must consider functions, which describe the spread of the light scattering in both reflection and transmission. Such functions, so-called the BRDF and the BTDF, are more difficult to evaluate, regarding time and financial considerations, but allow to fully describe the optical properties of a surface.

The BRDF and BTDF of a surface are evaluated with a goniospectrophotometer. The main characteristics of the OMS4, the goniospectrophotometer used during this study, were described in Sec. 4.2. The different light sources of illumination, the high angular resolution and the high dynamics of the detection of the OMS4, allow to measure a wide variety of surface with a high angular resolution.

In Sec. 4.3, the optical properties of the model surfaces were described and analyzed. We showed that the light scattering properties of the model surfaces are mainly governed by the diffraction phenomenon, despite the micrometric dimensions of the gratings. The experimental ccBTDF of the 1D model surfaces was related to the grating equation. A link between the slope describing the relaxed 1D structures and the shape of the ccBTDF was assessed.
Finally, the ccBTDF of the 2D model surfaces were examined. It appears that the 2D model surfaces induce optical properties composed of several optical phenomena, which lead to a final complex ccBTDF. Indeed, at least four different phenomena were identified: the diffraction effect induced by both a single pillar and the periodic arrangement of pillars, the Airy effect, and light scattering effect inside the glass substrate. This study also show the lack of accuracy of the haze integral parameter in the case of periodic surfaces, which could lead to misinterpretations of the actual properties of the surface.

Finally, the optical properties of the complex rough surfaces were characterized in Sec. 4.4. As recalled in Tables 4.12 and 4.13, the studied surfaces present a large range of optical properties, from glossy to highly diffuse surfaces.
The optical properties in reflection of the metallic surfaces were measured. These surfaces present highly diffusive optical properties, which can be related to the fabrication process. Indeed, it appears that samples blasted with particles of complex morphology (rough beads and grains) have very diffusive optical properties, which is consistent with their matte appearance. We also suggested that these highly diffusive properties could originate from multiple light scattering effects: this assumption being consistent with the increase of the diffuse properties with the incidence angle, and with the low level of reflectance of the surfaces. On the other hand, the surfaces blasted with spherical beads scatter light in an angular region which is narrower (even if it remains large) and more

important in amplitude.
The optical properties of the frosted glass samples were examined in both reflection and transmission. Their optical properties vary from high specular (sample G1) to diffuse (samples G4 and G5). The study of the ccBRDF and ccBTDF allow to identify light scattering properties which were not accessible through the measurements of integral parameters such as haze and gloss. Thereby, we identified that the optical properties of the sample G3 was composed of a narrow specular peak and a highly diffuse component. In the same way, the study of the ccBTDF shows the unusual properties of the sample G5, which is composed of an intense circular pattern in the vicinity of the specular direction.

The analysis of the optical properties was realized keeping in mind the actual topography of the samples. Unfortunately, for the majority of the samples, the link between the morphology and the angular distribution of the scattered light is not straightforward. Consequently, the following chapter will be dedicated to the study of the light scattering models that could establish such relation.

Chapter 5

Modeling of light scattering from rough surfaces

"Theoretical physics can also prove that an elephant can hang off a cliff with its tail tied to a daisy!
But use your eyes, your common sense."
Jim Garrison, JFK, 1991

Contents

When an electromagnetic wave is incident on a plane interface, separating two media, it is reflected according to well-known laws. Indeed, the properties of the reflected field depend on the angles of incidence and on the wavelength of the incident wave, and the intrinsic properties of the two media. Finally, the incident wave will be reflected in the specular direction. However, when the interface gets rough, the properties of the reflected wave are much more difficult to evaluate: the wave is scattered into various directions [14].

The problem of scattering from rough surfaces arose in the last decades in different domains. In radar, applications related to the detection of boats on a rough sea, have been extensively studied in the last century [117]. In radio astronomy, the surface topography of the Moon was studied by sending radar pulse on it, and then examining the properties of the signal back-scattered on the Earth [118]. These last two examples are, obviously

not of the same scale of roughness and wavelength compared to our study of the light scattering from rough surfaces, but they illustrate the complexity of the problem.

The light scattering properties of rough surfaces can be described by rigorous calculations based on the law of the physical optics. However these accurate calculations are often very complex and long. In some cases, optical responses of rough surfaces can be approximated by the law of geometrical optics, which gives way to less precise by significantly more rapid calculations. These two approaches offer models to describe the light scattering properties of rough surfaces, they are, of course, rather different.

However, it appears that only a small number of studies have compared the results of such light scattering models to experimental data that include both the morphological and the optical properties of rough surfaces. We saw in Chap. 4, that the optical and morphological properties of our samples could not be easily related, and that we therefore need light scattering models. This chapter will describe the different light scattering models that were used in this study, in order to relate the optical and morphological properties of the examined rough surfaces. First, techniques based on the laws of geometrical optics will be described and their results will be compared to experimental data. Parts of this work were realized with the help of E. Garcia in the context of a M2 internship. Then, a model based on the laws of physical optics will be described and used for the same purpose. We will finally conclude on the relevance of each of these models.

5.1 Geometrical Optics

In the Geometrical Optics (GO) approach, one considers light as a collection of rays, which can be reflected or refracted at plane interfaces. Thus, the light is simply represented as a straight line, which is deflected according to the refractive index of the two media that compose the interface. This approach is only valid when the light passes through objects of dimensions much bigger than its wavelength. On the other hand, when we consider objects of the typical size of the wavelength, or even smaller, this approximation is no longer valid. In fact, without considering the wave nature of light, one cannot predict the phenomena of diffraction or interference, which are not negligible at this scale.

One of the goals of the GO community is to serve the computer graphics needs. Indeed, for some applications, the production of virtual reality images is required. As an example, in the video game industry, the images produced must be either as realistic as possible or highly aesthetic or both, in order to immerse the user in a plausible environment. However, for this kind of application, the realism is not the only criteria, and one must balance between the realism and the speed of execution of the virtual scene. To quickly produce these aesthetic images, the light scattering problem can be drastically simplified.

A large number of light scattering models based on GO exists. They can be classified into different categories, according to their actual formulation. A review of these so-called "BRDF models" have been given by Montes and Urena[27]. All these models are built on a certain number of assumptions, which can lead to non-physical description.

This section aims to present two ways of modeling the light scattering from rough surfaces, with the GO approach. First, the microfacet theory, which gave rise to analytic models used to reproduce the light scattering from rough surfaces, will be described.

Then, numerical simulations, based on ray tracing approach will be presented. In both cases, a comparison between the modeled and the experimental results will be presented.

5.1.1 Microfacet theory

The microfacet theory relies on a particular description of the topography of a rough surface, and combines three functions: two are related to the surface topography, and the third one is related to the optical properties of the material from which the surface is made.

The microfacet theory states that if a surface is sufficiently rough, it can be seen as a collection of planar microfacets. The dimension of each microfacet must be larger than the wavelength of the incident light, so that the GO laws remain valid. The mean orientation of the macrosurface is assumed flat, and its normal vector, $\mathbf{n}$. The vector $\mathbf{n}$ and all the vectors that describe the microfacet theory are assumed to be unit normal vectors which pointed outside of the surface. The vector normal to each facet is denoted by $\mathbf{m}$. Thereby the orientation of each microfacet deviates from $\mathbf{n}$ by an angle, that is referred to as θ_m, as presented in Fig. 5.1(a). The sign of θ_m can be rather positive or negative in order to consider the orientation of each facet with respect to the normal direction of the macrosurface. The distribution of the orientation of the microfacets, usually referred to as $D(\mathbf{m})$, is the indicator chosen to represent the surface topography, where $\mathbf{m}$ is the normal direction of the microfacets. Microfacet theory presumes that each microfacet independently reflects the incoming light, and the light scattering can be seen as the sum of the light reflected from each microfacet of the surface: consequently, such models do not take into account multiple scattering effect.

However, due to the large roughness of the surface or to a large polar angle of incidence, the light ray may not strike all the microfacets. Indeed, some shadowing and masking effects can occur: microfacets cannot be illuminated because they are hidden by their neighbors, or the scattered light can be trapped after multiple reflection, as respectively presented in Figs. 5.1(b) and (c). This attenuation of the reflection is taken into account by the masking-shadowing function, which depends on the orientation of each facet, $\mathbf{m}$, and on the incident and scattered directions, which are respectively denoted $\mathbf{i}$ and $\mathbf{s}$. The masking-shadowing function is usually referred to as $G(\mathbf{m}, \mathbf{i}, \mathbf{s})$. Several analytic expressions have been developed in order to reproduce as well as the experimental results of light scattering [119]. The signal attenuation induced by G becomes more important when the incidence and detection angles increase and when the slope deviation increases from the mean orientation of the surface[22].

The amount of light reflected from each microfacet is obviously related to the material nature. This effect is taken into account by a Fresnel term, which is expressed in terms of the refractive index of the considered material, and is usually denoted by F. The value of $F(\mathbf{m}, \mathbf{i})$ is related to the local angles of incidence formed between the incident light and the microfacet orientation.

The analytic models based on the microfacet theory, use a combination of the three functions $D(\mathbf{m})$, $G(\mathbf{m}, \mathbf{i}, \mathbf{s})$ and $F(\mathbf{m}, \mathbf{i})$ to estimate the light scattering properties of rough surfaces. Numerous analytic models based on the microfacet theory exist [27]. They differ in the analytic expressions of the factors D and G, in the way a facet reflects

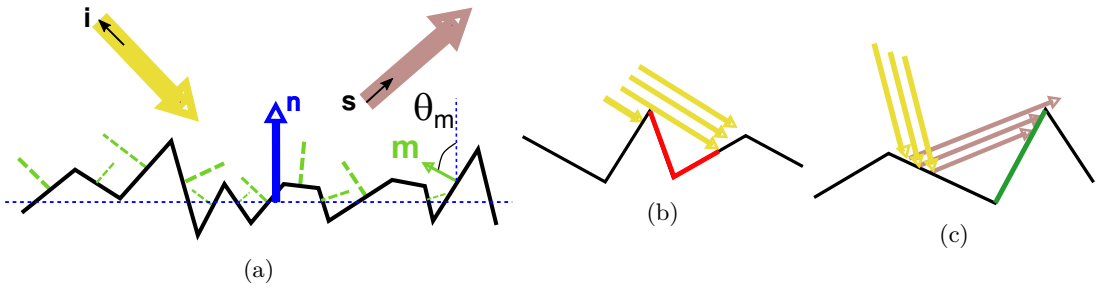

Fig. 5.1 *The normal unit vector of the average surface is noted* $\mathbf{n}$*, and the incident and scattered directions are respectively denoted* $\mathbf{i}$ *and* $\mathbf{s}$*. The factors D and G are parts of the factors involved in the microfacet theory. (a) The slope distribution* $D(\mathbf{m})$ *depends on the surface topography, which can be seen as a collection of microfacet with orientation* θ_m *(the normal direction of the microfacet is noted* $\mathbf{m}$*). One must consider the attenuation factor G, which takes into account (b) shadowing and (c) masking effects, due to the surface topography and to the illumination and scattering directions.*

the light (purely specular or diffuse reflection), and in the addition of different corrective factors. In 1967, Torrance and Sparrow presented one of the first BRDF models [120]. This model has been improved several times [121], but is still widely used nowadays.

Generally, these models are not used to predict the optical properties of a surface, but to provide an analytic expression that reproduces them in the best possible way. Thus, the functions D, G and F can be used as free mathematical functions (they are thus not correlated to the actual topography or the real nature of the surface), to reproduce the experimental BRDF curves. In this way, the scientific community aims to find the analytic functions that could efficiently reproduce the actual morphology of the surface, in order to be able to perform realistic and quick calculations.

The purpose of our study is to use experimental quantities, corresponding to the actual morphology of the samples, to see if physically based microfacet models can predict the optical properties of our rough surfaces.

5.1.1.1 The microfacet model considered

The microfacet model, used to describe the reflection properties of rough surfaces, during this study was implemented from a publication of Walter et al.[22]. The code was implemented in Python by S. Mazoyer (research engineer from O2M department, SGR).
The modeled BRDF, f_R, is evaluated as a product of the three functions F, G and D (defined previously in Sec.5.1.1):

$$f_R(\mathbf{i},\mathbf{s},\mathbf{n},\mathbf{m}) = \frac{F(\mathbf{i},\mathbf{m})G(\mathbf{i},\mathbf{s},\mathbf{m},\mathbf{n})D(\mathbf{m},\mathbf{n})}{4|\mathbf{i}\cdot\mathbf{n}||\mathbf{s}\cdot\mathbf{n}|}. \tag{5.1}$$

As mentioned in Sec. 5.1.1, usually, the microfacet models do not refer to the actual slope distribution of the surface, but to an analytic expression of it. In [22], the expressions of three different distributions are given, namely the Beckmann, the Phong and the GGX distributions. However, as presented in Fig. 5.2, the three distributions are not so different from each other: the Beckmann and Phong distributions are rather similar, and the GGX

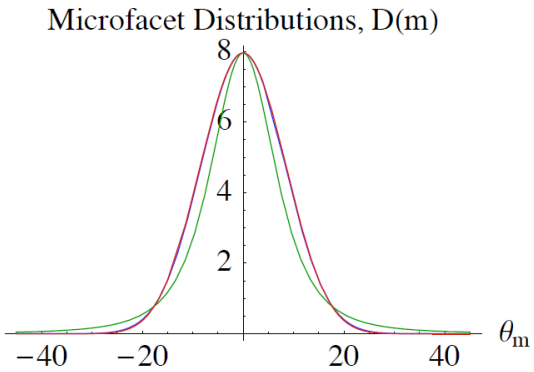

Fig. 5.2 *Beckmann (red), Phong (blue), and GGX (green) microfacets distributions, evaluated from analytic expressions presented by Walter and collaborators [22].*

is distribution has a narrower peak with stronger tails [22]. During this study, only the GGX distribution was tested, as the authors described it as the most efficient. Within GGX, the functions D and G are expressed as a function of the parameter α_g, which will, roughly speaking, determine the width of D. The function D is expressed as:

$$D(\mathbf{m},\mathbf{n}) = \frac{\alpha_g^2}{\pi \cos^4\theta_m(\alpha_g^2 + \tan^2\theta_m)^2}. \tag{5.2}$$

The function G is expressed as:

$$G(\mathbf{i},\mathbf{s},\mathbf{m}) = \left(\frac{2}{1+\sqrt{1+\alpha_g^2\tan^2\theta_I}}\right)\left(\frac{2}{1+\sqrt{1+\alpha_g^2\tan^2\theta_R}}\right), \tag{5.3}$$

where θ_I and θ_R, respectively denote the angle between $\mathbf{i}$ and $\mathbf{n}$ (the incident polar angle) and the angle between $\mathbf{s}$ and $\mathbf{n}$ (the reflected polar angle)[22].
Finally, the expression of the function F, is the following:

$$F(\mathbf{i},\mathbf{m}) = \frac{1}{2}\frac{(g-c)^2}{(g+c)^2}\left(1+\frac{(c(c+g)-1)^2}{(c(c-g)+1)^2}\right), \tag{5.4}$$

where

$$g = \sqrt{\frac{\eta^2}{\eta_i^2} - 1 + c^2} \text{ and } c = |\mathbf{i}.\mathbf{m}|, \tag{5.5}$$

where η and η_i respectively denote the index of refraction of the media to characterize and the index of refraction of the incident media (here the air). In the case of complex refractive index, η will be considered as:

$$\eta = n + ik, \tag{5.6}$$

where n and k respectively denote the real part of the refractive index of the material and its the extinction coefficient. The formulation of the Fresnel coefficient is quite different from the usual expressions that can be for example be found in [12], however, its consistency was checked. Moreover, we are well aware that its expression is not adapted to the use of complex refractive index. However, due to the lake of time, we chose to use it in this way, even for the description of the metallic samples.

Sample	α_g	Fit quality
Small Beads	0.24	Medium
Medium Beads	0.21	Good
Large Beads	0.22	Good

Sample	α_g	Fit quality
Beads	0.39	Bad
Rough beads	0.15	Medium
Beads & Grains	0.28	Medium
Grains	0.24	Good

Sample	α_g	Fit quality
G1	0.03	Good
G2	0.11	Good
G3	0.18	Medium
G4	0.22	Bad
G5	0.41	Bad

Table 5.1: The parameters α_g, which were used to fit as well as possible the slope distributions of the samples are summarized. A quality degree of the fit (arbitrary chosen) is also given for each sample.

5.1.1.2 Fitting of the experimental slope distributions

The D function, which represents the microfacet repartition of the surface, was defined in Eq. (5.2). In order to give a physical meaning to the microfacet model, the actual slope distribution of the surfaces (which were evaluated in Sec. 3.3), must be fitted as well as possible by D, using α_g as a free parameter.
As this microfacet model only accounts for isotropic surfaces, the study is only carried out on the following samples: the metallic samples blasted with beads of different sizes and particles of different shapes, and the frosted glass samples.
The fits were performed by the least square method, using a curve fitting function of Python (scipy.optimize.curvefit [122]). For some experimental slope distributions, the fit is satisfactory, as presented in Fig. 5.3(a). Indeed, the experimental slope distribution of the metallic surface blasted with medium beads, can be fairly represented by the D function, with $\alpha_g = 0.212$. On the other hand, the fits can be less consistent, considering other surfaces, as presented in Figs. 5.3(b) and (c). In Fig. 5.3(b), the fit is less accurate, especially in the tails of the distribution. In Fig. 5.3(c), the actual slope distribution of the sample is bimodal and cannot be consistently fitted by the function D, whatever the parameter α_g chosen.

The best α_g parameters were evaluated for each experimental slope distribution, and are presented in Table 5.1. A degree of fit quality is also mentioned (arbitrary chosen), in order to assess the consistency of the fit. Indeed, if the fit is not accurate, one cannot expect to achieve a modeled BRDF which is representative of the surface morphology. As an example, the Figs. 5.3(a), (b) and (c) were respectively classed in "good", "medium" and "bad" quality of fit.

5.1.1.3 Comparison with optical measurements

The best analytic function form of D was evaluated for each surface according to its actual slope distribution (numerical values of α_g are recalled in Table 5.1). The mask-

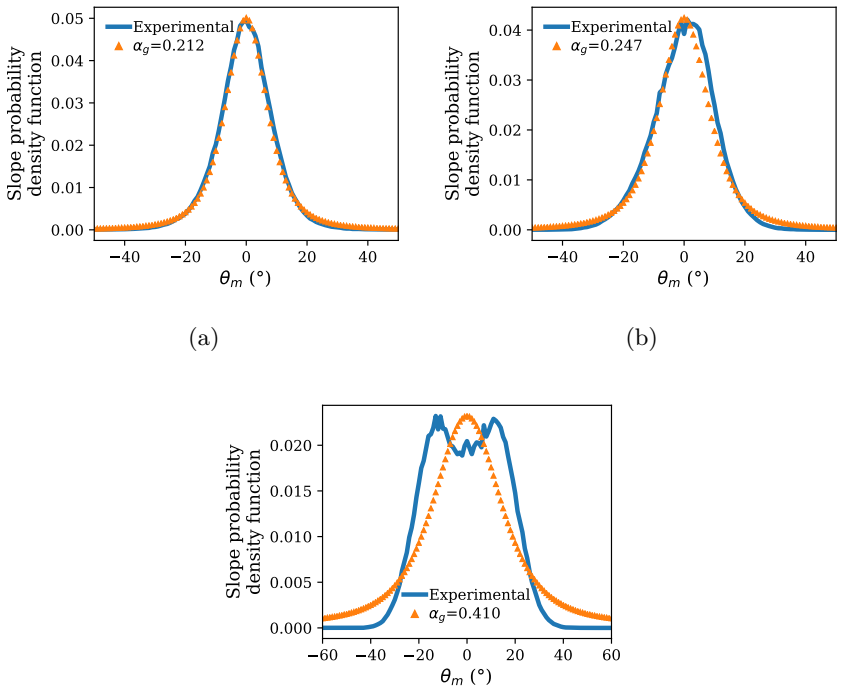

Fig. 5.3 *The experimental slope distributions of the samples are fitted by the function D, using α_g as parameter. (a) The fit of slope pdf of the metallic sample blasted with medium beads is consistent with $\alpha_g = 0.21$. (b) The fit of slope pdf of the metallic sample blasted with small beads is less accurate ($\alpha_g = 0.24$). (c) The fit of the slope pdf of the glass sample G5 is not consistent at all ($\alpha_g = 0.41$).*

ing/shadowing function G also depends on the parameter α_g, and should therefore be related to the surface topography.
The function F is related to the index of refraction of the material. In the case of the aluminum samples, it is quite difficult to know it. Indeed, the composition of the aluminum alloy used is not perfectly known, and, moreover, the aluminum could have been oxidized in the open air. Consequently, one should expect variations between the actual refractive index of the material and the refractive index of pure aluminum. On the other hand, since glass is a chemically inert material, we are quite confident about the value of its refractive index.
One can now evaluate the modeled BRDF defined in Eq. (5.1). For each sample, the experimental optical data will be compared to the results given by the microfacet model. The optical curves given by the model depend on the two parameters α_g and η: roughly speaking, α_g controls the width of the angular spread and η impacts its amplitude.
The blasted metallic samples and the frosted glass samples are examined independently.

Blasted metallic surfaces

The optical properties of the blasted metallic surfaces (presented in Sec. 4.4.1) are compared to the results of the microfacet model, using the GGX method. The results of all

the metallic samples are examined in the same way. The results of the sample blasted with small beads, presented in Fig. 5.4(a), are taken as an example.
The experimental ccBRDF of the sample (blue line) is compared to several results of the GGX model:

- Step 1: First, the experimental parameters are used as input for the model: α_g (which was deduced from the actual slope distribution of the sample) and the refractive index of the sample. These first modeled results are marked by the dashed orange line. For the aluminum samples, the refractive index is complex, and we then consider its real (n) and imaginary (k) parts: with data from [123], at $\lambda = 500\ nm$, $\eta = 6.84$ ($n = 0.80$ and $k = 6.04$). The numerical values of α_g and η can be found in Table 5.2(a), column S1.
- Step 2: Then, if the results of the model are not consistent, a second iteration of modeling is performed. As the chosen value of η may not be accurate, it is considered as a free parameter of the model, and it can therefore be modified to obtain the best fit of the optical measurements (doted green line). The fitted numerical value of η can be found in Table 5.2(a), column S2. From these modeling results, one can examine if the discrepancies between the experimental measurements and the results of the model are only related to the relative amplitudes of the curves.
- Step 3: Finally, if the results are still inconsistent, a last modeling is realized, where α_g and η are both considered as free parameters (red dot dashed line). This step aims to find the set of parameters that provides a prediction of optical properties which matches as close as possible the optical measurements. In this way, we are able to assess it the fitted α_g and η, given in Table 5.2(a), column S3, are plausible or not.

The results of the analysis of the three aluminum samples blasted with three different sizes of beads are presented in Fig. 5.4, and in Table. 5.2. Experimental values of η and α_g provide results of ccBRDF about two times higher compared to the experimental ccBRDF. The decrease of the refractive index allows to adjust the amplitude of the curve: this adjustment appears consistent, as the aluminum alloy of our sample should be less reflective than pure aluminum. However, the shape of the ccBRDF is too narrow, and consequently, α_g needs to be increased. Nevertheless, as the increase of α_g implies a diminution of the reflected light in the specular lobe, η must finally be increased.

Even if α_g and η are not constrained during fitting, there are still discrepancies: the model forecasts a ccBRDF too high for grazing angles and too low in the vicinity of the specular direction (Figs. 5.4(a) and (b)). The drop of the ccBRDF for grazing angles should be managed by the masking-shadowing factor, which is maybe not adapted to the actual topography of the surfaces. Moreover, there seems to be no logical relation between the fitted η and α_g values for the three samples: the best fitted values of η are different for the three samples, and there is no relation between the α_g of step 1 and the α_g of step 3. It is therefore difficult to think that these samples can be modeled by the GGX method of the microfacet approach.

The aluminum samples blasted with particles of different shapes were also examined and the results are presented in Fig. 5.5, and in Table 5.3.
For all samples, the amplitude of ccBRDF modeled with experimental values of η and α_g

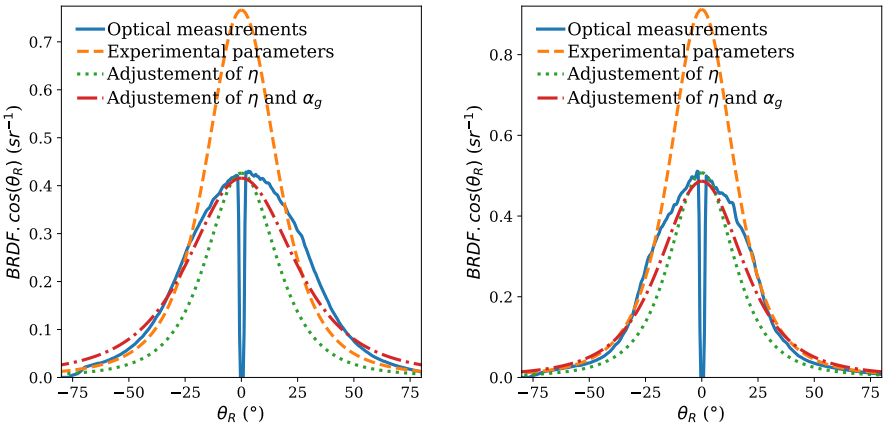

Fig. 5.4 *The optical measurements at normal incidence using the Xenon lamp (blue line) are compared to several iterations of the GGX model. First, experimental parameters which described the actual surface properties are used as input parameters of the model (orange dashed line). Then, only η is changed (dotted green line). Finally, the optical measurements are fitted as well as possible by changing both η and α_g (red dot dashed line). The parameters used for each iteration are summarized in Table 5.2. Here, (a) and (b) respectively present the results for the samples blasted with small and large beads.*

is noticeably higher than measured, except in the case of the sample blasted with beads (Fig. 5.5(a)). Then three different cases occur:

- The sample blasted with beads, Fig. 5.5(a), presents similar properties than previous samples (Figs. 5.4(a) and (b)). However, in this case, both η and α_g must be increased from step 1 to step 3, and finally, there are still discrepancies between the measured and modeled ccBRDF. In this case, we note that α_g was slightly increased, despite the fact that the fit of its slope distribution was categorized as "bad" (see Table 5.1(b)). On the other hand, the index of refraction was increased up to 25.
- The samples blasted with rough beads and grains, in Figs. 5.5(b) and (d), present quite similar results. For the two samples, from step 1 to step 3, η was decreased and α_g was increased. However, in this case, this is α_g that has been drastically modified (despite the medium and good quality of the fit of their slope distributions). Finally, there are still discrepancies between the model and the experimental data: the diffuse properties of the samples are not reproduced.
- The sample blasted with a mix of beads and grains, in Fig. 5.5(c), present a better agreement between the measurements and the model. Indeed, only η must be changed in order to obtain proper modeled results. However, from Fig. 5.5(c) and Table 5.3(c), one can see that several sets of parameters can lead to proper agreement between experimental and modeled results. This could indicate that this good result could only be due to a good set of parameters among others, and that they are not necessarily representative of the surface itself. The Fig. 5.6 presents the results of the model at 45° of incidence, using the parameters fitted at normal inci-

	S1	S2	S3
η	6.84	3.5	9
α_g	0.24	0.24	0.35

(a) Small Beads

	S1	S2	S3
η	6.84	2.8	6
α_g	0.21	0.21	0.32

(b) Medium Beads

	S1	S2	S3
η	6.84	3.5	6
α_g	0.22	0.22	0.28

(c) Large Beads

Table 5.2: The parameters used during the three steps of the model are summarized in (a), (b) and (c) for the sample blasted with respectively small, medium and large beads. The column S1 corresponds to experimental parameters (actual η and α_g). During the second iteration of modeling, η of the model is adjusted and is given in column S2. During the final step of modeling, both η and α_g are adjusted to obtain the best fit and are given in column S3.

	S1	S2	S3
η	6.84	12	25
α_g	0.39	0.39	0.42

(a) Beads

	S1	S2	S3
η	6.84	1.4	2.8
α_g	0.15	0.15	0.45

(b) Rough Beads

	S1	S2	S3
η	6.84	3.75	4.3
α_g	0.28	0.28	0.31

(c) Beads & Grains

	S1	S2	S3
η	6.84	1.9	4.8
α_g	0.24	0.24	0.50

(d) Grains

Table 5.3: The numerical values of α_g and η are presented in the same way as in Table 5.2, for the samples blasted with (a) beads, (b) rough beads, (c) a mix of beads and grains and (d) grains.

dence which are presented in the column S3 of the Table 5.1(c). If the two ccBRDF are similar in the vicinity of the specular direction, this is not the case for grazing θ_R angles. However, one could assume that the signal in this angular region could be related to multiple scattering effects, and can therefore not be described by the model: the results are then quite promising.

These results on the blasted metallic surfaces seem to suggest that their optical properties cannot be described by the GGX approach based on microfacet theory. Indeed, we fail to reproduce the optical properties of the surfaces by using parameters describing the actual morphology of the samples. Moreover, even if the parameters are left free, and consequently become unrealistic, it is difficult to obtain satisfactory results. However, since the GGX model was not created to predict the optical properties of metallic surfaces, other models might be more appropriate.

Frosted glass surfaces

The optical properties of the frosted glass surfaces, presented in Sec. 4.4.2, are compared to the results of the microfacet model, using the GGX method. All the frosted glass samples are examined in the same way.

First, the experimental measurements are compared to the model using the experimental parameters α_g (see Table 5.1) and the refractive index of the glass: $\eta = 1.5$. Unlike in the case of the metallic samples, the refractive index of the glass is a sure parameter.

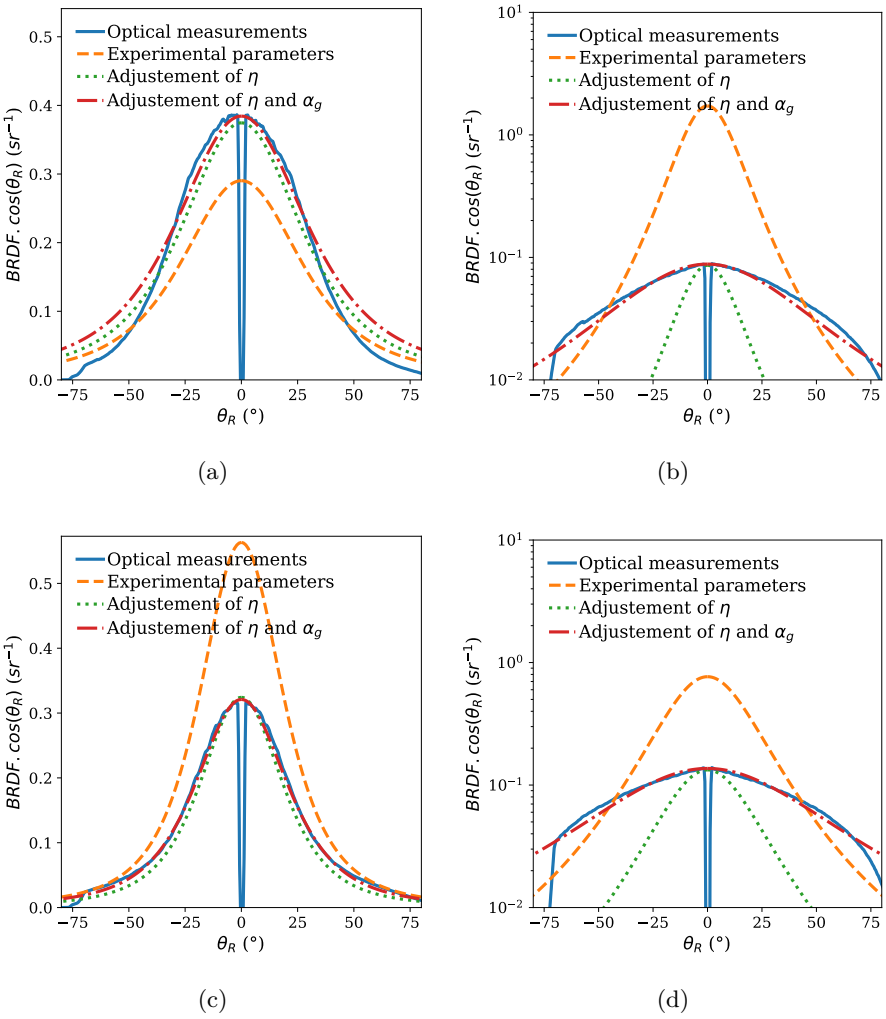

Fig. 5.5 *The results at normal incidence of optical measurements and microfacet model are presented in the same as in Fig. 5.4, for the samples blasted with (a) beads, (b) rough beads, (c) a mix of beads and grains and (d) grains. The numerical values of α_g and η are presented in Table 5.3. In (b) and (d) the ccBRDF is plotted within a logarithmic scale to enhance visibility.*

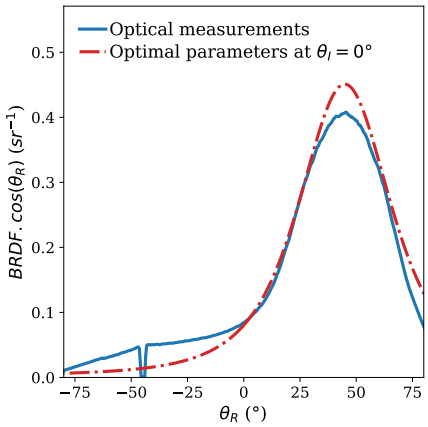

Fig. 5.6 *The experimental ccBRDF at 45° of incidence is compared to the results of the GGX model at 45° of incidence, with the parameters α_g and η fitted at normal incidence: $\alpha_g = 0.31$ and $\eta = 4.3$.*

Consequently, if the results modeled with experimental parameters are not consistent, the first parameter that is adjusted is α_g. Finally, both α_g and η are adjusted to obtain the best fit of the experimental measurements. As the GGX model was created to describe the light scattering properties of rough glasses [22], we expect to obtain better results than in the case of metallic surfaces.

The results are presented in Fig. 5.7, and the numerical values of α_g and η in Table 5.4. For the sake of visibility, the results of ccBRDF in Figs.5.7(a) and (b) are presented within a log scale.
Even if they are not perfect, the results of the model used with experimental parameters are more satisfactory than in the case of the aluminum samples. Moreover, for all samples, if η and α_g are adjusted, proper fit of the optical measurements can be obtained. One must therefore mention that the thin peak of the sample G3, Fig. 5.7(c), cannot be reproduced by the model.
Looking at the numerical values of η and α_g in Table 5.4, one can observe that the evolution of the parameters from step 1 to step 3, is different than those of metallic samples (Tables 5.2 and 5.3). Indeed α_g must always be decreased to obtain the appropriate fit, whereas it was systematically increased for the metallic samples. This observation tends to suggest that the issue is related to the model and not to the estimation of the experimental slope distribution. Indeed, if the problem was related to the evaluation of the experimental slope distribution, the modification of α_g would be similar in both cases.

The results obtained with the GGX model do not allow to relate the morphological and the optical properties of our samples. Indeed, to reproduce the experimental results, at least one of the parameters must be modified. When the two parameters are let free, the optical properties of the samples can be fairly well reproduced. Thus, the GGX model can be used to reproduce the optical properties of the frosted glass, but once again, not to forecast them from their morphological properties. This could suggest that similar models, with different expressions of the D and G functions could lead to consistent results.

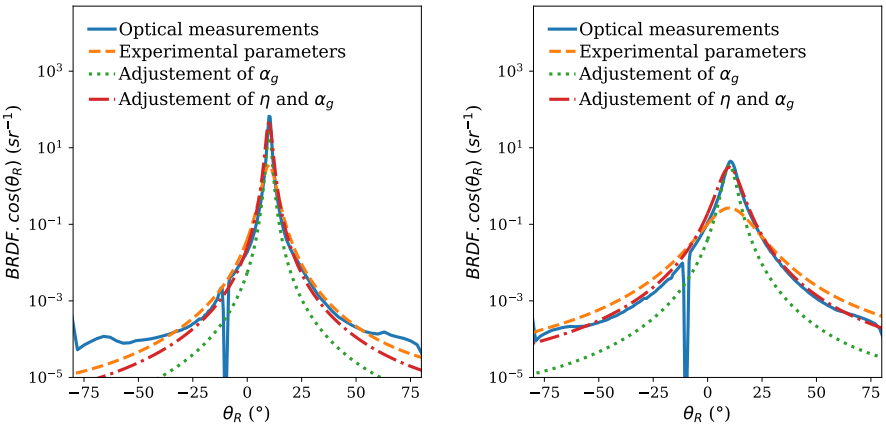

(a) (b)

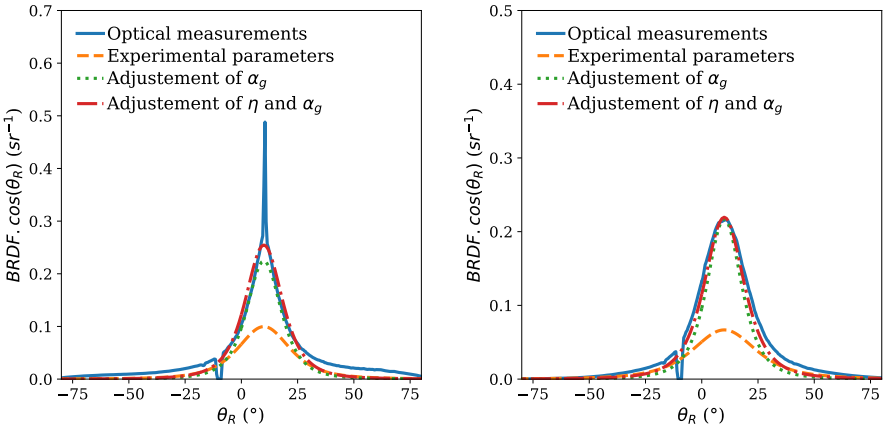

(c) (d)

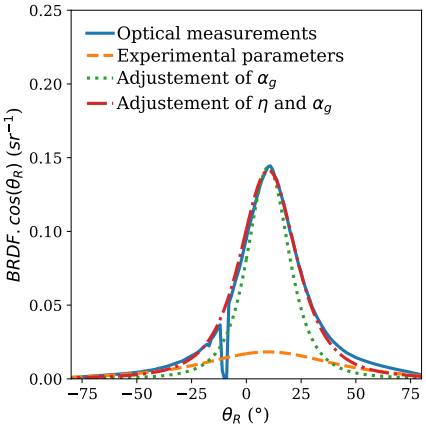

(e)

Fig. 5.7 *The optical measurements with $\theta_I = 10°$ using the Xenon lamp (blue line) are compared to several iterations of the model: first the physical parameters of the surface (orange dashed line). Then only α_g is changed (dotted green line). Finally, the optical measurements are fitted as well as possible by changing both η and α_g (red dot dashed line). The parameters used in each iteration are summarized in Table 5.4. (a)-(e) respectively present the results of the glass samples G1, G2, G3, G4 and G5.*

	S1	S2	S3
η	1.5	1.5	2
α_g	0.03	0.01	0.013

(a) G1

	S1	S2	S3
η	1.5	1.5	1.9
α_g	0.11	0.03	0.05

(b) G2

	S1	S2	S3
η	1.5	1.5	1.6
α_g	0.18	0.12	0.13

(c) G3

	S1	S2	S3
η	1.5	1.5	1.6
α_g	0.22	0.12	0.14

(d) G4

	S1	S2	S3
η	1.5	1.5	1.72
α_g	0.42	0.15	0.20

(e) G5

Table 5.4: The parameters used during the three steps of the model are summarized in (a), (b), (c), (d) and (e) for the frosted glass samples G1, G2, G3, G4 and G5. During the first modeling inputs parameters corresponds to experimental parameters (actual η and α_g), column S1. For the second modeling, column S2, only α_g is adjusted. Finally, for the last modeling, both η and α_g are adjusted to obtain the best fit, column S3.

5.1.1.4 Conclusion

In the current section, the microfacet theory was described. This approach, based on GO, aims to describe the light scattering properties of a surface by representing the scattered intensity as a product of three functions. Two of these functions, D and G, represent the topography of the surface, and the third one, F, is related to the nature of the substrate material.
Usually, the models based on the microfacet theory, do not take into account the actual topography of the sample, and thus each of them is limited to a narrow class of surfaces. The forms of the analytic slope distributions and masking/shadowing functions of the GGX model (a model created to forecast the optical properties of rough glass surface) were described in this section. These analytic expressions were fitted to reproduce as well as possible the actual slope distributions of the samples. This approach aims to assess if these kinds of microfacet models can relate morphological and optical properties of rough surfaces.
For all samples (blasted metallic surfaces and frosted glass samples), we were not able to reproduce the optical properties of the samples using the experimental parameters (actual refractive index and better fit of the slope distribution). In the case of the metallic samples, the optical properties cannot be reproduced, excepted in the case of one sample, even if the parameters of the model are let free (and thus become non-representative of the sample). However, as expected from the purpose of the GGX model (which is to deal with diffusive glass surfaces), the results are more promising for the frosted glass samples: indeed the optical properties can be reproduced with free parameters.
It is very likely that the GGX model is not the best suitable for our samples. In order to overcome the limit of the microfacet models (concerning the description of the surface morphology), the next section is dedicated to the study of the optical properties of the samples, provided by a ray tracing software.

5.1.2 Ray tracing simulations

The ray tracing is a rendering technique based on GO, widely used in computer graphics. The technique can produce a very high degree of realism but can be rather time and memory consuming. It consists of launching a huge number of rays of light through a scene. The path of each ray is followed and its interactions with the objects are simulated according to the laws of GO. There are two main ways to perform the simulations:

- Forward or light-based ray-tracing: the ray follows the natural path of light. It travels from the source, to the object and finally to the camera. This technique is highly accurate and can provide a high level of realism. Indeed, it can deal with multiple scattering and shadowing/masking effects. However, this is an inefficient method: many of the launched rays will never reach the camera (meaning that many rays that are examined do not contribute to the final image).
- Backward or eye-based ray-tracing, which has been created to be more efficient. In this method, a ray is launched in the 3D scene from each pixel of the camera. The first object that is hit by a ray is then related to a particular pixel. New rays are then emitted from the impacted object in the direction of each source of the scene. In this way, all the computed rays contribute to the final image. On the other hand, all rays that could have impacted the object from an indirect path are neglected.

Thus the forward ray tracing simulations allow to forecast the light scattering properties of an object, considering its actual topography. In this way, we will be able to assess the ability of the geometric optics law to reproduce the optical properties of our samples. If the simulations are conclusive, then we can conclude that the microfacet model used in the previous section is not adapted to our samples (but perhaps other models of microfacet might be effective). On the other hand, if the simulations are not conclusive, it would indicate either that the optical properties of our samples cannot be described by the laws of the geometrical optics, or that the morphological data used to describe the surface are not sufficiently sampled.

5.1.2.1 Ray tracing software

Lighttools is the ray tracing software that was used for the study. This commercial software allows to realize forward and backward ray-tracing simulations. In our case, the simulations were realized in the forward mode.
The 2D cartographies (realized by chromatic confocal profilometry) of the samples were used to shape the studied surfaces. For each sample, a $1 \times 1 mm^2$ or a $0.5 \times 0.5 mm^2$ surface was used. The morphological cartographies were down-sampled in order to be used in the software: the $1 \times 1 mm^2$ surfaces were defined by 200×200 points (5 μm per point), and the $0.5 \times 0.5 mm^2$ surfaces were sampled by 150×150 points (3.3 μm per point).
In the case of the metallic samples, the reflectance of the modeled material (without roughness) is fixed to the reflectance of the unblasted metallic surface (R=63%), which is the only reference we have. In the case of the frosted glass samples, the reflectance and the transmittance of the modeled glass are respectively fixed to R=4% and T=96%.
The light source is designed to have 1.5° of divergence, with a broad band spectrum (200 nm of FWHM centered at 550 nm) similar to the Xenon lamp of the OMS4 (see

Fig. **??**). The modeled surfaces are illuminated at normal incidence for the metallic samples and the frosted glass samples. The scattered light is collected by a far-field object, which is placed all around the sample, and can therefore collect all the scattered light.

5.1.2.2 Comparison with optical measurements

The results of the numerical simulations realized on Lighttools are compared to the experimental optical measurements of the samples. The optical properties in reflection of the blasted metallic samples and the frosted glass surfaces are examined independently.

Metallic blasted surfaces

The three samples blasted with beads of different diameters (Fig. 5.8) and the four samples blasted with particles of different shapes (Fig. 5.9) are examined. As it is difficult to compare the amplitude of the modeled and experimental ccBRDF, we choose to present normalized ccBRDF results. The results of the simulations in Figs. 5.8 and 5.9 are quite noisy. Indeed, due to the lack of time, only one simulation was realized per sample: we assumed that the fluctuations of the curves should be smoothed when the simulations are repeated on several cartographies. Moreover, a drop of the signal at $\theta_R = 0°$ can be observed, and as not be explained yet.
The consistency of the comparison between experimental and simulated data are not equivalent for all samples. In the case of the samples blasted with different bead sizes, there is a good agreement between the experimental and simulated ccBRDF. Indeed, despite the noise in the numerical data, the global shape of the experimental and simulated ccBRDF are rather similar. On the other hand, in the case of the samples blasted with particles of different shapes, the simulated results are not always consistent with the experimental results. Indeed, in the case of the sample blasted with beads (Fig. 5.9(a)), there is a good agreement between simulated and experimental results. When the sample is blasted with a mix of beads and grains (Fig. 5.9(c)), the global shape of the ccBRDF is reproduced by the simulation, except for grazing θ_R angles. This could suggest that this diffuse optical property, induced by the grains, cannot be reproduced by the simulation, due to the small typical size of the produced roughness or due to the down-sampling of the morphological data. These assumptions tend to be confirmed by the results of Figs. 5.8(b) and (d). Indeed, when the surfaces are blasted with rough beads or grains, the simulations are inconsistent: the diffuse properties of the surfaces are once again not reproduced.

These results suggest that the light scattering of part of the blasted metallic samples could be modeled by the GO law. Indeed, when the morphology of the sample is rather large and simple (in the case of sample blasted with beads), the GO law is enough to describe the light scattering phenomena. On the other hand, when the surfaces are blasted with particles which induce a smaller topography (rough beads or grains), the GO law is not sufficient.

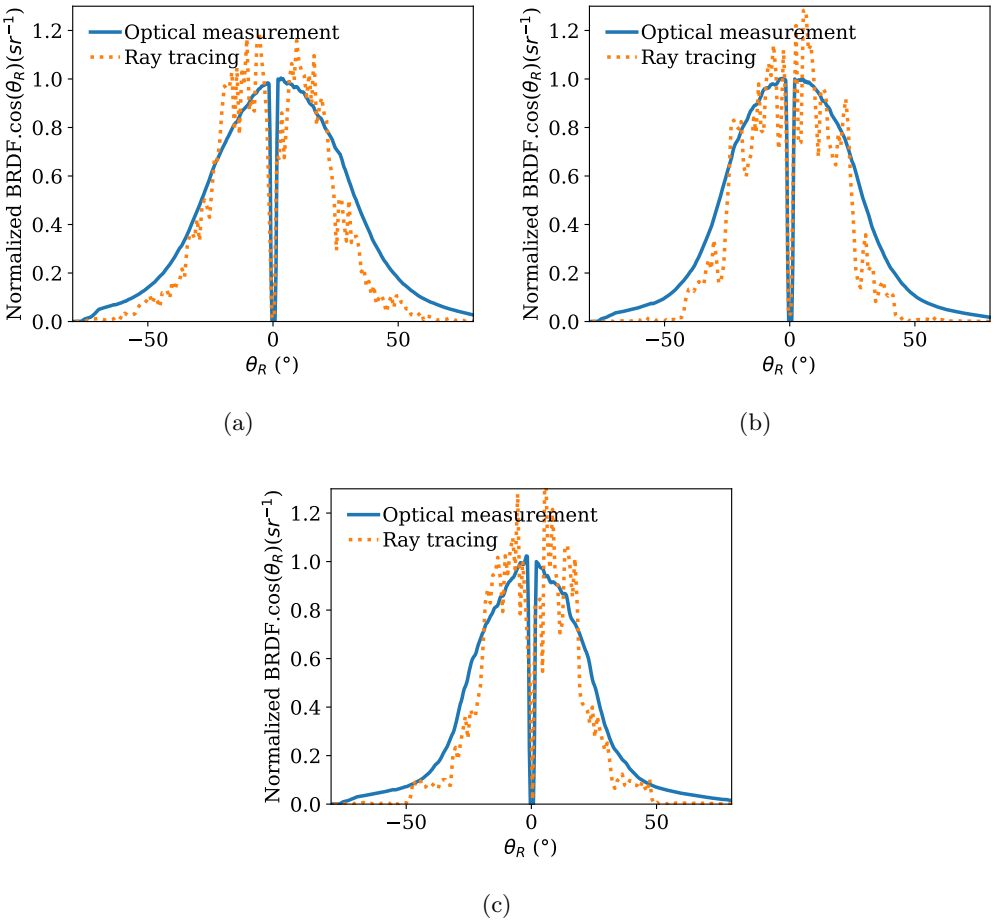

Fig. 5.8 *The optical measurements (in reflection) realized at $\theta_I = 0°$ using the Xenon lamp (blue line) are compared to the ray-tracing simulations (orange dotted line) realized as described in Sec. 5.1.2.1. (a), (b) and (c) respectively present the aluminum samples blasted with small, medium and large beads.*

Frosted glass surfaces

The results of the ray tracing simulations are presented in Fig. 5.10. The consistency of the results depend of the samples. The light scattering properties of the samples G1, G3 and G5 are well reproduced by the ray tracing simulations (despite the noisy data). However, the good results of the sample G3 must be carefully considered, indeed, the thin peak measured in the specular direction (see Fig. 4.23) is not measured at normal incidence (due to the OMS4 configuration (see Fig. 4.7), and consequently does not appear in Fig. 5.10(c). There are discrepancies in the cases of the samples G2 and G4. The width of the simulated normalized ccBRDF of the sample G2 is larger than the experimental data. Due to the actual thin roughness of the G2 sample, we could assume that this difference could be due to down-sampling of the data. In the case of the sample G4, the shape of the simulated ccBRDF has two local maximums (in the vicinity of the specular direction), which is not consistent with the experimental measurements. Despite this,

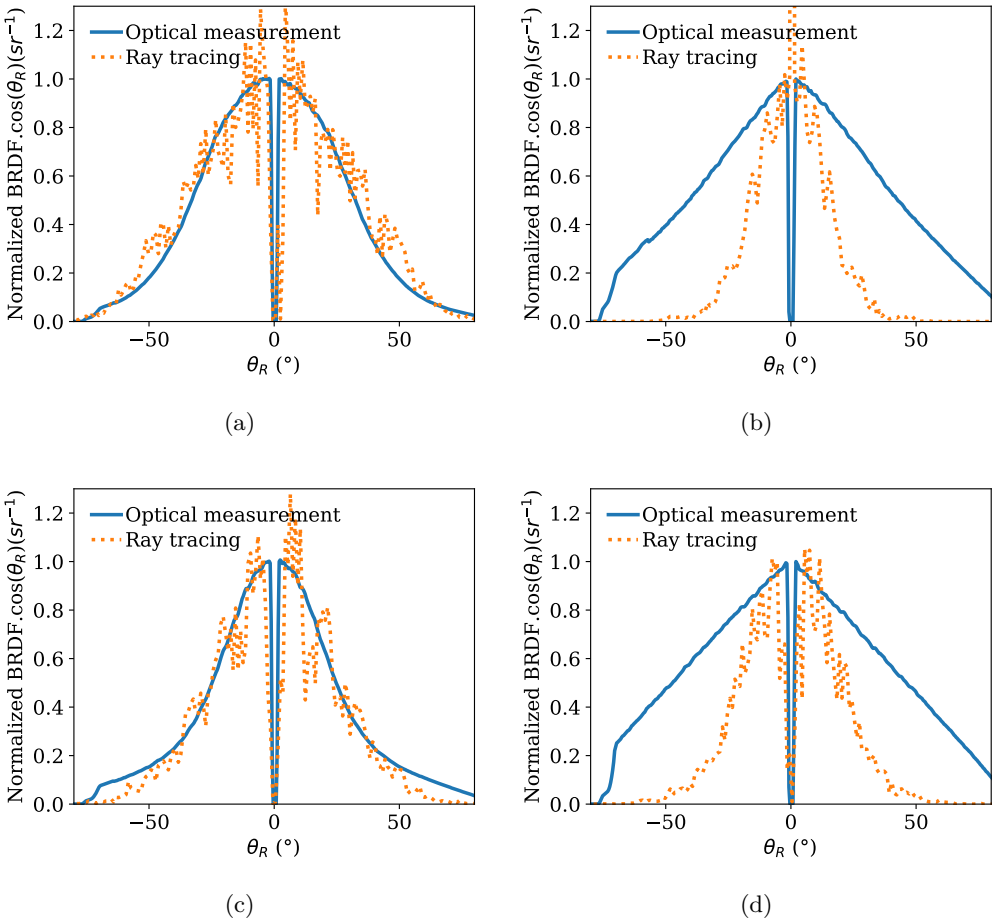

Fig. 5.9 *The results are presented in the same way as in Fig. 5.8. Here, (a), (b), (c) and (d) respectively present the aluminum samples blasted with beads, rough beads, a mix of beads and grains and grains.*

the width of the experimental and modeled ccBRDF are in good agreement. Additional simulations should be carried out to confirm or invalidate these results.

5.1.3 Conclusion

The optical properties (in reflection) of several rough surfaces were compared to models based on the geometrical optics law: a model based on the microfacet theory, and ray tracing simulations.

The model based on microfacet theory does not allow us to relate the morphology of the sample (represented by its slope distribution) and its optical properties. Moreover, even when the parameters of the model are free, we were able to reproduce the optical properties of the frosted glass surfaces, but not the one of the metallic samples. This shows that the morphological description of a microfacet model is highly specific to a type of morphology.

Then, some initial ray-tracing simulations were launched in order to overcome the slope

distribution description of the microfacet model. The results show inconsistent results in the case of rather small and complex roughness (as the metallic samples blasted with rough beads or with grains). It tends to suggest that the limit of the geometrical optics laws are reached and that consequently we need other methods to relate the morphological and optical properties of our samples.
Therefore, the next section will be dedicated to the modeling of the light scattering properties of rough surfaces by an approach based on the physical optics laws.

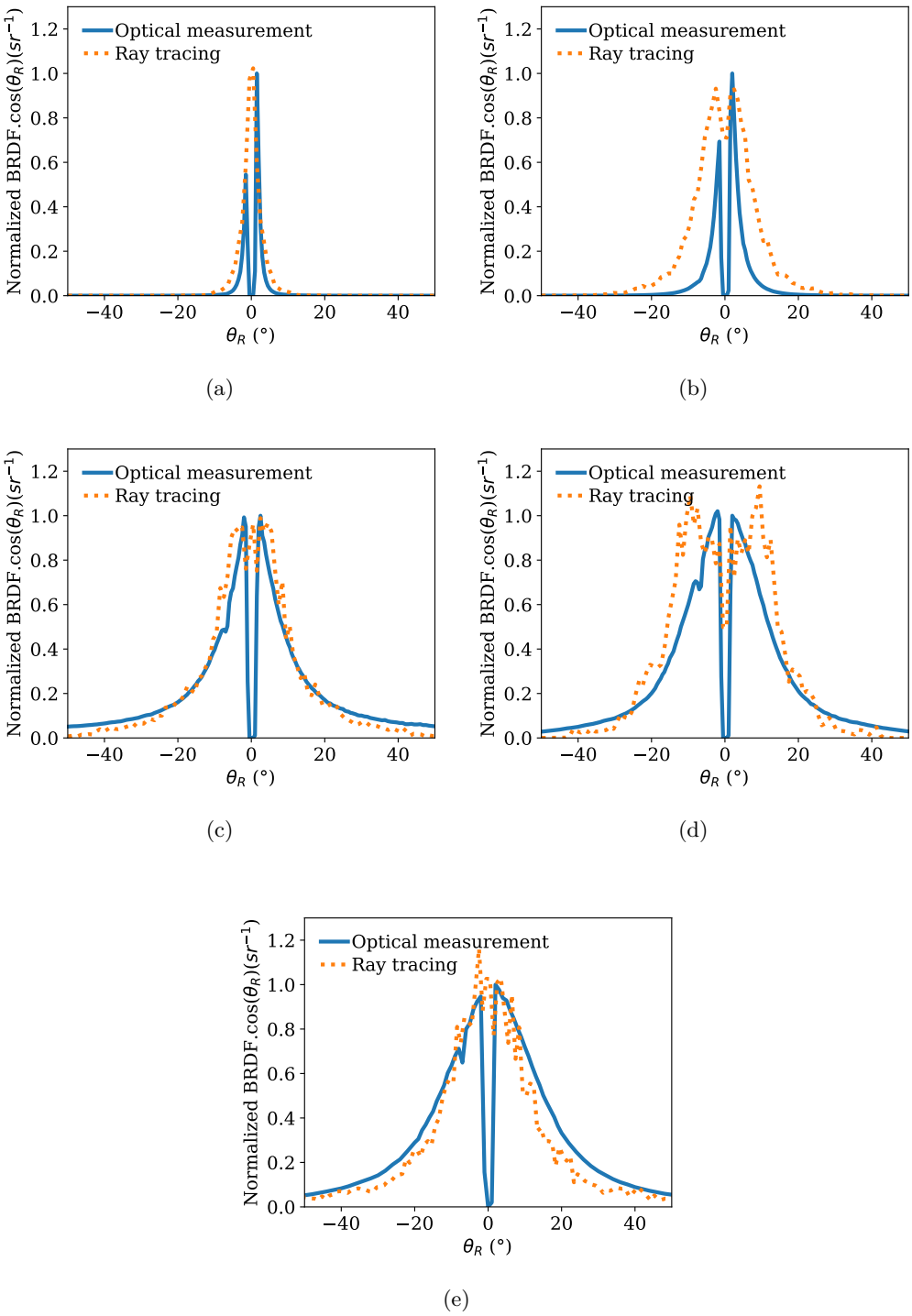

Fig. 5.10 *The results are presented in the same way as in Fig. 5.8. Here (a), (b), (c), (d) and (e) respectively present the results of the frosted glass samples G1, G2, G3, G4 and G5.*

5.2 Physical Optics

The physical optics, also referred to as waves optics, is the domain of optics that considers the light as an electromagnetic wave. In this way, physical phenomena such as interference, diffraction or polarization, which are beyond the limits of the law of geometrical optics, can be studied. The physical optics community aims to understand the physical phenomena induced by the light scattering effect at an examined interface. The considered interface is usually described by a set of statistical parameters and functions, as the one described in Sec. 3.2, such as the rms or the power spectrum density function.

The light scattering phenomena can be examined using rigorous calculations, which will provide exact solutions ; or calculations based on approximations of different nature. According to the assumptions made to simplify the description of the interface and of the incident light, the calculations can stand from several seconds on a standard laptop to several months on a supercomputer. The rigorous calculations thus cannot be done easily, especially on highly rough surfaces, which requires longer calculations. The difficulty is therefore to determine in which cases the simplifying hypotheses are accurate and can therefore be applied.
Historically, two approximate methods have been developed to model the light scattering properties of surfaces: the Small Perturbation Method (SPM) which accounts for slightly rough surfaces, and the Kirchhoff Approximation (KA), which accounts for the surfaces described by small slopes [11]. Since numerous approximate light scattering theories related to SPM or KA have been developed in order to extend their limits. In 2004, Elfouhaily and Guérin published a review of these approximate light scattering models [28]. The authors conclude saying that *"There is still room for improvement in the development of approximate scattering methods"*. Usually, the assumptions of the models rely on the material nature (dielectric, metallic, perfect conductor,...), the degree of roughness of the interface or the ability to deal with 2D surfaces[28]. As the limit of the assumptions are not always well-defined, such models are usually confronted to rigorous calculations [124][125] and in some rare cases to experimental optical characterizations [37][38].

This section aims to compare the optical characterization of the samples to the results of a model based on the Kirchhoff approximation, which was developed during the FRAXOS project. First, the Kirchhoff approximation and the bases of the used model will be described. Finally, the results of the model will be compared to experimental data, and analyzed.

5.2.1 The Kirchhoff approximation

The Kirchhoff approximation (KA) is one of the oldest and most employed approximate method used to describe the scattering from rough surfaces [11]. It is also known as the "tangent plane theory". Indeed, in this model, the field on the surface is assimilated to the field that would be produced by the plane tangent to this same point [28]. Thus it only depends on the Fresnel reflection coefficient at the local incident angle, between the incident light and the interface. The validity of this approximation is thus highly related to the radius of curvature of the surface topography or to the local slope. Indeed, this

approximation is accurate when the radius of curvature is large compared to the incident wavelength, but it breaks down if the roughness includes sharp points or sharp slopes. The KA is a single-scattering approximation: indeed, as it is limited to surfaces with gentle curvatures, it is therefore not suited for surfaces giving rise to shadowing or multiple scattering effects. Hence these two latter effects are favored by grazing angles of incidence and scattering, the KA approximation is known to be limited in such cases.

5.2.2 Description of the used model

The model used during this study was developed and implemented on Python, by Pr. Ingve Simonsen, in the context of the FRAXOS project. The bases of the model and its main assumptions are described in this section. Details about the calculations, which are not given here, can be found in [126].

The main assumptions of the model, which originate from the development of the model are the following:

- the scattered light is a scalar wave scattered from an impenetrable surface. Hence the reflectance of the surface is 1. This assumption is usually referred to as *scalar wave assumption*. This assumption also implies that the polarization state of the light is neglected.
- The boundary conditions of the rough surface, are either of the Dirichlet or Neumann type. However within the KA, the scattered field takes the same form for both of these boundary conditions [126].
- The statistical properties of the height distribution of the surface are assumed to be Gaussian-like, see Eq. (5.9).

Lets first recall and define the conventions that are considered in this work. Figure 5.11, recalls the coordinate system and the polar and azimuth angles of incidence and reflection. The incident and reflected wavevectors are respectively denoted $\mathbf{k}$ and $\mathbf{q}$, and their projections on the plane $z = 0$ are respectively noted $\mathbf{k}_{||}$ and $\mathbf{q}_{||}$. These latter quantities are defined in terms of the angles of incidence (θ_I,ϕ_I) and the angles of reflection (θ_R,ϕ_R) (see Fig. 5.11) as:

$$\mathbf{k}_{||} = \frac{\omega}{c} \sin\theta_I \left(\cos(\phi_I - \pi), \sin(\phi_I - \pi), 0\right), \tag{5.7}$$

$$\mathbf{q}_{||} = \frac{\omega}{c} \sin\theta_R \left(\cos\phi_R, \sin\phi_R, 0\right). \tag{5.8}$$

In Eqs. (5.7) and (5.8), ω and c respectively denote the angular frequency of the incident light and the speed of light in vacuum, so that $\omega/c = 2\pi/\lambda$.

The randomly rough surface $h(\mathbf{r}_{||})$ is assumed to constitute a zero-mean Gaussian random process so that the pdf of the heights is:

$$p(h) = \frac{1}{\sigma\sqrt{2\pi}} \exp\left(-\frac{h^2}{2\sigma^2}\right), \tag{5.9}$$

where σ is the rms roughness. Furthermore, the surface profile function $z = h(\mathbf{r}_{||})$ is defined by:

$$\langle h(\mathbf{r}_{||})\rangle = 0, \tag{5.10}$$

$$\langle h(\mathbf{r}_{||})h(\mathbf{r'}_{||})\rangle = \sigma^2 C(\mathbf{r}_{||} - \mathbf{r'}_{||}),, \tag{5.11}$$

$$\tag{5.12}$$

where $C(\mathbf{r}_{||} - \mathbf{r'}_{||})$ denotes the normalized height autocorrelation function of the profile, $\mathbf{r}_{||} = (x, y, 0)$ is the position vector in the plane $z = 0$, $\mathbf{r'}_{||}$ is another position vector, the $\langle\cdot\rangle$ operator denotes the average over an ensemble of surface realizations.

According to [126], the cosine corrected BRDF, (or mean differential reflection coefficient), which was defined in Sec. 4.1.2, can within the KA be written in the form:

$$f_R \cos\theta_R = \frac{\omega/c}{\alpha_0(k_{||})} \frac{\left[(\omega/c)^2 + \alpha_0(q_{||})\alpha_0(k_{||}) - \mathbf{q}_{||}\cdot\mathbf{k}_{||}\right]^2}{\left[\alpha_0(q_{||}) + \alpha_0(k_{||})\right]^2} L(\mathbf{q}_{||}|\mathbf{k}_{||}), \tag{5.13}$$

$$L(\mathbf{q}_{||}|\mathbf{k}_{||}) = \frac{1}{(2\pi)^2 S}\int d^2 r_{||}\int d^2 r'_{||}\exp\left(-i(\mathbf{q}_{||} - \mathbf{k}_{||})\cdot(\mathbf{r}_{||} - \mathbf{r'}_{||})\right) \times \left\langle \exp\left(-i\left(\alpha_0(q_{||}) + \alpha_0(k_{||})\right)\left(h(\mathbf{r}_{||}) - h(\mathbf{r'}_{||})\right)\right)\right\rangle \tag{5.14}$$

for both Dirichlet and Neumann boundary conditions, where S is the surface of the rough surface, $\alpha_0(k_{||})$ and $\alpha_0(q_{||})$ are defined as:

$$\alpha_0(k_{||}) = \frac{\omega}{c}\cos\theta_I, \tag{5.15}$$

$$\alpha_0(q_{||}) = \frac{\omega}{c}\cos\theta_R. \tag{5.16}$$

The aim of the calculation is to evaluate the quantity given by $\langle ...\rangle$ in Eq. (5.14). After mathematical evaluation, the term $L(\mathbf{q}_{||}|\mathbf{k}_{||})$ from Eq. (5.14), can be written as:

$$L(\mathbf{q}_{||}|\mathbf{k}_{||}) = \frac{1}{(2\pi)^2}\int d^2 u_{||}\exp\left(-i(\mathbf{q}_{||} - \mathbf{k}_{||})\cdot(\mathbf{u}_{||})\right) \times \exp\left[-\sigma^2\left(\alpha_0(q_{||}) + \alpha_0(k_{||})\right)^2\left(1 - C(\mathbf{u}_{||})\right)\right], \tag{5.17}$$

where $\mathbf{u}_{||} = \mathbf{r}_{||} - \mathbf{r'}_{||}$. The Eqs. (5.13) and (5.17) are valid for both anisotropic and isotropic autocorrelation functions, however, only the isotropic case is implemented yet.

5.2.3 Comparison with optical measurements

The model based on the Kirchhoff approximation that was used during this study has several input parameters: the rms of the height distribution (rms roughness), the analytic form of the autocorrelation function, and the wavelength of the incident light. As presented in the Tables 3.19 and 3.20, the experimental height autocorrelation functions

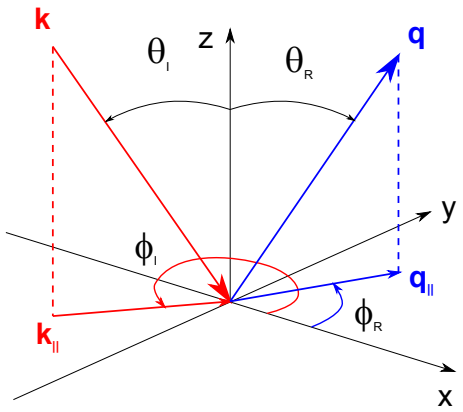

Fig. 5.11 *Schematics of the coordinates system that is considered in this work, adapted from [126]*

were fitted by analytic functions (see Table 3.20) and a length parameter, which was denoted a (see Table 3.19). The length parameter a is actually different from the correlation length, l_c. Indeed, l_c was defined as the length delay at which the experimental normalized autocorrelation function drop to 1/e (see Sec. 3.2.2.1), on the other hand, a is related to the analytic form of each experimental normalized autocorrelation function. All simulations are realized using an incident wavelength of 520 nm. However, the impact of the wavelength (considering visible light) is rather small, due to the high degree of roughness of the samples.

As described in Sec. 5.2.2, the model is built on a non-penetrable media assumption: it implies that all the incident light is reflected, and that consequently, the reflectance of the surface is 1. This is, of course, not the case of the studied samples. This assumption will therefore limit the accuracy of the results, regarding the intensity of the reflected light. To correct the results of the model, these latter will be normalized by the actual reflectance of the examined surface. Therefore, instead of presenting the modeled $f_r \cos\theta_R$ (ccBRDF), we will present $f_r \cos\theta_R R$, since we know a priori that the ccBRDF will have too high amplitude. Moreover, due to the non-penetrable media assumption, only the light scattering properties of opaque surfaces can be modeled. Consequently, only the metallic surfaces, blasted with different bead sizes and with particles of different shapes are modeled.
The modelings are realized in the same way for all samples. First, the light reflected properties are modeled using the experimental data: namely the rms roughness, the height normalized autocorrelation function (analytic expression and the length parameter a, which were presented in Tables 3.19 and 3.20), and the reflectance. Then these three parameters are adjusted in order to fit as well as possible the experimental ccBRDF realized at normal incidence. The results are also presented at $\theta_I = 45°$ of incidence, but the parameters of the model remain the same as for the normal incidence. In this way, we will be able to assess if the discrepancies between the experimental and modeled ccBRDF can be attributed to uncertainties of the morphological characterization or not.

5.2.3.1 Variation of the beads size

The comparison between experimental and modeled angular distribution of light of the samples blasted with three different sizes of beads are presented in Fig. 5.12 and Table 5.5. For the three samples, there are discrepancies despite the normalization of the modeled results. Indeed, compared to the experimental curve (solid line), the modeled curve (dashed line) is higher in the vicinity of the specular direction, and lower for large scattering angles. However, due to the reflectance normalization, if the two curves are integrated over the whole half space, they do have the same level of reflectance. This implies that if the full ccBRDF is considered (and not only the plane of incidence), the small difference of intensities for large scattering angles (which cover a large angular region) balance the high difference of intensities in the vicinity of the specular direction (which describes a smaller angular region). This discrepancy increases with the angle of incidence, which is consistent with the increase of the experimental curve for large scattering angles.

The next step is then to adjust the three parameters, as slightly as possible, in order to assess if the optical properties of the samples can be modeled by the KA. The adjusted parameters are presented in Table 5.5. In the three cases, a small adjustment of the three parameters (R, a and σ) is realized. In the three cases, the rms is increased (up to 9%), the parameter a is decreased (up to 11%), and the reflectance is decreased (up to 7%). Finally, the results of the model with adjusted parameters (dotted line) are in good accordance with the experimental data, for the both presented incident angles examined (one recalls that the three parameters are only fitted at normal incidence, and remain the same for the modeling at $\theta_I = 45°$). However, at $\theta_I = 45°$, the signal at large scattered angles is still not well reproduced, which is consistent with the multiple scattering effect, which is neglected by KA. Moreover, in the case of Fig. 5.12(a), one can observe a manifestation of a limit of the KA: indeed, by definition, the ccBRDF equals 0 at $\theta_R = 90°$, and it is actually not the case here.

Finally, these results show a good accordance between the morphological and optical properties of the three samples. They also stress the importance of performing accurate and representative morphological characterizations. Indeed, small variations (up to 400 nm for the rms, and up to 4 μm for the parameter a) can lead to quite different modeled properties. The origins of these discrepancies will be discussed at the end of the section.

5.2.3.2 Variation of the particle shape

The comparison between experimental and modeled results for the samples blasted with particles of different shapes are presented in Fig. 5.13 and Table 5.6.
The accordance between experimental and modeled results are rather different for the four samples. Three different cases can be described:

- in the case of the sample blasted with beads, Fig. 5.13(a), the experimental results are very well reproduced by the experimental parameters at normal incidence. One can slightly increase the parameter a, in order to narrow the curve around the specular direction. Moreover, the results are also very well reproduced at high

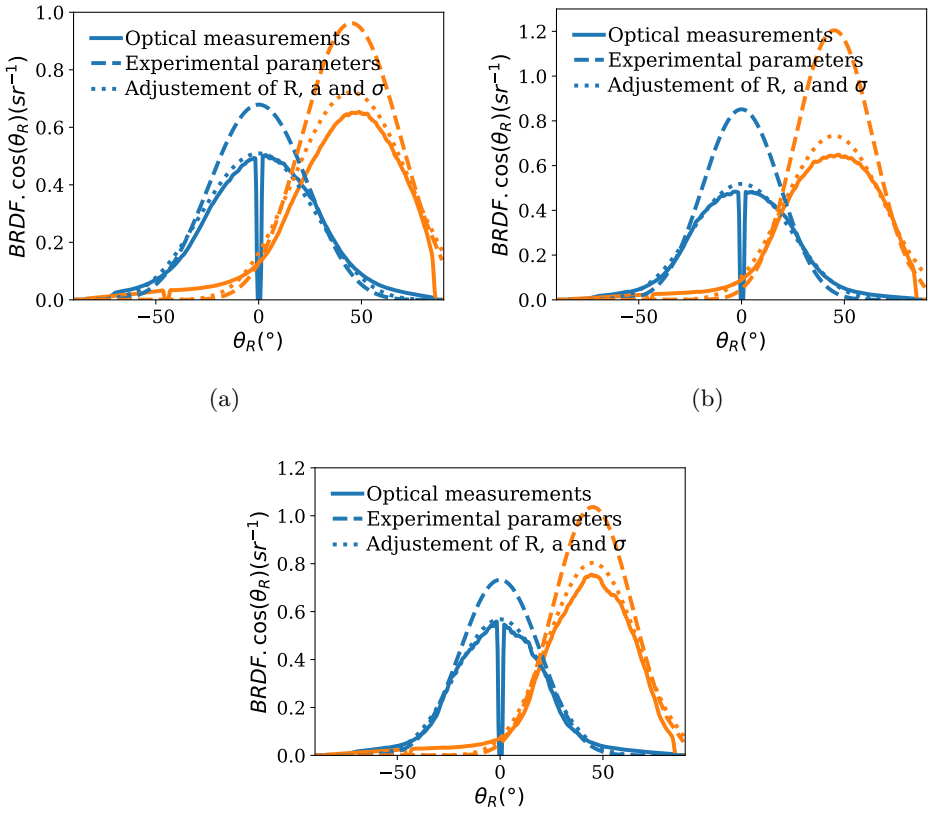

Fig. 5.12 *The optical measurements realized at $\theta_I = 0°$ and at $\theta_I = 45°$ and using the Xenon lamp (full line) are compared to several iterations of the model: first with the physical parameters of the surface (dashed line). Then the parameters are adjusted to fit the experimental ccBRDF at normal incidence (dotted line). The parameters used in each iteration are summarized in Table 5.5. Here, (a), (b) and (c) respectively present the results for the samples blasted with small, medium and large beads. The wavelength of the incident light in the model is 520 nm.*

incidence angle.

- In the case of the sample blasted with a mix of beads and grains, Fig. 5.13(c), there are high discrepancies at high scattered angles, and the effect increases with high incidence angle. Even if the parameters are adjusted, the model cannot reproduce the experimental data. This tends to suggest that the limit of the model is reached, mainly due to multiple scattering effect (which increase the signal at high scattered angles).
- In the cases of the samples blasted with rough beads and with grains, Figs. 5.13(b) and (d), it is difficult to model the light scattering properties. Using the experimental parameters, the shape of the modeled ccBRDF is far too narrow. At normal incidence, the experimental curve can be approximately reproduced by decreasing the parameter a. However, the results are not consistent when the incidence angle is increased to $\theta_I = 45°$, which is probably due to the enhancement of the multiple

	S1	S2
rms (μm)	1.18	1.23
a (μm)	9.7	8.9
R(%)	63	61

(a) Small Beads

	S1	S2
rms (μm)	2.55	2.80
a (μm)	30.6	27.10
R(%)	53	49

(b) Medium Beads

	S1	S2
rms (μm)	5.2	5.6
a (μm)	60.9	59.1
R(%)	47	45

(c) Large Beads

Table 5.5: The parameters used for the two steps of the model are summarized in (a), (b) and (c) for the sample blasted with respectively small, medium and large beads. The Step 1 corresponds to physical parameters. During Step 2, the parameters are adjusted to fit as well as possible the experimental ccBRDF at normal incidence.

scattering effect. Moreover, in Fig. 5.13(d), the modeled ccBRDF curve does not reach 0 at $\theta_R = 90°$, which stresses the limit of the model.

	S1	S2
rms (μm)	1.40	1.40
a (μm)	11.0	11.5
R(%)	63	63

(a) Beads

	S1	S2
rms (μm)	1.10	1.30
a (μm)	8.8	5.9
R(%)	21	21

(b) Rough beads

	S1	S2
rms (μm)	1.04	1.04
a (μm)	8.0	6.8
R(%)	43	43

(c) Beads & Grains

	S1	S2
rms (μm)	1.10	1.20
a (μm)	5.9	5.3
R(%)	37	37

(d) Grains

Table 5.6: The numerical values used to model the samples blasted with (a) beads, (b) rough beads, (a mix of beads and grains, and (d) grains are presented, in the same way as in Table. 5.5.

5.2.3.3 Origins of the discrepancies between experiment and model

The examination of the modeled and experimental optical results of the metallic blasted samples stresses discrepancies (see Secs. 5.2.3.1 and 5.2.3.2), which could have several origins and depend on the examined samples.

The KA is a small slope approximation and is therefore valid for surfaces with gentle curvatures One can quickly evaluate the typical slope of these surfaces, considering the ratio σ/a: small ratios denote small slopes and on the contrary, high ratios denote steep slopes. The results of this quick estimation are presented in Table 5.7: it allows to distinguish the surfaces for which the KA model was coherent or not. Indeed, from Secs. 5.2.3.1 and 5.2.3.2, we saw that the results were much more consistent for the samples blasted with spherical beads (denoted Small beads, Medium beads, Large beads and Beads in Table 5.7), and these samples are described by the smallest slopes.

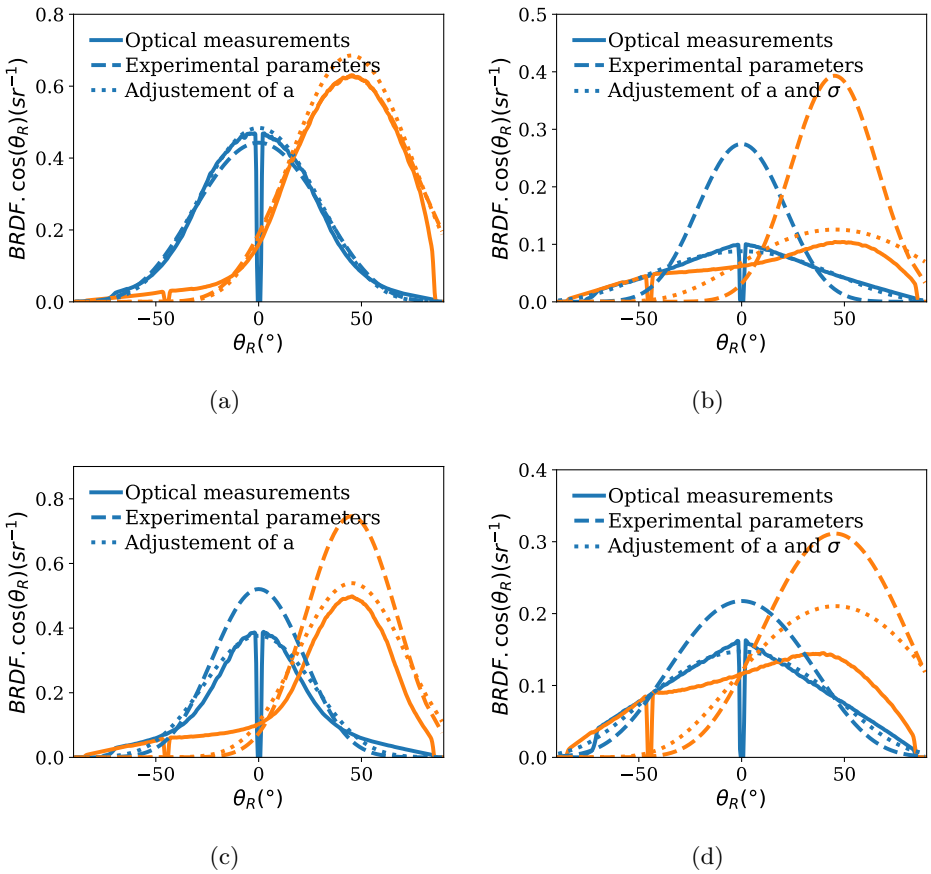

Fig. 5.13 *The results of the experimental and modeled data of the metallic surfaces blasted with (a) beads, (b) rough beads, (c) a mix of beads and grains, and (d) grains at $\theta_I = 0°$ and $\theta_I = 45°$ are presented, in the same way that in Fig. 5.12.*

Consequently, we suggest that for the samples blasted with spherical beads, the KA is valid. Thereby, the discrepancies between experimental results and modeling performed with the morphological parameters could originate from the morphological characterization. Indeed, the adjustment of the parameters, which were presented in Tables 5.5 and Table 5.6(a), are rather consistent with this assumption:

- when the rms roughness is adjusted, it is systematically increased. This is rather consistent with the limit of the experimental setups, which cannot measure all the small height variations: it therefore leads to an underestimation of the rms value.
- The parameter a (which can be considered as a kind of correlation length), can be rather decreased or increased between the two iterations of modeling. However, we demonstrate the numerical study in Sec. 3.2.4 that this parameter was highly sensitive to the experimental parameters and difficult to evaluate.
- The fitting of the shape of the experimental autocorrelation function is also difficult to evaluate. As shown in the numerical study in Sec. 3.2.4, the experimental ACFs present fluctuations on their tails. However, these fluctuations were not taking into

Sample	σ/a
Small beads	0.12
Medium beads	0.09
Large beads	0.09
Beads	0.12
Rough beads	0.15
Beads and Grains	0.17
Grains	0.20

Table 5.7: For each surface, the ratio σ/a is evaluated from the data of the Tables 5.5 and 5.6. The ratio can estimate the typical slope of the surface, using the a and σ parameters which were used in the model: smaller the ratio is, smaller the slope is.

account on the analytic fits, but they could have an impact on the light scattering properties of the surface.

The discrepancies of the model could also originate from the assumption of a Gaussian random process, which is actually not valid for all samples (see Sec. 3.4.1).

In the case of the three other samples, which were blasted with rough beads, with a mix of beads and grains, and with grains, the results of the model were quite inconsistent. Indeed, even if the parameters σ and a were adjusted at normal incidence, the results modeled at high incidence were inconsistent with the experimental data. In this case, we assume that the discrepancies between experimental and modeled data could originate from the small slope approximation of the model.

5.2.4 Conclusion

The model based on Kirchhoff approximation, governed by the physical optics approach, is a rather simple and quick model compared to others physical optics models. However, it allows to link the morphological properties of the studied samples to their light scattering properties. Even if the results are not perfect, mainly due to the scalar wave assumption, the optical properties of the majority of the samples were reproduced. This is a very promising result which confirms that the morphological characterizations of the samples are worth in order to be able to use physical optical models to realize predictive simulations. However, it also stresses that the light scattering properties of the samples are very sensitive to the morphology, and that consequently the morphological characterization must be realized very carefully.

However, for some samples, there are discrepancies when the incident angle θ_I is increased to 45°. This effect could be due to the limitations of the Kirchhoff approximation regarding grazing angles of incidence and detection (and consequently neglecting multiple scattering effect), and to a too high slope degree of the samples. The prospects of this work would be to set up a similar code, but dropping the scalar wave assumption and taking into account the material refractive index.

5.3 Conclusion

The optical properties of a part of the rough surfaces were confronted with the results of several light scattering models, based on both Geometrical Optics and Physical Optics approaches.

First, models based on the Geometrical Optics approach were examined: an analytic microfacet model, and ray-tracing simulations. The description of the surface morphology using the GGX microfacet model is rather approximative. Indeed, the slope distribution of the modeled surface must be of a particular analytic form, which is not always representative of the actual slope distribution of the surface. Consequently, the real morphology of the surface is neglected, and the results are not consistent. Moreover, even when the actual slope distribution of the surface is highly similar to the analytic distribution of the model, the results remain inconsistent. This tends to suggest that this particular microfacet model is not adapted to our sample and that therefore, it will not allow us to relate morphological and optical properties.
Then, some initial ray-tracing simulations were launched, using the actual morphology of the surface: experimental mappings of the sample (obtained by confocal profilometry) were used as input parameters in the ray-tracing software. The results are rather different for all samples, and need to be repeated to be conclusive. However, first results show inconsistent results for the samples blasted with particles of complex shapes. This inconsistency could originate from the limitation of the law of Geometrical Optics, or from a poor statistical description of the samples in this case.

Finally, a model based on the Physical Optics was tested. In this case, the statistical properties of the samples, deduced from experimental measurements were used as input for the model (rms and autocorrelation function). The model is dedicated to the study of surfaces described by small slope, and it is mainly limited by two assumptions: scalar wave approximation and an impenetrable interface.
Depending on the samples, the results of the model were rather consistent. For four of the samples (the four samples blasted with spherical beads), the results were quite consistent for both studied incident angles. However, to achieve this agreement between experimental and modeled results, we need to slightly modify the parameters and function used to describe the topography of the samples (up to 10% in the worst case for the rms and the correlation length). This adjustment of the parameter really stresses the need of consistent and a representative description of the sample topography.
On the other hand, the model failed to predict the light scattering properties of the samples blasted with particles of more complex shape. Even if the roughness parameters and functions are freely adjusted, there is no consistency. This tends to suggest that the limits of the models are reached: due to too high slopes, or to the neglect of multiple scattering effect.

Chapter 6

Summary and conclusions

"Things don't always go as planned. That's the beauty of science."
Nikola Tesla, The Prestige (2006)

Contents

This chapter aims to summarize the main results obtained in this thesis and to present the conclusions that can be drawn from them.

6.1 Summary

The main objectives of the thesis work were to examine the morphological and optical properties of a large number of rough surfaces. Our goals were:

- to grasp the variety of angular distributions of light scattered from real-world rough surfaces,
- to assess which experimental data could be used in order to validate light scattering models of different kinds, and especially those based on the geometrical and physical optics approaches,
- finally, to create a framework for validation of predictive optical models.

To this end, two classes of surfaces were considered: home-made model surfaces with controlled but not fully random topography and real-life randomly rough surfaces, manufactured by different industrial processes.

6.1.1 Model surfaces

The model surfaces were manufactured in the laboratory, using two experimental techniques well mastered at SVI: the photolithography and nano-imprint processes, which were presented in Sec. 2.1.1. These two experimental techniques allow for the control of the morphology of the surfaces, and the choice of the material they are made of.

Sets of 1D and 2D model surfaces were fabricated and slight modifications of their morphology were realized. The cross-section of the 1D surfaces were progressively smoothed, by thermal relaxation process. Thereby, the slopes of the surfaces were altered from 80° to 10° (see Sec. 3.3.1).

In the case of the 2D surfaces, which consist of an arrangement of cylindrical micropillars on a glass substrate, two sets of surfaces were manufactured. In the first set, the pillars were periodically arranged over the surface of the substrate. In the second set, on the other hand, the pillars were randomly dispersed over the surface of the substrate (see Sec. 2.1.3), but in such a way that the surface covering ratio was the same between the two sets. In this way, we obtained surfaces with similar rms roughness, but with highly different spatial correlations (see Sec. 3.3.2).

The optical properties of the 1D and 2D model surfaces were also examined. In the case of 1D surfaces, experimental measurements realized with the OMS4 goniospectrophotometer showed that the light scattering properties of the surfaces are highly impacted by the slope of the surfaces. A linear relation was found between the slope value of the surface, and the actual number of effective diffractive orders of the transmitted light (see Sec. 4.3.1).

In the case of the 2D periodic surfaces, we found that their light scattering properties were at least composed of a combination of different optical effects: light diffraction from the pillar grating; scattering and diffraction from individual pillars; and finally the scattering inside the glass substrate. These results will be submitted in a scientific journal before the PhD defense, and have already been preprinted [113].

6.1.2 Randomly rough surfaces

We now turn to the industrial randomly rough surfaces. Thanks to our collaboration with J. Cabrero from Zirpro, we were fortunate to have access to a series of two-dimensional, metallic randomly rough surfaces. These surfaces were manufactured by a controlled industrial process consisting of beads blasting of aluminum plates. By changing the blasting conditions, like type of beads being used, and the blasting time, different surface morphologies were obtained. For these kinds of surfaces, our morphology characterization allowed us to identify a strong link between the manufacturing process and the morphological properties of the samples.

In particular, we studied a set of three such rough metal surfaces obtained by varying the diameter of the beads used in the blasting process. We found that the height rms and the correlation lengths of the surfaces obtained in this way increased *linearly* with the size of the beads as presented in Fig. 6.1. This finding is consistent with their actual slope distributions being rather similar (see Fig. 3.48). Moreover, when the diameter of the beads increases, the surface height pdf becomes less and less Gaussian-like. This effect

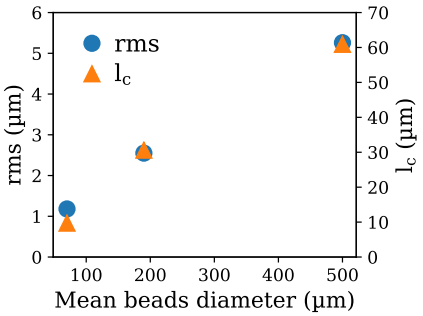

Fig. 6.1 *The rms and the correlation length of the surfaces increase linearly with the diameters of the beads used to blast the samples.*

is suspected of being related to the formation of impact craters when the beads hit the surface. This hypothesis was confirmed by a simple erosion model that was developed during the study, and that confirmed the increase of the skewness and kurtosis values of the surfaces with increasing diameter of the beads.

The spatial correlation of the surfaces were also examined and it can also be directly related to the diameters of the beads. First, looking at the PSD curves, one can relate the inverse of the dominant frequency to the actual diameter of beads (see Fig. 3.42(a)). Then, when the ACF of the surfaces were examined, one could identify an anticorrelation (see Fig. 3.42(b)); this latter feature can be related to the actual size of the craters that the surface is composed of. These results will be submitted in a scientific journal before the PhD defense.

The optical properties of the three samples display rather similar optical properties. However, it should be mentioned that one can notice difference between the FWHM and the maximum level of their ccBRDF curves. Looking carefully at the numerical values (see Table 3.19 and Table 4.12), one cannot establish a strong relationship between the morphological and optical indicators. However, the slope distributions of the three samples are rather similar, as for their ccBRDF curves, which tends to suggest that for this scale of morphology, the slope could be an interesting parameter.

A second set of blasted metal samples were produced with the intention of following the evolution of the blasting process. Hence, four samples were produced by terminating the blasted process of the untreated metal surface at different times (with all the remaining blasting parameters being the unchanged). Consequently the number of visible impacts increases with the time of blasting. We showed the evolution of the height pdf of a blasted sample in Fig. 3.50. The height pdf of the untreated sample is rather Gaussian-like. However, at the beginning of the blasting, the height pdf is highly deformed and is far from a Gaussian-like pdf. Finally, at the end of the process, the height pdf of the sample gets back to a Gaussian-like distribution (see Table 3.13). The evolution of the blasting process can also be followed by examining the PSD of the samples, as presented in Fig. 3.52. Indeed, as the covering of impacts increases on the surface, the PSD increases for the frequency related to the diameter of the beads used during the blasting.

The actual slope distributions of the samples do not look very different from each other, and do not show strong anisotropy. This anisotropy can be observed by examining

both the ACF and the PSD functions, as presented in Fig. 3.51, but due to the lack of time, we do not develop indicators to quantify it. However, the optical properties are strongly anisotropic, as presented in Fig. 4.20. Consequently, we were not able to relate optical and morphological properties for this series of samples.

A third and final set of metal samples were produced by blasted the untreated metal surface for a fixed time with particles of similar sizes (30-60 μm), but with four different shapes: beads, rough beads, a mix of beads and grains, and grains (so four samples in total). We find that the actual morphology of the particle used in the blasting process have a strong impact on the morphology of the resulting surfaces, and the main morphological differences are found at smaller scales. Thus, these differences can be mainly evaluated from the high frequency region of the PSD function of the surface morphology maps obtained by AFM. In this way, it appears that the actual size of the particle only weakly impacts the low frequency region of the PSD, and that the morphology of the particle impacts mainly its high frequency band (see Fig. 3.56).

The four samples blasted with particles of different shapes present a wide range of optical properties. The two samples, blasted with rough beads and with grains, are highly diffusive surfaces, with a FWHM of ccBRDF up to 80°, and the two samples blasted with beads and with a mix of beads and grains are diffusive surface (FWHM of ccBRDF up to 50°), as presented in Table. 4.12. These optical properties cannot be related to any of the morphological parameters that we have assessed. However, confronting both the PSD functions of the surfaces and their optical properties, one could suggest that a non negligeable component in the high frequency range of the PSD function leads to a wider scattering angular distribution. Thereby, the effect of the nanometer scale roughness on the light scattering properties is rather important.

We did also consider *dielectric* (in contrast to metallic) industrial, two-dimensional, randomly rough surfaces. This set of samples consisted of five frosted glass samples. They present a high variety of morphological and optical properties: going from specular properties to diffusive ones. The morphological and optical properties cannot be straightforwardly related. Indeed, for three of the samples, the slope distribution and the light scattering distribution are quite in good accordance, however, for the two remaining samples, the relation is not that simple.

6.1.3 Light scattering modeling

Numerous models for treating the scattering of light from rough surfaces do exist. In this thesis we have mainly been concerned with some models based on geometrical optics and on physical optics (see Chap. 5). We will now discuss them in turn.

Two methods, based on the law of geometrical optics, were tested during this work: an analytic model based on the microfacet theory and numerical simulations based on ray tracing technique.

The microfacet theory assumes that the light scattering from rough surfaces can be modeled as a combination of three functions: the slope distribution, the masking/shadowing function and a Fresnel function (see Sec. 5.1.1 for further details). The model used was

implemented from [22], and is referred to as GGX. Usually the slope distributions of such microfacet models are not related to the actual morphology of the samples. In our case, the input functions of the model were chosen to be as close as possible to the actual morphology and properties of our samples. The reflection of part of the blasted metallic surfaces and of the five frosted glass samples were modeled. For all samples, we were not able to reproduce the light scattering properties of the samples, using their actual properties (the slope distribution and actual refractive index of the material), as presented in Sec. 5.1.1.3. For some samples, if the slope distribution and the refractive index of the material are not constrained anymore (and consequently are not realistic anymore), the actual light scattering properties of the surfaces can be reproduced by the GGX model. However, for the majority of the samples, even with free inputs functions, the light scattering properties cannot be reproduced.

However such microfacet models rely on numerous assumptions related to the morphology of the samples. In order to overcome these limitations and to test if the light scattering properties of our samples could be modeled by the law of geometrical optics, we realized first attempts of simulations based on ray-tracing, presented in Sec. 5.1.2. Such simulations allow to consider the actual morphology of the sample, and to consider multiple scattering effects, however, only few simulations were performed. Results are promising for some samples, but we saw that in the case of the metallic samples blasted with rough beads and with grains, the results were highly inconsistent, as presented in Sec. 5.1.2.2. This tends to suggest that the light scattering properties of the samples cannot be described by the law of geometrical optics.

A model based on the law of physical optics was also tested during this study. The analytic model, based on the Kirchhoff approximation (see Sec. 5.2.1), was developed in the context of the FRAXOS project. The model also made the strong assumption of a scalar wave impacting an impenetrable material, which involved that polarization effects are neglected and that all the incident light is reflected.

For the majority of the samples, the model leads to consistent results using the actual morphology of the samples. Slight adjustments of the rms and correlation length values (up to 10%) are realized in order to obtain the best light scattering results. In this case, the light scattering properties are consistent for both normal and large incidence angles. However, in the case of the samples blasted with rough beads and with grains, the results are rather inconsistent. In these latter cases, we assume that the small slope approximation of the Kirchhoff theory is not valid anymore, and that consequently the light scattering properties of the surfaces cannot be reproduced using this approach.

6.2 Conclusions

Several conclusions can be drawn from the work reported in this thesis. The main conclusion is that the light scattering from the blasted metallic surfaces that we consider can fairly well be approximated using a model based on the physical optics approach, but the microfacet model is not capable of giving an adequate description of the same scattering data. Indeed, the comparison between experimental data and the modeled results are much more consistent in the case of the physical optics based model, than what it is

when using a model based on geometrical approach. This result tends to suggest that the optical response of the blasted metal samples should be based on a physical optics approach and not on a geometrical optics approach like the microfacet model; at least, this is the case for the set of blasted samples that we consider.

The second conclusion, which follows from the first, is the importance of the availability of the actual surface morphology or its statistical properties. The surface information is used very differently in the two modeling approaches. This could partly explain why these two models produce different results for the scattered intensity. Indeed, the description of the surface morphology, in the case of the microfacet model is rather approximate, as it weakly describes the spatial correlation of the heights of the examined surface. On the other hand, the relevance of the description of the surface morphology, considering both the height distribution and the spatial correlation function of heights, is strengthened by their consistency with the surface manufacturing parameters (such as the size or the shape of the blasted particles).

The evaluation of the consistency and accuracy of light scattering models require access to reliable and high quality experimental characterizations of both the angular intensity distribution of the scattered light and the surface morphology. However, such measurements are not straightforward to perform, especially if one deals with a large variety of samples, ranging from strongly rough to weakly rough surfaces, or from glossy to matte visual appearances. It is therefore crucial to be aware of the actual limitations of the experimental setups used to perform such measurements that lead to the characterization of both of these types of data, and hence to stay cautious about the experimental results. In this study, we choose to validate the consistency of the experimental results by repeating them on different parts of the sample under investigation, but also by using different experimental setups to assess similar features we obtained. In this way, the experimental data we obtained can be safely considered and the comparison with results of light scattering models can be performed more reliably.

Even if some tendencies and relations between morphological and optical properties of rough surfaces were identified in this thesis, we showed that these two kinds of properties cannot readily be related to each other, and that consequently, light scattering models are required. To achieve this, experimentalists and theoreticians must work together to extend the research effort to better understand the light scattering problem. Hence, ambitious projects, such as the FRAXOS project, are exceptional opportunities to gather scientists from different communities in order to extend the knowledge about the light scattering of light from rough surfaces.

Throughout this thesis we have underlined the drawbacks of existing micro-facet theory models and approaches to data fitting used in computer graphics community. Yet, taking into account the existing infrastructure for the creation of computer-generated images and the needs in terms of calculation speed, it is very difficult to imagine usage of physical optics models to this aim. However, one can imagine to use physical optics models as predictive models suitable for inverse design: once the link between the fabrication parameters and the optical properties of corresponding rough samples is established, as

for example aluminum plates blasted by beads of different size described in this thesis, this link can be exploited to find the morphologies and corresponding fabrication parameters that lead to willed optical properties.

Chapter 7

Directions for further research

"Roads? Where we're going, we don't need roads."
Dr. Emmett Brown, Back to the future (1985)

We have identified five main axes for further research based on the results of this thesis, which could be independently examined.

One of the objectives of this thesis was to develop a framework for the validation of the optical models on light scattering from rough surfaces, and to this end, we have gathered statistically representative proper morphological and optical data for a variety of rough surfaces. **As first axis of further research,** we believe this work should be continued and result in the creation of the database dedicated to validation of predictive models of the optical properties of rough surfaces. This database would contain following information:

- multiscale topography of the surface,
- refractive index of the material,
- BSDF measurements performed for different angular configurations,
- photographs, produced in a calibrated photo booth under controlled illumination.

Such database will be the first of a kind containing both optical and topography data, and will pave a way towards the development of topography-inspired models in both geometrical and physical optics communities.

Which brings us to the **second axis of the further development** of the work of this PhD: roadmap for the choice of models and development of new models. The work to be done in this direction can be summarized in three main questions:

- How to know if for given topography the geometrical optics is capable to produce satisfactory result?
- How to choose among existing models?
- And what improvements to existing models are necessary?

To answer the first question, instead of examining different models based on the law of geometrical optics, one could start with ray tracing simulations and in this way to assess the actual limits of the geometrical optics approach in the case of a chosen rough surface. If the GO approach is sufficient, the choice of an appropriate micro-facet model may be very long since there is still a need for a validation and road-map on existing models in terms of both topography and optical data. Finally, we believe that development of new models on slope distributions and shadowing/masking factors inspired by topography of real-life surfaces have a high potential.

We saw in this thesis that the model based on the physical optics approach related to the Kirchhoff approximation, leads to promising results, despite its strong assumptions (scalar wave impacting an impenetrable media). This model could be improved in two steps: first considering a perfect conductor material, which consists of assuming an incoming electromagnetic wave that is perfectly reflected by the surface. Furthermore, the model could be generalized to take into account the real refractive index of the material. Finally, some of those approximate results, could be compared to the results of rigorous calculations. However, as these rigorous calculations are highly time consuming, especially in the case of rough surfaces, samples should be carefully selected.

The third axis of research that could be explored, would be based on the improvement of both the Kirchhoff light scattering model, and the erosion model (that currently allows us to simulate the impact of spherical beads on a flat surface, as described in Sec. 3.4.1.2). The improvements would consist of:

- considering the index of refraction of the modeled material in the Kirchhoff model,
- developing the erosion model in order to consider: a non flat initial surface, the actual volume that is removed from the impact location, and incident particles of different shapes.

Thereby, the erosion model could be used to simulate the morphology of surface blasted with different types of particles (shape and diameter). Then the rms of the height distribution and the autocorrelation function of the modeled surfaces could be evaluated and finally be used as input in the Kirchhoff model, and one could therefore forecast the light scattering properties of blasted surfaces. This predictive model should, of course, be validated by actual blasted samples, but it could be of significant interest for surface manufacturers.

The fourth axis of further research could be related to a more extended study of the anisotropic surfaces, which would be based on the development of three features:

- the improvements of the erosion model, which were previously described,
- morphological indicators to properly describe and assess the surface anisotropy,
- optical indicators to describe the actual anisotropy of the scattered light and how it is related to the underlying surface.

By improving the erosion model, one could assess the properties of the height distribution of the surfaces blasted for different times (and therefore having different covering ratios of impact). Indeed, as presented in Fig. 3.50, we showed that the height distributions

of samples blasted during different times were rather different, and could be far from a Gaussian-like height distribution.

On the other hand, the development of the morphological and optical indicators of the anisotropic properties of a surface would be beneficial. Indeed, one could assess the threshold of roughness anisotropy that induces anisotropic light scattering properties. As the actual blasted surfaces are made from anisotropic raw aluminum surfaces, such indications could be of significant interest for surface manufacturers.

The fifth and last axis of further research that we suggest would be related to the fabrication of new rough surfaces, using the fabrication techniques which were described in the thesis. At least two interesting approaches could be considered.

The first approach would consist in going from model surfaces to complex ones, as we started to do it in the thesis. Indeed, in Chap. 2, two techniques of surface modification were presented: the thermal relaxation, which allows to progressively smooth a surface, and the change of spatial organization, to go from periodic to random dispersion of objets in the surface. A third technique of surface modification has already been tested at SVI: it consists in adding a nanometer scale roughness on a surface. This can be realized by the dip coating method, which consists in dipping a surface in a solution concentrated in silica nanoparticles. Such experiments were already realized at SVI during the internship of Gaolei Zhan, in 2014, in order to assess the wettability of such structures. Scanning electron microscopy images of the treated surfaces are presented in Fig. 7.1. Combining the three modification techniques, the model surfaces could be slightly modified, up to becoming a complex random surface. One could thereby answer the following questions: what is the impact of the nanometer scale roughness on the light scattering? Is the impact of a random nanometer scale roughness enough to modify or erase the diffractive optical properties induced by a periodic pattern of micrometer scale? What is therefore, the morphological threshold between light diffraction and "simple" light scattering effects?

On the other hand, the second approach would consist of starting with complex industrial surfaces and slightly modify them. First, to overcome the limit of the unknown index of refraction of the aluminum plate, the surfaces could be replicated in other materials by the Nano-imprint technique (see Sec. 2.1.1.2). In this way, one could assess the actual impact of the refractive index on the light scattering, considering the exact same surface morphology. Finally, one could apply the thermal relaxation process on the replicated surfaces. In this way, the high frequency of the surface morphology could be progressively erased, and that would allow us to assess the impact of the nanometer scale roughness on light scattering.

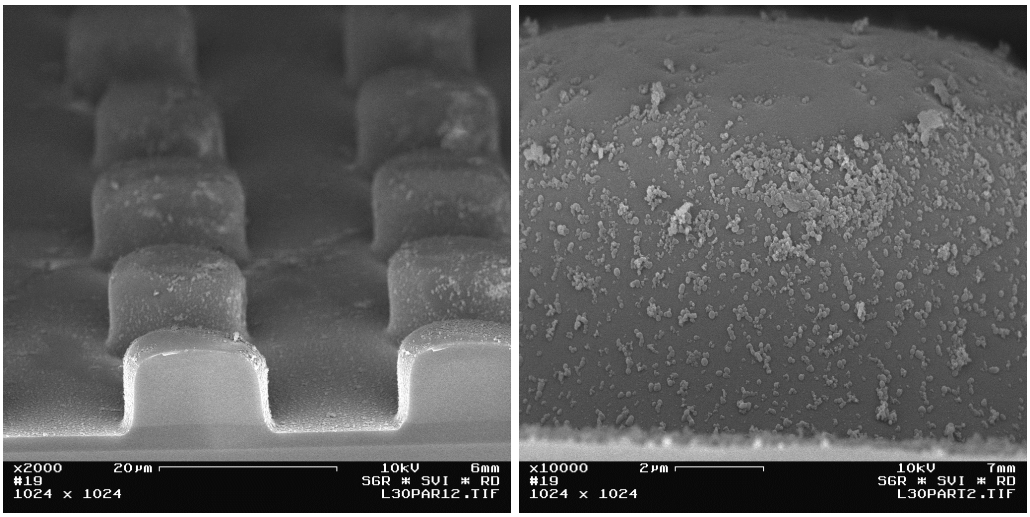

(a) (b)

Fig. 7.1 *The model surface can be covered by nanometer particles by dip-coating techniques. Here (a) and (b) are SEM images presented a 2D model surface covered by nanoparticles, observed at different scales. Images realized during the internship of Gaolei Zhan at SVI in 2014.*

Bibliography

[1] M. Singh & J. J. M. Braat; «Capping layers for extreme-ultraviolet multilayer interference coatings»; Opt. Lett. **26**, p. 259–261 (2001). 1

[2] Y. Wang & X. Jing; «Intrinsically conducting polymers for electromagnetic interference shielding»; Polymers for Advanced Technologies **16**, p. 344–351 (2005). 1

[3] N. Liu, T. Weiss, M. Mesch, L. Langguth, U. Eigenthaler, M. Hirscher, C. Sönnichsen & H. Giessen; «Planar Metamaterial Analogue of Electromagnetically Induced Transparency for Plasmonic Sensing»; Nano Letters **10**, p. 1103–1107 (2010). 1

[4] R. A. Shelby, D. R. Smith & S. Schultz; «Experimental Verification of a Negative Index of Refraction»; Science **292**, p. 77–79 (2001). 1

[5] N. I. Landy, S. Sajuyigbe, J. J. Mock, D. R. Smith & W. J. Padilla; «Perfect Metamaterial Absorber»; Phys. Rev. Lett. **100**, p. 207 402 (2008). 1

[6] T. Saison, C. Peroz, V. Chauveau, S. Berthier, E. Sondergard & H. Arribart; «Replication of butterfly wing and natural lotus leaf structures by nanoimprint on silica sol–gel films»; Bioinspiration Biomimetics **3**, p. 046 004. 2

[7] S.-H. Kang, T.-Y. Tai & T.-H. Fang; «Replication of butterfly wing microstructures using molding lithography»; Current Applied Physics **10**, p. 625 – 630 (2010); ISSN 1567-1739. 2

[8] D. Y. Lee, D. H. Lee, S. G. Lee & K. Cho; «Hierarchical gecko-inspired nanohairs with a high aspect ratio induced by nanoyielding»; Soft Matter **8**, p. 4905–4910 (2012). 2

[9] A. G. Voronovich; *Wave Scattering from Rough Surfaces* (Springer Berlin Heidelberg) (1994). 3, 6

[10] J. Bennett & L. Mattsson; *Introduction to surface roughness and scattering* (Optical Society of America) (1989). 3, 36

[11] P. Beckmann & A. Spizzichino; *The scattering of electromagnetic waves from rough surfaces* (1963). 3, 7, 8, 161

[12] M. Born & E. Wolf; *Principles of optics: electromagnetic theory of propagation, interference and diffraction of light*; 6e édition (Pergamon Press) (1980). 3, 145

[13] J. Lambert & E. Anding; *Photometrie: Photometria, sive De mensura et gradibus luminis, colorum et umbrae (1760)* (W. Engelmann) (1892). 3

[14] I. Simonsen; «Optics of surface disordered systems. A random walk through rough surface scattering phenomena»; European Physical Journal Special Topics (2010). 3, 115, 141

[15] J. C. Wyant; «White light interferometry»; Proc.SPIE (2002). 5

[16] Wikipedia; «Illuminant D65 — Wikipedia, The Free Encyclopedia»; (2018); online: accessed 19-July-2018. 5

[17] ANR; «Project-ANR-15-CHIN-0003»; (2018); online: accessed 22-October-2018. 5

[18] J. E. Harvey, N. Choi & A. Krywonos; «Scattering from moderately rough interfaces between two arbitrary media»; Proc.SPIE (2010). 7

[19] J. Qiu, W. J. Zhang, L. H. Liu, P. f. Hsu & L. J. Liu; «Reflective properties of randomly rough surfaces under large incidence angles»; J. Opt. Soc. Am. A (2014). 7

[20] M. Trost, S. Schröder, T. Feigl, A. Duparré & A. Tünnermann; «Influence of the substrate finish and thin film roughness on the optical performance of Mo/Si multilayers»; Appl. Opt. (2011). 7

[21] J. C. Stover; *Optical scattering: measurement and analysis*; 3e édition (SPIE Press) (2012). 7, 42

[22] B. Walter, S. R. Marschner, H. Li & K. E. Torrance; «Microfacet Models for Refraction Through Rough Surfaces»; dans «Proceedings of the 18th Eurographics Conference on Rendering Techniques», p. 195–206 (Eurographics Association, Aire-la-Ville, Switzerland, Switzerland) (2007). 7, 143, 144, 145, 152, 175

[23] S. K. Nayar, K. Ikeuchi & T. Kanade; «Surface Reflection: Physical and Geometrical Perspectives»; IEEE Trans. Pattern Anal. Mach. Intell. (1991). 7, 42, 57, 58, 102

[24] A. Ngan, F. Durand & W. Matusik; «Experimental Analysis of BRDF Models»; dans «Eurographics Symposium on Rendering (2005)», (The Eurographics Association) (2005). 7

[25] A. Krywonos; *Predicting surface scatter using a linear systems formulation of non-paraxial scalar diffraction*; Thèse de doctorat (2006). 8, 10

[26] J. Harvey, A. Krywonos & C. L. Vernold; «Modified Beckmann-Kirchhoff scattering model for rough surfaces with large incident and scattering angles»; Optical Engineering (2007). 8

[27] R. Montes & C. Ureña; «An Overview of BRDF Models»; Rapport technique; University of Granada (2012). 8, 142, 143

[28] T. M. Elfouhaily & C.-A. Guérin; «A critical survey of approximate scattering wave theories from random rough surfaces»; Waves in Random Media (2004). 8, 161

[29] R. G. Pinnick, D. E. Carroll & D. J. Hofmann; «Polarized light scattered from monodisperse randomly oriented nonspherical aerosol particles: measurements»; Appl. Opt. **15**, p. 384–393 (1976). 8

[30] P. J. Chandley; «Surface roughness measurements from coherent light scattering»; Optical and Quantum Electronics **8**, p. 323–327 (1976). 8, 102

[31] P. C. Colby, L. M. Narducci, V. Bluemel & J. Baer; «Light-scattering measurements from dense optical systems»; Phys. Rev. A **12**, p. 1530–1538 (1975). 8, 102

[32] K. A. O'Donnell & E. R. Mendez; «Experimental study of scattering from characterized random surfaces»; J. Opt. Soc. Am. A **4**, p. 1194–1205 (1987). 8, 102

[33] M.-J. Kim, J. C. Dainty, A. T. Friberg & A. J. Sant; «Experimental study of enhanced backscattering from one- and two-dimensional random rough surfaces»; J. Opt. Soc. Am. A **7**, p. 569–577 (1990). 8, 102

[34] W. Matusik, H. Pfister, M. Brand & L. McMillan; «A Data-driven Reflectance Model»; ACM Trans. Graph. (2003). 8, 9, 102

[35] M. Mcknight, T. V. Vorburger, E. Marx, M. la E. Nadal, P. Y. Barnes & M. Galler; «Measurements and predictions of light scattering by clear coatings.»; Applied optics (2001). 9, 10

[36] J. E. Proctor & P. Y. Barnes; «NIST High Accuracy Reference Reflectometer-Spectrophotometer»; (1996). 9

[37] S. Schröder, A. Duparré, L. Coriand, A. Tünnermann, D. H. Penalver & J. E. Harvey; «Modeling of light scattering in different regimes of surface roughness»; Opt. Express (2011). 10, 161

[38] Z. Dong, B. Walter, S. Marschner & D. P. Greenberg; «Predicting Appearance from Measured Microgeometry of Metal Surfaces»; ACM Trans. Graph. (2015). 10, 161

[39] Glassnews; «SGG Decorglass: Exclusive Range of Traditional Patterned Glasses»; (2018); online; accessed 22-October-2018. 11

[40] P. Rai-Choudhury; *Handbook of Microlithography, Micromachining, and Microfabrication* (SPIE Optical Engineering Press) (1997). 16

[41] W. W. Hu, K. Sarveswaran, M. Lieberman & G. H. Bernstein; «Sub-10 nm electron beam lithography using cold development of poly(methylmethacrylate)»; Journal of Vacuum Science & Technology B: Microelectronics and Nanometer Structures Processing, Measurement, and Phenomena (2004). 16

[42] S. Y. Chou, P. R. Krauss & P. J. Renstrom; «Nanoimprint lithography»; Journal of Vacuum Science & Technology B: Microelectronics and Nanometer Structures Processing, Measurement, and Phenomena (1996). 16

[43] B. Brudieu; *Matériaux pour la gestion de la lumière fabriqués par voie liquide*; Thèse de doctorat; Univ. Pierre et Marie Curie (2015). 16

[44] P. Jacquet; *Vers la compréhension et le contrôle du démouillage de couches d'argent*; Thèse de doctorat; Univ. Pierre et Marie Curie (2017). 16

[45] A. L. Dubov, K. Perez-Toralla, A. Letailleur, E. Barthel & J. Teisseire; «Superhydrophobic silica surfaces: fabrication and stability»; Journal of Micromechanics and Microengineering (2013). 16, 70

[46] M. Rivetti, J. Teisseire & E. Barthel; «Surface Fraction Dependence of Contact Angles Induced by Kinks in the Triple Line»; Phys. Rev. Lett. (2015). 16

[47] B. Brudieu, I. Gozhyk, W. R. Clements, S. Mazoyer, T. Gacoin & J. Teisseire; «Scalable simple liquid deposition techniques for the enhancement of light absorption in thin films: Distributed Bragg reflectors coupled to 1D nanoimprinted textures»; AIP Advances (2017). 16

[48] B. Brudieu, A. Le Bris, J. Teisseire, F. Guillemot, G. Dantelle, S. Misra, P. R. I. Cabarrocas, F. Sorin & T. Gacoin; «Sol-gel route toward efficient and robust Distributed Bragg Reflector for light management applications»; Advanced Optical Materials . 17

[49] J. Teisseire, A. Revaux, M. Foresti & E. Barthel; «Confinement and flow dynamics in thin polymer films for nanoimprint lithography»; Applied Physics Letters (2011). 22

[50] L. Slătineanu, Ş. Potârniche, M. Coteaţă, I. Grigoraş, L. Gherman & F. Negoescu; «Surface roughness at aluminium parts sand blasting»; Proceedings in Manufacturing Systems **6** (2011). 25

[51] R. Ourahmoune, M. Salvia, T. Mathia & N. Mesrati; «Surface morphology and wettability of sandblasted PEEK and its composites: Surface morphology and wettability»; Scanning . 26

[52] M. Schwankl, R. Kellner, R. F. Singer & C. Körner; «The influence of sandblasting on the morphology of electroless deposited zinclayers on aluminum sheets»; Applied Surface Science (2013). 26

[53] *ASM Handbook, Volume 2: Properties and Selection: Nonferrous Alloys and Special-Purpose Materials*; chapitre Properties of Wrought Aluminum and Aluminum Alloys, p. 622–122 (ASM International) (1990). 26

[54] Z. Li, G. Winther & N. Hansen; «Anisotropy in rolled metals induced by dislocation structure»; Acta Materialia **54**, p. 401 – 410 (2006). 26

[55] J. Frayret, O. Eterradossi, A. Castetbon, M. Potin-Gautier, G. Trouvé & H. de Roulhac; «Determination of the correlation between physical measurements of roughness, optical properties, and perception of frosted glass surfaces»; Applied Optics (2008). 30

[56] Z. Pápa, J. Budai, B. Farkas & Z. Toth; «Investigation of surface roughness on etched glass surfaces»; Thin Solid Films (2011). 30

[57] Cultilene; «Horticulture glass»; Online: accessed 22-October-2018. 30

[58] C. Oatley, W. Nixon & R. Pease; «Scanning Electron Microscopy»; p. 181 – 247 (Academic Press) (1966). 36

[59] G. Binnig, C. F. Quate & C. Gerber; «Atomic Force Microscope»; Phys. Rev. Lett. **56**, p. 930–933 (1986). 36, 39

[60] J. M. Bennett; *Characterization of Surface Roughness*; p. 1–33 (Springer US) (2007). 36, 42

[61] J. M. Bennett; «Measurement of the rms roughness, autocovariance function and other statistical properties of optical surfaces using a FECO scanning interferometer»; Applied Optics (1976). 36

[62] C. Y. Poon & B. Bhushan; «Comparison of surface roughness measurements by stylus profiler, AFM and non-contact optical profiler»; Wear (1995). 36

[63] A. Duparré, J. Ferre-Borrull, S. Gliech, G. Notni, J. Steinert & J. M. Bennett; «Surface characterization techniques for determining the root-mean-square roughness and power spectral densities of optical components»; Appl. Opt. (2002). 36, 55

[64] F. Blateyron; *Chromatic Confocal Microscopy* (Leach, Richard) (2011). 37

[65] W. Smith; *Modern Optical Engineering, 4th Ed.*; chapitre 3 - Aberrations, p. 61–90; McGraw Hill professional (McGraw-Hill Education) (2007). 37

[66] H.-J. Jordan, M. Wegner & H. Tiziani; «Highly accurate non-contact characterization of engineering surfaces using confocal microscopy»; Measurement Science and Technology **9**, p. 1142 (1998). 37

[67] G. Udupa, M. Singaperumal, R. S. Sirohi & M. P. Kothiyal; «Characterization of surface topography by confocal microscopy: I. Principles and the measurement system»; Measurement Science and Technology **11**, p. 305 (2000). 37

[68] Nanofocus; «Chromatic sensor - CLA»; (2018); online: accessed 22-October-2018. 38

[69] «Characterisation of membrane surfaces: direct measurement of biological adhesion using an atomic force microscope»; Journal of Membrane Science **154**, p. 205 – 212 (1999). 39

[70] Z. Yiping, W. Gwo-Ching & L. Toh-Ming; «2. - Statistical Nature of Rough Surfaces»; dans «Characterization of Amorphous and Crystalline Rough Surface: Principles and Applications», (Academic Press) (2001). 42, 49

[71] J. M. Elson & J. M. Bennett; «Calculation of the power spectral density from surface profile data»; Appl. Opt. (1995). 43, 49

[72] T. D. B. Jacobs, T. Junge & L. Pastewka; «Quantitative characterization of surface topography using spectral analysis»; Surface Topography: Metrology and Properties (2017). 43, 54

[73] F. Dekking, C. Kraaikamp, H. Lopuhaä & L. Meester; *A Modern Introduction to Probability and Statistics: Understanding Why and How*; chapitre 9 - Joint distributions and independence, p. 115–134 (Springer) (2005). 44

[74] W. H. Press, B. P. Flannery, S. A. Teukolsky & W. T. Vetterling; *Numerical Recipes in Fortran 77: The Art of Scientific Computing*; chapitre Fast Fourier Transform, p. 490 – 520 (Cambridge University Press) (1992). 49, 50

[75] J. C. Stover; *Optical scattering: measurement and analysis*; chapitre 2 - Quantifying Surface Roughness, p. 23–45; 3^{e} édition (SPIE Press, Bellingham, Washington) (2012). 49, 51

[76] E. L. Church & P. Z. Takacs; *Handbook of Optics: Fundamentals, techniques, and design*; chapitre SURFACE SCATTERING (McGraw-Hill) (1994). 53

[77] A. Gujrati, S. R. Khanal, L. Pastewka & T. D. B. Jacobs; «Combining TEM, AFM, and Profilometry for Quantitative Topography Characterization Across All Scales»; ACS Applied Materials & Interfaces **10**, p. 29 169–29 178 (2018). 55

[78] S. Gupta & S. G. Mazumdar; «Sobel Edge Detection Algorithm»; (2013). 58

[79] R. Y. Takimoto, M. de Sales Guerra Tsuzuki, E. K. Ueda, A. K. Sato, T. de Castro Martins, T. Cousseau, D. Tanaka & A. Sinatora; «Rough Surface Wear Analysis Using Image Processing Techniques»; IFAC-PapersOnLine **49**, p. 7 – 12 (2016). 58

[80] A. A. Maradudin, T. Michel, A. R. McGurn & E. R. Méndez; «Enhanced backscattering of light from a random grating»; Ann. Phys. **203**, p. 255–307 (1990). 64

[81] «Light scattering from anisotropic, randomly rough, perfectly conducting surfaces»; Computer Physics Communications **182**, p. 1904 – 1908 (2011). 64

[82] U. D. Schwarz, H. Haefke, P. Reimann & H.-J. Güntherodt; «Tip artefacts in scanning force microscopy»; Journal of Microscopy (1994). 70

[83] C. Peroz, C. Heitz, E. Barthel, E. Sondergård & V. Goletto; «Glass nanostructures fabricated by soft thermal nanoimprint»; Journal of Vacuum Science & Technology B: Microelectronics and Nanometer Structures (2007). 70

[84] J. J. Koenderink & A. J. van Doorn; «Surface shape and curvature scales»; Image and Vision Computing (1992). 80

[85] S. van der Walt, J. L. Schönberger, J. Nunez-Iglesias, F. Boulogne, J. D. Warner, N. Yager, E. Gouillart, T. Yu & the scikit-image contributors; «scikit-image: image processing in Python»; PeerJ **2**, p. e453 (2014). 80

[86] V. Pejchal, G. Zagar, M. Fornabaio, R. Charvet, C. Denerez & A. Mortensen; «Measuring the strength of brittle microscopic spheres by means of compression tests»; (2015). 82

[87] S. D. Mesarovic & N. A. Fleck; «Spherical indentation of elastic-plastic solids»; Proceedings of the Royal Society A: Mathematical, Physical and Engineering Sciences (1999). 82

[88] I. Hutchings; «A model for the erosion of metals by spherical particles at normal incidence»; Wear **70**, p. 269 – 281 (1981). 82

[89] S. Walley, J. Field & P. Yennadhiou; «Single solid particle impact erosion damage on polypropylene»; Wear **100**, p. 263 – 280 (1984). 82

[90] G. J. Ward; «Measuring and Modeling Anisotropic Reflection»; SIGGRAPH Comput. Graph. **26**, p. 265–272 (1992); ISSN 0097-8930. 102

[91] S. R. Marschner, S. H. Westin, E. P. F. Lafortune, K. E. Torrance & D. P. Greenberg; «Image-Based BRDF Measurement Including Human Skin»; dans «Rendering Techniques' 99», p. 131–144 (Lischinski, Dani and Larson, Greg Ward) (1999). 102

[92] K. J. Dana, B. van Ginneken, S. K. Nayar & J. J. Koenderink; «Reflectance and Texture of Real-world Surfaces»; ACM Trans. Graph. **18**, p. 1–34 (1999); ISSN 0730-0301. 102

[93] G. Ged, G. Obein, Z. Silvestri, J. Le Rohellec & F. Vienot; «Recognizing real materials from their glossy appearance»; Journal of Vision (2010). 102

[94] G. Ged; *Métrologie du brillant : développement et caractérisation psychophysique d'échelles de brillants*; Thèse de doctorat; Conservatoire National des Arts et Metiers (2017). 102, 108, 118

[95] G. Westheimer; «Neural principles in vision»; Journal of Neurobiology **8**, p. 395–395 (1976). 102

[96] ISO; «Paints and varnishes – Determination of gloss value at 20 degrees, 60 degrees and 85 degrees»; (2014). 103, 104, 114

[97] E. D. Palik; *Handbook of Optical Constants of Solids*; chapitre 2 - Refractive Index (Academic Press) (1997). 103

[98] F. Leloup, P. Hanselaer, j. versluys & S. A. B. Forment; «BRDF and gloss measurements»; CIE (Commission International d'Eclairage) (2007). 104

[99] ASTM; «Standard Test Method for Haze and Luminous Transmittance of Transparent Plastics»; (2013). 105

[100] F. E. Nicodemus; «Directional Reflectance and Emissivity of an Opaque Surface»; Appl. Opt. (1965). 105

[101] W. C. Snyder; «Reciprocity of the bidirectional reflectance distribution function (BRDF) in measurements and models of structured surfaces»; IEEE Transactions on Geoscience and Remote Sensing **36**, p. 685–691 (1998). 106

[102] Hoskin-Scientifique; «Goniophotometre»; Online: accessed 24-October-2018. 108

[103] Eldim; «Optical metrology»; Online: accessed 24-October-2018. 108

[104] Radiant-Imaging; «Radiant vision systems products»; Online: accessed 24-October-2018. 108

[105] ANSYS-OPTIS; «Add realism to your simulation»; Online: accessed 24-October-2018. 108

[106] M. G. Moharam & T. K. Gaylord; «Rigorous coupled-wave analysis of planar-grating diffraction»; J. Opt. Soc. Am. **71**, p. 811–818 (1981). 115

[107] M. G. Moharam & T. K. Gaylord; «Diffraction analysis of dielectric surface-relief gratings»; J. Opt. Soc. Am. **72**, p. 1385–1392 (1982). 115

[108] S. S. Wang, R. Magnusson, J. S. Bagby & M. G. Moharam; «Guided-mode resonances in planar dielectric-layer diffraction gratings»; J. Opt. Soc. Am. A **7**, p. 1470–1474 (1990). 115

[109] D. Maystre; «Diffraction gratings»; Scholarpedia **7**, p. 11 403 (2012). 115

[110] J. C. Stover; *Optical scattering: measurement and analysis*; chapitre 1 - Quantifying Light Scattering, p. 1–22; 3^{e} édition (SPIE Press, Bellingham, Wash) (2012). 115

[111] A. Kumar & G. M. Whitesides; «Patterned Condensation Figures as Optical Diffraction Gratings»; Science **263**, p. 60–62 (1994). 115

[112] C. Turbil, I. Gozhyk, J. Teisseire, I. Simonsen, G. Ged & G. Obein; «Predicting changes in visual appearance of periodic surface from brdf measurements»; (CIE Expert Symposium on Visual Appearance) (2016). 118

[113] C. Turbil, T. Sang HyukYoo, I. Simonsen, J. Teisseire, I. Gozhyk & E. Garcia-Caurel; «Impact of light diffraction on haze and gloss in transmission through supported micro-pillar arrays»; arXiv:1810.09972v1 [physics.optics] (2018). 118, 172

[114] K. Kunz; *The Finite Difference Time Domain Method for Electromagnetics* (CRC Press) (1993). 120

[115] Wikipedia; «Airy disk»; (2018); online: accessed 24-October-2018. 121

[116] I. Lindseth, A. Bardal & R. Spooren; «Reflectance measurements of aluminium surfaces using integrating spheres»; Optics and Lasers in Engineering **32**, p. 419 – 435 (1999). 126

[117] I. M. Fuks; «Theory of radio wave scattering at a rough sea surface»; Soviet Radiophysics **9**, p. 513–519 (1966). 141

[118] P. Beckmann; «Radar backscatter from the surface of the Moon»; Journal of Geophysical Research **70**, p. 2345–2350 (1965). 141

[119] E. Heitz; «Understanding the Masking-Shadowing Function in Microfacet-Based BRDFs»; Journal of Computer Graphics Techniques (JCGT) **3**, p. 48–107 (2014). 143

[120] K. E. Torrance & E. M. Sparrow; «Theory for Off-Specular Reflection From Roughened Surfaces∗»; J. Opt. Soc. Am. **57**, p. 1105–1114 (1967). 144

[121] R. L. Cook & K. E. Torrance; «A Reflectance Model for Computer Graphics»; ACM Trans. Graph. **1**, p. 7–24 (1982). 144

[122] «SciPy: Open source scientific tools for Python»; (2001–); online: accessed 24-October-2018. 146

[123] «Optical constants of Al (Aluminium)»; (2008–2018); online: accessed 24-October-2018. 148

[124] O. S. Hetland, A. A. Maradudin, T. Nordam, P. A. Letnes & I. Simonsen; «Numerical studies of the transmission of light through a two-dimensional randomly rough interface»; Phys. Rev. A **95**, p. 043 808 (2017). 161

[125] T. Nordam, P. A. Letnes & I. Simonsen; «Validity of the Rayleigh hypothesis for two-dimensional randomly rough metal surfaces»; Journal of Physics: Conference Series **454**, p. 012 033 (2013). 161

[126] D. Strand, T. Nesse, J. B. Kryvi, T. S. Hegge & I. Simonsen; «Wave scattering from two-dimensional self-affine Dirichlet and Neumann surfaces and its application to the retrieval of self-affine parameters»; Phys. Rev. A **97**, p. 063 825 (2018). 162, 163, 164